Optical preparation and detection of spin coherence in molecules and crystal defects

university of
groningen

zernike institute for
advanced materials

Zernike Institute PhD thesis series 2020-01
ISSN: 1570-1530
ISBN: 978-94-034-2204-6 (printed version)
ISBN: 978-94-034-2203-9 (electronic version)

The work described in this thesis was performed in the research groups Physics of Nanodevices and Theoretical Chemistry of the Zernike Institute for Advanced Materials at the University of Groningen, the Netherlands. The project was funded by the Zernike Institute.

Printed by: Ipskamp Printing, Enschede

university of
groningen

Optical preparation and detection of spin coherence in molecules and crystal defects

PhD thesis

to obtain the degree of PhD at the
University of Groningen
on the authority of the
Rector Magnificus Prof. C. Wijmenga
and in accordance with
the decision by the College of Deans.

This thesis will be defended in public on

Friday 10 January 2020 at 14.30 hours

by

Gerrit Jan Jacob Lof

born on 30 March 1988
in Capelle aan den IJssel, the Netherlands

Supervisors
Prof. C. H. van der Wal
Prof. M. A. Loi

Co-supervisor
Dr. R. W. A. Havenith

Assessment committee
Prof. H. B. Braam
Prof. M. Orrit
Prof. J. Koehler

Contents

Chapter 1

Introduction

1.1 Coherence and polarization of electron spins and photons

For a physical description of the interaction of light and matter, electron spin and polarization of light are of profound importance. Although these concepts have been thoroughly investigated, our understanding of their interaction is far from complete. Common text book examples are e.g. the optical selection rules for the hydrogen atom and GaAs, which are well understood and widely applied for the orientation and probing of spin in these systems. On the other hand, the electronic spin and optical properties of more complex atomic structures such as molecules and crystal defects (with lower symmetry) have not been fully explored. Consequently, modern technology does not fully exploit their potential. The aim of this thesis is to advance the understanding of how optical fields can control and probe electronic spin coherence in molecules and crystal defects.

In 1808, Malus introduced the name polarization for light, while in 1669 already an effect due to light polarization (double refraction) had been reported by Bartholin[1]. The concept of light polarization is used in many applications. Optical communication, however, is mainly based on the detection of light intensity, such that each photon carries at most one bit of information. A polarized photon is said to be in a coherent superposition of polarization states. When information is encoded in the polarization of a photon, each photon can contain a much higher information density, where the practical limitation is set by the ability to discriminate between different polarization states.

In 1925, Uhlenbeck and Goudsmit proposed the concept of spin[2], based on the observation of anisotropic magnetoresistance in 1857[3], and the Stern-

Gerlach experiment in 1922[4]. The most common manifestation of electron spins is in the form of magnetism, for which more and more technological applications are found. Still, within electronic information processing, a bit of information is usually based on the absence or presence of charge. Analogous to polarized photons, spin polarized electrons allow for a larger information density. Also, they are believed to allow for information processing at much lower energy cost. Electron spin polarization occurs when there is a surplus of a certain spin substate, i.e. an imbalance in the (spin-up and spin-down) populations (diagonal elements of the density matrix[5]). For an electron spin brought in a coherent superposition of spin states, the coherences (off-diagonal elements of the density matrix) and spin expectation value oscillate with the so-called Bohr frequencies of the system[5]. Measuring such spin precession instead of merely spin orientation has the experimental advantage that it is much easier to trace back the origin of a small signal when it oscillates. Moreover, one can learn about decoherence and dephasing mechanisms in addition to population relaxation. The electron spin seems very promising to revolutionize electronics[6], particularly through exploiting new (quantum mechanical) concepts like superposition[7] and entanglement[8].

In material systems with selective coupling of photons to electronic spin, they form an attractive pair for opto-electronic functionalities and the transfer of quantum information. This introductory chapter will review different ways to all-optically induce spin coherence (and probe spin dynamics) in various materials, and introduce main concepts that will be used in this thesis. The chapter ends with introducing the specific questions that were addressed in this PhD research, and providing a thesis outline.

1.2 Optical orientation

In many materials, there is naturally an equal amount of both up and down spins. However, in the field of spintronics, which aims to exploit the electron spin, it is important to be able to manipulate the population of spin (or in general total angular momentum) sublevels. More advanced quantum technologies also rely on controlling quantum coherence between spin sublevels. Spin polarization implies an excess of up or down spin, which might e.g. be obtained by applying a strong magnetic field. Alternatively, it can be obtained with a technique called optical orientation (also known as optical spin injection)[9, 10]. Here, an imbalance in the population of spin sublevels is based on different transition strengths for sublevel

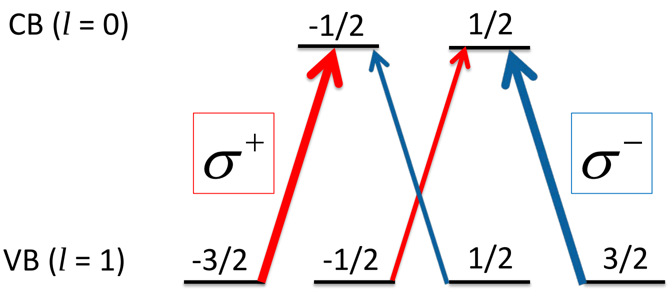

Figure 1.1: Optical selection rules for interband transitions in GaAs for circularly polarized light. The valence band (VB) levels resemble $p_{j=3/2}$ levels of the hydrogen atom, whereas the conduction band (CB) resembles $s_{j=1/2}$ levels. The levels are labeled with m_j-values. The oscillator strengths f of the allowed circular transitions have ratio 1 : 3, where the strong transitions are indicated by thick arrows.

transitions.

Let us as an example consider a direct gap III-V semiconductor like GaAs (with the energy level scheme given in Fig. 1.1). The conduction band (CB) consists of s-like atomic states ($l = 0$), while the valence band (VB) consists of p-like states ($l = 1$). Since electrons and holes have spin $s = 1/2$, the CB consists of a $j = 1/2$ level, while the VB consists of $j = 1/2$ and $j = 3/2$. Due to spin-orbit coupling (SOC) the VB splits, with the $j = 3/2$ level becoming higher in energy.

The VB levels resemble $p_{j=3/2}$ levels of the hydrogen atom, whereas the CB resembles $s_{j=1/2}$ levels. The oscillator strengths f of the allowed circular transitions have ratio 1 : 3, thereby resembling the optical selection rules of hydrogen (Section 2.10, Table 2.5). As illustrated in Fig. 1.1, $\sigma^{\pm}$ light generates three times more electrons with $m_{j=\mp 1/2}$ than with $m_{j=\pm 1/2}$ (when all ground state sublevels are originally equally occupied), thereby inducing spin polarization.

1.3 Spin precession

The Time-Resolved Kerr Readout (TRKR) and Time-Resolved Faraday Rotation (TRFR) technique are techniques (based on the magneto-optical Kerr effect) used to detect spin dynamics and to measure the corresponding lifetime[12, 13]. The difference between TRKR and TRFR is the use of reflected and transmitted light, respectively. These techniques have been applied to many solid state systems like e.g. GaAs. The techniques are optical pump-probe methods with picosecond laser pulses tuned near resonance with transitions across the band gap.

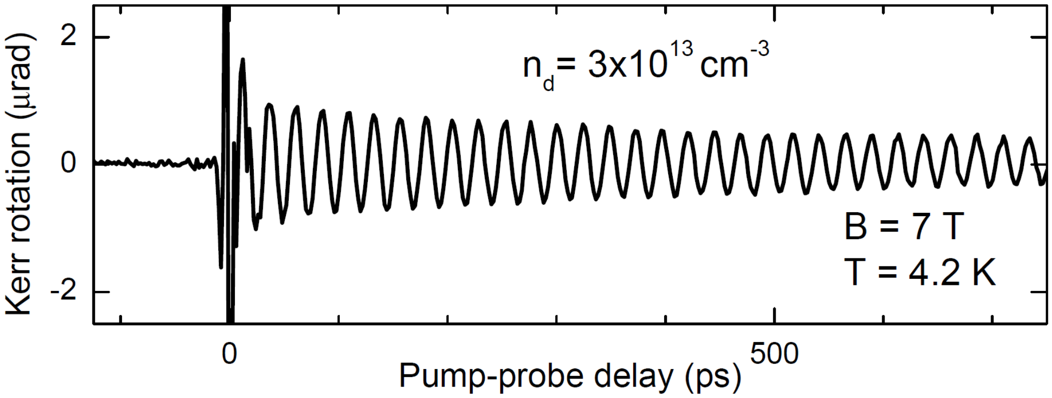

Figure 1.2: Typical result of a Time-Resolved Kerr Rotation (TRKR) experiment, with the Kerr rotation angle as a function of pump-probe delay. The oscillatory character reflects spin precession about the magnetic field. Figure adapted from [11].

Spin polarization is induced with a polarized pump pulse. Let us assume that at time $t = t_{pump}$ the system of Fig. 1.1 is excited with a σ^+ pump pulse propagating along x (with originally the ground state sublevels equally populated), causing population imbalance of the m_j sublevels (in the x-basis) of the excited state, i.e. spin polarization (along the x-axis). With a magnetic field in the z-direction, Larmor spin precession occurs during the interval (t_{pump}, t_{probe}), where the system is in the dark. The spin precesses around the z-axis implying that the expectation value $\langle S_x \rangle (t)$ oscillates. The same holds for $\langle S_y \rangle (t)$, but usually spin precession is measured in one direction only. The precession corresponds to population transfer between the m_j sublevels (in the x-basis).

To detect the spin dynamics, a polarized probe pulse is used. A linearly polarized (denoted as π; here referring to the polarization and not the duration of a pulse) probe pulse propagating in the x-direction arrives at delay time $\Delta t = t_{probe} - t_{pump}$. If the system at time t_{probe} has a net spin polarization, an interesting phenomenon occurs. The unequal filling of the up and down spin sublevels of the conduction band gives rise to a difference in the absorption coefficient for σ^+ and σ^-, resulting in a different refractive index through the Kramers-Kronig relation. Given that π is a superposition of σ^+ and σ^-, a polarization rotation of the linearly polarized probe is induced after interaction with the sample. This rotation angle is called the Kerr or Faraday rotation angle, depending on whether TRKR or TRFR is applied. A typical measurement result of the TRKR technique is depicted in Fig. 1.2, where each data point is obtained from a seperate TRKR measurement[11, 14].

1.4 Coherent population trapping

An alternative way to optically induce spin coherence is via a phenomenon known as coherent population trapping (CPT)[15], which is of great significance in quantum-optical operations that use ground-state spin coherence. This phenomenon occurs when two lasers address a so-called Λ system (with its name derived from the arrows in Fig. 1.3 forming the shape of a Λ) at exact two-photon resonance, i.e. when the two-laser detuning matches the ground-state splitting, as in Fig. 1.3. The ground-state spin system is then driven towards a superposition state that approaches $|\Psi_{CPT}\rangle \propto \Omega_2 |g_1\rangle - \Omega_1 |g_2\rangle$ for ideal spin coherence. Here Ω_n is the Rabi frequency for the driven transition from the $|g_n\rangle$ state to the common excited state. Since the system is now coherently trapped in the ground state, the photoluminescence decreases.

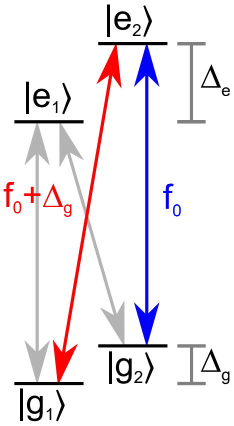

Figure 1.3: Two-laser Λ scheme with optical transitions between $S = 1/2$ ground and excited state sublevels. Two lasers are resonant with transitions from both ground state sublevels $|g_1\rangle$ (red arrow) and $|g_2\rangle$ (blue arrow) to a common excited state sublevel $|e_2\rangle$. This is achieved when the detuning equals the ground-state splitting Δ_g. The gray arrows indicate a secondary Λ scheme via $|e_1\rangle$.

1.5 Jones calculus

To describe how polarized light is affected by interaction with an optical element (or a sample), it is often convenient to use Jones calculus[16] (see also Supplementary Information Section 2.12 (p. 41)). Within this method, light is represented by a Jones vector and the optical element by a Jones matrix. The Jones vector contains the amplitude and phase of the electric field components of the beam

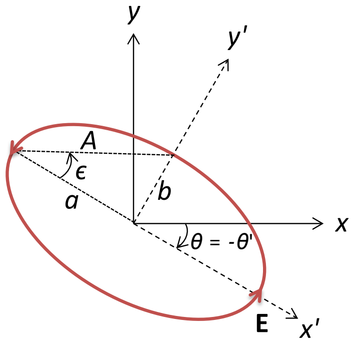

Figure 1.4: The polarization ellipse. The main parameters that define the polarization ellipse are the azimuth θ of the semi-major axis a with respect to the x-axis, and the ellipticity angle ϵ, which is defined through the ellipticity $e = \frac{b}{a}$ (with b the semi-minor axis) such that $e = \pm \tan \epsilon$, where the + and - signs correspond to right- and left-handed polarization respectively. The total amplitude of the electric field is given by $A = \sqrt{a^2 + b^2}$. For convenience, one usually takes $A = 1$. It is also common to assume a global phase factor $\delta = 0$.

orthogonal to its propagation direction. Commonly, the amplitudes are normalized, such that their intensities add up to 1. Any elliptical polarization can be described, including the special cases of linear and circular polarization.

A convenient way to visualize the Jones vector is the polarization ellipse, which is mainly described by the azimuth θ and the ellipticity angle ϵ, as illustrated in Fig. 1.4. Here, the azimuth θ is the angle between the semi-major axis a and the horizontal x-axis, where $-\frac{1}{2}\pi \leqslant \theta \leqslant \frac{1}{2}\pi$. The ellipticity angle ϵ is defined through the ellipticity $e = \frac{b}{a}$ (with b the semi-minor axis) such that $e = \pm \tan \epsilon$, where $-\frac{1}{4}\pi \leqslant \epsilon \leqslant \frac{1}{4}\pi$. The + and − signs correspond to right- and left-handed polarization respectively. In Fig. 1.4 the indicated polarization is left-handed.

Within the $\{\hat{\mathbf{x}}', \hat{\mathbf{y}}'\}$-basis, the corresponding Cartesian Jones vector of a light beam with azimuth $\theta' = 0$ with respect to the x'-axis is given by the unit vector

$$\hat{\mathbf{E}}\{\hat{\mathbf{x}}', \hat{\mathbf{y}}'\} = \begin{bmatrix} \cos(\epsilon) \\ i \sin(\epsilon) \end{bmatrix} \tag{1.1}$$

with amplitude $A = 1$ and global phase $\delta = 0$. This Jones vector can be transformed through a counter-clockwise rotation $\theta' = -\theta$ to

$$\hat{\mathbf{E}}\{\hat{\mathbf{x}}, \hat{\mathbf{y}}\} = T(-\theta) \begin{bmatrix} \cos(\epsilon) \\ i \sin(\epsilon) \end{bmatrix} = \begin{bmatrix} \cos(\theta)\cos(\epsilon) - i \sin(\theta)\sin(\epsilon) \\ \sin(\theta)\cos(\epsilon) + i \cos(\theta)\sin(\epsilon) \end{bmatrix} \tag{1.2}$$

with azimuth $\theta = -\theta'$ (w.r.t the x-axis) and ellipticity angle ϵ. A convenient method to visualize the Jones vector is via the Poincaré-sphere representation. Within this method, the longitude 2θ and latitude 2ϵ determine a point representing the ellipse of polarization with azimuth θ and ellipticity angle ϵ (Fig. 2.4a).

When light crosses an optical element the resulting polarization of the emerging light is found by taking the product of the Jones matrix J of the optical element and the Jones vector $\mathbf{E}_{in}$ of the incident light, which in the $\{\hat{\mathbf{x}}, \hat{\mathbf{y}}\}$-basis implies

$$\mathbf{E}_{out}\{\hat{\mathbf{x}}, \hat{\mathbf{y}}\} = J\{\hat{\mathbf{x}}, \hat{\mathbf{y}}\}\mathbf{E}_{in}\{\hat{\mathbf{x}}, \hat{\mathbf{y}}\} = J\{\hat{\mathbf{x}}, \hat{\mathbf{y}}\} \begin{bmatrix} E_{in,x} \\ E_{in,y} \end{bmatrix}. \tag{1.3}$$

To build $J\{\hat{\mathbf{x}}, \hat{\mathbf{y}}\}$ we first build $J\{\hat{\mathbf{x}}', \hat{\mathbf{y}}'\}$, which describes how light defined in the $\{\hat{\mathbf{x}}', \hat{\mathbf{y}}'\}$-basis is affected, i.e.

$$\mathbf{E}_{out}\{\hat{\mathbf{x}}', \hat{\mathbf{y}}'\} = J\{\hat{\mathbf{x}}', \hat{\mathbf{y}}'\}\mathbf{E}_{in}\{\hat{\mathbf{x}}', \hat{\mathbf{y}}'\}. \tag{1.4}$$

The Jones matrix is given by

$$J\{\hat{\mathbf{x}}', \hat{\mathbf{y}}'\} = \begin{bmatrix} \mathrm{e}^{i\Lambda n_{x'}} & 0 \\ 0 & \mathrm{e}^{i\Lambda n_{y'}} \end{bmatrix} \tag{1.5}$$

which expresses the retardation of (light polarized along) principal axis $\hat{\mathbf{j}}$ by Λn_j where $\Lambda \equiv 2\pi d/\lambda$, with d the thickness of the sample and λ the wavelength of the light[16].

1.6 Theoretical chemistry methods

The elegance of theoretical chemistry (and physics) calculations and predictions is that properties of matter can be revealed independent of experiments. In this section the theoretical chemistry methods are introduced that are used throughout this work. The methods belong to the realm of quantum chemistry (also known as molecular quantum mechanics), which is a branch of theoretical chemistry aimed to apply quantum mechanics in physical models of chemical systems. As with real experiments, calculations become usually increasingly complicated and expensive with increasing size of the system. To gain better insight into and intuition for chemical and physical properties, it is convenient to first apply theoretical chemistry calculations to a small model system, often allowing for general predictions about more complex matter. For that reason we consider in Chapter 2 the hydrogen atom as a model system. The knowledge obtained here serves as a theoretical basis for Chapter 3, where several metal-organic molecules are investigated. The main theoretical chemistry method for both chapters is the so-called CASSCF/CASPT2/RASSI–SO method[17, 18], which is an expensive though accurate method for chemical systems to study effects related to spin-orbit coupling (SOC). Additionally, in the Supplementary Information of Chapter 3 also several calculations have been performed based on the density-functional theory (DFT) method, which is one of the most popular quantum chemistry methods due to its versatility and relatively low computational cost.

It is well-known that relativistic effects affect atomic and molecular properties[19–22], particularly when heavy atoms are involved. To account in an accurate way for such effects on excited state properties of molecular systems, the CASSCF/CASPT2/RASSI–SO method was introduced by Roos and Malmqvist[17, 18] (within the quantum chemistry software package MOLCAS[23]). This is a multiconfigurational approach where relativistic effects are treated in two steps, both based on the Douglas–Kroll Hamiltonian[18]. Scalar terms are included in the basis set generation and used to determine wave functions and energies, which include static (through the use of the CASSCF method[24]) and dynamic correlation effects (using multiconfigurational perturbation theory, CASPT2[25, 26]). SOC is added a posteriori by means of the RASSCF state interaction (RASSI[27]) method.

Density functional theory (DFT) is a quantum chemistry method based on the Hohenberg-Kohn (HK) theorem[28], which investigates the electronic structure of many-body systems. Electronic properties can be determined using the spatially dependent electron density functional (i.e. it is a function of another function). The main disadvantage of DFT is the lack of a systematic approach to improve results towards an exact solution[24]. To investigate electronic properties in the presence of time-dependent potentials like electromagnetic waves, time-dependent DFT (TDDFT) is a convenient method, based on the Runge-Gross theorem[29], which is the time-dependent analogue of the HK theorem. In our TDDFT calculations SOC was included perturbatively[30]. For the DFT calculations in this work, we used the Amsterdam Density Functional (ADF) program[31, 32].

1.7 Scope of this research and thesis outline

This thesis focuses on theoretical and experimental studies of optical preparation and detection of spin coherence in molecules and crystal defects. The scientific progress of this work expands the range of material systems that can have functionalities based on the selective coupling of photons to electronic spin states. Also, it allows for a better opto-electronic characterization of these materials by providing new probing tools. The work consists of a theoretical investigation of underlying fundamentals and forthcoming requirements (Chapter 2-4), and experimental work on a crystal defect in silicon carbide, demonstrating optical characterization of its spin properties and optically induced electron spin coherence (Chapter 5).

Chapter 2 presents a theoretical study of how charged items in the environment of a hydrogen atom perturb its polarization selection rules. We focus on the optical transitions between $1s$ and $2p$ sublevels of the hydrogen atom. We investigate the effect of a gradual distortion of the symmetry by surrounding charges, which provides insight in the gradual evolution of the polarization selection rules. This ability to manipulate optical selection rules allows for better control of the interaction between photons and electrons, which potentially allows for new mechanisms to control the flow of quantum information. Also, this study provides a useful theoretical framework for the more complex systems of later chapters focusing on molecules and crystal defects.

The enormous variety of molecules and their ease of processing make them interesting candidates for many applications. Metal-organic molecules can have large spin-orbit coupling (SOC), which may facilitate mechanisms for optical spin manipulation. The Time-Resolved Faraday Rotation technique (TRFR, already widely applied to conventional semiconductors) is here of interest, since it is an all-optical technique that can induce and probe the quantum dynamics of spin with ultra-fast time resolution. However, whether (and how) TRFR can be applied to study spin dynamics of triplet (spin $S = 1$) states in molecules was an open question. We explore in **Chapter 3** how TRFR can be applied to molecules with strong SOC, exploiting the optical selection rules for transitions between singlet and triplet states in such molecules. We define how one can study polarization and quantum dynamics of spin after excitation to a superposition of triplet sublevels, using an ultrashort pump pulse. We use the polarization rotation of an ultrashort probe pulse as a measure for the coherent spin dynamics. Besides using this in fundamental studies of the spin properties of such molecules, these results are of value for advancing opto-electronic and spintronic applications.

Until now, all cases where the TRFR technique was used for studying coherent spin dynamics concerned materials systems with strong SOC. Strong SOC may seem a requirement, since it facilitates optical selection rules with allowed transitions that alter the spin state (otherwise only spin-conserving transitions seem allowed). However, **Chapter 4** defines how the TRFR technique can also be applied to certain material systems with negligible SOC. In our derivations we focus on the characterization of spin-active color centers in materials like silicon carbide and diamond. Such color centers are recognized as promising systems for quantum technologies since they can combine long-coherent electronic spin and bright optical properties. We introduce the theory of a TRFR experiment applied to divacancies in silicon carbide, based on non-spin-conserving optical selection rules that can emerge due to the anisotropic spin $S = 1$ Hamiltonian for the electronic ground and excited state of this system.

Finally, **Chapter 5** presents an experimental investigation of the molybdenum-impurity in silicon carbide. We demonstrate an all-optical technique for characterizing the spin Hamiltonians for the ground and excited state, and find that these are $S = 1/2$ systems with highly anisotropic spin properties. In turn, we exploit these properties for tuning control schemes where two-laser driving addresses transitions of a Λ system, and observe coherent population trapping for the ground-state spin. These results demonstrate that the Mo defect and similar transition-metal impurities in silicon carbide may be relevant for advancing quantum communication and quantum sensing technology. In particular, these systems have optical transitions at near-infrared wavelengths (in or close to telecom communication bands), and the device technology for silicon carbide is already available at a high level in industry.

Supplementary Information (SI)

1.8 SI: Change of basis

A choice of a basis is not unique. Let us perform a change of orthonormal bases, from the (old) basis $\{\hat{\mathbf{x}}', \hat{\mathbf{y}}'\}$ to the (new) basis $\{\hat{\mathbf{x}}, \hat{\mathbf{y}}\}$, through a counter-clockwise rotation with angle θ', as depicted in Fig. 1.5. Consider the vector $\mathbf{E}$ (which e.g. can be considered as the electric field component of a light beam),

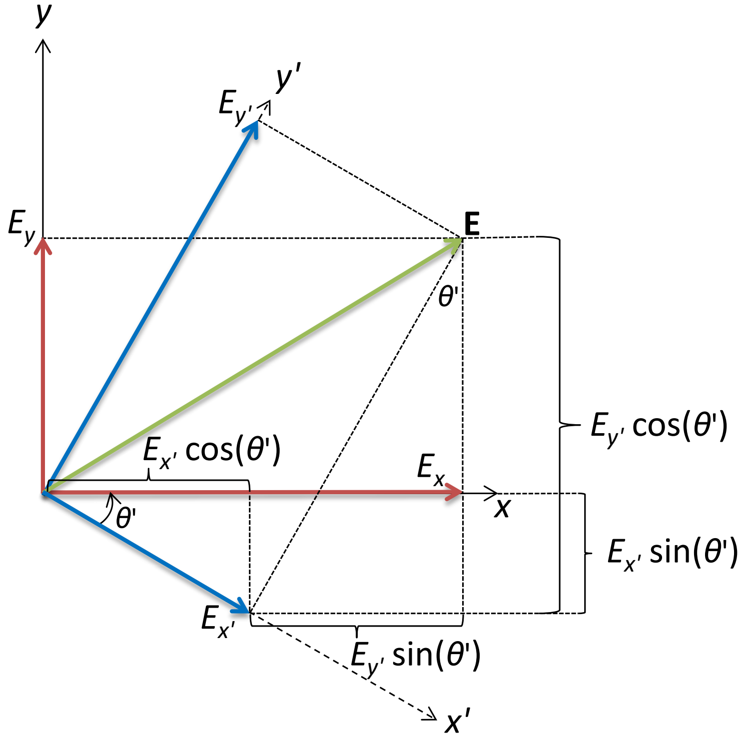

Figure 1.5: Illustration of a change of orthonormal bases. The transformation is from the (old) basis $\{\hat{\mathbf{x}}', \hat{\mathbf{y}}'\}$ to the (new) basis $\{\hat{\mathbf{x}}, \hat{\mathbf{y}}\}$, through a counter-clockwise rotation with angle θ'. To derive the transformation matrix $T_{\{\hat{\mathbf{x}}', \hat{\mathbf{y}}'\} \to \{\hat{\mathbf{x}}, \hat{\mathbf{y}}\}}$, the change of basis is applied to the vector $\mathbf{E}$, which e.g. can be considered as the electric field component of a light beam.

which in the old basis is given by

$$\mathbf{E}\{\hat{\mathbf{x}}',\hat{\mathbf{y}}'\} = E_{x'}\hat{\mathbf{x}}' + E_{y'}\hat{\mathbf{y}}' = \begin{bmatrix} E_{x'} \\ E_{y'} \end{bmatrix} \tag{1.6}$$

In the new basis, we have instead

$$\mathbf{E}\{\hat{\mathbf{x}},\hat{\mathbf{y}}\} = E_x\hat{\mathbf{x}} + E_y\hat{\mathbf{y}} = \begin{bmatrix} E_{x'}\cos(\theta') + E_{y'}\sin(\theta') \\ E_{y'}\cos(\theta') - E_{x'}\sin(\theta') \end{bmatrix} \tag{1.7}$$

The vector $\mathbf{E}$ can be easily transformed from the old basis to the new one through the matrix transformation

$$\mathbf{E}\{\hat{\mathbf{x}},\hat{\mathbf{y}}\} = T_{\{\hat{\mathbf{x}}',\hat{\mathbf{y}}'\}\to\{\hat{\mathbf{x}},\hat{\mathbf{y}}\}}\mathbf{E}\{\hat{\mathbf{x}}',\hat{\mathbf{y}}'\} \tag{1.8}$$

which corresponds to

$$\begin{bmatrix} E_x \\ E_y \end{bmatrix} = \begin{bmatrix} \cos(\theta') & \sin(\theta') \\ -\sin(\theta') & \cos(\theta') \end{bmatrix} \begin{bmatrix} E_{x'} \\ E_{y'} \end{bmatrix} \tag{1.9}$$

where the transformation matrix $T(\theta')$ has as its columns the old unit vectors as written in the new basis, i.e.

$$\hat{\mathbf{x}}'\{\hat{\mathbf{x}},\hat{\mathbf{y}}\} = x'_x\hat{\mathbf{x}} + x'_y\hat{\mathbf{y}} = \begin{bmatrix} x'_x \\ x'_y \end{bmatrix} = \begin{bmatrix} \cos(\theta') \\ -\sin(\theta') \end{bmatrix} \tag{1.10}$$

$$\hat{\mathbf{y}}'\{\hat{\mathbf{x}},\hat{\mathbf{y}}\} = y'_x\hat{\mathbf{x}} + y'_y\hat{\mathbf{y}} = \begin{bmatrix} y'_x \\ y'_y \end{bmatrix} = \begin{bmatrix} \sin(\theta') \\ \cos(\theta') \end{bmatrix} \tag{1.11}$$

where e.g. x'_x denotes the x-component of $\hat{\mathbf{x}}'$, i.e. the projection of $\hat{\mathbf{x}}'$ onto $\hat{\mathbf{x}}$.

Any matrix M defined in the old basis can be described by the new basis through the following unitary similarity transformation

$$M\{\hat{\mathbf{x}},\hat{\mathbf{y}}\} = T_{\{\hat{\mathbf{x}}',\hat{\mathbf{y}}'\}\to\{\hat{\mathbf{x}},\hat{\mathbf{y}}\}}M\{\hat{\mathbf{x}}',\hat{\mathbf{y}}'\}T^\dagger \tag{1.12}$$

with $T^\dagger$ the Hermitian adjoint (conjugate transpose) of T, which has the properties $T^\dagger(\theta') = T^{-1}(\theta') = T(-\theta')$, and it has the unit vectors $\hat{\mathbf{x}}\{\hat{\mathbf{x}}',\hat{\mathbf{y}}'\}$ and $\hat{\mathbf{y}}\{\hat{\mathbf{x}}',\hat{\mathbf{y}}'\}$ as its columns, i.e.

$$\hat{\mathbf{x}}\{\hat{\mathbf{x}}',\hat{\mathbf{y}}'\} = x_{x'}\hat{\mathbf{x}}' + x_{y'}\hat{\mathbf{y}}' = \begin{bmatrix} x_{x'} \\ x_{y'} \end{bmatrix} = \begin{bmatrix} \cos(\theta') \\ \sin(\theta') \end{bmatrix} \tag{1.13}$$

$$\hat{\mathbf{y}}\{\hat{\mathbf{x}}',\hat{\mathbf{y}}'\} = y_{x'}\hat{\mathbf{x}}' + y_{y'}\hat{\mathbf{y}}' = \begin{bmatrix} y_{x'} \\ y_{y'} \end{bmatrix} = \begin{bmatrix} -\sin(\theta') \\ \cos(\theta') \end{bmatrix} \tag{1.14}$$

1.9 SI: Jones calculus applied to a waveplate

To get familiar with Jones calculus, we take here waveplates as an example. We will show that an optical element can be described by a Jones matrix, which transforms the electric vector of an incoming beam via a matrix multiplication. We also illustrate the transformation of one coordinate system to another via a matrix transformation.

Usually, a waveplate has real-valued principal axes (often denoted as $|H\rangle$ and $|V\rangle$), which we denote as $\hat{\mathbf{x}}'$ and $\hat{\mathbf{y}}'$. Consequently, the corresponding Jones matrix is diagonal in the $\{\hat{\mathbf{x}}', \hat{\mathbf{y}}'\}$-basis, and given by Eq. (1.5).

Let us consider two special cases of the waveplate, namely the half-waveplate (HWP) and the quarter-waveplate (QWP). A HWP has its thickness such that the phase difference between the components is given by $\Lambda n_{y'} - \Lambda n_{x'} = \pi$. Also, only the vertical component $\hat{\mathbf{y}}'$ (slow axis) gets retarded by the HWP, whereas the horizontal component $\hat{\mathbf{x}}'$ (fast axis) is not affected, such that the Jones matrix is given by

$$J_{HWP}\{\hat{\mathbf{x}}', \hat{\mathbf{y}}'\} = \begin{bmatrix} 1 & 0 \\ 0 & -1 \end{bmatrix} \tag{1.15}$$

The effect of a HWP on an incident linearly polarized beam is that its azimuth (w.r.t. the fast axis x') gets reflected in the fast axis, as illustrated in Fig. 1.6. This follows from substituting Eq. (1.15) into Eq. (1.4) and taking real-valued $E_{x'}$ and $E_{y'}$, which yields $E_{y'} \to -E_{y'}$, i.e. $\theta' \to -\theta'$. Alternatively, one could apply Eq. (1.3), which requires the transformation $J\{\hat{\mathbf{x}}', \hat{\mathbf{y}}'\} \to J\{\hat{\mathbf{x}}, \hat{\mathbf{y}}\}$ via Eq. (1.12). For a HWP with its fast axis at angle $\theta = -\theta'$ (w.r.t. the x-axis) this requires a counter-clockwise rotation with angle θ' (w.r.t. the x'-axis), which gives according to Eq. (1.12)

$$\begin{aligned} J_{HWP}\{\hat{\mathbf{x}}, \hat{\mathbf{y}}\} &= \begin{bmatrix} \cos(\theta') & \sin(\theta') \\ -\sin(\theta') & \cos(\theta') \end{bmatrix} \begin{bmatrix} 1 & 0 \\ 0 & -1 \end{bmatrix} \begin{bmatrix} \cos(\theta') & -\sin(\theta') \\ \sin(\theta') & \cos(\theta') \end{bmatrix} \\ &= \begin{bmatrix} \cos(2\theta') & -\sin(2\theta') \\ -\sin(2\theta') & -\cos(2\theta') \end{bmatrix} \end{aligned} \tag{1.16}$$

Substituting into Eq. (1.3) gives for an incident beam with Jones vector $\hat{\mathbf{E}}_{in} = \hat{\mathbf{x}}$

$$\hat{\mathbf{E}}_{out}\{\hat{\mathbf{x}}, \hat{\mathbf{y}}\} = \begin{bmatrix} \cos(2\theta') & -\sin(2\theta') \\ -\sin(2\theta') & -\cos(2\theta') \end{bmatrix} \begin{bmatrix} 1 \\ 0 \end{bmatrix} = \begin{bmatrix} \cos(2\theta') \\ -\sin(2\theta') \end{bmatrix} \tag{1.17}$$

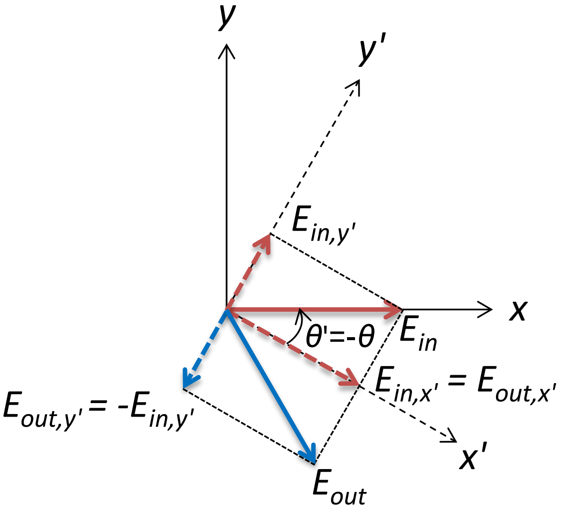

Figure 1.6: The effect of a half-waveplate (HWP) on an incident linearly polarized beam. For a beam polarized along $\hat{\mathbf{x}}$, the azimuth θ' (w.r.t. the fast axis $\hat{\mathbf{x}}'$) gets reflected in the fast axis.

which corresponds to an azimuth of $\theta = -2\theta'$ (w.r.t. the x-axis), as it should.

A QWP has its thickness such that the phase difference between the components is given by $\Lambda n_{y'} - \Lambda n_{x'} = \pi/2$. Also, only the vertical component (slow axis) gets retarded by the QWP, whereas the horizontal component (fast axis) is not affected, such that the Jones matrix is given by

$$J_{QWP}\{\hat{\mathbf{x}}', \hat{\mathbf{y}}'\} = \begin{bmatrix} 1 & 0 \\ 0 & i \end{bmatrix} \tag{1.18}$$

which e.g. makes a linear beam with azimuth $\theta' = 45°$ (w.r.t. the fast x'-axis) circularly polarized. For a QWP with its fast axis at angle $\theta = -\theta'$ w.r.t. the x-axis (i.e. the x-axis is at θ' w.r.t. the x'-axis), one obtains in analogy to Eq. (1.16)

$$J_{QWP}\{\hat{\mathbf{x}}, \hat{\mathbf{y}}\} = \begin{bmatrix} \cos^2(\theta') + i\sin^2(\theta') & (-1+i)\sin(\theta')\cos(\theta') \\ (-1+i)\sin(\theta')\cos(\theta') & \sin^2(\theta') + i\cos^2(\theta') \end{bmatrix} \tag{1.19}$$

Chapter 2

Evolution of atomic optical selection rules upon gradual symmetry lowering

Abstract

For atoms and crystals with a high symmetry, the optical selection rules for electronic transitions are well covered in physics textbooks. However, in studies of material systems one often encounters systems with a weakly distorted symmetry. Insight and intuition for how optical selection rules change when the high symmetry is gradually distorted is, nevertheless, little addressed in literature. We present here a detailed analysis of how a gradual symmetry distortion leads to a complete alteration of optical selection rules. As a model system, we consider the transitions between $1s$ and $2p$ sublevels of the hydrogen atom, which get distorted by placing charged particles in its environment. Upon increasing the distortion, part of the optical selection rules evolve from circular via elliptical to linear character, with an associated evolution between allowed and forbidden transitions. Our presentation combines an analytical approach with quantitative results from numerical simulations, thus providing insight in how the evolution occurs as a function of the strength of the distortion.

This chapter is based on Ref. 1 on p. 177.

2.1 Introduction

A physical system is never completely isolated. Even in atomic clocks[33], which use quantum oscillations in atoms that are relatively insensitive to surrounding matter and fields, the symmetry and dynamics of the quantum system of interest are affected by the environment. In practice, systems with high symmetry nevertheless seem to exist since the distortions due to an asymmetric environment can be so weak that their influence is not significant.

The symmetry of a system dictates its optical selection rules for electronic transitions. Well-known behavior of such optical selection rules is that absorbing circularly polarized light can orient the spin (or, more generally, electronic angular momentum) of an electron that gets excited[5, 34, 35]. This occurs in systems of high symmetry, and is widely applied. A key example is the use of alkali atoms (with spherical symmetry) such as hydrogen, rubidium and cesium, for quantum optical studies and technologies. A second important example is the optoelectronic control in semiconductors with the tetrahedral zincblende lattice structure (with GaAs as key example), where spintronic applications use spin orientation by circularly polarized light[10].

For other material systems, with a lower symmetry, optical transitions couple more frequently purely to linearly polarized light. This holds for excitonic transitions in most organic molecules[35, 36], and transitions of molecule-like color centers in crystals, such as the strongest transitions of the nitrogen-vacancy defect in diamond[37] (a widely-studied system for quantum technologies).

There exist also many material systems which have a high but still weakly distorted symmetry. For these cases it is much harder to assess the optical selection rules with analytical methods, and this topic is little covered in textbooks. Here detailed numerical calculations can provide predictions, but it is much harder to obtain intuitive insight from the output of such calculations. Still, the elegance of computational physics and chemistry calculations is that they can relatively easily reveal how the properties of matter vary in dependence of parameter values.

In this work we provide a detailed theoretical analysis of how a gradual symmetry distortion leads to a complete alteration of optical selection rules. As a model system we use the hydrogen atom, and our results give insight in how its optical selection rules (for transitions between a $1s$ and $2p$ sublevel) change gradually for a gradual symmetry change due to a disturbing environment. The optical selection rules of the bare hydrogen atom can be described analytically, and are well-known[5]. We use this as a starting point. We include in the discussion how they behave in a weak magnetic field, since this is of interest for highlighting the properties of the selection rules. We model the symmetry lowering due to an environment by placing the hydrogen atom in a C_{2v}-symmetry arrangement of four negative point charges, where the magnitude of the charges is varied. For this situation the analytical calculations are too complicated, and we link the analysis to numerical calculations of this system. Our work thus also provides an interesting example of how modern methods for numerically simulating matter can give insight in its properties at a quantum mechanical level.

This manuscript is organized as follows. In Section 2.2, we will introduce the bare hydrogen atom, first without considering spin, and we focus on the electronic transitions between the $1s$ and $2p$ states. This serves as a summary of how this is treated in many textbooks on atomic physics[5], and for introducing the notations we use. We also shortly summarize how a magnetic field affects these transitions (summarized in more detail in Supplementary Information Section 2.7 and 2.8). Next, we expand this model in the usual manner by also considering the electron spin and the effect of spin-orbit coupling (SOC). This is presented in Section 2.3 and Supplementary Information Section 2.10. In Section 2.4, we add the symmetry disturbance to the modeling, by considering the hydrogen atom in a C_{2v} arrangement of negative point charges. For the analysis of this case we use numerical simulation methods, that are also introduced in this section (we use the CASSCF/RASSI–SO method[17, 18]). We focus on calculating energy eigenstates and transition dipole moments, and study how a gradual symmetry lowering affects the optical selection rules. For describing the polarizations of light associated with atomic electric dipole oscillations we use the Jones-vector formulation, which is introduced in Supplementary Information Section 2.12.

2.2 The resonance lines of the hydrogen atom without spin

2.2.1 The hydrogen atom in the absence of a magnetic field

The resonance lines of electronic transitions between the $1s$ and $2p$ levels of the hydrogen atom occur around a wavelength of 120 nm. We use the notation $|1s\rangle$ ($n = 1$; $l = 0$) and $|2p\rangle$ ($n = 2$; $l = 1$), for the ground and excited states respectively, as adopted from the book of Cohen-Tannoudji, Diu and Laloë[5]. At zero magnetic field, the Hamiltonian H_0 (containing the kinetic and electrostatic interaction energy) of the hydrogen atom has energy eigenvalues $E_n = -E_I/n^2$, with E_I the ionization energy. Note that we will often omit the quantum number n, i.e. $|s\rangle = |1s\rangle$ and $|p\rangle = |2p\rangle$. Without considering spin, the hydrogen atom has a single $1s$ level and three degenerate $2p$ levels. Because of this degeneracy, a single resonance line occurs, and any linear combination of orthonormal $|p\rangle$ eigenstates is a suitable eigenbasis for the Hamiltonian. A possible choice would be the basis $\{|s\rangle, |p_x\rangle, |p_y\rangle, |p_z\rangle\}$. The three p orbitals are real-valued and have the same double-lobed shape, but are aligned along the x-, y-, and z-axes, respectively[35].

A convenient measure for the strength of a transition is the real-valued oscillator strength f (Supplementary Information Eq. (2.26) (p. 41)), which is proportional to the absolute square of the transition dipole moment (which is a vector, with Cartesian components defined in Supplementary Information Eq. (2.25) (p. 40)). In general, the total oscillator strength f_{tot} is dimensionless and for all possible transitions it adds up to the number of electrons (known as the Kuhn–Thomas sum rule[35]). Since we consider only a small subset of all transitions within the hydrogen atom (having $f_{tot} = 1$), the total oscillator strength of our subset will be smaller than 1. However, we will consider relative values f_{rel}, for which the sum ($f_{rel,tot}$) will exceed 1 (see below).

The corresponding matrix elements of the transition dipole moment between the $|s\rangle$ and $|p_i\rangle$ states, with $i \in \{x, y, z\}$, are[5]

$$\langle p_i|D_i|s\rangle = \frac{eI_R}{\sqrt{3}} \tag{2.1}$$

where D_i is the i-component of $\mathbf{D} = e\mathbf{R}$, with e the elementary charge and $\mathbf{R}$ the position operator, and the constant value I_R is a radial integral independent of i. For an electron in the $1s$ orbital there are three possible transitions to a $2p$ sublevel, each with a single nonzero transition dipole moment (Eq. (2.1)) and relative oscillator strength $f_{rel} = 3$ (according to Supplementary Information Eq. (2.27) (p. 41)). The corresponding total relative oscillator strength ($3\times 3 = 9$) follows from Supplementary Information Eq. (2.28) (p. 41), which for this case can be simplified to $f_{rel,1s,tot} = \frac{9}{(eI_R)^2} \sum\limits_{i=x,y,z} |\langle p_i|D_i|s\rangle|^2 = 9$. Note that when only the $1s$ orbital is occupied, the absorption strength is equal for all normalized linear (complex) combinations of D_x, D_y and D_z (due to the degeneracy of the $2p$ sublevels), i.e. the probability of a transition to $2p$ does not depend on the polarization.

2.2.2 The hydrogen atom in the presence of a magnetic field

In the presence of a static magnetic field $\mathbf{B}$ along z, the resonance line of the hydrogen atom is modified. A detailed description of how a magnetic field affects the transitions is treated in Supplementary Information Section 2.7 and 2.8. The field does not only change the resonance frequencies, but also the polarization of the atomic lines, which is called the Zeeman effect. The Hamiltonian is given by $H = H_0 + H_1$, with H_1 the paramagnetic coupling term (here only acting on the orbital, since we still neglect spin). Now, the eigenbasis in which H is diagonal is $\{|s\rangle, |p_{-1}\rangle, |p_0\rangle, |p_1\rangle\}$, where

$$\begin{aligned} |p_{-1}\rangle &= \frac{|p_x\rangle - i|p_y\rangle}{\sqrt{2}} \\ |p_0\rangle &= |p_z\rangle \\ |p_1\rangle &= -\frac{|p_x\rangle + i|p_y\rangle}{\sqrt{2}} \end{aligned} \tag{2.2}$$

with the indices $-1, 0, 1$ corresponding to the m_l quantum number along z.

2.2.3 Electric dipole radiation

In Supplementary Information Section 2.8 (p. 34) we present a calculation of how the expectation value of the electric dipole $\langle \mathbf{D} \rangle_{m_l}(t)$ of a hydrogen atom oscillates when it is in a superposition of the ground state $|s\rangle$ and an excited state $|p_{m_l}\rangle$, again following [5]. For all three cases $m_l = -1, 0, 1$ the mean value of the electric dipole oscillates as a function of time, corresponding to the emission of electromagnetic energy. The type of electric dipole oscillation determines the type of polarization of the emitted radiation. Still, the polarization of light that an observer sees depends on its orientation with respect to the source (see Supplementary Information Section 2.8).

For convenience, we will name a polarization after (the complex linear combination of) the components of $\mathbf{D}$ for which (the absolute value of) the transition dipole moment is maximized. A convenient way to find this complex linear combination is the application of the Jones-vector formalism (Supplementary Information Section 2.12 (p. 41)). For the hydrogen atom in the presence of a magnetic field (without considering spin), the matrix elements are maximized when we take the operators $\sigma^+ = \frac{x+iy}{\sqrt{2}}$ (right circular), $\sigma^- = \frac{x-iy}{\sqrt{2}}$ (left circular) and $\pi_z = z$ (linear along z), respectively. As such, the only nonzero matrix elements related to transitions between 1s and 2p levels are

$$\begin{aligned}\langle p_{-1}|\frac{D_x - iD_y}{\sqrt{2}}|s\rangle &= \frac{eI_R}{\sqrt{3}}\\ \langle p_0|D_z|s\rangle &= \frac{eI_R}{\sqrt{3}}\\ \langle p_1|\frac{D_x + iD_y}{\sqrt{2}}|s\rangle &= -\frac{eI_R}{\sqrt{3}}\end{aligned} \tag{2.3}$$

Hence, the polarization of the radiation is σ^-, π_z or σ^+, depending on whether the nonzero matrix element is that of $\frac{D_x-iD_y}{\sqrt{2}}$, D_z or $\frac{D_x+iD_y}{\sqrt{2}}$, respectively.

2.3 The resonance lines of the hydrogen atom including spin

Due to the electron and proton spins, the resonance lines of the hydrogen atom are also affected by the fine- and hyperfine structure. In this work we will only consider the electron spin, which can be either up ($\langle S_z\rangle = \hbar/2$) or down ($\langle S_z\rangle = -\hbar/2$), to which we will refer as α and β, respectively. Hence, the orbitals 1s, 2p_{-1}, 2p_0 and 2p_1 allow for eight possible spinorbitals[35], which are products of a spatial and spin function. These spinorbitals form the basis $\{|s\beta\rangle, |s\alpha\rangle, |p_{-1}\beta\rangle, |p_{-1}\alpha\rangle, |p_0\beta\rangle, |p_0\alpha\rangle, |p_1\beta\rangle, |p_1\alpha\rangle\}$ to which we refer as the uncoupled representation[5]. Alternatively, these basis functions are often labeled with the quantum numbers l, s, m_l and m_s, as tabulated in Supplementary Information Table 2.3 (p. 38).

The Hamiltonian H_0 (containing the kinetic and electrostatic interaction energy) is diagonal in this basis and the eigenvalues on the diagonal resemble the 2- and 6-fold degeneracies in energy. When the spin-orbit coupling (SOC) term $H_{SO} = \mathbf{L}\cdot\mathbf{S}$ is added to the Hamiltonian, the 6-fold degeneracy of the 2p levels is lifted into sublevels with quantum number $j = 1/2$ and $j = 3/2$, i.e. 2$p_{1/2}$ (2-fold degenerate) and 2$p_{3/2}$ (4-fold)[5]. Here, j is the total angular momentum quantum number related to J^2 (with eigenvalues $\hbar^2 j(j+1)$) for the total angular momentum $\mathbf{J} = \mathbf{L} + \mathbf{S}$ (Supplementary Information Section 2.9 (p. 36)). The degeneracy can be further lifted by e.g. a magnetic field (which introduces an additional term to H). Also, the magnetic field induces a quantization axis. It is now convenient to use an approach based on time-independent degenerate perturbation theory[5]. Since the field is applied in the z-direction, we define a basis formed by the eigenstates of the total angular momentum J_z. Constructing

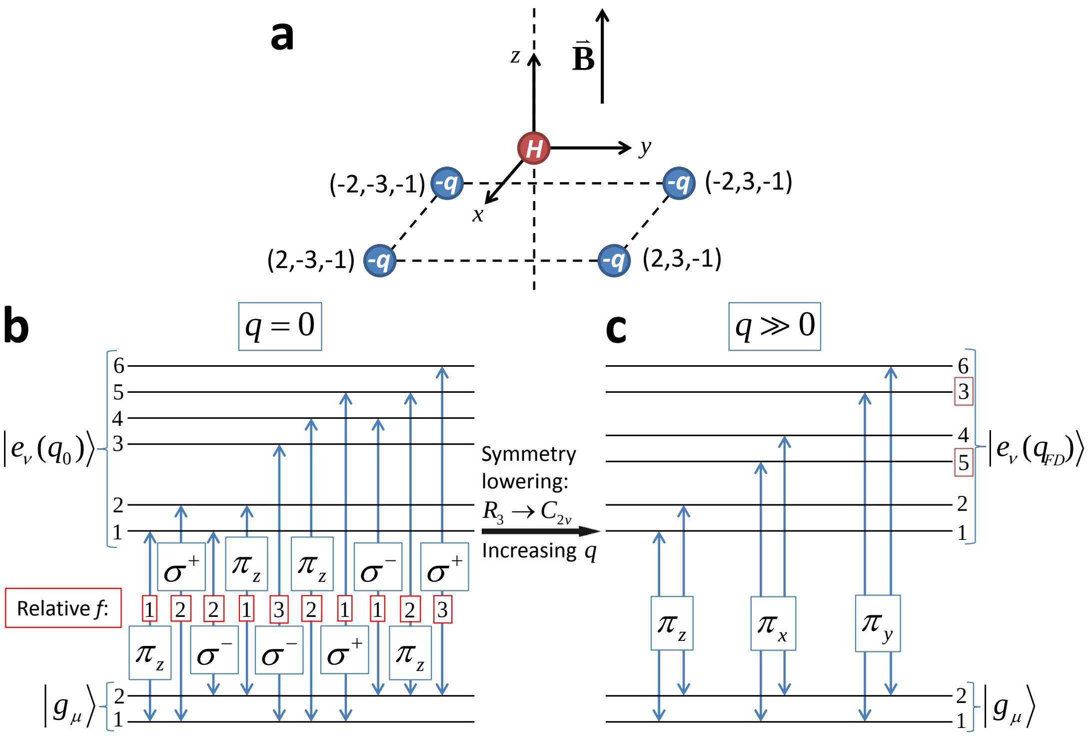

Figure 2.1: Evolution of the polarization selection rules for the hydrogen atom upon symmetry lowering due to a C_{2v} arrangement of negative point charges, in the presence of a weak magnetic field. **a**, A hydrogen atom (in red, positioned at the origin) in a C_{2v} arrangement (C_2 rotation axis along z and two vertical mirror planes) of four negative point charges (in blue, positioned at (2,3,-1), (2,-3,-1), (-2,3,-1), (-2,-3,-1) in Bohrs). Each point charge has the value $-q$, where q is gradually varied from 10^{-6} to 10^{-2} in atomic units. The weak magnetic field points in the z-direction. **b**, Energy levels with Zeeman splitting for the ground (g) state $1s$ (g_μ) and excited (e) state $2p$ (e_ν) sublevels of the hydrogen atom in the presence of a weak magnetic field and absence of point charges (q_0). Supplementary Information Section 2.10 gives a detailed analysis of the polarizations and the relative oscillator strengths f_{rel} (given in red). Spin-orbit coupling (SOC) has been included. **c**, In the limit of very strong charge ($q_{F(ull)D(istortion)}$, i.e. the perturbation due to the charges is much larger than that of the magnetic field), the excited states converge to one of the basis functions of the set $\{|p_z\beta\rangle, |p_z\alpha\rangle, |p_x\beta\rangle, |p_x\alpha\rangle, |p_y\beta\rangle, |p_y\alpha\rangle\}$ and arrange in three doublets (split by the magnetic field). Only six transitions between the $1s$ and $2p$ levels remain allowed (equal f), and their polarizations are linear. Note that the different ordering of ν for the excited states affected by charge (as indicated by the two red boxes).

the matrix $J_z = L_z + S_z$ in the basis in which H is diagonal, one finds that J_z is block-diagonal, i.e. the basis does not necessarily consist of eigenstates of J_z. We determine the eigenfunctions of J_z via diagonalization of the 2- and 4-fold degenerate subspaces, which provide the basis to which we refer as the coupled representation (where H remains diagonal), which is the convenient one for the case with SOC. Good quantum numbers are now j, m_j, l and s. The basis can be expressed as a linear combination of the basis functions of the uncoupled representation (Supplementary Information Table 2.4 (p. 38)), where the prefactors are the so-called Clebsch-Gordan coefficients[5].

A transition (via excitation or emission) between a 1s and 2p sublevel is possible if a nonzero value is obtained for the transition dipole moment $\langle p_{j,m_j}|\mathbf{D}|s_{m_j}\rangle$, with $|s_{m_j}\rangle = |j = \frac{1}{2}, m_j = \pm\frac{1}{2}, l = 0, s = \frac{1}{2}\rangle$ and $|p_{j,m_j}\rangle = |j, m_j, l = 1, s = \frac{1}{2}\rangle$. The corresponding matrix elements and polarizations are presented in Supplementary Information Table 2.5 (p. 39). The relative oscillator strength f_{rel} is given by Supplementary Information Eq. (2.27) (p. 41), which directly depends on the Clebsch-Gordan coefficients. Now ten of the twelve possible transitions between a 1s and 2p sublevel have nonzero oscillator strength (Fig. 2.1b). In contrast, only six transitions are allowed when SOC is not taken into account (three for either up or down spin). We will determine the polarizations and f_{rel}-values also numerically in Section 2.4, where the 1s and 2p sublevels will be denoted as ground and excited states $|g_\mu\rangle$ and $|e_\nu\rangle$ (see also Fig. 2.1b).

2.4 Evolution of optical selection rules for the hydrogen atom in a C_{2v} arrangement of point charges

In this section, we report on ab initio calculations that study the evolution of the optical selection rules for transitions between the 1s and 2p sublevels of the hydrogen atom upon gradual symmetry lowering due to a C_{2v} arrangement of negative point charges (each with charge $-q$), in the presence of a weak magnetic field (Fig. 2.1a). Such a relatively simple system is already too complicated to solve in an analytical way, such that we have to use numerical methods. First, we numerically calculate functions that are relatively good approximations for the eigenstates of the Hamiltonian. Strictly speaking, these functions are not eigenstates because a numerical calculation uses a finite basis set. They are nevertheless good approximations, and we will often refer to these functions as eigenstates (or eigenfunctions). Secondly, we numerically calculate the Cartesian components of the corresponding transition dipole moments (with the relevant ones defined in Supplementary Information Eq. (2.25) (p. 40)). An accurate way to calculate these is the use of the CASSCF/RASSI–SO method (which combines the Complete Active Space Self Consistent Field (CASSCF) and Restricted Active Space State Interaction (RASSI) method with the inclusion of SOC), as introduced by Roos and Malmqvist[17, 18]. We perform such calculations using the MOLCAS[23] software. To approximate the $1s$ and $2p$ orbital we use the large ANO basis set[38], which for the excited states of the hydrogen atom does actually not very accurately approximate the energies. Our purpose, however, is to illustrate how the mixing of sublevels affects transition dipole moments. In this regard, the quality of the orbitals is expected to be sufficient, since they have the required symmetry.

Including a magnetic field within ab initio calculations is not straightforward. We will therefore mimic the field by inducing a quantization axis z (Fig. 2.1a), through diagonalization of J_z within degenerate subspaces (see Section 2.3). This provides the required eigenbasis to which the calculated transition dipole moments are transformed. From the transition dipole moments, we can calculate the relative oscillator strength f_{rel} for each transition between a $1s$ and $2p$ sublevel, according to Supplementary Information Eq. (2.27) (p. 41). The evolution of f_{rel} as a function of q is depicted in Fig. 2.3.

We will use the Jones-vector formulation (see also Supplementary Information Section 2.12 (p. 41)) to investigate how the polarization selection rules are affected as a function of q. The Jones-vector formulation assigns a polarization ellipse (Fig. 1.4) with azimuth θ ($-\frac{1}{2}\pi \leqslant \theta < \frac{1}{2}\pi$) and ellipticity angle ϵ ($-\frac{1}{4}\pi \leqslant \epsilon \leqslant \frac{1}{4}\pi$) to the oscillation of an electric vector[16]. Normally, this electric vector is the electric field component of a light wave. Instead, we will assign such a polarization ellipse to the oscillation of an atomic electric dipole related to an electronic transition, with the components of the electric vector given by the (normalized) components of the corresponding transition dipole moment (Supplementary Information Eq. (2.32) (p. 42)). A convenient method to visualize the Jones vector is via the Poincaré-sphere representation[16]. Within this method, the longitude 2θ and latitude 2ϵ determine a point (labeled P in Fig. 2.4a) representing the ellipse of polarization with azimuth θ and ellipticity angle ϵ (Fig. 1.4).

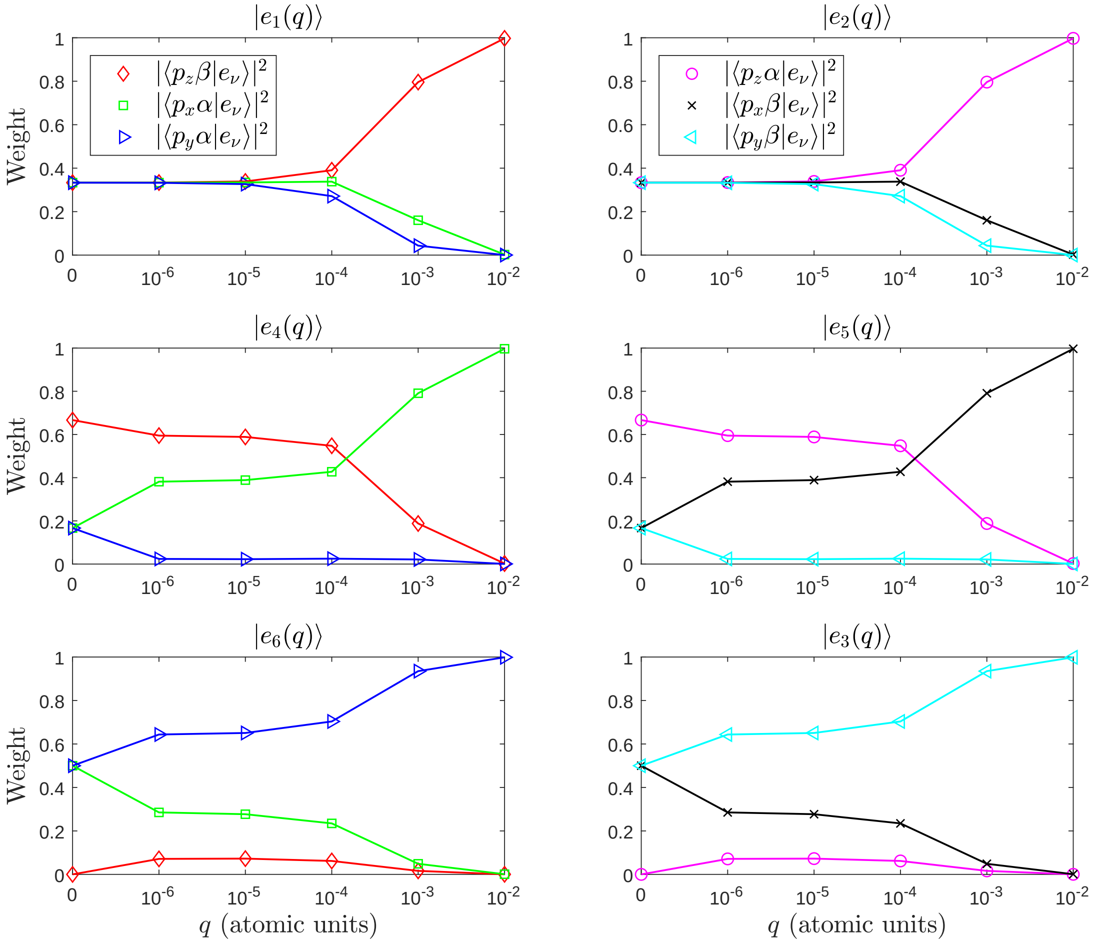

Figure 2.2: Evolution of the excited states for the hydrogen atom upon gradual symmetry lowering due to a C_{2v} arrangement of negative point charges, in the presence of a weak magnetic field. Weights (absolute squares of the coefficients) for the excited states $|e_\nu(q)\rangle$ with $-q$ the value of the point charges in atomic units and $\nu \in \{1, ..., 6\}$ as written in the basis as used for the bare H atom, i.e. $\{|s\beta\rangle, |s\alpha\rangle, |p_z\beta\rangle, |p_z\alpha\rangle, |p_x\beta\rangle, |p_x\alpha\rangle, |p_y\beta\rangle, |p_y\alpha\rangle\}$. The left plots ($\nu \in \{1, 4, 6\}$) have in common that $|e_\nu(q)\rangle$ is a superposition of the states $|p_z\beta\rangle$, $|p_x\alpha\rangle$ and $|p_y\alpha\rangle$, whereas for the right plots $|e_\nu(q)\rangle$ is a superposition of $|p_z\alpha\rangle$, $|p_x\beta\rangle$ and $|p_y\beta\rangle$. Furthermore, the plots are ordered in rows based on the fact that the weights as a function of q are the same within each row. In the limit of very strong charge (q_{FD}, i.e. the perturbation due to the charges is much larger than due to the magnetic field), the excited states converge to one of the basis states of the set $|\{p_z\beta\rangle, |p_z\alpha\rangle, |p_x\beta\rangle, |p_x\alpha\rangle, |p_y\beta\rangle, |p_y\alpha\rangle\}$. For the first row, there is convergence towards $|p_z\rangle$, towards $|p_x\rangle$ for the second, and $|p_y\rangle$ for the third. Data points are connected to guide the eye.

2.4.1 The hydrogen atom in the presence of a weak magnetic field

As a proof of principle calculation, we will first perform numerical calculations on the pure atom (i.e. $q = q_0 = 0$), to see whether we obtain the same optical selection rules as the analytical solution. Fig. 2.1b considers a hydrogen atom in the presence of a magnetic field in the z-direction (without point charges), where we label the $1s$ and $2p$ sublevels as the ground and excited state sublevels $|g_\mu\rangle$ ($\mu \in \{1, 2\}$) and $|e_\nu(q = q_0)\rangle$ ($\nu \in \{1, ..., 6\}$), respectively. For $|e_\nu(q)\rangle$ a notation with dependence on q is already introduced for later use (and we omit this for $|g_\mu\rangle$ since we found no significant dependence on q for these states in our results). For the case of q_0, the numbering of μ and ν increases with increasing energy for both ground and excited states.

From the CASSCF/RASSI–SO calculations, the eigenfunctions of the Hamiltonian are obtained. As introduced before, we mimic the magnetic field by diagonalization of J_z within the 2- and 4-fold degenerate subspaces. As such, we obtain the states $|g_\mu\rangle$ and $|e_\nu(q_0)\rangle$ (Table 2.1), which are the same states (apart from a global phase factor) as those obtained from the analytical solution, i.e. the coupled representation (Supplementary Information Table 2.4 (p. 38)). The weights (i.e. the absolute squares of the coefficients) of the excited states (when decomposing as in Eq. (2.4) and (2.5)) are presented in Fig. 2.2 (first data point of each subplot corresponds to $q = 0$).

The CASSCF/RASSI–SO calculations also provide transition dipole moments. We transform the matrix elements to the basis obtained after diagonalization of J_z within the degenerate subspaces. Now we have obtained the i-components $\langle e_\nu(q_0)|D_i|g_\mu\rangle$ ($i \in \{x, y, z\}$) of the transition dipole moment related to the $|g_\mu\rangle \leftrightarrow |e_\nu(q_0)\rangle$ transitions. From Supplementary Information Eq. (2.27) (p. 41), the corresponding relative oscillator strengths (f_{rel}) are obtained, which are the first data points ($q = 0$) of each series in Fig. 2.3. Since the numerical f_{rel}-values are exactly the same as the analytical ones (Supplementary Information Table 2.5 (p. 39)), i.e. $f_{rel} \in \{0, 1, 2, 3\}$, we conclude that our method is accurate.

Using the Jones-vector formalism (see also Supplementary Information Section 2.12), our numerical calculations also provide the same polarization selection rules as in Supplementary Information Table 2.5 (p. 39). The evolution of the optical selection rules as a function of q for the six transitions having their electric dipole oscillating in the xy-plane has been visualized in Fig. 2.4a and b, where the first data point of each series corresponds to $q = 0$, for which the transitions are circular.

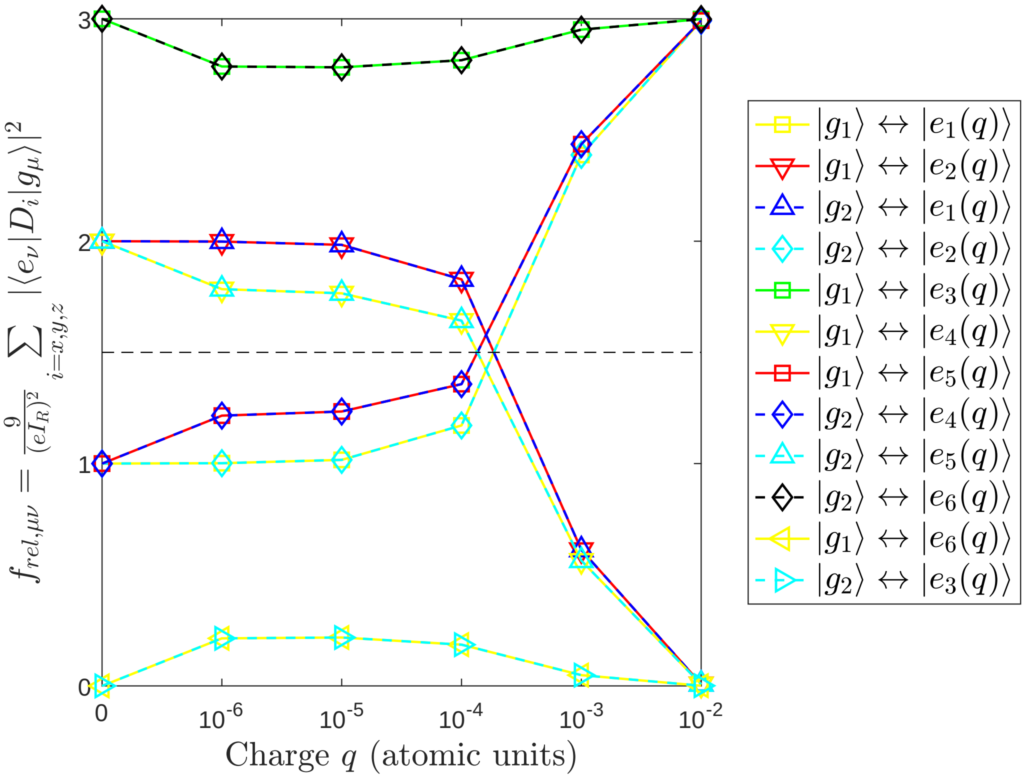

Figure 2.3: Evolution of the relative oscillator strengths for transitions between $1s$ (g_μ) and $2p$ (e_ν) sublevels of the hydrogen atom upon gradual symmetry lowering due to a C_{2v} arrangement of negative point charges, in the presence of a weak magnetic field. The relative oscillator strength $f_{rel,\mu\nu}$ for a transition between $|g_\mu\rangle$ and $|e_\nu\rangle$ has been defined in Supplementary Information Eq. (2.27) (p. 41). Interestingly, the two originally forbidden transitions become slightly allowed (π_z polarization) for small q-values (forbidden for zero charge q_0 and very strong charge q_{FD}). Note that the sum of the relative f-values does not vary as a function of q, i.e. $f_{rel,1s\alpha,tot} = f_{rel,1s\beta,tot} = 9$. This becomes particularly clear from the fact that the plot has a horizontal mirror plane (dashed line) at $f = 1.5$. Data points are connected to guide the eye. See Table 2.2 for the q-dependent optical selection rules.

2.4.2 The hydrogen atom in the presence of a C_{2v} arrangement of point charges and a weak magnetic field

To study the dependence of the atomic electric dipole oscillation on a charged environment, we consider the hydrogen atom in a C_{2v} arrangement of four negative point charges $-q$ (positioned at (2,3,-1), (2,-3,-1), (-2,3,-1), (-2,-3,-1) in Bohrs with respect to the hydrogen atom), as depicted in Fig. 2.1a. The symmetry of the hydrogen atom is gradually distorted by increasing q, and this will gradually affect the Hamiltonian and its eigenstates.

Again, from the CASSCF/RASSI–SO calculations, the eigenfunctions of the Hamiltonian and the transition dipole moments are obtained. In the absence of a magnetic field and in the presence of charges, the six excited states form three doublets. A magnetic field will further lift these degeneracies and impose additional optical selection rules. As before, we mimic a magnetic field by diagonalizing J_z, now within the 2-fold degenerate subspaces. We thus obtain the states $|g_\mu\rangle$ and $|e_\nu(q \neq 0)\rangle$ for the case that the perturbation due to the magnetic field is weaker than that due to the charges (i.e. the magnetic field affects the energies only by slightly lifting the degeneracies).

The excited states depend on the magnitude of the surrounding charges and are denoted as $|e_\nu(q)\rangle$, with $\nu \in \{1, ..., 6\}$. The labeling of ν is based on the evolution of these coefficients: with each gradual increase of charge ($q \to q'$), the states are slightly affected and the new state $|e_{\nu'}(q')\rangle$ is labeled with the ν-value that most resembles $|e_\nu(q)\rangle$ (i.e. $\nu' = \nu$ for the ν' with largest overlap $\langle e_\nu(q)|e_{\nu'}(q')\rangle$). Accordingly, we find a different order of ν for the excited states affected by charge (compare Fig. 2.1b,c). Whereas q_0 (Fig. 2.1b) denotes the absence of charge, q_{FD} (Fig. 2.1c) denotes the limit of a very strong charge that saturates in fully distorting the symmetry (but small enough to not ionize the hydrogen atom).

It turns out that we can write the excited states always as a linear combination of at most three basis functions of the set $\{|p_z\beta\rangle, |p_z\alpha\rangle, |p_x\beta\rangle, |p_x\alpha\rangle, |p_y\beta\rangle, |p_y\alpha\rangle\}$. We find the following relations (where the coefficients are the projections onto each of the basis functions)

$$|e_{\nu=1,4,6}(q)\rangle = \langle p_z\beta|e_\nu(q)\rangle|p_z\beta\rangle + \langle p_x\alpha|e_\nu(q)\rangle|p_x\alpha\rangle + \langle p_y\alpha|e_\nu(q)\rangle|p_y\alpha\rangle \quad (2.4)$$

$$|e_{\nu=2,5,3}(q)\rangle = \langle p_z\alpha|e_\nu(q)\rangle|p_z\alpha\rangle + \langle p_x\beta|e_\nu(q)\rangle|p_x\beta\rangle + \langle p_y\beta|e_\nu(q)\rangle|p_y\beta\rangle \quad (2.5)$$

of which the weights (absolute squares of the coefficients) are presented in Fig. 2.2. For each of the doublets (first row in Fig. 2.2: $\nu = 1, 2$; second row: $\nu = 4, 5$;

Table 2.1: The excited states of the hydrogen atom upon symmetry lowering due to a C_{2v} arrangement of negative point charges. The excited states $|e_\nu(q)\rangle$ are tabulated for the case of zero charge (q_0) and very strong charge (q_{FD}). In the latter case the final excited states converge to one of the basis functions of the set $\{|p_z\beta\rangle, |p_z\alpha\rangle, |p_x\beta\rangle, |p_x\alpha\rangle, |p_y\beta\rangle, |p_y\alpha\rangle\}$. The ground states $|g_\mu\rangle$ ($|s\beta\rangle$ and $|s\alpha\rangle$) are not significantly affected for the range of q values that we consider.

ν	$\|e_\nu(q_0)\rangle$	$\|e_\nu(q_{FD})\rangle$
1	$\frac{1}{\sqrt{3}}(\|p_z\beta\rangle - \|p_x\alpha\rangle + i\|p_y\alpha\rangle)$	$\|p_z\beta\rangle$
2	$\frac{1}{\sqrt{3}}(\|p_z\alpha\rangle + \|p_x\beta\rangle + i\|p_y\beta\rangle)$	$\|p_z\alpha\rangle$
3	$-\frac{1}{\sqrt{2}}(i\|p_x\beta\rangle + \|p_y\beta\rangle)$	$\|p_y\beta\rangle$
4	$-\sqrt{\frac{2}{3}}\|p_z\beta\rangle + \frac{1}{\sqrt{6}}(-\|p_x\alpha\rangle + i\|p_y\alpha\rangle)$	$\|p_x\alpha\rangle$
5	$-\sqrt{\frac{2}{3}}\|p_z\alpha\rangle + \frac{1}{\sqrt{6}}(\|p_x\beta\rangle + i\|p_y\beta\rangle)$	$\|p_x\beta\rangle$
6	$\frac{1}{\sqrt{2}}(-i\|p_x\alpha\rangle + \|p_y\alpha\rangle)$	$\|p_y\alpha\rangle$

third row: $\nu = 6, 3$) the weights of the two different sublevels are the same.

In the limit of very strong charge (q_{FD}), the excited states converge to one of the basis functions of the set $\{|p_z\beta\rangle, |p_z\alpha\rangle, |p_x\beta\rangle, |p_x\alpha\rangle, |p_y\beta\rangle, |p_y\alpha\rangle\}$ (see Fig. 2.2 and Table 2.1). Consequently, a nonzero value for the transition dipole moment is only obtained for transitions between sublevels with equal spin, e.g. $\langle p_x\alpha|D_x|s\alpha\rangle = \langle p_x|D_x|s\rangle\langle\alpha|\alpha\rangle = \frac{eI_R}{\sqrt{3}}$ (see also Eq. (2.1)). As such, only six of the twelve transitions are allowed (ten for $q = 0$), with linear polarization π_x, π_y or π_z, depending on whether the excited state is $|p_x\rangle$, $|p_y\rangle$ or $|p_z\rangle$, respectively (see Fig. 2.1c). Apparently, the interaction with the surrounding charges outweighs the contribution from SOC, such that only spin-conserving transitions are allowed.

To study the optical selection rules for intermediate q-values, we use the transition dipole moments as obtained from our CASSCF/RASSI–SO calculations. Again, we transform the transition dipole moments to the basis obtained after diagonalization of J_z within the degenerate subspaces, such that we obtain the i-components $\langle e_\nu(q)|D_i|g_\mu\rangle$ ($i \in \{x, y, z\}$) of the transition dipole moment related to the $|g_\mu\rangle \leftrightarrow |e_\nu(q)\rangle$ transitions. Interestingly, we can divide the twelve possible transitions into two groups (Table 2.2), based on the direction in which the electric dipole oscillates. For Group XY (red) it oscillates in the xy-plane (the z-component of the transition dipole moment remains zero for increasing q). For Group Z (blue) it oscillates in the z-direction (zero x- and y-components).

Fig. 2.3 depicts the gradual evolution of the relative oscillator strength (f_{rel})

Table 2.2: Evolution of the polarization selection rules of $|g_\mu\rangle \leftrightarrow |e_\nu(q)\rangle$ transitions for the hydrogen atom upon symmetry lowering due to a C_{2v} arrangement of negative point charges. The twelve possible $|g_\mu\rangle \leftrightarrow |e_\nu(q)\rangle$ transitions are divided into two groups (both containing six transitions), based on the direction in which the electric dipole oscillates: for Group XY (red) it oscillates in the xy-plane (the z-component of the transition dipole moment remains zero for increasing q), whereas for Group Z (blue) it oscillates in the z-direction (zero x- and y-components). Cells with an arrow denote how the polarization changes from zero charge q_0 (left value) to very strong charge q_{FD} (right), where a zero denotes a transition with zero oscillator strength f. Two cells contain only π_z, implying that the polarization is unaffected (although f increases with q). The values $0(\pi_x)$ denote a polarization change towards π_x, whereas $\lim\limits_{q \to q_{FD}} f(q) = 0$. The two originally forbidden transitions become slightly allowed (π_z-polarized) for nonzero q, but $\lim\limits_{q \to q_{FD}} f(q) = 0$, which is denoted as $0(\pi_z)$.

ν μ	1	2	3	4	5	6
1	π_z	$\sigma^+ \rightarrow 0(\pi_x)$	$\sigma^- \rightarrow \pi_y$	$\pi_z \rightarrow 0$	$\sigma^+ \rightarrow \pi_x$	$0 \rightarrow 0(\pi_z)$
2	$\sigma^- \rightarrow 0(\pi_x)$	π_z	$0 \rightarrow 0(\pi_z)$	$\sigma^- \rightarrow \pi_x$	$\pi_z \rightarrow 0$	$\sigma^+ \rightarrow \pi_y$

as a function of q for all twelve $|g_\mu\rangle \leftrightarrow |e_\nu(q)\rangle$ transitions, as obtained from Supplementary Information Eq. (2.27) (p. 41). Although certain transitions become even forbidden with increasing charge magntitudes q, the total emission and absorption remain the same, because the sum of the oscillator strengths of all transitions from or to $|1s\alpha\rangle$ or $|1s\beta\rangle$ is unaffected, i.e. $f_{rel,1s\alpha,tot} = f_{rel,1s\beta,tot} = 9$ (compare Section 2.2 for the orbitals and f_{rel}-values for the q_{FD}-case, and Supplementary Information Table 2.5 (p. 39) for the f_{rel}-values when $q = 0$). This becomes also clear from the fact that the plot has a horizontal mirror plane (dashed line) at $f = 1.5$. Since the transitions have different polarizations, the dependence of the oscillator strengths of each transition on q implies that the amount of light emitted in a specific direction depends on q as well. However, when light would be collected from all directions simultaneously, no variation would be observed in the intensity. Particularly interesting is the fact that the two originally forbidden transitions ($q = 0$ and SOC included, see Supplementary Information Table 2.5) become slightly allowed (π_z polarization) for $0 < q < q_{FD}$, which results from the fact that $|e_3(q)\rangle$ and $|e_6(q)\rangle$ gain some contribution from $|p_z\alpha\rangle$ and $|p_z\beta\rangle$, respectively (Fig. 2.2).

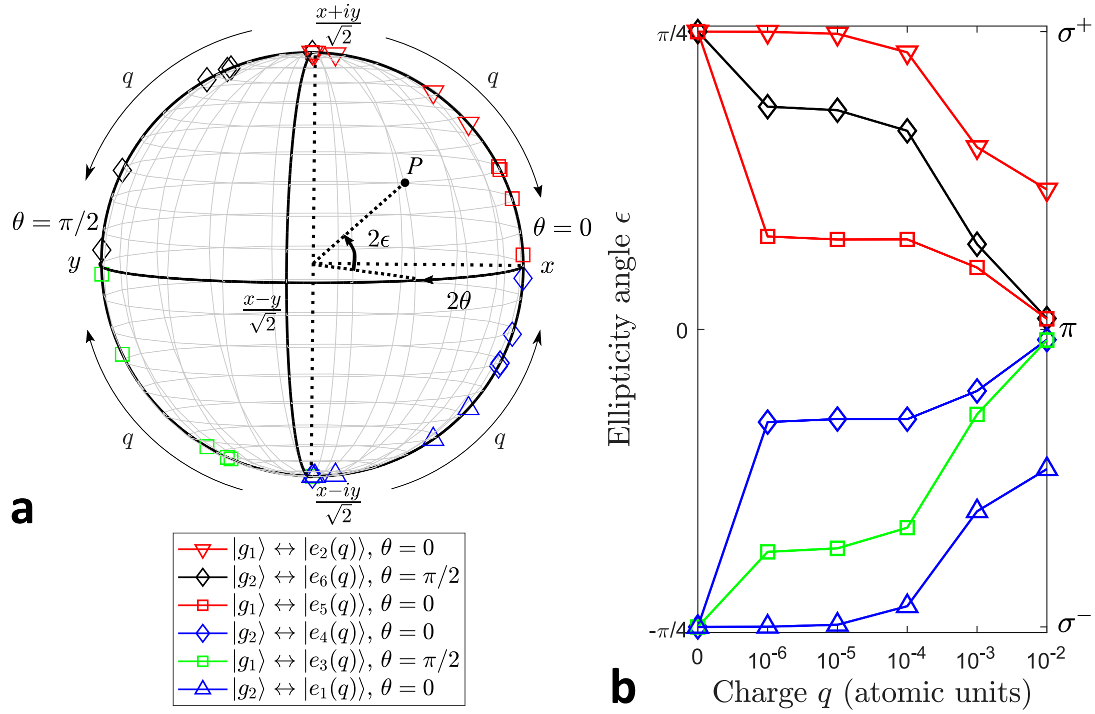

Figure 2.4: Evolution of the ellipticity angle ϵ and azimuth θ for the hydrogen atom upon gradual symmetry lowering. We consider the six transitions (see legend) that have the electric dipole oscillating in the xy-plane (Group XY in Table 2.2). **a**, For these six transitions, the polarization change as a function of q is represented on a Poincaré sphere[16]. The longitude $-\pi \leqslant 2\theta < \pi$ and latitude $-\frac{1}{2}\pi \leqslant 2\epsilon \leqslant \frac{1}{2}\pi$ determine a point P, that represents a polarization ellipse with azimuth θ and ellipticity angle ϵ (Fig. 1.4). For the green (squares) and black (diamond) series the y-axis is the major axis, hence $\theta = \pi/2$. For the other four (red and blue) series the x-axis is the major axis of the polarization ellipse, hence $\theta = 0$. The four arrows outside the sphere indicate for the data points the direction of increasing q. **b**, Ellipticity angle values ϵ from **a** as a function of charge magnitude q for the six different transitions, changing all from circular ($\epsilon = \pm\pi/4$) towards linear ($\epsilon = 0$). Data points are connected to guide the eye.

To study the gradual evolution of the optical selection rules as a function of q, we use the Jones-vector formalism (see also Supplementary Information Section 2.12). For the six transitions having the electric dipole oscillating in the xy-plane (Group XY, red in Table 2.2), the Jones vectors are visualized in Fig. 2.4a via the Poincaré-sphere representation[16], and the ellipticity angles ϵ are plotted as a function of q in Fig. 2.4b. We find for all six Group XY transitions that the polarization of the atomic electric dipoles changes gradually upon a gradual increase of the point charges. More specific, the polarization changes from circular (σ) via elliptical towards linear (π). The change to linear goes most rapid for the transitions where $|e_4\rangle$ and $|e_5\rangle$ are involved, a bit slower for the transitions with $|e_3\rangle$ and $|e_6\rangle$, and slowest for the transitions with $|e_1\rangle$ and $|e_2\rangle$ (which actually become forbidden for large q). This corresponds, respectively, to excited states that evolve towards $|p_x\rangle$, $|p_y\rangle$ and $|p_z\rangle$ character (see also Fig. 2.2). The fact that the evolution towards linear polarization goes faster for the transitions associated with $|p_x\rangle$ than for the ones associated with $|p_y\rangle$ is related to the particular design of the distortion used in our study: the charges $-q$ are in x-direction closer to the atom than in y-direction (see Fig. 2.1a).

For the six allowed transitions at q_{FD}, the π_z-transitions originate from π_z (for q_0), whereas π_x and π_y originate from σ (and are elliptical for intermediate q-values). An observer at the $+z$-direction will (with gradually increasing charge) see that the polarization of emitted light changes gradually from circular to linear. Similarly, absorption of light becomes with increasing q ultimately most efficient for linearly polarized light.

A final observation to discuss is the fact that the character of the eigenstates and the selection rules have their strongest evolution in the range between $q = 10^{-4}$ and $q = 10^{-3}$ (see the traces in Fig. 2.2, Fig. 2.3 and Fig. 2.4b). In Supplementary Information Section 2.13 (p. 43) we present a perturbation-theory approach aimed at analyzing why the transition occurs most strongly in this range. This confirms the notion that the transition occurs when the energy scale associated with the Coulomb distortion by the point charges starts to dominate over the spin-orbit coupling of the hydrogen atom.

2.5 Summary and Outlook

Studying the electronic transitions of the $1s$ and $2p$ levels of the hydrogen atom in the presence of negative point charges (and a weak magnetic field) provided a better understanding of the relation between the electronic wavefunctions and the polarizations of the interacting light. By external lowering of the symmetry of the hydrogen atom by gradually changing the magnitude of negative point charges in a C_{2v} arrangement, it was found that the polarization selection rules were affected gradually as well (both oscillator strength and polarization). Only six transitions (equal oscillator strength and linear polarization) remain allowed between $1s$ and $2p$ sublevels in the limit of very strong charge.

This study has provided a simple model system to show the principle of symmetry dependent optical selection rules. We have shown for the hydrogen atom that varying the magnitude of the negative point charges allows to switch the optical selection rules of certain transitions between circular and linear (elliptical in between) and to switch other transitions between allowed (on) and forbidden (off). Such switching could be interesting for the storage and transfer of (quantum) information. The study also provides a better intuition for polarization selection rules of systems with (relatively) low symmetry (like molecules or crystal defects).

2.6 Author contributions

This chapter is based on Ref. 1 on p. 177. The project was initiated by all authors. Calculations and data analysis were performed by G.J.J.L. and he had the lead on writing the manuscript. All authors contributed to improving the manuscript.

Supplementary Information (SI)

In the main text we have considered the resonance lines of the hydrogen atom around 120 nm, corresponding to an atomic transition between the ground state $|1s\rangle$ ($n = 1$; $l = m_l = 0$) and the excited state $|2p\rangle$ ($n = 2$; $l = 1$; $m_l = -1, 0, 1$). We have investigated the modification of the optical selection rules in the presence of surrounding negative point charges. Relevant fundamentals are given for reference in the Supplementary Information below. Analogous to the book of Cohen-Tannoudji, Diu and Laloë[5] (which gives a derivation for the spinless case), the optical selection rules are derived for electronic transitions between $1s$ and $2p$ levels in the presence of a magnetic field while considering spin-orbit coupling, with the result tabulated in Table 2.5. With these optical selection rules as a starting point (Fig. 2.1b), we introduce point charges in the main text and study how the optical selection rules are modified.

2.7 SI: Energy levels of the hydrogen atom in a magnetic field

For the hydrogen atom at zero magnetic field, the Hamiltonian H_0 (containing the kinetic and electrostatic interaction energy) has energy eigenvalues $E_n = -E_I/n^2$, with E_I the ionization energy. In the presence of a static magnetic field $\mathbf{B}$ along z, the resonance line is modified. This field does not only change the frequency, but also the polarization of the atomic lines, which is called the Zeeman effect. In addition, due to the electron and proton spins, the resonance line is affected by the fine- and hyperfine structure. However, let us neglect spin for the moment (in Section 2.7 and 2.8), following [5]. As such, the Hamiltonian is given by $H = H_0 + H_1$, with H_1 the paramagnetic coupling term. The corresponding eigenvalue equation becomes

$$(H_0 + H_1)|\phi_{n,l,m_l}\rangle = (E_n - m_l\mu_B B))|\phi_{n,l,m_l}\rangle \tag{2.6}$$

with $\mu_B = \frac{e\hbar}{2m_e}$ the Bohr magneton, e the elementary charge, $\hbar$ the reduced Planck constant, and m_e the electron mass. For the states involved in the resonance line, we obtain

$$(H_0 + H_1)|\phi_{1,0,0}\rangle = -E_I|\phi_{1,0,0}\rangle \tag{2.7}$$

$$(H_0 + H_1)|\phi_{2,1,m_l}\rangle = (-E_I + \hbar(\Omega + m_l\omega_L))|\phi_{2,1,m_l}\rangle \tag{2.8}$$

with the Larmor angular velocity given by $\omega_L = \frac{eB}{2m_e}$. At zero field this gives the angular frequency of the resonance line

$$\Omega = \frac{E_2 - E_1}{\hbar} = \frac{3E_I}{4\hbar} \tag{2.9}$$

2.8 SI: Electric dipole oscillations

The electric dipole operator is given by

$$\mathbf{D} = e\mathbf{R} \tag{2.10}$$

with $\mathbf{R}$ the position operator. Hence, $\mathbf{D}$ is a three-dimensional vector, with components D_x, D_y, D_z. Considering the $|1s\rangle$ and $|2p\rangle$ states of the hydrogen atom, the only nonzero matrix components of $\mathbf{D}$ are[5]

$$\begin{aligned}
\langle\phi_{2,1,1}|D_x|\phi_{1,0,0}\rangle &= -\langle\phi_{2,1,-1}|D_x|\phi_{1,0,0}\rangle = -\frac{eI_R}{\sqrt{6}} \\
\langle\phi_{2,1,1}|D_y|\phi_{1,0,0}\rangle &= \langle\phi_{2,1,-1}|D_y|\phi_{1,0,0}\rangle = i\frac{eI_R}{\sqrt{6}} \\
\langle\phi_{2,1,0}|D_z|\phi_{1,0,0}\rangle &= \frac{eI_R}{\sqrt{3}}
\end{aligned} \tag{2.11}$$

where the constant value I_R is a radial integral. If a system is in a stationary state, the mean value of the operator $\mathbf{D}$ is zero, i.e. the system cannot emit any light. Let us therefore assume that the system is in a linear superposition of the ground state $|1s\rangle$ and one of the $|2p\rangle$ excited state sublevels

$$|\psi_{m_l}(t=0)\rangle = \cos(\alpha)|\phi_{1,0,0}\rangle + \sin(\alpha)|\phi_{2,1,m_l}\rangle \tag{2.12}$$

with α real. As a function of time, this state evolves as

$$|\psi_{m_l}(t)\rangle = \cos(\alpha)|\phi_{1,0,0}\rangle + \sin(\alpha)\mathrm{e}^{-i(\Omega+m\omega_L)t}|\phi_{2,1,m_l}\rangle \tag{2.13}$$

where the global phase factor $\mathrm{e}^{-iE_it/\hbar}$ has been omitted. The mean value of the electric dipole is given by

$$\langle\mathbf{D}\rangle_{m_l}(t) = \langle\psi_{m_l}(t)|\mathbf{D}|\psi_{m_l}(t)\rangle \tag{2.14}$$

For $m_l = 1$, we obtain

$$\begin{aligned}
\langle D_x \rangle_1 &= -\frac{eI_R}{\sqrt{6}} \sin(2\alpha) \cos((\Omega + \omega_L)t) \\
\langle D_y \rangle_1 &= -\frac{eI_R}{\sqrt{6}} \sin(2\alpha) \sin((\Omega + \omega_L)t) \\
\langle D_z \rangle_1 &= 0
\end{aligned} \tag{2.15}$$

which implies that $\langle \mathbf{D} \rangle_1 (t)$ rotates in the xy-plane in the counter-clockwise direction, with angular velocity $\Omega + \omega_L$.

For $m_l = 0$, we obtain

$$\begin{aligned}
\langle D_x \rangle_0 &= \langle D_y \rangle_0 = 0 \\
\langle D_z \rangle_0 &= \frac{eI_R}{\sqrt{3}} \sin(2\alpha) \cos(\Omega t)
\end{aligned} \tag{2.16}$$

which implies that $\langle \mathbf{D} \rangle_0 (t)$ oscillates linearly along z, with angular frequency Ω.

For $m_l = -1$, we obtain

$$\begin{aligned}
\langle D_x \rangle_{-1} &= \frac{eI_R}{\sqrt{6}} \sin(2\alpha) \cos((\Omega - \omega_L)t) \\
\langle D_y \rangle_{-1} &= -\frac{eI_R}{\sqrt{6}} \sin(2\alpha) \sin((\Omega - \omega_L)t) \\
\langle D_z \rangle_{-1} &= 0
\end{aligned} \tag{2.17}$$

which implies that $\langle \mathbf{D} \rangle_{-1} (t)$ rotates in the xy-plane in the clockwise direction, with angular velocity $\Omega - \omega_L$.

For all three cases ($m_l = -1, 0, 1$) the mean value of the electric dipole oscillates as a function of time, corresponding to the emission of electromagnetic energy. The type of electric dipole oscillation determines the type of polarization of the emitted radiation. Still, the polarization of light that an observer sees depends on its orientation with respect to the source. For the $m_l = 1$ case, the electric dipole oscillates in the counter-clockwise direction with respect to the z-axis. An observer will at the positive (negative) side of the z-axis therefore detect σ^+ (σ^-) radiation, where $\sigma^\pm = \frac{x \pm iy}{\sqrt{2}}$. However, if the observer detects in the xy-plane, the radiation will be linearly polarized, perpendicular to $\mathbf{B}$. In any other direction, the radiation is elliptically polarized. For the $m_l = -1$ case, an observer will detect the opposite direction for circular and elliptical polarization. For the $m_l = 0$ case, an observer in the z-direction will not observe any radiation, since an oscillating linear dipole does not radiate along its axis. In any other direction the detected radiation will be linearly polarized, parallel to $\mathbf{B}$.

If one is interested in excitation by means of polarized light, the process just takes place in the reverse direction. Upon excitation, the electric dipole oscillation will become resonant to the oscillation of the electromagnetic field of a photon, where the polarization of the electric dipole oscillation is determined by the polarization of the photon. The type of dipole oscillation that is induced will be exactly the same as the type of oscillation that would be responsible for emission of this light. For example, if at $+z$ you observe σ^- light induced by a clockwise rotation of the dipole (as seen from $+z$), you should excite the system with σ^- with the source of light being positioned at $-z$, in order to induce the same oscillation (now counter-clockwise as seen from the origin).

2.9 SI: Spin-orbit coupling

According to special relativity, an electron moving in the electrostatic field of a proton experiences this field in its reference frame as a magnetic field[35]. The intrinsic magnetic moment due to the electron spin can interact with this magnetic field. The corresponding interaction energy is found to be proportional to the inner product of L and S, i.e.

$$H_{SO} \propto \mathbf{L} \cdot \mathbf{S} \tag{2.18}$$

Including this spin-orbit coupling (SOC), one obtains the total Hamiltonian

$$H = H_0 + H_{SO} \tag{2.19}$$

with H_0 the original Hamiltonian without the spin-orbit interaction.

It is useful to define the total angular momentum operator

$$J^2 = L^2 + S^2 + 2\mathbf{L} \cdot \mathbf{S} \tag{2.20}$$

which allows to write

$$\mathbf{L} \cdot \mathbf{S} = \frac{1}{2}(J^2 - L^2 - S^2) \tag{2.21}$$

where the corresponding energies are determined from

$$\langle \mathbf{L} \cdot \mathbf{S} \rangle = \frac{1}{2}(\langle J^2 \rangle - \langle L^2 \rangle - \langle S^2 \rangle) = \frac{\hbar^2}{2}(j(j+1) - l(l+1) - s(s+1)) \tag{2.22}$$

which implies that the spin-orbit interaction induces an energy splitting

$$\Delta E \propto j(j+1) - l(l+1) - s(s+1) \tag{2.23}$$

For atoms, the proportionality constant is proportional to Z^4, with Z the atomic number[35]. Hence, spin-orbit interaction is strong for (systems consisting of) heavy atoms.

2.10 SI: The resonance line of the hydrogen atom including spin

The electron spin can be either up ($\langle S_z \rangle = \hbar/2$) or down ($\langle S_z \rangle = -\hbar/2$), to which we refer as α and β, respectively. The orbitals $1s$, $2p_{-1}$, $2p_0$ and $2p_1$ allow for eight possible spinorbitals. These spinorbitals span a basis to which we refer as the uncoupled representation[5]. It is convenient to label the basis states with the quantum numbers l, s, m_l and m_s, as tabulated in Table 2.3.

SOC lifts the 6-fold degeneracy of the $2p$ levels into sublevels with quantum number j, i.e. $2p_{1/2}$ (2-fold degenerate) and $2p_{3/2}$ (4-fold degenerate). The degeneracy can be further lifted by e.g. a magnetic field (which introduces an additional term to H, which we neglect for the moment though), which induces a quantization axis. When the field is applied in the z-direction, it is convenient to define a basis spanned by the eigenstates of the total angular momentum J_z. Constructing the matrix $J_z = L_z + S_z$ in the basis in which H is diagonal, one finds that J_z is block-diagonal, i.e. the basis does not consist of eigenstates of J_z. Diagonalization of the 2- and 4-fold degenerate subspaces provides the basis to which we refer as the coupled representation (where H remains diagonal).

When the spin and orbital angular momentum are coupled, it is convenient to work in the coupled representation (Table 2.4). Good quantum numbers are now j, m_j, l and s. The basis can still be expressed as a linear combination of the basis states of the uncoupled representation, where the prefactors are the so-called Clebsch-Gordan coefficients.

Excitation or emission between a $1s$ and $2p$ sublevel is possible if a nonzero value is obtained for the transition dipole moment $\langle \psi_e | \mathbf{D} | \psi_g \rangle$, with $|\psi_g\rangle = |j = \frac{1}{2}, m_j = \pm\frac{1}{2}, l = 0, s = \frac{1}{2}\rangle$ and $|\psi_e\rangle = |j, m_j, l = 1, s = \frac{1}{2}\rangle$. As tabulated in Table 2.5, we see that now ten of the twelve possible transitions from the $1s$ to $2p$ sublevels have nonzero oscillator strength. Instead, in the case without SOC only six transitions are possible (three for either up or down spin).

Table 2.3: Uncoupled representation for the spinorbitals originating from the $1s$, $2p_{-1}$, $2p_0$ and $2p_1$ orbitals.

Spinorbital	$\|l, s, m_l, m_s\rangle$
$\|s\beta\rangle$	$\|0, \frac{1}{2}, 0, -\frac{1}{2}\rangle$
$\|s\alpha\rangle$	$\|0, \frac{1}{2}, 0, \frac{1}{2}\rangle$
$\|p_{-1}\beta\rangle$	$\|1, \frac{1}{2}, -1, -\frac{1}{2}\rangle$
$\|p_{-1}\alpha\rangle$	$\|1, \frac{1}{2}, -1, \frac{1}{2}\rangle$
$\|p_0\beta\rangle$	$\|1, \frac{1}{2}, 0, -\frac{1}{2}\rangle$
$\|p_0\alpha\rangle$	$\|1, \frac{1}{2}, 0, \frac{1}{2}\rangle$
$\|p_1\beta\rangle$	$\|1, \frac{1}{2}, 1, -\frac{1}{2}\rangle$
$\|p_1\alpha\rangle$	$\|1, \frac{1}{2}, 1, \frac{1}{2}\rangle$

Table 2.4: Coupled representation for the spinorbitals originating from the $1s$, $2p_{-1}$, $2p_0$ and $2p_1$ orbitals. The left column contains the basis states of the coupled representation. The middle column gives the same states in the basis of the uncoupled representation, where the prefactors are the so-called Clebsch-Gordan coefficients. The right column gives the notation as used in the main text, (for the excited state) corresponding to the case where no surrounding charges are present.

$\|j, m_j, l, s\rangle$	$\sum C_{m_l,m_s}\|l, s, m_l, m_s\rangle$	
$\|\frac{1}{2}, -\frac{1}{2}, 0, \frac{1}{2}\rangle$	$\|0, \frac{1}{2}, 0, -\frac{1}{2}\rangle$	$\|g_1\rangle$
$\|\frac{1}{2}, \frac{1}{2}, 0, \frac{1}{2}\rangle$	$\|0, \frac{1}{2}, 0, \frac{1}{2}\rangle$	$\|g_2\rangle$
$\|\frac{1}{2}, -\frac{1}{2}, 1, \frac{1}{2}\rangle$	$\frac{1}{\sqrt{3}}\|1, \frac{1}{2}, 0, -\frac{1}{2}\rangle - \sqrt{\frac{2}{3}}\|1, \frac{1}{2}, -1, \frac{1}{2}\rangle$	$\|e_1(q_0)\rangle$
$\|\frac{1}{2}, \frac{1}{2}, 1, \frac{1}{2}\rangle$	$\sqrt{\frac{2}{3}}\|1, \frac{1}{2}, 1, -\frac{1}{2}\rangle - \frac{1}{\sqrt{3}}\|1, \frac{1}{2}, 0, \frac{1}{2}\rangle$	$\|e_2(q_0)\rangle$
$\|\frac{3}{2}, -\frac{3}{2}, 1, \frac{1}{2}\rangle$	$\|1, \frac{1}{2}, -1, -\frac{1}{2}\rangle$	$\|e_3(q_0)\rangle$
$\|\frac{3}{2}, -\frac{1}{2}, 1, \frac{1}{2}\rangle$	$\frac{1}{\sqrt{3}}\|1, \frac{1}{2}, -1, \frac{1}{2}\rangle + \sqrt{\frac{2}{3}}\|1, \frac{1}{2}, 0, -\frac{1}{2}\rangle$	$\|e_4(q_0)\rangle$
$\|\frac{3}{2}, \frac{1}{2}, 1, \frac{1}{2}\rangle$	$\sqrt{\frac{2}{3}}\|1, \frac{1}{2}, 0, \frac{1}{2}\rangle + \frac{1}{\sqrt{3}}\|1, \frac{1}{2}, 1, -\frac{1}{2}\rangle$	$\|e_5(q_0)\rangle$
$\|\frac{3}{2}, \frac{3}{2}, 1, \frac{1}{2}\rangle$	$\|1, \frac{1}{2}, 1, \frac{1}{2}\rangle$	$\|e_6(q_0)\rangle$

Table 2.5: Transition dipole moments, polarizations (pol.) and transition strengths for transitions between $1s$ and $2p$ sublevels, in the presence of a magnetic field. See main text Fig. 2.1 for definitions of $|g_\mu\rangle$ and $|e_\nu\rangle$. The relative oscillator strengths f_{rel} (Eq. (2.27)) for all transitions from either $|s_{-\frac{1}{2}}\rangle$ or $|s_{\frac{1}{2}}\rangle$ add up to $f_{rel,tot} = 9$, equal to the case without SOC (main text Section 2.2).

$\vert s_{m_j}\rangle \leftrightarrow \vert p_{j,m_j}\rangle$ $= \vert g_\mu\rangle \leftrightarrow \vert e_\nu\rangle$	$\langle e_\nu \vert D \vert g_\mu\rangle$ in the uncoupled representation. Vanishing terms are omitted.	Pol.	f_{rel}
$\vert s_{-\frac{1}{2}}\rangle \leftrightarrow \vert p_{\frac{1}{2},-\frac{1}{2}}\rangle$ $= \vert g_1\rangle \leftrightarrow \vert e_1\rangle$	$\left(\frac{1}{\sqrt{3}}\langle 1,\frac{1}{2},0,-\frac{1}{2}\vert - \sqrt{\frac{2}{3}}\langle 1,\frac{1}{2},-1,\frac{1}{2}\vert\right) D\vert 0,\frac{1}{2},0,-\frac{1}{2}\rangle$ $= \frac{1}{\sqrt{3}}\langle\phi_{2,1,0}\vert D_z\vert\phi_{1,0,0}\rangle = \frac{1}{3}eI_R$	π	1
$\vert s_{-\frac{1}{2}}\rangle \leftrightarrow \vert p_{\frac{1}{2},\frac{1}{2}}\rangle$ $= \vert g_1\rangle \leftrightarrow \vert e_2\rangle$	$\left(\sqrt{\frac{2}{3}}\langle 1,\frac{1}{2},1,-\frac{1}{2}\vert - \frac{1}{\sqrt{3}}\langle 1,\frac{1}{2},0,\frac{1}{2}\vert\right) D\vert 0,\frac{1}{2},0,-\frac{1}{2}\rangle$ $= \sqrt{\frac{2}{3}}\langle\phi_{2,1,1}\vert\frac{D_x+iD_y}{\sqrt{2}}\vert\phi_{1,0,0}\rangle = -\frac{\sqrt{2}}{3}eI_R$	σ^+	2
$\vert s_{-\frac{1}{2}}\rangle \leftrightarrow \vert p_{\frac{3}{2},-\frac{3}{2}}\rangle$ $= \vert g_1\rangle \leftrightarrow \vert e_3\rangle$	$\langle 1,\frac{1}{2},-1,-\frac{1}{2}\vert D\vert 0,\frac{1}{2},0,-\frac{1}{2}\rangle$ $= \langle\phi_{2,1,-1}\vert\frac{D_x-iD_y}{\sqrt{2}}\vert\phi_{1,0,0}\rangle = \frac{1}{\sqrt{3}}eI_R$	σ^-	3
$\vert s_{-\frac{1}{2}}\rangle \leftrightarrow \vert p_{\frac{3}{2},-\frac{1}{2}}\rangle$ $= \vert g_1\rangle \leftrightarrow \vert e_4\rangle$	$\left(\frac{1}{\sqrt{3}}\langle 1,\frac{1}{2},-1,\frac{1}{2}\vert + \sqrt{\frac{2}{3}}\langle 1,\frac{1}{2},0,-\frac{1}{2}\vert\right) D\vert 0,\frac{1}{2},0,-\frac{1}{2}\rangle$ $= \sqrt{\frac{2}{3}}\langle\phi_{2,1,0}\vert D_z\vert\phi_{1,0,0}\rangle = \frac{\sqrt{2}}{3}eI_R$	π	2
$\vert s_{-\frac{1}{2}}\rangle \leftrightarrow \vert p_{\frac{3}{2},\frac{1}{2}}\rangle$ $= \vert g_1\rangle \leftrightarrow \vert e_5\rangle$	$\left(\sqrt{\frac{2}{3}}\langle 1,\frac{1}{2},0,\frac{1}{2}\vert + \frac{1}{\sqrt{3}}\langle 1,\frac{1}{2},1,-\frac{1}{2}\vert\right) D\vert 0,\frac{1}{2},0,-\frac{1}{2}\rangle$ $= \frac{1}{\sqrt{3}}\langle\phi_{2,1,1}\vert\frac{D_x+iD_y}{\sqrt{2}}\vert\phi_{1,0,0}\rangle = -\frac{1}{3}eI_R$	σ^+	1
$\vert s_{-\frac{1}{2}}\rangle \leftrightarrow \vert p_{\frac{3}{2},\frac{3}{2}}\rangle$ $= \vert g_1\rangle \leftrightarrow \vert e_6\rangle$	$\langle 1,\frac{1}{2},1,\frac{1}{2}\vert D\vert 0,\frac{1}{2},0,-\frac{1}{2}\rangle = 0$		0
$\vert s_{\frac{1}{2}}\rangle \leftrightarrow \vert p_{\frac{1}{2},-\frac{1}{2}}\rangle$ $= \vert g_2\rangle \leftrightarrow \vert e_1\rangle$	$\left(\frac{1}{\sqrt{3}}\langle 1,\frac{1}{2},0,-\frac{1}{2}\vert - \sqrt{\frac{2}{3}}\langle 1,\frac{1}{2},-1,\frac{1}{2}\vert\right) D\vert 0,\frac{1}{2},0,\frac{1}{2}\rangle$ $= \langle\phi_{2,1,-1}\vert\frac{D_x-iD_y}{\sqrt{2}}\vert\phi_{1,0,0}\rangle = -\frac{\sqrt{2}}{3}eI_R$	σ^-	2
$\vert s_{\frac{1}{2}}\rangle \leftrightarrow \vert p_{\frac{1}{2},\frac{1}{2}}\rangle$ $= \vert g_2\rangle \leftrightarrow \vert e_2\rangle$	$\left(\sqrt{\frac{2}{3}}\langle 1,\frac{1}{2},1,-\frac{1}{2}\vert - \frac{1}{\sqrt{3}}\langle 1,\frac{1}{2},0,\frac{1}{2}\vert\right) D\vert 0,\frac{1}{2},0,\frac{1}{2}\rangle$ $= -\frac{1}{\sqrt{3}}\langle\phi_{2,1,0}\vert D_z\vert\phi_{1,0,0}\rangle = -\frac{1}{3}eI_R$	π	1
$\vert s_{\frac{1}{2}}\rangle \leftrightarrow \vert p_{\frac{3}{2},-\frac{3}{2}}\rangle$ $= \vert g_2\rangle \leftrightarrow \vert e_3\rangle$	$\langle 1,\frac{1}{2},-1,-\frac{1}{2}\vert D\vert 0,\frac{1}{2},0,\frac{1}{2}\rangle = 0$		0
$\vert s_{\frac{1}{2}}\rangle \leftrightarrow \vert p_{\frac{3}{2},-\frac{1}{2}}\rangle$ $= \vert g_2\rangle \leftrightarrow \vert e_4\rangle$	$\left(\frac{1}{\sqrt{3}}\langle 1,\frac{1}{2},-1,\frac{1}{2}\vert + \sqrt{\frac{2}{3}}\langle 1,\frac{1}{2},0,-\frac{1}{2}\vert\right) D\vert 0,\frac{1}{2},0,\frac{1}{2}\rangle$ $= \frac{1}{\sqrt{3}}\langle\phi_{2,1,-1}\vert\frac{D_x-iD_y}{\sqrt{2}}\vert\phi_{1,0,0}\rangle = \frac{1}{3}eI_R$	σ^-	1
$\vert s_{\frac{1}{2}}\rangle \leftrightarrow \vert p_{\frac{3}{2},\frac{1}{2}}\rangle$ $= \vert g_2\rangle \leftrightarrow \vert e_5\rangle$	$\left(\sqrt{\frac{2}{3}}\langle 1,\frac{1}{2},0,\frac{1}{2}\vert + \frac{1}{\sqrt{3}}\langle 1,\frac{1}{2},1,-\frac{1}{2}\vert\right) D\vert 0,\frac{1}{2},0,\frac{1}{2}\rangle$ $= \sqrt{\frac{2}{3}}\langle\phi_{2,1,0}\vert D_z\vert\phi_{1,0,0}\rangle = \frac{\sqrt{2}}{3}eI_R$	π	2
$\vert s_{\frac{1}{2}}\rangle \leftrightarrow \vert p_{\frac{3}{2},\frac{3}{2}}\rangle$ $= \vert g_2\rangle \leftrightarrow \vert e_6\rangle$	$\langle 1,\frac{1}{2},1,\frac{1}{2}\vert D\vert 0,\frac{1}{2},0,\frac{1}{2}\rangle$ $= \langle\phi_{2,1,1}\vert\frac{D_x+iD_y}{\sqrt{2}}\vert\phi_{1,0,0}\rangle = -\frac{1}{\sqrt{3}}eI_R$	σ^+	3

2.11 SI: Transition dipole moment and oscillator strength

For a system with N states, the transition dipole moment related to a transition from the initial state $|\psi_I\rangle$ to the final state $|\psi_F\rangle$ is given by $\boldsymbol{\mu}_{FI}$, where $I \in \{1...N\}$ and $F \in \{1...N\}$. Within a Cartesian coordinate system ($i = \{x, y, z\}$), the corresponding components of this complex vector are given by

$$\mu_{FI,i} = \langle\psi_F|D_i|\psi_I\rangle \tag{2.24}$$

where D_i is the i-component of the electric dipole operator $\mathbf{D} = e\mathbf{R}$, with e the elementary charge and $\mathbf{R}$ the position operator. The transition dipole moment is Hermitian, implying that $\mu_{IF,i} = \langle\psi_I|D_i|\psi_F\rangle = \mu^*_{FI,i}$, where the $*$ denotes the complex conjugate.

When we consider spinorbitals, the $1s$ and $2p$ contain 2 and 6 sublevels, respectively. The total basis set contains thus 8 spinorbitals, for which one can write down the matrix elements of the transition dipole moment. For each i-component, we obtain an 8×8 matrix. Since we are only interested in $|1s\rangle \leftrightarrow |2p\rangle$ transitions, the lower left 6×2 submatrix contains all the information we need, i.e. the ones with $I \in \{1, 2\}$ (1s sublevels) and $F \in \{3, 8\}$ (2p sublevels). This submatrix contains the elements of the transition dipole moment related to transitions from a $1s$ to a $2p$ sublevel. The upper right 2×6 submatrix is related to transitions from a $2p$ to a $1s$ sublevel and contains the complex conjugates.

Let us from now on merely focus on the 6×2 lower left submatrix of $\mu_{FI,i}$ and relabel the states (according to main text Fig. 2.1b and c). We denote $\boldsymbol{\mu}_{\nu\mu}$ as the transition dipole moment related to a transition from a ground state sublevel $|g_\mu\rangle$ ($\mu \in \{1, 2\}$) to an excited state sublevel $|e_\nu\rangle$ ($\nu \in \{1, 6\}$). Within a Cartesian coordinate system ($i = \{x, y, z\}$), the corresponding components of this complex vector are given by

$$\mu_{\nu\mu,i} = \langle e_\nu|D_i|g_\mu\rangle \tag{2.25}$$

where D_i is the i-component of $\mathbf{D} = e\mathbf{R}$, with e the elementary charge and $\mathbf{R}$ the position operator. For each i-component, the transition dipole moments are conveniently put into a 6×2 matrix with values given by Eq. (2.25).

A convenient measure for the strength of a transition is the real-valued oscillator strength f, which is proportional to the absolute square of the transition dipole moment[35]. In this work, we will consider only a small subset of all possible transitions in the hydrogen atom, i.e. the $|1s\rangle \leftrightarrow |2p\rangle$ transitions, where we refer to the sublevel transitions as $|g_\mu\rangle \leftrightarrow |e_\nu\rangle$. The oscillator strength related to such a transition is therefore proportional to the absolute square of the transition dipole moment $\boldsymbol{\mu}_{\nu\mu}$ (which is a vector, such that we have to take the sum of the absolute squares of the components), i.e.

$$f_{\mu\nu} \propto |\boldsymbol{\mu}_{\nu\mu}|^2 = \sum_{i=x,y,z} |\mu_{\nu\mu,i}|^2 \tag{2.26}$$

where $f_{\mu\nu} = f_{\nu\mu}$. For our work it is convenient to define the relative oscillator strength related to a transition between a ground state $|g_\mu\rangle$ and an excited state $|e_\nu\rangle$ as

$$f_{rel,\mu\nu} = \frac{9}{(eI_R)^2}|\boldsymbol{\mu}_{\nu\mu}|^2 = \frac{9}{(eI_R)^2}\sum_{i=x,y,z} |\mu_{\nu\mu,i}|^2 = \frac{9}{(eI_R)^2}\sum_{i=x,y,z} |\langle e_\nu|D_i|g_\mu\rangle|^2 \tag{2.27}$$

For an electron occupying the ground state sublevel $|g_\mu\rangle$, we define the total relative oscillator strength as

$$f_{rel,g_\mu,tot} = \sum_\nu f_{rel,\mu\nu} = \frac{9}{(eI_R)^2}\sum_{\nu,i} |\langle e_\nu|D_i|g_\mu\rangle|^2 \tag{2.28}$$

2.12 SI: Jones calculus applied to the oscillation of an atomic electric dipole

To describe how polarized light is affected by interaction with an optical element (or a sample), it is often convenient to use Jones calculus. Within this method, light is represented by a Jones vector and the optical element by a Jones matrix. Within the Jones-vector formulation, a Jones vector contains the amplitude and phase of the electric field components of a light beam (orthogonal to its propagation direction). Commonly, the amplitudes are normalized, such that their intensities add up to 1. Any elliptical polarization can be described, including the special cases of linear and circular polarization.

The polarization ellipse is described by the azimuth θ and the ellipticity angle ϵ, as illustrated in main text Fig. 1.4. The azimuth θ is the angle between the semi-major axis a and the horizontal axis, where $-\frac{1}{2}\pi \leqslant \theta < \frac{1}{2}\pi$. Note that a and θ are ill-defined for circularly polarized light. The ellipticity angle ϵ is defined through the ellipticity $e = \frac{b}{a}$ (with b the semi-minor axis) such that $e = \pm \tan\epsilon$, where $-\frac{1}{4}\pi \leqslant \epsilon \leqslant \frac{1}{4}\pi$ (where the $+$ and $-$ signs correspond to right- and left-handed polarization respectively).

The general definition of the Jones vector representing an electric vector oscillating in the xy-plane is given by[16]

$$\mathbf{E}\{\hat{\mathbf{x}},\hat{\mathbf{y}}\} = A\mathrm{e}^{i\delta}\mathbf{R}(-\theta)\begin{bmatrix}\cos(\epsilon)\\ i\sin(\epsilon)\end{bmatrix} = A\mathrm{e}^{i\delta}\begin{bmatrix}\cos(\theta)\cos(\epsilon)-i\sin(\theta)\sin(\epsilon)\\ \sin(\theta)\cos(\epsilon)+i\cos(\theta)\sin(\epsilon)\end{bmatrix} \tag{2.29}$$

where we will take for convenience the amplitude $A = 1$ and the global phase $\delta = 0$. The transformation matrix $\mathbf{R}(-\theta)$ rotates the primed basis with an angle $-\theta$ (to the unprimed basis) in main text Fig. 1.4. It turns out that we have to distinguish only two cases in this work, i.e. $\theta = 0$ (the x-axis is the major axis) and $\theta = \pi/2$ (the y-axis is the major axis). Within the $\{\hat{\mathbf{x}},\hat{\mathbf{y}}\}$-basis, the corresponding Cartesian Jones vectors follow from Eq. (2.29) by substituting for θ, from which we can easily find ϵ, i.e.

$$\theta = 0: \quad \hat{\mathbf{E}}\{\hat{\mathbf{x}},\hat{\mathbf{y}}\} = \begin{bmatrix}\cos(\epsilon)\\ i\sin(\epsilon)\end{bmatrix}, \quad \epsilon = \sin^{-1}(-iE_y) \tag{2.30}$$

$$\theta = \pi/2: \quad \hat{\mathbf{E}}\{\hat{\mathbf{x}},\hat{\mathbf{y}}\} = \begin{bmatrix}-i\sin(\epsilon)\\ \cos(\epsilon)\end{bmatrix}, \quad \epsilon = \sin^{-1}(iE_x) \tag{2.31}$$

which for both cases corresponds to a clockwise rotation (right-handed polarization) for $\epsilon > 0$. Note that $|E_x| > |E_y|$ when $\theta = 0$, whereas $|E_y| > |E_x|$ when $\theta = \pi/2$.

We find it convenient to assign a Jones vector to the oscillation of an atomic electric dipole related to an electronic transition, with the components of the electric vector $\mathbf{E}$ given by the (normalized) components of the corresponding transition dipole moment. As such, an electric dipole oscillating in the xy-plane is represented by the Jones vector

$$\hat{\mathbf{E}}\{\hat{\mathbf{x}},\hat{\mathbf{y}}\} = N\begin{bmatrix}\langle\phi_f|D_x|\phi_i\rangle\\ \langle\phi_f|D_y|\phi_i\rangle\end{bmatrix} \tag{2.32}$$

with N a normalization constant and $|\phi_{i(f)}\rangle$ the initial (final) state. We will always take the ground state $|\phi_f\rangle = |g_{1,2}\rangle$ for the initial state.

For the $1s \leftrightarrow 2s$ transitions of the hydrogen atom, it turns out that for six of the twelve possible transitions the transition dipole moment has only nonzero z-components for increasing charge q, i.e. the electric dipole oscillates only in the z-direction (these six have been named Group Z (blue) in main text Table 2.2). For this Group Z, only the oscillator strength varies as a function of q (i.e. the polarization selection rules vary only in the sense of varying between forbidden and allowed). For the other six transitions (Group XY (red) in main text Table 2.2), the transition dipole moment has only nonzero x- and y-components, i.e. the electric dipole oscillates in the xy-plane. For these transitions the polarization seletion rules are also affected in the sense of a change of the ellipticity (actually, only the ellipticity angle ϵ turns out to be affected). We find for this Group XY for increasing charge q that of the components E_x and E_y always one is purely real and the other imaginary (or zero). This implies that we have either $\theta = 0$ or $\theta = \pi/2$. More specific, for increasing q the polarization selection rules for each of the Group XY series change from circular to linear, without affecting θ. Therefore, we can for each series always write the Jones vector in the form of either Eq. (2.30) or (2.31), where we multiply with a global phase factor $\mathrm{e}^{i\delta'}$ with the phase δ' taken such that E_x becomes real when $|E_x| > |E_y|$ and E_y becomes real when $|E_y| > |E_x|$. Subsequently, we can easily determine the ellipticity angle ϵ.

2.13 SI: Perturbation-theory description of distortion by extra charges

In this section we present a perturbation-theory approach for analyzing why the character of the eigenstates and the selection rules have their strongest evolution in the range between $q = 10^{-4}$ and $q = 10^{-3}$ (see the traces in Fig. 2.2, Fig. 2.3 and Fig. 2.4b). This confirms that this occurs at the value for q where the perturbation due to the charges becomes stronger than the spin-orbit coupling in the bare hydrogen atom.

The notation used for this perturbation-theory description mostly follows[5]. However, for consistency with the main text we introduce H_{0so} as notation for the unperturbed Hamiltonian of the hydrogen atom with spin-orbit coupling already included,

$$H_{0so} = H_0 + H_{SO} \tag{2.33}$$

The Hamiltonian with the perturbation due to the extra charges $-q$ is then

$$H = H_{0so} + V \tag{2.34}$$

where V is

$$V = \sum_i \frac{q_i \cdot e}{|\mathbf{R} - \mathbf{r}_i|} \tag{2.35}$$

The summation runs here over the set of extra charges put in the environment, each labeled by a value for i. Further, e is the elementary charge, $\mathbf{R}$ is the position operator for the electron, and $\mathbf{r}_i$ are the positions of the extra charges. We will restrict ourselves to the case with identical magnitude for all charges q_i, that is, for all i we use $q_i = q$.

The unperturbed H_{0so} has degenerate eigenstates for the states that belong to the $2p_{1/2}$ and $2p_{3/2}$ manifolds. We therefore work out degenerate perturbation theory by rotating the degenerate orbitals[5] in such a way that in each degenerate set $\langle p_k| V |p_l\rangle = 0$, for all cases $k \neq l$ and k, l an index for labeling the p states. The perturbation theory then gives for the first-order energy shift (with $|\phi_n\rangle$, $|\phi_p\rangle$, E_n, E_p eigenstates and eigenvalues of H_{0so})

$$\langle \phi_n| V |\phi_n\rangle = q \cdot e \cdot \left\langle \phi_n \left| \sum_i \frac{1}{|\mathbf{R} - \mathbf{r}_i|} \right| \phi_n \right\rangle \tag{2.36}$$

The first order correction to the wave function has probability amplitudes

$$c_{np} = \frac{\langle \phi_p| V |\phi_n\rangle}{E_n - E_p} = \frac{q \cdot e}{E_n - E_p} \cdot \left\langle \phi_p \left| \sum_i \frac{1}{|\mathbf{R} - \mathbf{r}_i|} \right| \phi_n \right\rangle \tag{2.37}$$

where (given the above remark on degeneracies) we only need to consider terms that combine $1s$ and $2p$ states. The last expression shows that the effect strongly depends on the particular geometry of the perturbation with charges: the state mixing is proportional to q and to a spatial integral that only concerns the operators $1/|\mathbf{R} - \mathbf{r}_i|$. For our particular geometry, we find via numerical evaluation of the integral that the sum of the amplitudes c_{np} is of order $0.01 \cdot q \cdot e/(E_n - E_p)$. That is, the state mixing is governed by matrix elements $\langle \phi_p| V |\phi_n\rangle \approx 0.01 \cdot q \cdot e$. In the atomic units we use, the strength of the spin-orbit coupling is about 10^{-6} Hartree[5]. Hence, the perturbation by the charges will dominate over the spin-orbit coupling for values of $q > 10^{-4}$. This is in agreement with the trends in traces in Fig. 2.2, Fig. 2.3 and Fig. 2.4b.

Notably, for describing the effective strength of the distortion, the above analysis shows how a spatial integral over the volume that is occupied by the electron wave function is an important factor. When comparing two situations with the extra charges either inside or outside the volume where the wave function has significant amplitude, but with otherwise identical symmetry and identical Coulomb distortion at the hydrogen nucleus, the effective strength of the distortion is therefore very different. That is, a distortion with charges $-q$ at a distance a (with a of order the Bohr radius) has a stronger influence than placing charges of magnitude $-C \cdot q$ moved out radially to a distance $C \cdot a$.

Chapter 3

Proposal for time-resolved optical preparation and detection of triplet-exciton spin coherence in organic molecules

Abstract

Changes in optical polarization upon light-matter interaction can probe chirality, magnetization and non-equilibrium spin orientation of matter, and this underlies fundamental optical phenomena such as circular dichroism and Faraday and Kerr rotation. With fast optical pulses electronic spin dynamics in materials can be initiated and detected in a time-resolved manner. This has been applied to material systems with high order and symmetry (giving distinct optical selection rules), such as clouds of alkali atoms and direct-band-gap semiconductor systems, also in relation to proposals for spintronic and quantum technologies. For material systems with lower symmetry, however, the potential of these phenomena for studying and controlling spin is not well established. We present here how pulsed optical techniques give access to preparing and detecting the dynamics of triplet spin coherence in a broad range of (metal-)organic molecules that have significant spin-orbit coupling. We establish how the time-resolved Faraday rotation technique can prepare and detect spin coherence in flat molecules with C_{2v} symmetry, and extrapolate that the effects persist upon deviations from this ideal case, and upon ensemble averaging over fully randomized molecular orientations. For assessing the strength and feasibility of the effects in reality, we present detailed theoretical-chemistry calculations.

3.1 Introduction

Organic molecules are increasingly used for opto-electronic devices, because of their chemical tunability, low-cost, and ease of processing. In such devices, the ratio of singlet to triplet excitons can be an important performance parameter[39]. Moreover, because of the many interesting spin-related phenomena discovered in organic semiconductors and molecules[40–45], further exploration of spintronic applications in these materials is of interest. Both for organic opto-electronics and spintronics, being able to control and probe triplet-exciton spin coherence will be of great value for better material studies and improving the functionalities. A handle for this may rely on the optical polarization of the interacting light. Correlations between electronic spin states and optical polarization are well established for inorganic semiconductors with strong spin-orbit coupling (SOC)[9], and a particular example for using such correlations is the Time-Resolved Faraday Rotation (TRFR) technique[12, 13, 46]. This is a pump-probe technique based on measuring the polarization rotation (optical rotation angle) of a probe pulse upon transmission through a sample, as a measure for the (precessing) spin orientation induced by a pump pulse. The oscillation of the polarization rotation as a function of the delay time between pump and probe then directly reflects coherent spin dynamics. The aim of the theoretical work in this chapter is to study how this pump-probe technique also allows for optical control and probing of coherent triplet-exciton spin dynamics in organic molecules.

3.2 Theoretical proof of principle for a molecular TRFR experiment

To realize a molecular TRFR experiment (Fig. 3.1), we suggest to use an ultrashort polarized pump pulse that excites a molecular system from the singlet ground state into a coherent superposition of two sublevels of the lowest triplet excited state (Fig. 3.2a), for the zero-phonon optical transition. This energy level scheme differs from the most common TRFR scenario, which focuses on electron spin coherence (with spin $S = 1/2$) in inorganic semiconductors[12, 13]. For

---

This chapter is based on Ref. 2 on p. 177.

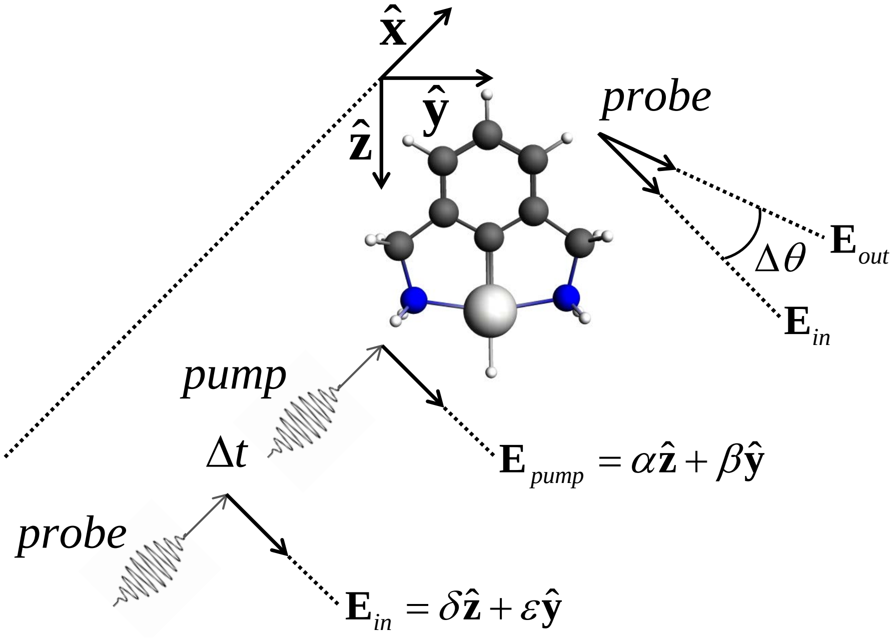

Figure 3.1: Schematic of a molecular Time-Resolved Faraday Rotation (TRFR) experiment. The pump and probe pulse propagate in the x-direction, whereas the molecule lies in the yz-plane. Depending on the state of the molecule, the probe pulse experiences optical rotation upon transmission, where the optical Faraday rotation angle $\Delta\theta$ (in the yz-plane) is a measure for the spin orientation induced by the pump pulse. Coherent spin dynamics occurs along the x-axis and is revealed by varying the delay time between pump and probe, involving an oscillation of $\Delta\theta$. In view of this work, the metal-organic molecule (2,6-bis(aminomethyl)phenyl)(hydrido)platinum is depicted, which is referred to as $PtN_2C_8H_{12}$. This molecule has C_{2v} symmetry. The Jones vectors $\mathbf{E}$ with corresponding (in general complex) prefactors (α, β, δ and ϵ) are in general not normalized, unless representing polarizations (i.e. normalized electric vectors which we denote with a hat, in which case we call the prefactors polarization parameters).

these systems optical transitions can be described as excitations of single electrons, from valence-band to conduction-band states. For the relevant electrons in chemically stable organic molecules the typical situation is very different: the ground state has two localized electrons in a spin singlet $S = 0$ configuration. Without SOC effects, optical transitions are only allowed to excited states that are also singlet states. Spin coherence can be carried out by excited states with the electrons in a triplet spin $S = 1$ configuration, and these states have energies that are typically ~200 meV lower in energy than their singlet equivalents. Optical transitions directly into the triplet excited states are only possible when

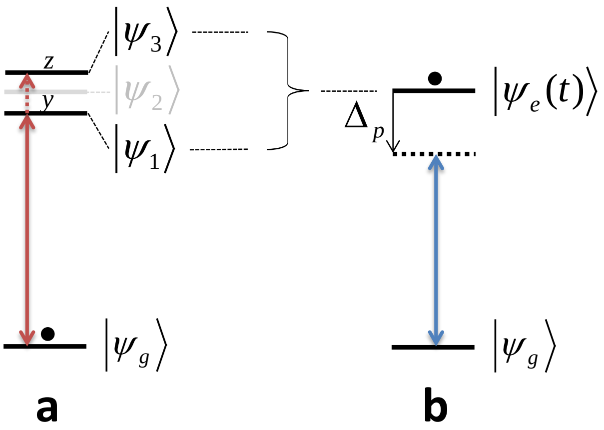

Figure 3.2: Energy level scheme and laser (de)tuning for the pump and probe pulse in a molecular Time-Resolved Faraday Rotation (TRFR) experiment. **a**, For $PtN_2C_8H_{12}$ all three (x, y, z, as defined in Fig. 3.1) components of $\langle\psi_2|\,\mathbf{r}\,|\psi_g\rangle$ are zero, wherefore we neglect $|\psi_2\rangle$. When the pump pulse (red arrow) arrives at $t = 0$, only $|\psi_g\rangle$ is populated, as indicated with the dot. Full absorption of a photon out of a short (thus spectrally broad) optical pump pulse polarized in both the y and z-direction induces a superposition of $|\psi_1\rangle$ and $|\psi_3\rangle$. **b**, Directly after excitation with the pump, $|\psi_e(t)\rangle$ (being a superposition of $|\psi_1\rangle$ and $|\psi_3\rangle$) is populated, as indicated with the dot. A linearly polarized probe pulse (blue arrow) with detuning Δ_p experiences a polarization rotation $\Delta\theta$, which oscillates as a function of the delay time Δt. This oscillation is a measure for the coherent spin dynamics $\langle\mathbf{J}\rangle(t)$, related to the evolution $|\psi_e(t)\rangle$.

the system has significant SOC, with more oscillator strength for the transitions as the SOC strength increases. Typical molecular systems with large SOC are metal-organic complexes containing a heavy metal atom[47, 48], and molecules with strong curvature at carbon-carbon bonds[49]. Such molecules are particularly used in organic light-emitting diodes (OLEDs) for efficient triplet-exciton harvesting.

For our analysis we will assume that the pump pulse exactly transfers all population from the singlet to the triplet state (i.e. and exact optical π-pulse for this transition). In practice this will often not be the case, but for the essential aspects in our analysis this does not compromise its validity. Instead, an ultrafast pump pulse will in general bring the system in a quantum superposition of $|\psi_g\rangle$ and $|\psi_e(t = 0)\rangle$. However, the quantum coherence between these two states will typically decohere very fast, and this will bring the system in an incoherent mixture of $|\psi_g\rangle$ and $|\psi_e(t \approx 0)\rangle$. Then, the population in $|\psi_g\rangle$ will not contribute to the TRFR signal (for our probing scheme, see below). At the same time, the population in $|\psi_e(t \approx 0)\rangle$ will contribute to the TRFR signal in the same manner as a system that is purely in this state. The main reason to still aim for excitation with an optical π-pulse is that this maximizes the TRFR signal, and our estimates below here assume this case.

We thus assume that the pump pulse brings the molecules in a state that is purely a superposition of triplet sublevels ($|\psi_e(t)\rangle$ in Fig. 3.2b). This state will show coherent spin dynamics as a function of time (also at zero magnetic field the triplet sublevels are typically not degenerate[50]). We will study this by calculating both $\langle \mathbf{S} \rangle (t)$ and $\langle \mathbf{J} \rangle (t)$, where $\mathbf{J} = \mathbf{L} + \mathbf{S}$ is the total electronic angular momentum in conventional notation, and t is the time after the arrival of the pump pulse (to be clear, we use t for time in the system's free evolution, and Δt for the pump-probe delay). As commonly done in literature on spintronics[51], we will use the word spin for well-defined states of $\mathbf{J}$. The discussion will clarify whether a net spin orientation refers to a nonzero expectation value for $\mathbf{J}$ or $\mathbf{S}$.

For our calculations we focus on a molecule that contains a heavy-metal atom in order to have large SOC. In literature, usually density-functional theory (DFT) calculations are used to study such complexes theoretically, like e.g. for platinum porphyrins[45] and iridium complexes[52]. We use the more accurate combined CASSCF/CASPT2/RASSI–SO method instead, as introduced by Roos and Malmqvist[17, 18] in MOLCAS[23], in order to have a better basis for extracting physically relevant wave functions and spin expectation values. Since this is computationally a very expensive method, we chose the relatively small metal-organic complex (2,6-bis(aminomethyl)phenyl)(hydrido)platinum (to which we refer in this work as $PtN_2C_8H_{12}$ (Fig. 3.1)). Note that this molecule is (possibly) not chemically stable, in contrast to the related molecule[53] with Cl substituted for the H bound to Pt and $N(CH_3)_2$ for NH_2. However, it is computationally much less demanding and therefore more suitable for our proof of principle calculation.

The sublevels of the lowest triplet (including SOC) of $PtN_2C_8H_{12}$ are labeled as $|\psi_1\rangle$, $|\psi_2\rangle$ and $|\psi_3\rangle$ (Fig. 3.2 and Supplementary Information Fig. 3.9 (p. 84)). The energies of these levels with respect to $|\psi_g\rangle$ are 3.544, 3.558 and 3.564 eV respectively, as obtained from the CASPT2 calculation. The corresponding nonzero components of the transition dipole moments are $\langle \psi_1 | \, y \, | \psi_g \rangle \approx 0.0003 - i0.0112$ and $\langle \psi_3 | \, z \, | \psi_g \rangle \approx 0.0063$ in atomic units (where the conversion factor to SI-units is $8.47836 \cdot 10^{-30}$ Cm). In other words, a transition from $|\psi_g\rangle$ is allowed only with y and z polarized light to state $|\psi_1\rangle$ and $|\psi_3\rangle$, respectively, but forbidden to state $|\psi_2\rangle$. Having this type of selection rules for singlet-triplet transitions is a generic property of systems with C_{2v} symmetry (for details see Supplementary Information Sec. 3.12 (p. 83)), and introduces a way to selectively excite to (a specific superposition of) triplet sublevels. Such an imbalance in populating the triplet sublevels is essential for inducing spin orientation (see also below).

A spectrally broad pump pulse with polarization in both the y and z-direction can thus bring the system into a superposition of $|\psi_1\rangle$ and $|\psi_3\rangle$. From the CASPT2 calculations, an energy splitting $E_3 - E_1 = 20$ meV (30 THz angular frequency) has been obtained (Supplementary Information Table 3.3 (p. 83)). To simultaneously address $|\psi_1\rangle$ and $|\psi_3\rangle$, we thus need to use ultrashort laser pulses with an uncertainty in the photon energy given by $\sigma_{E_{ph}} > E_3 - E_1$. This requires that the time duration of the pulses does not exceed 16 fs (defined as the standard deviation of the envelope), as follows from the time−energy uncertainty relation.

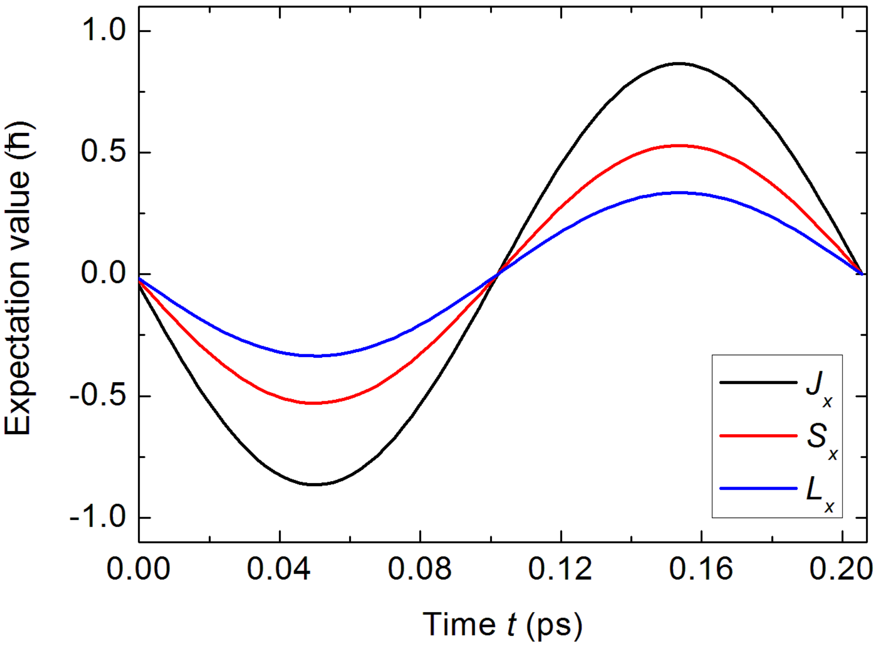

Figure 3.3: Calculation of $\langle J_x\rangle(t)$, $\langle L_x\rangle(t)$ and $\langle S_x\rangle(t)$ for a superposition of two triplet sublevels of a single $PtN_2C_8H_{12}$ molecule. This calculation originates from a superposition of triplet sublevels $|\psi_1\rangle$ and $|\psi_3\rangle$ (which interact with y and z polarized light respectively, Fig. 3.2), induced by an ultrashort pump pulse having electric unit vector $\hat{\mathbf{E}}_{pump} = \frac{\hat{\mathbf{z}}+\hat{\mathbf{y}}}{\sqrt{2}}$. Spin oscillation occurs in the x direction only. More specific, $\langle J_x\rangle(t)$, $\langle L_x\rangle(t)$ and $\langle S_x\rangle(t)$ oscillate with frequency $\omega_{31} = (E_3 - E_1)/\hbar$, while the y and z components remain zero.

For the pure triplet spin states T_x, T_y and T_z (defined in Supplementary Information Eq. (3.77-3.79) (p. 84)), all (x, y, z) components of $\langle \mathbf{S} \rangle$ are zero. Instead, for a superposition of these sublevels the net spin can be nonzero. More specifically, for a superposition of two of these spin states (say, T_i and T_j), the spin expectation value oscillates with only a nonzero component in the direction perpendicular to i and j, and with a frequency corresponding to the energy difference between the sublevels. To induce nonzero spin and subsequent spin dynamics for $PtN_2C_8H_{12}$, we therefore propose a direct excitation from $|\psi_g\rangle$ to the state $|\psi_e(t = 0)\rangle$, being a superposition of $|\psi_1\rangle$ and $|\psi_3\rangle$ (Fig. 3.2a, for details see Supplementary Information Eq. (3.26) (p. 67)). As a function of time, this superposition evolves as $|\psi_e(t)\rangle$ (Fig. 3.2b and Supplementary Information Eq. (3.28) (p. 67)), for which $\langle J_x \rangle (t)$, $\langle L_x \rangle (t)$ and $\langle S_x \rangle (t)$ oscillate with frequency $\omega_{31} = (E_3 - E_1)/\hbar$, while the y and z components remain zero. Fig. 3.3 shows the result of a calculation of such an oscillation, for the case where the electric unit vector of the pump pulse is $\hat{\mathbf{E}}_{pump} = \frac{\hat{\mathbf{z}}+\hat{\mathbf{y}}}{\sqrt{2}}$.

We aim to probe this oscillating spin (orientation) via Faraday rotation, which can be realized my measuring the polarization rotation $\Delta\theta$ (as introduced in Fig. 3.1). The optical transitions and selection rules that we have introduced in the above can be used for calculating $\Delta\theta$ (for details see Supplementary Information Sec. 3.7 (p. 64) and Sec. 3.8 (p. 66)). Fig. 3.4 shows results of such a calculation, for an ensemble of isolated and identically oriented $PtN_2C_8H_{12}$ molecules (e.g. realized by using a crystal host). We have assumed a detuned linearly polarized probe pulse, and present $\Delta\theta$ as a function of the delay time Δt between an ultrashort polarized pump and probe pulse. Taking a detuned probe (Fig. 3.2) limits probe-pulse induced population transfer back to the ground state, which allows to consider dispersion only[54]. We take a detuning where dispersion is near maximal, while probe absorption is strongly suppressed.

While we do not present the full equations for the above calculation in the main text (but in the Supplementary Information), we will discuss here some notable aspects. The polarization of the probe pulse after transmission $\mathbf{E}_{out}$ is affected when its components experience a different real part of the refractive index[16] (birefringence). A generic description of light-matter interaction in such a medium requires formulating the linear susceptibility and relative permittivity as a tensor. However, the refractive index does not have a tensor representation due to its square-root relation with these parameters[55]. Speaking about refractive indices only makes sense when a transformation is performed to the basis of the principal axes, which are the eigenvectors of the linear susceptibility tensor

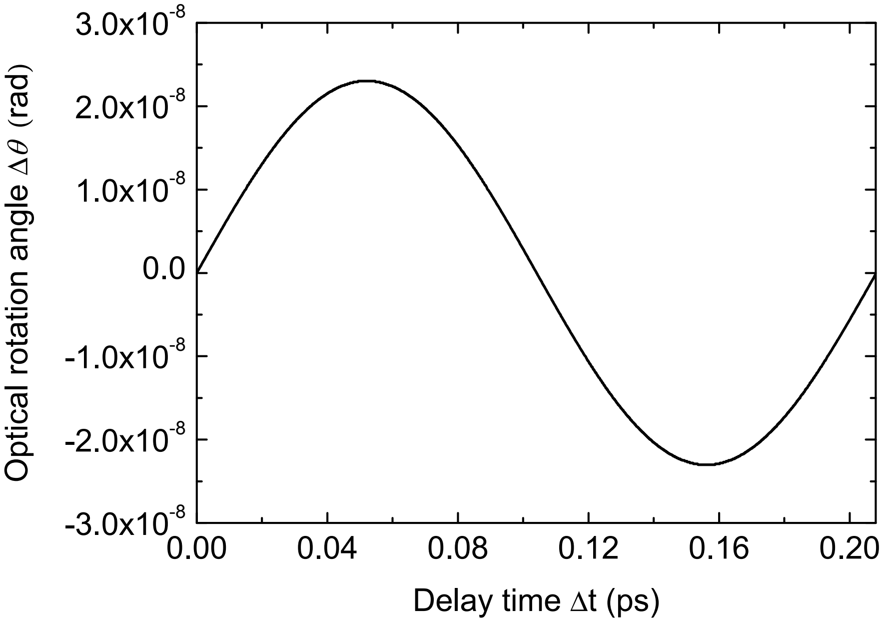

Figure 3.4: Calculation of the polarization rotation $\Delta\theta = \theta_{out} - \theta_{in}$ as a function of Δt for an ensemble of isolated and identically oriented $\mathbf{PtN_2C_8H_{12}}$ molecules. The curve was calculated with Supplementary Information Eq. (3.61) (p. 73) with the following parameter values: Polarization parameters $\alpha = \beta = \delta = \varepsilon = 1/\sqrt{2}$, i.e. electric unit vectors $\hat{\mathbf{E}}_{pump} = \hat{\mathbf{E}}_{in} = \frac{\hat{\mathbf{z}}+\hat{\mathbf{y}}}{\sqrt{2}}$ (where $\hat{\mathbf{E}}_{in}$ is the initial polarization of the probe); Transition dipole moments $d_1 = 0.0003 - i0.0112$ and $d_3 = 0.0063$ a.u.; Triplet sublevel splitting $E_3 - E_1 = 20$ meV; Probe wavelength $\lambda = 349$ nm; Detuning $\Delta_p = -60$ meV, which is assumed to satisfy the requirements $|\Delta_p| >> \gamma$ and $|\Delta_p| >> |E_3 - E_1|/\hbar$; Thickness $d = 100$ nm; Number density $N = 10^{24}$ m^{-3}.

$\tilde{\boldsymbol{\chi}}^{(1)}$ (Eq. (3.31) in the Supplementary Information (p. 68)). For our system, the oscillating dynamics of $|\psi_e(t)\rangle$ yields that the principal axes oscillate with time (see Eq. (3.38) and (3.41)). While accounting for this, the electric-field components of the probe after transmission (Eq. (3.56)), and in turn the corresponding azimuth θ_{out} (Eq. (3.59)), and polarization rotation $\Delta\theta = \theta_{out} - \theta_{in}$ (Eq. (3.61)) can be calculated, for results as in Fig. 3.4.

Comparing Fig. 3.3 with Fig. 3.4, we conclude that $\Delta\theta(\Delta t)$ is an appropriate measure for $\langle \mathbf{J} \rangle (t)$, since both oscillate in phase with frequency ω_{31}. The experimental advantage of measuring oscillating coherent spin dynamics instead of merely spin orientation is that it is much easier to trace back the origin of a small signal when it oscillates, and it gives access to observing the dephasing time of the dynamics.

3.3 Feasibility analysis

The experimental feasibility of a molecular TRFR experiment particularly depends on the amplitude of the oscillation of the polarization rotation $\Delta\theta$ as a function of the delay time Δt. Typically, the accuracy of a TRFR experiment is in the order of nrads[56]. Fig. 3.4 gives a value of 23 nrad for this amplitude, well within the required range. In Supplementary Information Sec. 3.10 (p. 75) we discuss how this signal can be enhanced by several orders of magnitude. In the remainder of this section we address other aspects of the feasibility of a molecular TRFR experiment.

3.3.1 TRFR experiment with an ensemble of randomly oriented molecules

In Supplementary Information Sec. 3.15 (p. 91) we show for an ensemble of randomly oriented $PtN_2C_8H_{12}$ molecules that the TRFR signal is only reduced by a factor 2 as compared to the case with all molecules oriented such that the maximum signal is obtained (i.e. perpendicular to the incoming light). Hence, optically induced spin orientation does not necessarily require the same orientation for the molecules of interest when put in a crystal host. Moreover, this shows that a nonzero TRFR signal can be obtained for molecules in the gas phase and in solution. In these cases it can be satisfied that the molecules of interest are well isolated from each other. Still, the spin lifetime might be affected by several effects.

The spin dynamics might be affected by thermal fluctuations within the molecule. Although this is usually hardly the case for pure spins, the effect might be nonnegligible in our case due to the orbital part being mixed in via SOC. As long as this orbital contribution is small, these effects will not be severe. The strength of the SOC effect drives in fact a trade off between positive and negative effects for observing long-coherent spin oscillations with TRFR. Strong SOC makes the direct singlet-triplet transition stronger. However, it will also shorten the effective triplet-spin dephasing time because it shortens the optical life time of the triplet state, and since it enhances the mentioned coupling to thermal fluctuations. In addition, rapid tumbling of molecules in solution might limit for how long coherent spin oscillations can be observed. This effect might be suppressed by e.g. taking a high viscosity of the solvent, large molecules or a low temperature (for details see Supplementary Information Sec. 3.15). Another trade off lies in the triplet sublevel splitting for the system of choice. A larger splitting gives faster spin oscillations, but is thus more demanding on the need for ultrashort laser pulses. A larger energy scale for the splitting probably increases to what extent the spin dynamics couples to other dynamics of the system.

3.3.2 Single molecule TRFR experiment

In earlier work, the optically detected magnetic resonance (ODMR) technique has been used to study triplet spin polarization in molecular ensembles[57] and single molecules[58]. Within this technique, a microwave field drives the spin dynamics. An advantage of our TRFR technique may lie in that it is an all-optical technique, and fast laser pulses give access to a much higher time resolution. Other advantages are the absence of a magnetic field and the applicability to ensembles of randomly oriented molecules.

It would be very interesting to be able to also apply the TRFR experiment to a single molecule. Hence, we qualitatively determine whether such an experiment is possible. As an approximation for the signal obtained with a single molecule experiment, we can take the thickness d equal to the separation between two molecules (determined by N). In our calculation for $PtN_2C_8H_{12}$, we have $d =$ 100 nm and N corresponding to a separation of 10 nm. Our approximation thus implies only one order of magnitude loss of $\Delta\theta$ signal when taking a single molecule into account. We thus conclude that the signal of a TRFR experiment applied to a single $PtN_2C_8H_{12}$ molecule lies within the measurable range ($>$ nrad) which offers a strong indication that the TRFR technique can be used to probe the spin of single molecules as well. Likewise, the TRFR technique has already been applied successfully to probing of a single spin in a semiconductor quantum dot[59].

3.3.3 Franck-Condon suppression of optical transitions

Although our proof-of-principle calculation was performed for (2,6-bis(aminomethyl)phenyl)(hydrido)platinum, this particular molecule seems unfavorable for an actual demonstration of a molecular TRFR experiment since the Franck-Condon (FC) factor for the zero-phonon transition is extremely small (Supplementary Information Sec. 3.13 (p. 85)). Using the zero-phonon transition is still preferred to avoid a strongly disturbing coupling between the coherent spin dynamics and phonons. The zero-phonon-line FC factors for platinum porphyrins are much larger (Supplementary Information Sec. 3.13), which make them promising candidates for spintronics applications in general[45], and for a molecular TRFR experiment in particular (Supplementary Information Sec. 3.14 (p. 86)).

3.3.4 Persistence of spin-orientation effects for symmetries lower than C_{2v}

For our proof-of-principle study we have focused on a system with C_{2v} symmetry, for which the complexity of the description can be kept at a moderate level. This case is also relevant since many organic molecules have a flat structure (around the location with the optically active electrons). For molecules that only weakly deviate from this C_{2v} symmetry, the effects are most likely only weakly suppressed. That is, the effects demonstrated in this chapter only fade out gradually when one gradually distorts the C_{2v} symmetry.

The nonzero TRFR signal in our proposal comes mainly forward due to the strong selection rules that link particular optical polarizations to transitions from the singlet ground state into specific triplet sublevels. More specific, since one of the three electric dipole moments for the singlet-to-triplet transitions is zero (directly following from the C_{2v} symmetry), the TRFR signal shows a single spin oscillation, originating from the quantum superposition of two triplet sublevels. In the case of a relatively large deviation from C_{2v}, these selection rules become usually less strict in two ways: excitations are allowed (1) to all three sublevels, and (2) with all polarizations (x, y, z). However, the oscillator strengths of the different polarizations are usually not equally strong for the different sublevels. As such, an imbalance in the populations of the triplet sublevels can still be created, such that the TRFR signal will not be fully suppressed. Additionally, the total TRFR signal will then consist of a sum of three oscillations with frequencies $|\omega_{ij}| = |E_i - E_j|/\hbar$, with i and j two different triplet sublevel indices.

3.4 Summary and Outlook

We have derived the fundamentals of a TRFR experiment applied to organic molecules with strong spin-orbit coupling allowing for singlet-triplet excitations. We have shown how the optical selection rules can be exploited to induce a quantum superposition of triplet sublevels of the excited state of the molecular system, using an ultrashort pump pulse. We have derived how the polarization of an optical probe pulse is affected upon transmission, from which the requirements for polarization rotation follow. As a proof-of-principle calculation, the metal-organic complex (2,6-bis(aminomethyl)phenyl)(hydrido)platinum has been considered to study the possibility of a molecular TRFR experiment. Using the results of ab initio calculations, we have calculated the time dependence of the polarization rotation angle and of the expectation value of the total electronic angular momentum. Both oscillate in phase with a frequency corresponding to the sublevel splitting, implying that the oscillation of polarization rotation is a suitable measure for coherent spin dynamics. Nevertheless, metal-organic molecules like platinum porphyrins seem better candidates for a molecular TRFR experiment because of their larger Franck-Condon factors for the zero-phonon transition.

Using the TRFR technique to study triplet-exciton spin dynamics in organic molecules offers an interesting tool for probing material properties and new functionalities. An obvious example is a study of the lifetime of coherent spin dynamics, and the TRFR technique also allows for studying (extremely small or zero) energy splittings between triplet sublevels. Such studies are useful for judging whether the molecules can be applied in spintronic or quantum information applications via light-induced spin orientation, or sensors based on spin dynamics.

3.5 Author contributions

This chapter is based on Ref. 2 on p. 177. The project was initiated by C.H.W., R.W.A.H. and G.J.J.L. Derivations, calculations and data analysis were performed by G.J.J.L. and X.G. G.J.J.L. had the lead on writing the manuscript. All authors contributed to improving the manuscript. We acknowledge M. Wobben for her contribution to the calculation of Franck-Condon factors in several metal-organic molecules.

Supplementary Information (SI)

3.6 SI: Principles of the TRFR technique for an idealized $\Pi-$system

We give here the theoretical basis of the Time-Resolved Faraday Rotation (TRFR) technique (main text Fig. 3.1) as applied to the artificial system of Fig. 3.5 which contains a single electron and where a weak magnetic field is applied in the z-direction. For the sake of simplicity, we assume that the levels $|3\rangle$ and $|4\rangle$ lie significantly lower than the levels $|1\rangle$ and $|2\rangle$. As such, this system closely resembles quantum wells with a zinc-blende band structure having a conduction band that is derived from s-like atomic states and a valence band from p-like states. For such quantum wells, the concept of spin injection is discussed by Fox[10] (2^{nd} ed., chapter 6.4.5).

The TRFR technique is a pump-probe technique, where a resonant pump pulse induces spin polarization and where the polarization rotation of a detuned (usually linearly polarized) probe pulse is measured as a function of delay time, as a measure for the spin dynamics of the system. We will assume that the photon energy of both the pump and probe pulses equals $E_{ph} = E_+ - E_2 = E_- - E_1$. As such, we can neglect $|3\rangle$ and $|4\rangle$, implying that the system behaves as a four-level Π-system. The physics behind the TRFR technique as applied to a Π-system (Fig. 3.5) offers a useful basis for this technique applied to V-systems like the singlet-triplet system on which the rest of this work focuses. Note that if the energies E_3 and E_4 would be equal to E_1 and E_2, the system would resemble direct gap III-V semiconductors (Fox[10], 2^{nd} ed., chapter 3.3.7). As such, the concept of spin injection becomes slightly more complicated. Now, σ^+ and σ^- also allow for the transitions $|3\rangle_x \to |+\rangle_x$ and $|4\rangle_x \to |-\rangle_x$ respectively, though with a probability three times as small as the transitions depicted in Fig. 3.5. For direct gap III-V semiconductors, one can therefore induce at most 50% spin polarization.

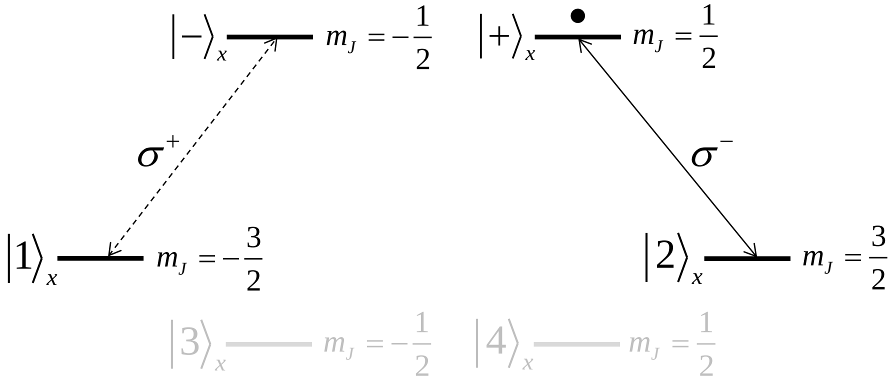

Figure 3.5: Selection rules for circularly polarized light for an isolated system closely resembling a quantum well with the zinc-blende band structure. Using ultrashort pulses (with a Heisenberg uncertainty in E_{ph} larger than the Zeeman splittings), the optical selection rules apply to the quantization axis defined by the x-direction in which the pulses propagate (whereas the magnetic field is in the z-direction). For the sake of simplicity, we assume that the probe light is close to resonance with the transition to the states $|1\rangle$ and $|2\rangle$ such that we can neglect $|3\rangle$ and $|4\rangle$, implying that the system behaves as a four-level Π-system. Hence, the only nonzero transition dipole moments are $\mu^{\sigma^+}_{-1} = -e\ {}_x\langle -|\sigma^+|1\rangle_x \equiv -ed_1$ and $\mu^{\sigma^-}_{+2} = -e\ {}_x\langle +|\sigma^-|2\rangle_x \equiv -ed_2$. Spin polarization in the excited state is induced with a circularly polarized pump pulse ($\sigma^- = \frac{\hat{\mathbf{y}}-i\hat{\mathbf{z}}}{\sqrt{2}}$) which prepares the system in the state $|+\rangle_x$ (see Eq. (3.1)), where we assume full absorption for a system having initially only $|2\rangle_x$ populated. Directly after excitation, the wave function is given by $|+\rangle_x$. A magnetic field in the z-direction induces population transfer to $|-\rangle_x$. Accordingly, the wave function is given by Eq. (3.6) as a function of time. The polarization rotation of a linearly polarized probe pulse (originating from a different refractive index for its circular components) as a function of the delay time Δt is a suitable measure for the spin dynamics.

Let us consider (for the system in Fig. 3.5) a circularly polarized pump pulse propagating in the x-direction (corresponding to the so-called Voigt geometry, i.e. perpendicular to the magnetic field) with polarization $\sigma^- = \frac{\hat{\mathbf{y}}-i\hat{\mathbf{z}}}{\sqrt{2}}$. Using ultrashort laser pulses (with a Heisenberg uncertainty in E_{ph} larger than the Zeeman splittings), the optical selection rules apply to the quantization axis defined by the propagation direction. For light propagating in the x-direction, the relevant transition dipole moments for the system of Fig. 3.5 are $\mu^{\sigma^+}_{-1} = -e\ {}_x\langle -|\sigma^+|1\rangle_x \equiv -ed_1$ and $\mu^{\sigma^-}_{+2} = -e\ {}_x\langle +|\sigma^-|2\rangle_x \equiv -ed_2$. Note that $\mu^{\sigma^-}_{-1}$, $\mu^{\sigma^+}_{+2}$, μ_{-2} and μ_{+1} are zero according to the selection rules. Let us assume that the electron initially populates $|2\rangle_x$. Assuming full absorption, the pulse spin polarizes the system such that only the state $|+\rangle_x$ is populated, We use a subscript x to refer to the optical $\{|+\rangle_x, |-\rangle_x\}$-basis, and z to refer to the $\{|+\rangle_z, |-\rangle_z\}$-basis. Let us define for the wave function at time $t = 0$

$$|\psi_e(t=0)\rangle = |+\rangle_x = \frac{|+\rangle_z + |-\rangle_z}{\sqrt{2}} \tag{3.1}$$

The corresponding spin polarization amounts $\Pi = 1$, according to

$$\Pi = \left| \frac{N(+) - N(-)}{N(+) + N(-)} \right| \tag{3.2}$$

Due to the magnetic field, the spin undergoes a Larmor precession, since $|+\rangle_x$ is not an eigenstate of the Hamiltonian. As a function of time, the wave function is given by (neglecting decay processes)

$$|\psi_e(t)\rangle = \frac{\mathrm{e}^{-iE_+t/\hbar}|+\rangle_z + \mathrm{e}^{-iE_-t/\hbar}|-\rangle_z}{\sqrt{2}} \tag{3.3}$$

After multiplication with a global phase factor, and defining $\Omega = \frac{E_+ - E_-}{\hbar}$, this yields

$$|\psi_e(t)\rangle = \frac{|+\rangle_z + \mathrm{e}^{i\Omega t}|-\rangle_z}{\sqrt{2}} \tag{3.4}$$

For a TRFR experiment, the polarization rotation $\Delta\theta$ of a linearly polarized pump pulse is recognized to be a measure for the amount of spin polarization. Spin dynamics is studied experimentally by measuring $\Delta\theta$ as a function of the delay time Δt between the pump and probe. Let us derive $\Delta\theta(\Delta t)$ for a probe pulse propagating in the x-direction with $\mathbf{E}_{in} = E_0\hat{\mathbf{y}}$. The origin of a polarization rotation lies in a different (real part of the) refractive index for the circularly polarized components of the probe pulse. Written as a superposition of circular components, we have $\hat{\mathbf{y}} = \frac{\sigma^+ + \sigma^-}{\sqrt{2}}$. Note that the probe pulse is detuned in order to prevent population transfer. Since the selection rules for electronic dipole transitions apply in the optical basis, let us perform the transformation $|\psi_e(t)\rangle_z \rightarrow |\psi_e(t)\rangle_x$ using the transformation matrix

$$U_{S_z \rightarrow S_x} = \begin{bmatrix} \frac{1}{\sqrt{2}} & \frac{1}{\sqrt{2}} \\ \frac{1}{\sqrt{2}} & -\frac{1}{\sqrt{2}} \end{bmatrix} \tag{3.5}$$

This yields

$$|\psi_e(t)\rangle = \frac{1 + \mathrm{e}^{i\Omega t}}{2}|+\rangle_x + \frac{1 - \mathrm{e}^{i\Omega t}}{2}|-\rangle_x \tag{3.6}$$

To determine the refractive indices, let us first consider the linear susceptibility tensor $\tilde{\boldsymbol{\chi}}^{(1)}$, with components given by Boyd[54] (3rd Ed. Eq. (3.5.18))

$$\tilde{\chi}^{(1)}_{ij}(\omega_p) = \frac{N}{\varepsilon_0\hbar}\sum_{nm}\rho^{(0)}_{mm}\left[\frac{\mu^i_{mn}\mu^j_{nm}}{(\omega_{nm}-\omega_p)-i\gamma_{nm}}+\frac{\mu^i_{nm}\mu^j_{mn}}{(\omega_{nm}+\omega_p)+i\gamma_{mn}}\right] \tag{3.7}$$

where we use a tilde to denote a complex number. Here, we consider an ensemble with N the number density of isolated systems (each represented by Fig. 3.5), $\varepsilon_0 = 8.854... \cdot 10^{-12}\ \mathrm{F\,m^{-1}}$ is the vacuum permittivity, $\hbar = 1.054... \cdot 10^{-34}\ \mathrm{J\,s}$ is Planck's constant, $\rho^{(0)}_{mm}$ is the first term in a power series for the diagonal elements of the density matrix, $\mu^i_{en} = -e\langle\psi_e(t)|i|\psi_n\rangle$ is the i-component of the transition dipole moment (with $i = x, y, z$), $\omega_{mn} = (E_m - E_n)/\hbar$ is the transition frequency, ω_p is the probe laser frequency, and γ is the damping rate. Note that in Eq. (3.7) ε_0 should be omitted when using Gaussian units (as in older editions of Boyd) instead of SI-units.

When the probe pulse arrives at the sample, the system (Fig. 3.5) populates the excited state given by Eq. (3.6). This implies that $\rho^{(0)}_{ee} = 1$, whereas $\rho^{(0)}_{11} = \rho^{(0)}_{22} = 0$. Since the levels $|1\rangle_x$ and $|2\rangle_x$ are empty, only the (detuned) downward transitions $|-\rangle_x \to |1\rangle_x$ and $|+\rangle_x \to |2\rangle_x$ are relevant for the description of the polarization rotation (since an upward transition with the probe is impossible with zero population in the lower states). This implies that the second term in Eq. (3.7) corresponds to resonance and is the so-called rotating term, whereas the first term is the counter-rotating one and can be omitted. Hence, we can write the components of the linear susceptibility tensor $\tilde{\boldsymbol{\chi}}^{(1)}$ to a good approximation as

$$\tilde{\chi}^{(1)}_{ij}(\omega_p) = \frac{N}{\varepsilon_0\hbar}\sum_{n=1}^{2}\frac{\mu^i_{ne}\mu^j_{en}}{\Delta_{p,ne}+i\gamma_{ne}} \tag{3.8}$$

where we define $\Delta_{p,ne} = \omega_{ne} + \omega_p$. The eigenvectors of $\tilde{\boldsymbol{\chi}}^{(1)}$ are the so-called principal axes. For a probe pulse propagating in the x-direction, we can neglect the x-components of $\tilde{\boldsymbol{\chi}}^{(1)}$. The other two principal axes turn out to be $\sigma^+ = \frac{\hat{\mathbf{y}}+i\hat{\mathbf{z}}}{\sqrt{2}}$ and $\sigma^- = \frac{\hat{\mathbf{y}}-i\hat{\mathbf{z}}}{\sqrt{2}}$, with corresponding transition dipole moments

$$\mu^{\sigma^+}_{e1} = -e\ {}_x\langle\psi_e(\Delta t)|\sigma^+|1\rangle_x = -e\frac{1-\mathrm{e}^{-i\Omega\Delta t}}{2}d_1 = \left(\mu^{\sigma^+}_{1e}\right)^* \tag{3.9}$$

$$\mu^{\sigma^-}_{e2} = -e\ {}_x\langle\psi_e(\Delta t)|\sigma^-|2\rangle_x = -e\frac{1+\mathrm{e}^{-i\Omega\Delta t}}{2}d_2 = \left(\mu^{\sigma^-}_{2e}\right)^* \tag{3.10}$$

In the $\{\sigma^+, \sigma^-\}$-basis the only nonzero components of $\tilde{\boldsymbol{\chi}}^{(1)}$ are

$$\tilde{\chi}^{(1)}_{\sigma^+\sigma^+} = \frac{N}{\varepsilon_0\hbar}\frac{\mu^{\sigma^+}_{1e}\mu^{\sigma^+}_{e1}}{\Delta_{p,1e}+i\gamma_{1e}} = \frac{N}{\varepsilon_0\hbar}\frac{e^2|d_1|^2}{\Delta_{p,1e}+i\gamma_{1e}}\frac{1-\cos(\Omega\Delta t)}{2} \tag{3.11}$$

$$\tilde{\chi}^{(1)}_{\sigma^-\sigma^-} = \frac{N}{\varepsilon_0\hbar}\frac{\mu^{\sigma^-}_{2e}\mu^{\sigma^-}_{e2}}{\Delta_{p,2e}+i\gamma_{2e}} = \frac{N}{\varepsilon_0\hbar}\frac{e^2|d_2|^2}{\Delta_{p,2e}+i\gamma_{2e}}\frac{1+\cos(\Omega\Delta t)}{2} \tag{3.12}$$

Assuming $d_1 = d_2 \equiv d_0$, $\Delta_{p,1e} = \Delta_{p,2e} \equiv \Delta_p$ and $\gamma_{1e} = \gamma_{2e} \equiv \gamma$ allows us to write

$$\tilde{\boldsymbol{\chi}}^{(1)} = \frac{Ne^2|d_0|^2}{\varepsilon_0\hbar}\frac{\Delta_p - i\gamma}{\Delta_p^2+\gamma^2}\begin{bmatrix} \frac{1-\cos(\Omega\Delta t)}{2} & 0 \\ 0 & \frac{1+\cos(\Omega\Delta t)}{2} \end{bmatrix} \tag{3.13}$$

Clearly, $\tilde{\boldsymbol{\chi}}^{(1)}$ depends on Δt. However, since $\tilde{\boldsymbol{\chi}}^{(1)}$ is diagonal (independent of Δt), the principal axes do not depend on Δt. It is important to realize that we have considered a Π-system here. In Section 3.8 we will consider a V-system for which the principal axes turn out to oscillate as a function of Δt.

To determine how the circular components of a linear probe are affected upon transmission, we have to consider their refractive indices. The refractive index is given by[54]

$$\tilde{n}_j = \sqrt{1+\tilde{\chi}^{(1)}_{jj}} \approx 1 + \frac{1}{2}\tilde{\chi}^{(1)}_{jj} \tag{3.14}$$

where the latter approximation is valid for $\left|\tilde{\chi}^{(1)}_{jj}\right| << 1$. We assume that the probe is sufficiently detuned from the $|-\rangle \rightarrow |1\rangle$ and $|+\rangle \rightarrow |2\rangle$ transitions, such that the imaginary part of $\tilde{\boldsymbol{\chi}}^{(1)}$ can be neglected, and with that population transfer as well (as explained in Section 3.7). From Eq. (3.13) and Eq. (3.14) it follows that the difference between the real parts of the refractive indices amounts

$$\Delta n \equiv n_{\sigma^-} - n_{\sigma^+} \approx \frac{Ne^2|d_0|^2}{\varepsilon_0\hbar}\frac{\Delta_p}{\Delta_p^2+\gamma^2}\frac{\cos(\Omega\Delta t)}{2} \tag{3.15}$$

To describe how the probe pulse is affected by the sample, one should consider the Jones matrix $J\{\sigma^+,\sigma^-\}$, which performs the following transformation

$$\mathbf{E}_{out}\{\sigma^+,\sigma^-\} = J\{\sigma^+,\sigma^-\}\mathbf{E}_{in}\{\sigma^+,\sigma^-\} = J\{\sigma^+,\sigma^-\}\begin{bmatrix} E_0/\sqrt{2} \\ E_0/\sqrt{2} \end{bmatrix} \tag{3.16}$$

The Jones matrix is given by

$$J\{\sigma^+,\sigma^-\} = \begin{bmatrix} \mathrm{e}^{i\Lambda n_{\sigma^+}} & 0 \\ 0 & \mathrm{e}^{i\Lambda n_{\sigma^-}} \end{bmatrix} \tag{3.17}$$

which expresses the retardation of (light polarized along) principal axis $\hat{\mathbf{j}}$ by Λn_j where $\Lambda \equiv 2\pi d/\lambda$, with d the thickness of the sample and λ the wavelength of the light[16]. It is more convenient to multiply the Jones vector with the global phase factor $\mathrm{e}^{-i\Lambda n_{\sigma^+}}$ which gives for Eq. (3.16)

$$\mathbf{E}_{out}\{\sigma^+,\sigma^-\} = \frac{E_0}{\sqrt{2}}\begin{bmatrix}1\\ \mathrm{e}^{i\Lambda\Delta n}\end{bmatrix} \tag{3.18}$$

To determine the polarization rotation we follow the circular complex-plane representation of polarized light as defined in the book of Azzam and Bashara[16]. In line with Eq. (1.92) of [16] we define the ratio

$$\kappa = E_{\sigma^+}/E_{\sigma^-} \tag{3.19}$$

where we use κ in contrast to [16] (which uses χ). From Eq. (1.95) of [16] we adopt the expression for the azimuth θ

$$\theta = -\frac{\arg(\kappa)}{2} \tag{3.20}$$

For the incoming and outcoming probe, Eq. (3.19) yields $\kappa_{in} = 1$ and $\kappa_{out} = \mathrm{e}^{-i\Lambda\Delta n}$, corresponding to $\theta_{in} = 0$ and $\theta_{out} = \frac{\Lambda\Delta n}{2}$ respectively, according to Eq. (3.20). The polarization rotation (optical rotation angle) $\Delta\theta$ is now given by

$$\Delta\theta = \theta_{out} - \theta_{in} \tag{3.21}$$

which gives $\Delta\theta = \frac{\pi d\Delta n}{\lambda}$, with Δn proportional to $\cos(\Omega\Delta t)$ as given by Eq. (3.15). Measuring $\Delta\theta$ as a function of Δt will show an oscillation with angular frequency $\Omega = \frac{E_+ - E_-}{\hbar}$ and amplitude

$$max(\Delta\theta) = \frac{\pi d}{2\lambda}\frac{Ne^2|d_0|^2}{\varepsilon_0\hbar}\frac{\Delta_p}{\Delta_p^2+\gamma^2} \tag{3.22}$$

In literature[13, 46] this oscillation of the polarization rotation is recognized to be a suitable measure for the Larmor spin precession in the excited state, since the angular frequency is the same for both oscillations. The reader is referred to the book of Cohen-Tannoudji, Diu and Laloë[5] for a derivation of the oscillation of a Larmor spin precession of a spin 1/2 in the presence of a uniform magnetic field: for a spin initially populating the state $|+\rangle_x$, the angular frequency of the time-variation of the expectation value $\langle S_x\rangle$ equals the energy splitting between the sublevels (in units of $\hbar$) induced by the field.

So far, we considered an ensemble of isolated Π-systems (with number density N), where each system is represented by Fig. 3.5. Let us now shortly elaborate on how to theoretically describe a TRFR experiment applied to a coherently coupled ensemble of Π-systems (with number density N). We will see that also the upward transitions affect the probe polarization and contribute to the total TRFR signal.

A pump pulse driving the upward transition $|2\rangle_x \to |+\rangle_x$ does not only induce electron spin polarization in the state $|+\rangle_x$. Simultaneously, the hole spin in the state $|2\rangle_x$ ($m_J = 3/2$) is polarized. However, e.g. in III-V direct gap semicondutors the corresponding hole spin dynamics in the valence band is usually neglected (i.e. an equal distribution of the valence band states is assumed) because of the fast thermalization (particularly because the valence bands with $m_J = -1/2, 1/2$ lie closeby), happening on a much shorter timescale than the conduction band's electron spin dynamics. Nevertheless, the probe polarization will be affected also by the (detuned) upward transitions $|1\rangle_x \to |-\rangle_x$ and $|2\rangle_x \to |+\rangle_x$, since the hole spin in the conduction band is polarized as well. Here, the reader is referred to Fig. 3.5, but one should now understand the bars as bands. Also, there is now (partial) population in the valence band states ($|1\rangle_x$ up to $|4\rangle_x$). Particularly interesting is the case where thermalization of the valence band states does not occur faster than the spin dynamics in the conduction band, as can e.g. be realized for quantum wells with a zinc-blende band structure where the valence band states $|3\rangle_x$ and $|4\rangle_x$ lie sufficiently low. Accordingly, Larmor spin precession happens also in the valence band, accompanied by population transfer between the bands with $m_J = -3/2$ and $3/2$. Correspondingly, one can write down a time-dependent ground state (analogous to Eq. (3.6)) and follow the procedure as above for calculation of the refractive indices and resulting polarization rotation for a linearly polarized probe pulse.

One might wonder whether the contributions from the downward and upward transitions do not cancel. To show that this is not the case, let us consider the case where the probe pulse arrives at the sample directly after spin polarization with the pump pulse, i.e. $\Delta t = 0$. Let us consider the contributions separately by considering first (Case I) an artificial system as in Fig. 3.5, with only $|+\rangle_x$ populated, i.e. $\rho^{(0)}_{++} = 1$, and secondly (Case II) an artificial system as in Fig. 3.5, with only $|1\rangle_x$ populated, i.e. $\rho^{(0)}_{11} = 1$.

Case I: $\rho^{(0)}_{++} = 1$. This case simply follows from the theory above, where we can substitute $\Delta t = 0$ in Eq. (3.6) and replace the subscript e by $+$ in Eq. (3.8). It follows that the only nonzero component of $\tilde{\boldsymbol{\chi}}^{(1)}$ is

$$\tilde{\chi}^{(1)}_{\sigma_-\sigma_-}(\omega_p) = \frac{N}{\varepsilon_0\hbar}\frac{\mu^{\sigma_-}_{2+}\mu^{\sigma_-}_{+2}}{(\omega_{2+}+\omega_p)+i\gamma_{2+}} = \frac{N}{\varepsilon_0\hbar}\frac{|\mu|^2}{\Delta_p+i\gamma} = \frac{N}{\varepsilon_0\hbar}|\mu|^2\frac{\Delta-i\gamma}{\Delta_p^2+\gamma^2} \quad (3.23)$$

where we have defined (in line with the theory above) $\Delta_p \equiv \omega_{2+} + \omega_p$ where

$\omega_{2+} = (E_2 - E_+)/\hbar < 0$. Also, we assume $\gamma_{2+} = \gamma_{-1} \equiv \gamma$ and $\mu_{2+}^{\sigma_-} = \mu_{1-}^{\sigma_+} \equiv \mu$.

Case II: $\rho_{11}^{(0)} = 1$. For this case the wave function is given by $|1\rangle_x$. For the linear susceptibility this implies that the first term in Eq. (3.6) corresponds to resonance and is the so-called rotating term, whereas the second term is the counter-rotating one and can be omitted. It follows that the only nonzero component of $\tilde{\boldsymbol{\chi}}^{(1)}$ is

$$\tilde{\chi}^{(1)}_{\sigma_+\sigma_+}(\omega_p) = \frac{N}{\varepsilon_0\hbar}\frac{\mu_{1-}^{\sigma_+}\mu_{-1}^{\sigma_+}}{(\omega_{-1}-\omega_p) - i\gamma_{-1}} = \frac{N}{\varepsilon_0\hbar}\frac{|\mu|^2}{-\Delta_p - i\gamma} = \frac{N}{\varepsilon_0\hbar}|\mu|^2\frac{-\Delta + i\gamma}{\Delta_p^2+\gamma^2} \quad (3.24)$$

where $\omega_{-1} = (E_- - E_1)/\hbar > 0$. Also, we have $\omega_{-1} = -\omega_{2+}$, which implies $\omega_{-1} - \omega_p = -\Delta_p$.

We see that $\tilde{\chi}^{(1)}_{\sigma_+\sigma_+}(\omega_p)$ in Eq. (3.24) equals $-\tilde{\chi}^{(1)}_{\sigma_-\sigma_-}(\omega_p)$ in Eq. (3.23). For a coherent ensemble (e.g. a quantum well with a zinc-blende band structure) of the systems in Fig. 3.5 one might have that both the downward and upward transitions contribute to the total TRFR signal, thereby resembling Case I and Case II simultaneously. Considering the extreme (i.e. $\rho_{mm}^{(0)} = 1$) cases of Eq. (3.23) and Eq. (3.24), following Eq. (3.14) and Eq. (3.15) shows that at $\Delta t = 0$ the total TRFR amplitude can become twice the value of Eq. (3.22). In practice, one will not realize $\rho_{mm}^{(0)} = 0, 1$ (i.e. completely full or empty bands) for a coherent ensemble. The total TRFR signal will therefore be mitigated, but it is important to realize that both the downward and upward transitions can contribute to a polarization rotation of the probe pulse.

3.7 SI: Fundamentals of a molecular TRFR experiment

Let us study here the theoretical application of the Time-Resolved Faraday Rotation (TRFR) technique (main text Fig. 3.1) to a model system (main text Fig. 3.2) in the absence of a magnetic field. The system consists of the states $|\psi_g\rangle$, $|\psi_1\rangle$, $|\psi_2\rangle$ and $|\psi_3\rangle$, with energies E_g, E_1, E_2 and E_3, respectively, with $E_g = 0$. The only nonzero components of the transition dipole moments related to $|\psi_g\rangle$ are $\mu_{1g}^y = -e\langle\psi_1|y|\psi_g\rangle = -ed_1$ and $\mu_{3g}^z = -e\langle\psi_3|z|\psi_g\rangle = -ed_3$, with e the elementary charge. Considering absorption, the system behaves therefore as a three-level V-system where $|\psi_2\rangle$ can be neglected, but it is nevertheless displayed (main text Fig. 3.2) since in this work the excited state levels are sublevels of a triplet. In this regard it is interesting to mention the V-system of a GaAs quantum well, which has been studied theoretically[60] and for which electron spin dynamics experiments have been performed[61, 62]. In these experiments, a magnetic field ensures Larmor spin precession. Although we do not consider a magnetic field, most of the theory of Sections 3.7 and 3.8 can be directly applied to this V-system.

Although ultrashort pulses with a substantial energy uncertainty will be considered, monochromatic waves are assumed, for which (by definition) the time variation of the electric (field) vector $\mathbf{E}$ is exactly sinusoidal. Usually within the Jones formalism[63], the electric vector is denoted as $\mathbf{E} = E_x\hat{\mathbf{x}} + E_y\hat{\mathbf{y}}$, with $\hat{\mathbf{x}}$ and $\hat{\mathbf{y}}$ the orthonormal Jones unit vectors. In this work however, the propagation of light will be taken along the x-direction, such that the electric vector has nonzero components only in the y and z-direction.

At $t = 0$, an ultrashort pump pulse, for which the electric vector is given by $\mathbf{E}_{pump} = \alpha\hat{\mathbf{z}} + \beta\hat{\mathbf{y}}$ (with α and β in general complex), excites the system of main text Fig. 3.2a to $|\psi_e\rangle$, being a superposition of the states $|\psi_1\rangle$ and $|\psi_3\rangle$. The following assumptions are made: (*i*) Before the pump arrives, only $|\psi_g\rangle$ is populated, (*ii*) the photon energy is $E_{ph} = \frac{E_3+E_1}{2}$, with (*iii*) a quantum uncertainty $\sigma_{E_{ph}} > |E_3 - E_1|$, where a block function is assumed for the intensity distribution of the pulse instead of a Gaussian, and (*iv*) only $|\psi_e\rangle$ is populated after excitation with the pump pulse (i.e. full absorption).

Consider a sample, consisting of a homogeneous ensemble of these model systems with number density N. To ensure that the systems are well isolated from each other, N should be relatively small, which can be realized by putting the molecules in a molecular host crystal (i.e. a matrix) or liquid host (i.e. in solution), which should be transparent to the pump and probe pulse, or taking an ensemble of molecules in gas phase. In our derivation (Sec. 3.8 and 3.9) and calculations (Sec. 3.10) we will first assume that all molecules are oriented similarly, which can be realized via a (solid) host crystal. Later (Sec. 3.15), we will show that a net TRFR signal can even be obtained for an ensemble of randomly oriented molecules. Considering the host crystal, we assume that (*iv*) is satisfied for each system of the ensemble. In practice, it is sufficient when the vast majority of the systems satisfies (*iv*). Still, this will usually require the tuning of a very intense pump pulse, given the typical small transition dipole moment between ground and excited state. It is assumed that each system is evolving according to Eq. (3.27). After a delay time Δt, the sample is illuminated with an ultrashort probe pulse (also obeying assumptions (*ii*) and (*iii*)) for which the electric vector is given by $\mathbf{E}_{in} = \delta\hat{\mathbf{z}} + \varepsilon\hat{\mathbf{y}}$, to which we refer as the incoming probe.

Given the small transition dipole moment, the probability for a created exciton to recombine during the delay time between pump and probe is small as well.

Hence, it is reasonable to assume that the system has still no population in $|\psi_g\rangle$ once the probe pulse arrives at the sample (main text Fig. 3.2b). If one would now take a resonant probe pulse, all population would be transferred to $|\psi_g\rangle$ via stimulated emission, which is unfavourable in view of the lifetime of the spin dynamics. In this work therefore, we will assume that we are allowed to consider only the dispersion (related to stimulated emission). This implies neglecting $\left|\mathrm{Im}\left\{\tilde{\chi}^{(1)}_{ij}\right\}\right|$ with respect to $\left|\mathrm{Re}\left\{\tilde{\chi}^{(1)}_{ij}\right\}\right|$, with $\tilde{\boldsymbol{\chi}}^{(1)}$ the linear susceptibility tensor (see Eq. (3.29), as adapted from Boyd[54]). This can be realized by taking an off-resonant probe pulse (as illustrated in Fig. 3.2b) having a detuning $\Delta_p = \omega_{ge} + \omega_p$ (with $\omega_{ge} = (E_g - E_e)/\hbar < 0$ the transition frequency and $\omega_p > 0$ the probe laser frequency). Since $\tilde{\chi}^{(1)}_{ij}$ is proportional to $\frac{\Delta_p - i\gamma}{\Delta_p^2 + \gamma^2}$, we can neglect $\left|\mathrm{Im}\left\{\tilde{\chi}^{(1)}_{ij}\right\}\right|$ if we ensure $|\Delta_p| >> \gamma$, which for the remaining real part implies $\frac{\Delta_p}{\Delta_p^2 + \gamma^2} \approx \Delta_p^{-1}$. It is also instructive to plot the real and imaginary part of $\tilde{\chi}^{(1)}_{ij}$ as a function of ω_p (Boyd[54], 3rd ed., Fig. 3.5.1), illustrating that the tails of $\mathrm{Im}\left\{\tilde{\chi}^{(1)}_{ij}\right\}$ fall off faster than the ones of $\mathrm{Re}\left\{\tilde{\chi}^{(1)}_{ij}\right\}$. Note that we have defined the excited state $|\psi_e\rangle$ being a superposition of $|\psi_1\rangle$ and $|\psi_3\rangle$. However, it is somewhat misleading to consider for the calculation of Δ_p an energy E_e, since $|\psi_e\rangle$ is not an eigenstate of the Hamiltonian (naturally, one would take the expectation value $E_e = \langle\psi_e|H|\psi_e\rangle$). Strictly speaking, a probe laser has a different detuning with respect to the levels $|\psi_1\rangle$ and $|\psi_3\rangle$. However, we will use one and the same value for Δ_p for both $|\psi_1\rangle$ and $|\psi_3\rangle$ (within the calculation of $\tilde{\boldsymbol{\chi}}^{(1)}$ for a superposition of $|\psi_1\rangle$ and $|\psi_3\rangle$), which is a reasonable assumption if we take $|\Delta_p| >> |E_3 - E_1|/\hbar$.

To explain the requirements for the polarization rotation $\Delta\theta$ to oscillate as a function of the delay time Δt, both the general (Section 3.8) and an idealized (Section 3.9) scenario are considered.

3.8 SI: Polarization rotation for a TRFR experiment applied to a V-system

Here we derive the polarization of an ultrashort detuned probe pulse ($\mathbf{E}_{in} = \delta\hat{\mathbf{z}} + \varepsilon\hat{\mathbf{y}}$), as a function of the delay time Δt after the arrival of an ultrashort pump pulse ($\mathbf{E}_{pump} = \alpha\hat{\mathbf{z}} + \beta\hat{\mathbf{y}}$), for a model system as in main text Fig. 3.2 (nonzero μ^y_{1g} and μ^z_{3g}).

For the general case of full absorption of a pump pulse having $\mathbf{E}_{pump} = \xi\hat{\mathbf{x}} + \beta\hat{\mathbf{y}} + \alpha\hat{\mathbf{z}}$, for a system initially populated in $|\psi_i\rangle$, the state directly after a coherent excitation becomes

$$|\psi(t=0)\rangle = C\sum_{n}\langle\psi_n|\xi x + \beta y + \alpha z|\psi_i\rangle|\psi_n\rangle \tag{3.25}$$

with n the amount of involved excited state levels, and C the normalization factor. It is assumed that the pump pulse has an equal intensity for all energies $E_n - E_i$ (block pulse).

In our case, the superposition of states directly after excitation becomes

$$|\psi_e(t=0)\rangle = \frac{\beta d_1|\psi_1\rangle + \alpha d_3|\psi_3\rangle}{\sqrt{|\beta d_1|^2 + |\alpha d_3|^2}} \tag{3.26}$$

According to the time-dependent Schrödinger equation, this wave function evolves as

$$|\psi_e(t)\rangle = \frac{\mathrm{e}^{-iE_1t/\hbar}\beta d_1|\psi_1\rangle + \mathrm{e}^{-iE_3t/\hbar}\alpha d_3|\psi_3\rangle}{\sqrt{|\beta d_1|^2 + |\alpha d_3|^2}} \tag{3.27}$$

For convenience, Eq. (3.27) is multiplied with the global phase factor $\mathrm{e}^{iE_1t/\hbar}$ to give

$$|\psi_e(t)\rangle = \frac{\beta d_1|\psi_1\rangle + \mathrm{e}^{i\Omega t}\alpha d_3|\psi_3\rangle}{\sqrt{|\beta d_1|^2 + |\alpha d_3|^2}} \tag{3.28}$$

with $\Omega \equiv \omega_{13} = (E_1 - E_3)/\hbar$.

The polarization of a probe pulse upon transmission, i.e. $\mathbf{E}_{out}$, might be affected, which follows from considering the linear susceptibility tensor $\tilde{\boldsymbol{\chi}}^{(1)}$. Assuming that for each system only $|\psi_e(t)\rangle$ is populated (Fig. 3.2b), following Boyd[54] (3rd ed., Eq. (3.5.20)) gives

$$\tilde{\chi}^{(1)}_{ij}(\omega_p) = \frac{N}{\varepsilon_0\hbar}\sum_{n}\left[\frac{\mu^i_{en}\mu^j_{ne}}{\Delta'_{p,ne} - i\gamma_{ne}} + \frac{\mu^i_{ne}\mu^j_{en}}{\Delta_{p,ne} + i\gamma_{ne}}\right] \tag{3.29}$$

where we use a tilde to denote a complex number. Here, N is the system's number density, $\varepsilon_0 = 8.854... \cdot 10^{-12}$ F m^{-1} is the vacuum permittivity, $\hbar = 1.054... \cdot 10^{-34}$ J s is Planck's constant, $\mu^i_{en} = -e\langle\psi_e(t)|i|\psi_n\rangle$ with $i = x, y, z$, $\Delta'_{p,ne} = \omega_{ne} - \omega_p$ and $\Delta_{p,ne} = \omega_{ne} + \omega_p$ with ω_p the probe laser frequency, γ_{ne} is the damping rate. Note that in Eq. (3.29) ε_0 should be omitted when using Gaussian units (as in older editions of Boyd[54]) instead of SI-units.

Assuming that the laser can only address the ground state (via stimulated emission), we can drop the summation sign and substitute g for n, which yields

$$\tilde{\chi}^{(1)}_{ij}(\omega_p) = \frac{N}{\varepsilon_0\hbar}\left[\frac{\mu^i_{eg}\mu^j_{ge}}{\Delta'_p - i\gamma} + \frac{\mu^i_{ge}\mu^j_{eg}}{\Delta_p + i\gamma}\right] \tag{3.30}$$

where we have dropped the subscript n for Δ_p, Δ'_p and γ. Since the transition frequency $\omega_{ge} = (E_g - E_e)/\hbar < 0$ (and $\omega_p > 0$), only the second term in Eq. (3.30) can become resonant, and is therefore the rotating term (and the first the counter-rotating term). Within this rotating wave approximation the first term is therefore neglected when ω_p is nearly resonant with the transition frequency ω_{ge}. To a good approximation the linear susceptibility now becomes (after rewriting)

$$\tilde{\chi}^{(1)}_{ij}(\omega_p) = \frac{N}{\varepsilon_0 \hbar}\mu^i_{ge}\mu^j_{eg}\frac{\Delta_p - i\gamma}{\Delta_p^2 + \gamma^2} \tag{3.31}$$

where the detuning $\Delta_p = \omega_{ge} + \omega_p$ is positive for $\omega_p > |\omega_{ge}|$ and negative when $\omega_p < |\omega_{ge}|$.

The polarization of the probe pulse upon transmission $\mathbf{E}_{out}$ is affected when its components experience a different real part of the refractive index[16]. The refractive index does not have a tensor representation, due to the square root relationship with the dielectric constant[55]. Hence, speaking about refractive index only makes sense when a transformation is performed to the basis of the principal axes, which are the eigenvectors of $\tilde{\boldsymbol{\chi}}^{(1)}$. To determine these, we first write down the (only nonzero) transition dipole moments

$$\begin{aligned}\mu^z_{eg} = \left(\mu^z_{ge}\right)^* &= -e\langle\psi_e(\Delta t)|z|\psi_g\rangle \\ &= -e\left(\frac{\beta^* d_1^*\langle\psi_1| + \mathrm{e}^{-i\Omega\Delta t}\alpha^* d_3^*\langle\psi_3|}{\sqrt{|\beta d_1|^2 + |\alpha d_3|^2}}\right) z|\psi_g\rangle \\ &= -e\frac{\mathrm{e}^{-i\Omega\Delta t}\alpha^*|d_3|^2}{\sqrt{|\beta d_1|^2 + |\alpha d_3|^2}}\end{aligned} \tag{3.32}$$

$$\begin{aligned}\mu^y_{eg} = \left(\mu^y_{ge}\right)^* &= -e\langle\psi_e(\Delta t)|y|\psi_g\rangle \\ &= -e\frac{\beta^*|d_1|^2}{\sqrt{|\beta d_1|^2 + |\alpha d_3|^2}}\end{aligned} \tag{3.33}$$

Neglecting constant prefactors, diagonalization of $\tilde{\boldsymbol{\chi}}^{(1)}$ involves diagonalization of the matrix

$$\begin{bmatrix}\mu^z_{ge}\mu^z_{eg} & \mu^z_{ge}\mu^y_{eg} \\ \mu^y_{ge}\mu^z_{eg} & \mu^y_{ge}\mu^y_{eg}\end{bmatrix} = \frac{e^2}{|\beta d_1|^2 + |\alpha d_3|^2}\begin{bmatrix}|\alpha|^2|d_3|^4 & \mathrm{e}^{i\Omega\Delta t}\beta^*\alpha|d_1|^2|d_3|^2 \\ \mathrm{e}^{-i\Omega\Delta t}\beta\alpha^*|d_1|^2|d_3|^2 & |\beta|^2|d_1|^4\end{bmatrix} \tag{3.34}$$

One obtains the eigenvalues $\lambda_1 = 0$ and $\lambda_2 = |\beta|^2|d_1|^4 + |\alpha|^2|d_3|^4$ after diagonalization of the latter matrix, i.e. solving

$$\begin{vmatrix} |\alpha|^2|d_3|^4 - \lambda & \mathrm{e}^{i\Omega\Delta t}\beta^*\alpha|d_1|^2|d_3|^2 \\ \mathrm{e}^{-i\Omega\Delta t}\beta\alpha^*|d_1|^2|d_3|^2 & |\beta|^2|d_1|^4 - \lambda \end{vmatrix} = 0 \tag{3.35}$$

The corresponding (normalized) eigenvectors $\hat{\mathbf{z}}'$ and $\hat{\mathbf{y}}'$ are the principal axes that we are looking for. For $\lambda_1 = 0$ we have

$$\begin{bmatrix} |\alpha|^2|d_3|^4 & \mathrm{e}^{i\Omega\Delta t}\beta^*\alpha|d_1|^2|d_3|^2 \\ \mathrm{e}^{-i\Omega\Delta t}\beta\alpha^*|d_1|^2|d_3|^2 & |\beta|^2|d_1|^4 \end{bmatrix} \begin{bmatrix} z_1' \\ z_2' \end{bmatrix} = 0 \tag{3.36}$$

which implies

$$\frac{z_1'}{z_2'} = -\mathrm{e}^{i\Omega\Delta t}\frac{\beta^*|d_1|^2}{\alpha^*|d_3|^2} \tag{3.37}$$

Normalization yields for the first principal axis

$$\hat{\mathbf{z}}' = \frac{-\mathrm{e}^{i\Omega\Delta t}\beta^*|d_1|^2\hat{\mathbf{z}} + \alpha^*|d_3|^2\hat{\mathbf{y}}}{\sqrt{|\beta|^2|d_1|^4 + |\alpha|^2|d_3|^4}} \tag{3.38}$$

which is clearly time-dependent. For $\lambda_2 = |\beta|^2|d_1|^4 + |\alpha|^2|d_3|^4$ we have

$$\begin{bmatrix} -|\beta|^2|d_1|^4 & \mathrm{e}^{i\Omega\Delta t}\beta^*\alpha|d_1|^2|d_3|^2 \\ \mathrm{e}^{-i\Omega\Delta t}\beta\alpha^*|d_1|^2|d_3|^2 & -|\alpha|^2|d_3|^4 \end{bmatrix} \begin{bmatrix} y_1' \\ y_2' \end{bmatrix} = 0 \tag{3.39}$$

which implies

$$\frac{y_1'}{y_2'} = \mathrm{e}^{i\Omega\Delta t}\frac{\alpha|d_3|^2}{\beta|d_1|^2} \tag{3.40}$$

Normalization yields for the second time-dependent principal axis

$$\hat{\mathbf{y}}' = \frac{\mathrm{e}^{i\Omega\Delta t}\alpha|d_3|^2\hat{\mathbf{z}} + \beta|d_1|^2\hat{\mathbf{y}}}{\sqrt{|\beta|^2|d_1|^4 + |\alpha|^2|d_3|^4}} \tag{3.41}$$

Note that the third principal axis $\hat{\mathbf{x}}$ remains unaffected (if the x-component of $\mathbf{E}_{pump}$ equals zero) and will therefore not be taken into account anymore. Determining the polarization of the probe pulse upon transmission is based on determining the refractive indices of these time-dependent principal axes. In the inertial frame of these principal axes, i.e. the $\{\hat{\mathbf{z}}', \hat{\mathbf{y}}'\}$-basis, the only nonzero element of $\tilde{\boldsymbol{\chi}}^{(1)}$ is the eigenvalue

$$\tilde{\chi}^{(1)}_{y'y'} = \frac{N}{\varepsilon_0\hbar}\mu^{y'}_{ge}\mu^{y'}_{eg}\frac{\Delta_p - i\gamma}{\Delta_p^2 + \gamma^2} \tag{3.42}$$

where

$$\mu_{ge}^{y'}\mu_{eg}^{y'} = e^2 \frac{|\beta|^2|d_1|^4 + |\alpha|^2|d_3|^4}{|\beta d_1|^2 + |\alpha d_3|^2} \tag{3.43}$$

In general, the complex refractive index of principal axis $\hat{\mathbf{j}}$ is given by

$$\tilde{n}_j = \sqrt{1 + \tilde{\chi}_{jj}^{(1)}} \approx 1 + \frac{1}{2}\tilde{\chi}_{jj}^{(1)} \tag{3.44}$$

where the latter approximation is valid for $\left|\tilde{\chi}_{jj}^{(1)}\right| << 1$. In our case we have $\tilde{n}_{y'} \approx 1 + \frac{1}{2}\tilde{\chi}_{y'y'}^{(1)}$ and $\tilde{n}_{z'} = 1$. Since the refractive index differs in one direction, the sample behaves as a (singly) birefringent material. To describe how the probe pulse is affected by the sample, one should consider the Jones matrix $J\{\hat{\mathbf{z}}, \hat{\mathbf{y}}\}$, which performs the following transformation

$$\mathbf{E}_{out}\{\hat{\mathbf{z}}, \hat{\mathbf{y}}\} = J\{\hat{\mathbf{z}}, \hat{\mathbf{y}}\}\mathbf{E}_{in}\{\hat{\mathbf{z}}, \hat{\mathbf{y}}\} = J\{\hat{\mathbf{z}}, \hat{\mathbf{y}}\} \begin{bmatrix} \delta \\ \varepsilon \end{bmatrix} \tag{3.45}$$

To build $J\{\hat{\mathbf{z}}, \hat{\mathbf{y}}\}$ we first build $J\{\hat{\mathbf{z}}', \hat{\mathbf{y}}'\}$, which describes how a probe pulse in the $\{\hat{\mathbf{z}}', \hat{\mathbf{y}}'\}$-basis is affected, i.e.

$$\mathbf{E}_{out}\{\hat{\mathbf{z}}', \hat{\mathbf{y}}'\} = J\{\hat{\mathbf{z}}', \hat{\mathbf{y}}'\}\mathbf{E}_{in}\{\hat{\mathbf{z}}', \hat{\mathbf{y}}'\} \tag{3.46}$$

The Jones matrix is given by

$$J\{\hat{\mathbf{z}}', \hat{\mathbf{y}}'\} = \begin{bmatrix} \mathrm{e}^{i\Lambda n_{z'}} & 0 \\ 0 & \mathrm{e}^{i\Lambda n_{y'}} \end{bmatrix} \tag{3.47}$$

which expresses the retardation of (light polarized along) principal axis $\hat{\mathbf{j}}$ by Λn_j where $\Lambda \equiv 2\pi d/\lambda$, with d the thickness of the sample and λ the wavelength of the light[16]. Note that we consider here only the real part of the complex refractive index, which is valid for a sufficiently detuned probe pulse. In Section 3.7 we therefore required $|\Delta_p| >> \gamma$, implying $\frac{\Delta_p - i\gamma}{\Delta_p^2 + \gamma^2} \approx \Delta_p^{-1}$. It is convenient to define

$$\Delta n \equiv n_{y'} - n_{z'} \approx \frac{N}{2\varepsilon_0 \hbar \Delta_p} e^2 \frac{|\beta|^2|d_1|^4 + |\alpha|^2|d_3|^4}{|\beta d_1|^2 + |\alpha d_3|^2} \tag{3.48}$$

Multiplication of the Jones matrix with the global phase factor $\mathrm{e}^{-i\Lambda n_{z'}}$ gives

$$J\{\hat{\mathbf{z}}', \hat{\mathbf{y}}'\} = \begin{bmatrix} 1 & 0 \\ 0 & \mathrm{e}^{i\Lambda\Delta n} \end{bmatrix} \tag{3.49}$$

The eigenvectors of the Jones matrix are called eigenpolarizations, which are equivalent to the principal axes. As it should, the Jones matrix in Eq. (3.47) satisfies the requirement that the eigenpolarizations correspond to the two polarization states that pass through the optical system unaffected[16]. However, since the polarizations have different retardations, the resulting polarization of a passing light pulse consisting of a superposition of the principal axes might be affected. In this work, polarization rotation is considered in particular, which implies for linearly polarized light a rotation of the plane in which the electric field component oscillates.

The Jones matrix $J\{\hat{\mathbf{z}}, \hat{\mathbf{y}}\}$ is obtained using the transformation matrix T which has as its columns the unit vectors $\hat{\mathbf{z}}'\{\hat{\mathbf{z}}, \hat{\mathbf{y}}\}$ (Eq. 3.38) and $\hat{\mathbf{y}}'\{\hat{\mathbf{z}}, \hat{\mathbf{y}}\}$ (Eq. 3.41), respectively. Let us build the matrices T and $T^\dagger$ that perform a transformation from the $\{\hat{\mathbf{z}}', \hat{\mathbf{y}}'\}$-basis to the $\{\hat{\mathbf{z}}, \hat{\mathbf{y}}\}$-basis and back, respectively.

$$T = \frac{1}{\sqrt{|\beta|^2|d_1|^4 + |\alpha|^2|d_3|^4}} \begin{bmatrix} -\mathrm{e}^{i\Omega\Delta t}\beta^*|d_1|^2 & \mathrm{e}^{i\Omega\Delta t}\alpha|d_3|^2 \\ \alpha^*|d_3|^2 & \beta|d_1|^2 \end{bmatrix} \tag{3.50}$$

where the conjugate transpose is given by

$$T^\dagger = \frac{1}{\sqrt{|\beta|^2|d_1|^4 + |\alpha|^2|d_3|^4}} \begin{bmatrix} -\mathrm{e}^{-i\Omega\Delta t}\beta|d_1|^2 & \alpha|d_3|^2 \\ \mathrm{e}^{-i\Omega\Delta t}\alpha^*|d_3|^2 & \beta^*|d_1|^2 \end{bmatrix} \tag{3.51}$$

of which the columns consist of the unit vectors $\hat{\mathbf{z}}\{\hat{\mathbf{z}}', \hat{\mathbf{y}}'\}$ and $\hat{\mathbf{y}}\{\hat{\mathbf{z}}', \hat{\mathbf{y}}'\}$, respectively, i.e.

$$\hat{\mathbf{z}} = \mathrm{e}^{-i\Omega\Delta t}\frac{-\beta|d_1|^2\hat{\mathbf{z}}' + \alpha^*|d_3|^2\hat{\mathbf{y}}'}{\sqrt{|\beta|^2|d_1|^4 + |\alpha|^2|d_3|^4}} \tag{3.52}$$

$$\hat{\mathbf{y}} = \frac{\alpha|d_3|^2\hat{\mathbf{z}}' + \beta^*|d_1|^2\hat{\mathbf{y}}'}{\sqrt{|\beta|^2|d_1|^4 + |\alpha|^2|d_3|^4}} \tag{3.53}$$

Altogether the Jones matrix of Eq. (3.45) becomes

$$\begin{aligned} J\{\hat{\mathbf{z}}, \hat{\mathbf{y}}\} &= TJ\{\hat{\mathbf{z}}', \hat{\mathbf{y}}'\}T^\dagger \\ &= j_0 \begin{bmatrix} -\mathrm{e}^{i\Omega\Delta t}\beta^*|d_1|^2 & \mathrm{e}^{i\Omega\Delta t}\alpha|d_3|^2 \\ \alpha^*|d_3|^2 & \beta|d_1|^2 \end{bmatrix} \begin{bmatrix} 1 & 0 \\ 0 & \mathrm{e}^{i\Lambda\Delta n} \end{bmatrix} \begin{bmatrix} -\mathrm{e}^{-i\Omega\Delta t}\beta|d_1|^2 & \alpha|d_3|^2 \\ \mathrm{e}^{-i\Omega\Delta t}\alpha^*|d_3|^2 & \beta^*|d_1|^2 \end{bmatrix} \\ &= j_0 \begin{bmatrix} j_{zz} & j_{zy} \\ j_{yz} & j_{yy} \end{bmatrix} \end{aligned} \tag{3.54}$$

where

$$\begin{aligned}
j_0 &\equiv \frac{1}{|\beta|^2|d_1|^4+|\alpha|^2|d_3|^4} \\
j_{zz} &\equiv \mathrm{e}^{i\Lambda\Delta n}|\alpha|^2|d_3|^4+|\beta|^2|d_1|^4 \\
j_{zy} &\equiv \mathrm{e}^{i\Omega\Delta t}\left(\mathrm{e}^{i\Lambda\Delta n}-1\right)\beta^*\alpha|d_1|^2|d_3|^2 \\
j_{yz} &\equiv \mathrm{e}^{-i\Omega\Delta t}\left(\mathrm{e}^{i\Lambda\Delta n}-1\right)\beta\alpha^*|d_1|^2|d_3|^2 \\
j_{yy} &\equiv \mathrm{e}^{i\Lambda\Delta n}|\beta|^2|d_1|^4+|\alpha|^2|d_3|^4
\end{aligned} \tag{3.55}$$

Substitution into Eq. (3.45) yields the following components

$$\begin{aligned}
E_{out,z} &= j_0\left(\mathrm{e}^{i\Omega\Delta t}\left(\mathrm{e}^{i\Lambda\Delta n}-1\right)P_1+\mathrm{e}^{i\Lambda\Delta n}P_2+P_3\right) \\
E_{out,y} &= j_0\left(\mathrm{e}^{-i\Omega\Delta t}\left(\mathrm{e}^{i\Lambda\Delta n}-1\right)Q_1+\mathrm{e}^{i\Lambda\Delta n}Q_2+Q_3\right)
\end{aligned} \tag{3.56}$$

with

$$\begin{aligned}
P_1 &= \beta^*\alpha\varepsilon|d_1|^2|d_3|^2 \\
Q_1 &= \beta\alpha^*\delta|d_1|^2|d_3|^2 \\
P_2 &= |\alpha|^2\delta|d_3|^4 \\
Q_2 &= |\beta|^2\varepsilon|d_1|^4 \\
P_3 &= |\beta|^2\delta|d_1|^4 \\
Q_3 &= |\alpha|^2\varepsilon|d_3|^4
\end{aligned}$$

To determine the polarization rotation we follow the Cartesian complex-plane representation of polarized light, according to the book of Azzam and Bashara[16]. Using Eq. (1.77) of [16], we define the ratio

$$\kappa = E_y/E_z \tag{3.57}$$

where we use κ in contrast to [16] (which uses χ). In line with Eq. (1.86) of [16], we adopt the expression for the azimuth θ

$$\tan(2\theta) = \frac{2\,\mathrm{Re}\{\kappa\}}{1-|\kappa|^2} \tag{3.58}$$

which implies

$$\theta = \frac{1}{2}\tan^{-1}\left(\frac{\kappa^*+\kappa}{1-\kappa^*\kappa}\right) \tag{3.59}$$

Note that the $\tan^{-1}$ function returns a value in the range $(-\pi/2, \pi/2)$. In practice therefore, to return a value for θ in the range $(-\pi, \pi]$, we actually use the atan2 function (as implemented in most programming languages), i.e.

$$\theta = \frac{1}{2}\,\mathrm{atan}\,2\left(\kappa^*+\kappa, 1-\kappa^*\kappa\right) \tag{3.60}$$

The polarization rotation (optical rotation angle) $\Delta\theta$ is now given by

$$\Delta\theta = \theta_{out} - \theta_{in} \tag{3.61}$$

From Eq. (1.87) of [16] we obtain for the ellipticity angle ϵ

$$\sin(2\epsilon) = \frac{2\,\mathrm{Im}\{\kappa\}}{1 + |\kappa|^2} \tag{3.62}$$

which implies

$$\epsilon = \frac{1}{2}\sin^{-1}\left(i\frac{\kappa^* - \kappa}{1 + \kappa^*\kappa}\right) \tag{3.63}$$

3.9 SI: Idealized TRFR scenario for a V-system

Let us consider the simplest model example (with reference to main text Fig. 3.2) that satisfies the conditions for the TRFR experiment, i.e. transition dipole moments $d_1 = d_3 \equiv d_0$ and real-valued $\alpha = \beta = \delta = \varepsilon \equiv E_0/\sqrt{2}$, i.e. $\mathbf{E}_{pump} = \mathbf{E}_{in} = E_0\frac{\hat{\mathbf{z}}+\hat{\mathbf{y}}}{\sqrt{2}}$ (main text Fig. 3.1). From Eq. (3.28) it follows that

$$|\psi_e(t)\rangle = \frac{|\psi_1\rangle + \mathrm{e}^{i\Omega t}|\psi_3\rangle}{\sqrt{2}} \tag{3.64}$$

with $\Omega \equiv \omega_{13} = (E_1 - E_3)/\hbar$. Assuming that ω_p is nearly resonant with the transition from $|\psi_e(t)\rangle$ to $|\psi_g\rangle$, i.e. with the transition frequency $\omega_{ge} = (E_g - E_e)/\hbar < 0$, the only nonzero eigenvalue of $\tilde{\boldsymbol{\chi}}^{(1)}$ is to a good approximation given by[54]

$$\tilde{\chi}^{(1)}_{y'y'}(\omega_p) \approx \frac{N}{\varepsilon_0\hbar}e^2|d_0|^2\frac{\Delta_p - i\gamma}{\Delta_p^2 + \gamma^2} \tag{3.65}$$

where the tilde denotes a complex number, $\Delta_p = \omega_{ge} + \omega_p$ the detuning and γ the damping rate. The eigenvectors of $\tilde{\boldsymbol{\chi}}^{(1)}$ are the principal axes

$$\hat{\mathbf{z}}' = \frac{\mathrm{e}^{i\Omega\Delta t}\hat{\mathbf{z}} + \hat{\mathbf{y}}}{\sqrt{2}} \tag{3.66}$$

$$\hat{\mathbf{y}}' = \frac{-\mathrm{e}^{i\Omega\Delta t}\hat{\mathbf{z}} + \hat{\mathbf{y}}}{\sqrt{2}} \tag{3.67}$$

as obtained from Eq. (3.38) and (3.41), respectively. The polarization of the probe pulse upon transmission (to which we refer as the outcoming probe) is given by Eq. (3.56), which for this idealized scenario becomes

$$\mathbf{E}_{out}\{\hat{\mathbf{z}}, \hat{\mathbf{y}}\} = \frac{E_0}{2\sqrt{2}}\begin{bmatrix}\mathrm{e}^{i\Omega\Delta t}\left(\mathrm{e}^{i\Lambda\Delta n} - 1\right) + \mathrm{e}^{i\Lambda\Delta n} + 1 \\ \mathrm{e}^{-i\Omega\Delta t}\left(\mathrm{e}^{i\Lambda\Delta n} - 1\right) + \mathrm{e}^{i\Lambda\Delta n} + 1\end{bmatrix} \tag{3.68}$$

where $\Lambda \equiv 2\pi d/\lambda$, d the thickness of the sample, λ the wavelength of the light, and $\Delta n \approx \mathrm{Re}\left\{\tilde{\chi}^{(1)}_{y'y'}\right\}/2$ as follows from Eq. (3.48).

At one and three quarters of the period of oscillation $P = 2\pi/\Omega$ (or at any multiple of P later), the principal axes are circular. Let us consider the case $\Delta t = \frac{1}{4}P$ with principal axes

$$\hat{\mathbf{z}}'(\Delta t = \frac{1}{4}P) = \frac{i\hat{\mathbf{z}} + \hat{\mathbf{y}}}{\sqrt{2}} \tag{3.69}$$

$$\hat{\mathbf{y}}'(\Delta t = \frac{1}{4}P) = \frac{-i\hat{\mathbf{z}} + \hat{\mathbf{y}}}{\sqrt{2}} \tag{3.70}$$

Since these circular principal axes experience different refractive indices, the polarization of a linear probe pulse will be (maximally) rotated upon interaction with the sample when the probe pulse arrives at delay time $\Delta t = \frac{1}{4}P$. To derive the expression for the optical rotation angle, $\Delta t = \frac{1}{4}P$ is substituted into Eq. (3.68), which yields the following real components after multiplication with the global phase factor $\mathrm{e}^{-i\Lambda\Delta n/2}$

$$E_{z,out}(\Delta t = \frac{1}{4}P) = E_0 \cos\left(\frac{\Lambda\Delta n}{2} + \frac{\pi}{4}\right) \tag{3.71}$$

$$E_{y,out}(\Delta t = \frac{1}{4}P) = E_0 \sin\left(\frac{\Lambda\Delta n}{2} + \frac{\pi}{4}\right) \tag{3.72}$$

For the case of a Jones vector with real components, the azimuth θ is directly obtained from

$$\theta = \tan^{-1}\left(\frac{E_y}{E_z}\right) \tag{3.73}$$

With the electric vector of the incoming probe given by $\mathbf{E}_{in} = E_0\frac{\hat{\mathbf{z}}+\hat{\mathbf{y}}}{\sqrt{2}}$, and the outcoming probe pulse by Eq. (3.71) and (3.72), the optical rotation angle at $\Delta t = \frac{1}{4}P$ is given by

$$\begin{aligned} \Delta\theta_{max} &= \tan^{-1}\left(\frac{\sin\left(\frac{\Lambda\Delta n}{2} + \frac{\pi}{4}\right)}{\cos\left(\frac{\Lambda\Delta n}{2} + \frac{\pi}{4}\right)}\right) - \frac{\pi}{4} \\ &= \frac{\Lambda\Delta n}{2} = \frac{\pi d\Delta n}{\lambda} \end{aligned} \tag{3.74}$$

This is the well-known expression for the optical rotation angle of linearly polarized light in case of circular principal axes. Analogously, at $\Delta t = \frac{3}{4}P$, one finds $\Delta\theta = -\Delta\theta_{max}$.

3.10 SI: TRFR model results and discussion

As long as the polarization of the probe remains to a good approximation linear (i.e. small ellipticity angle), $\Delta\theta$ behaves as a sinusoid with angular frequency Ω and amplitude $\Delta\theta_{max}$ as a function of the delay time Δt. See main text Fig. 3.4 for an example of such oscillation of $\Delta\theta$, using the following input parameters: Polarization parameters $\alpha = \beta = \delta = \varepsilon = 1/\sqrt{2}$, i.e. $\hat{\mathbf{E}}_{pump} = \hat{\mathbf{E}}_{in} = \frac{\hat{\mathbf{z}}+\hat{\mathbf{y}}}{\sqrt{2}}$; Transition dipole moments $d_1 = 0.0003 - i0.0112$ and $d_3 = 0.0063$ (atomic units); Triplet sublevel splitting $E_3 - E_1 = 20$ meV (30 THz angular frequency); Probe wavelength $\lambda = 349$ nm ($\frac{\omega_p}{2\pi} = 846$ THz) based on $E_e - E_g = 3.55$ eV; Detuning $\Delta_p = -60$ meV $= 14.5$ THz. Note that this value is assumed to satisfy the requirements $|\Delta_p| >> \gamma$ and $|\Delta_p| >> |E_3 - E_1|/\hbar$ (Section 3.7). Also, we neglect the effect of detuning on λ (the probe's wavelength) since it amounts only 1.7% of the probe's frequency; Sample thickness $d = 100$ nm; Number density $N = 10^{24}$ m^{-3}, corresponding to 1 molecule per 1000 nm^3. This is considered to be small enough to prevent the molecules from affecting each other, given that the length of the molecule is 7.5 Å along the C_2-axis (main text Fig. 3.1), according to the scalar relativistic calculation of the ground state geometry (Table 3.1 (right)). This number density corresponds to on average 1 molecule per 10 nm, i.e. 10 molecules along the thickness d.

Substituting these parameters into Eq. (3.42) gives $\mathrm{Re}\left\{\tilde{\chi}^{(1)}_{y'y'}\right\} \approx -8.92 \cdot 10^{-8}$ for which the absolute value is much smaller than 1, which allows to use Eq. (3.44) for the approximation of $n_{y'}$. Using Eq. (3.48), we obtain $\Delta n = \mathrm{Re}\left\{\tilde{\chi}^{(1)}_{y'y'}\right\}/2 \approx -4.46 \cdot 10^{-8}$, which is substituted into Eq. (3.56). Following Eq. (3.57)−(3.61), we calculate $\Delta\theta(\Delta t)$, as is depicted in main text Fig. 3.4. The ellipticity angle of the outcoming probe is calculated with Eq. (3.63). The ellipticity angle change is given by $\Delta\epsilon = \epsilon_{out} - \epsilon_{in}$. Since the incoming probe is linear, we have $\epsilon_{in} = 0$. The ellipticity angle change turns out to be constant as a function of Δt, i.e. $\Delta\epsilon \approx -3.28 \cdot 10^{-8}$ rad. Moreover, this change turns out to be small enough, to be allowed to assume that the outcoming probe pulse remains linear. This follows from calculating

$$\theta_{out} \approx \tan^{-1}\left(\frac{|E_{out,y}|}{|E_{out,z}|}\right) \tag{3.75}$$

which to a good approximation equals the exact calculation of Eq. (3.59). Eq. (3.75) also illustrates for the case of a small ellipticity angle change, that the azimuth can be determined experimentally by simply measuring the intensity of the outcoming probe in the directions $\hat{\mathbf{y}}$ and $\hat{\mathbf{z}}$, i.e.

$$\theta_{out} \approx \tan^{-1}\left(\sqrt{\frac{I_y}{I_z}}\right) \tag{3.76}$$

Let us consider the ideal scenario ($d_1 = d_3$ and real-valued $\alpha = \beta = \delta = \varepsilon$), to evaluate some pathways to come up with an ideal molecular sample for a TRFR experiment. The signal is affected by different parameters, of which we consider the ones that can be adjusted relatively easily:

(i) $\Delta\theta$ is proportional to Δn (Eq. (3.74)), which is proportional to the linear susceptibility (Eq. (3.65)) and depends therefore quadratically on the transition dipole moment (and thus linearly on the oscillator strength). Taking a molecule with larger transition dipole moments (which requires larger SOC) will thus significantly increase the amplitude of oscillation. One should keep in mind here that the probability for exciton recombination also increases with increasing transition dipole moments, which implies a decreasing lifetime. Hence, the most suitable molecule for a TRFR experiment satisfies a trade-off between a) large enough SOC to be able to measure $\Delta\theta$, and b) not too large SOC in order to have large lifetime.

(ii) $\Delta\theta$ depends linearly on the number density N, since Δn (Eq. (3.74)) is proportional to N.

(iii) $\Delta\theta$ depends linearly on the thickness d (Eq. (3.74)).

(iv) $\Delta\theta$ depends strongly on the detuning Δ_p, since $\Delta\theta$ is proportional to $\frac{\Delta_p}{\Delta_p^2+\gamma^2}$, which equals approximately Δ_p^{-1} for $|\Delta_p| >> \gamma$ (which is required to prevent population transfer). Since we take $\Delta_p = 3(E_3 - E_1)$ (assumed to satisfy equal detuning for both sublevels), we can increase the signal by decreasing the energy splitting (as long as $|\Delta_p| >> \gamma$ is satisfied). Since we consider isolated molecules that individually contribute to the total TRFR signal, we should consider single molecules for typical values of the damping rate γ. In general, the width of an absorption line is given by two times γ. Typical absorption line widths of single molecules are in the order of (tens of) MHz[64]. As a rule of thumb, the order of magnitude of the energy splitting for a molecular TRFR experiment should thus be at least 100 MHz. Regarding Δ_p it is also useful to note that when working with an ensemble of systems it is wise to take $\Delta_p = \omega_{ge} + \omega_p$ negative, i.e. $\omega_p < |\omega_{ge}|$. The reason for this is that for positive Δ_p one might induce unwanted excitations with the probe for systems still having the ground state populated to an excited state that lies slightly above the lowest triplet state. Consequently, this reduces the intensity of the probe laser and the amplitude of the TRFR signal. However, if it is ensured that the vast majority of systems has been excited already (with an intense pump pulse), this will only have a small effect. When this effect is neglected, taking a detuning of $-\Delta_p$ shifts the TRFR signal half a period (main text Fig. 3.4) with respect to Δ_p. Here it is assumed again that we can neglect the effect of detuning on λ (the wavelength of the probe pulse) when substituting λ into Eq. (3.61) (through Eq. (3.56)) for the calculation of $\Delta\theta$.

Let us vary the input parameters to calculate how the signal ($\Delta\theta$) depends on them. Consider the same input parameters as in main text Fig. 3.4. For $PtN_2C_8H_{12}$ the calculated splitting between $|\psi_1\rangle$ and $|\psi_3\rangle$ is 4.8 THz. If we consider a splitting of 4.8 MHz instead, and $\gamma = 1$ MHz, we have $\mathrm{Re}\left\{\tilde{\chi}^{(1)}_{y'y'}\right\} \approx -0.089$. Since $\left|\mathrm{Re}\left\{\tilde{\chi}^{(1)}_{y'y'}\right\}\right| << 1$ is not valid now, we should take the exact expression for Δn, using the exact part of Eq. (3.44). The oscillation of $\Delta\theta(\Delta t)$ is still approximately sinusoidal, but the approximation of Eq. (3.75) deviates about 2.5% from using the exact Eq. (3.59). This deviation illustrates that the outcoming probe cannot be assumed to be linearly polarized anymore. This is directly reflected by the ellipticity angle change $\Delta\epsilon$, which as a function of Δt shows a sine with equilibrium value 0.034 rad and amplitude 0.4 mrad. However, 4.8 MHz does not satisfy our rule of thumb to take at least a splitting of 100 MHz, implying that $|\Delta_p| >> \gamma$ is usually not satisfied. Hence, one should expect to have a small signal lifetime due to population transfer to the ground state. Therefore, it will be very challenging to experimentally observe an oscillation of $\Delta\theta$ for a sample having such parameters.

The amplitudes of oscillation of both $\Delta\theta$ and $\Delta\epsilon$ become much larger when we besides increase the transition dipole moments. Taking it 10^2 times as large (molecules like e.g. $Ir(ppy)_3$[52] have such large transition dipole moments), together with a splitting 10^3 times as small with respect to the original parameters (main text Fig. 3.4), shows a non-sinusoidal behavior for $\Delta\theta$ and a nonzero equilibrium value. Still, $\Delta\epsilon$ oscillates sinusoidally. This illustrates that in the extreme case when we do not satisfy $\left|\mathrm{Re}\left\{\tilde{\chi}^{(1)}\right\}\right| << 1$, that the oscillation of $\Delta\theta$ is not suitable as a measure for the oscillation of $\langle \mathbf{J}\rangle(t)$, but one might consider to measure $\Delta\epsilon(\Delta t)$ instead.

We have shown that the TRFR experiment can be applied to molecules without using a magnetic field. This requires that there is a so-called zero-field splitting (ZFS), which is usually defined in terms of the so-called D- and E-parameter. In some cases one might want to perform the TRFR experiment at nonzero magnetic field, e.g. to study magnetic field dependence. Particularly interesting for this seem molecules with two sublevels of the lowest triplet excited state being degenerate ($E = 0$), combined with large transition dipole moments between the ground state and these sublevels. There are numerous examples of molecules with $E = 0$, while D is nonzero, i.e. the splitting between these sublevels and the third (e.g. Ir(ppy)$_3$[52]). The D-parameter directly depends on the amount of SOC. Depending on the symmetry of the molecule, E can be zero, which simultaneously allows to obtain large transition dipole moments by choosing a system with large SOC. One might now use a small magnetic field to slightly separate the degenerate sublevels. One should still ensure that the splitting is significantly larger than the damping rate γ.

When choosing a molecule for performing the TRFR experiment, one should also consider the following. Depending on the polarization and frequency of the light, one might excite to a superposition of more than two triplet sublevels. Consequently, the oscillation consists of a sum of sines with frequencies $|\omega_{ij}| = |E_i - E_j|/\hbar$ for levels for which $\langle\psi_i|\mathbf{J}|\psi_j\rangle$ is nonzero.

3.11 SI: Computational details and methods

In this work, we study as a function of time the oscillation of the polarization rotation $\Delta\theta$ and of the expectation value of the total angular momentum $\mathbf{J}$ for $PtN_2C_8H_{12}$ in case of a superposition of two triplet sublevels (Fig. 3.2a). The former requires i.a. the calculation of transition dipole moments between the ground state and excited state sublevels, whereas the latter also requires total angular momentum integrals. An accurate but costly way to calculate these is the use of the Complete Active Space SCF (CASSCF) and the second order perturbative correlation (CASPT2) methods combined with the restricted active space state interaction (RASSI) method to include SOC. This combined CASSCF/CASPT2/RASSI–SO method has been introduced by Roos and Malmqvist[17, 18].

To obtain the ground state geometry of $PtN_2C_8H_{12}$, a scalar relativistic density functional theory (DFT) calculation (using the one-component formulation of the zeroth-order regular approximation (ZORA)[65–68]) is performed with the Amsterdam Density Functional (ADF) program[31, 32], where the B3LYP[69] functional and TZP[70–72] basis set are used. According to this calculation, the lowest energy conformation of the molecule has C_2 symmetry (to which is referred as the C_2 geometry (Table 3.1 (left))), for which no imaginary frequencies are obtained. In view of computational efficiency for the CASSCF/CASPT2/RASSI–SO method however, the C_{2v} geometry (Table 3.1 (right)) is assumed to represent the ground state although it possesses two imaginary frequencies, i.e. $65i$ and $78i$ cm^{-1}, having symmetry b_1 and a_2, respectively, corresponding to vibrations that lower the symmetry from C_{2v} to C_s and C_2, respectively. This approach seems reasonable when the molecule is at room temperature, since the calculated energy difference between the two geometries amounts 22 meV. Also, the UV-Vis spectra for both geometries are calculated via time-dependent DFT (TDDFT)[73–76] (using ZORA) including SOC perturbatively[30]. No significant differences are obtained (Fig. 3.6). Hence, we conclude that we can safely assume the C_{2v} geometry for the ground state.

We have applied the CASSCF/CASPT2/RASSI–SO method to the $PtN_2C_8H_{12}$ molecule, using the MOLCAS[23] software using ANO-RCC[38, 77, 78] basis sets (contracted for Pt to $8s7p5d2f$, for N to $4s3p1d$, for C to $4s3p1d$, for H to $3s1p$) and the Douglas-Kroll method[79]. The first stage of the method is a CASSCF calculation. The selected CAS is given in Fig. 3.7, where also the labeling of the molecular orbitals (MOs) is explained. The lower lying inactive MOs are doubly occupied (31, 10, 5 and 21 MOs for the symmetries a_1, b_1, a_2 and b_2,

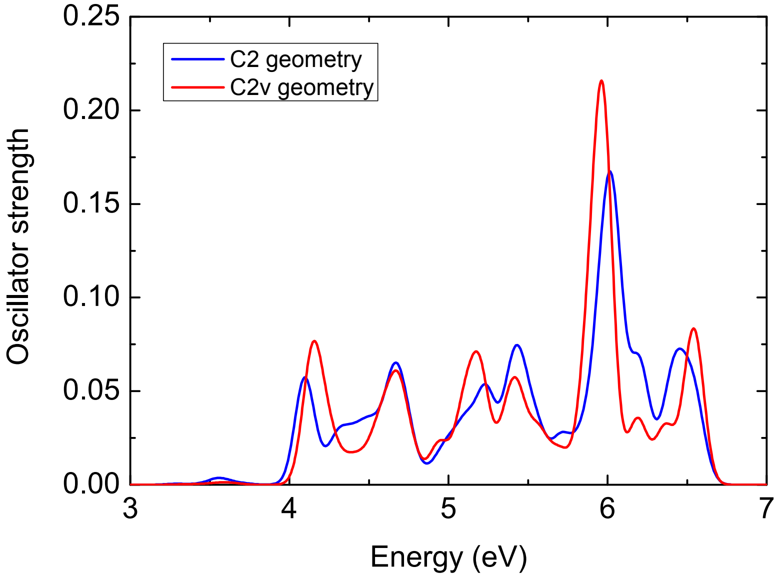

Figure 3.6: Excitation spectra as determined from TDDFT calculations, for the C_2 and C_{2v} geometry of $PtN_2C_8H_{12}$.

respectively). The Hartree-Fock configuration is $(1a_1)^2...(34a_1)^2(1b_1)^2...(13b_1)^2$ $(1a_2)^2...(7a_2)^2(1b_2)^2...(22b_2)^2$. Within our CASSCF calculation, 18 active electrons are distributed over 14 MOs. We have performed a state averaged CASSCF, calculating the 10 lowest roots for each symmetry. This results in 80 roots, which we call *spin-free* states in line with Molcas. The oscillator strengths between the excited *spin-free* states and the ground state 1^1A_1 are depicted in red in Fig. 3.8. Since SOC is not considered within this calculation, excitations from the singlet ground state can only take place to singlet excited states.

Using the CASSCF wave function, a CASPT2 calculation is performed to obtain a second order perturbation estimate of the correlation energy. The resulting energies are taken as an input for the RASSI method.

This work considers a direct excitation for $PtN_2C_8H_{12}$ when initially populated in the singlet ground state $|\psi_g\rangle$, to a superposition of two sublevels of the

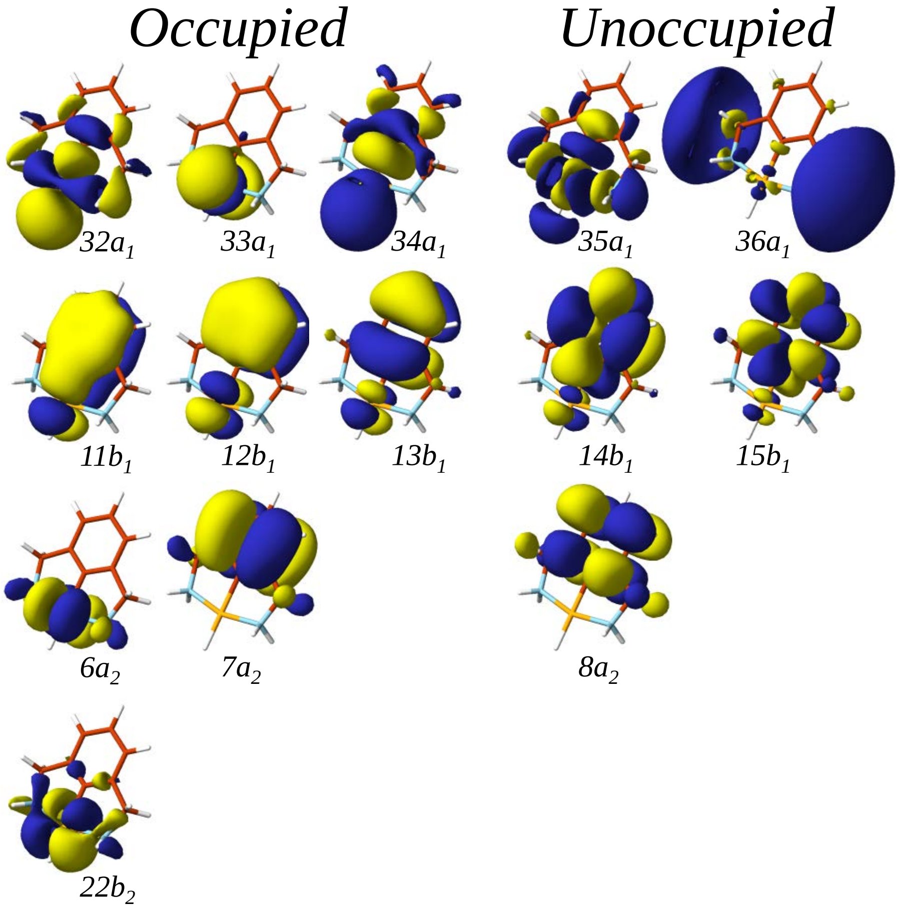

Figure 3.7: Selected molecular orbitals (MOs) for the Complete Active Space (CAS) of $PtN_2C_8H_{12}$.

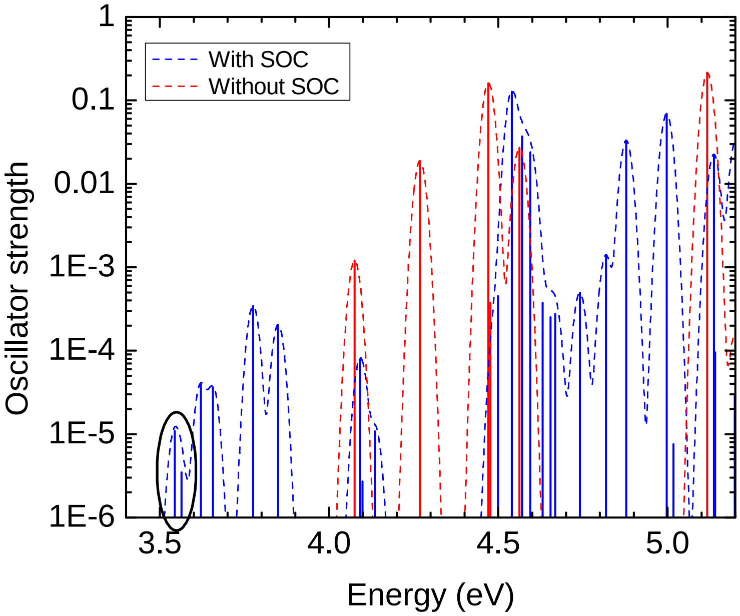

Figure 3.8: Excitation spectrum on semi-log scale, as obtained from ab initio calculations for the *spin-orbit* states (with SOC) and the *spin-free* states (without SOC). The height of the bars correspond to the oscillator strength for a transition from the ground state. The curves are intended as a guide to the eye, representing the excitation spectra broadened by Gaussians with $\sigma = 0.02$ eV. This work considers the lowest triplet (encircled), for which excitation is allowed to only two of the three sublevels (Fig. 3.9). Note that all nonzero f-values below 5.2 eV are contained in this plot.

lowest triplet excited state. SOC induces mixing of triplets into singlets and vice versa, which allows for excitations between them. In line with Molcas, we use the term *spin-orbit* to refer to the eigenbasis obtained after diagonalization of the Hamiltonian that includes the SOC term, which is performed within the RASSI method. Strictly speaking, because of the mixing one should not speak about singlet and triplet states anymore within the *spin-orbit* basis, but one usually does because the hybridised *spin-orbit* states often resemble the original *spin-free* states.

The RASSI calculation gives the *spin-orbit* states as a linear combination of *spin-free* states. Table 3.3 tabulates the main contributions of the four lowest *spin-orbit* states, where the corresponding transitions between MOs are tabulated in Table 3.2. Particularly interesting are the singlets mixed into the triplets and vice versa, since these are the contributions that give nonzero transition dipole moments between the ground and excited states and therefore enable a transition.

Table 3.1: Atomic coordinates (Å) for the C_2 (left) and C_{2v} (right) geometry of $PtN_2C_8H_{12}$.

Atom	X	Y	Z
Pt	0.000000	0.000000	-0.045142
N	-0.191499	2.057399	-0.390104
N	0.191499	-2.057399	-0.390104
C	0.000000	0.000000	-2.046215
C	-0.036646	-1.215345	-2.727430
C	0.036646	1.215345	-2.727430
C	0.026445	1.220441	-4.122237
C	-0.026445	-1.220441	-4.122237
C	0.000000	0.000000	-4.807534
C	0.143797	2.430631	-1.828603
C	-0.143797	-2.430631	-1.828603
H	0.000000	0.000000	-5.891159
H	0.047114	2.146972	-4.688039
H	-0.047114	-2.146972	-4.688039
H	-0.496914	3.257069	-2.147392
H	0.496914	-3.257069	-2.147392
H	1.170515	2.801231	-1.816104
H	-1.170515	-2.801231	-1.816104
H	1.164990	-2.276992	-0.194498
H	-1.164990	2.276992	-0.194498
H	-0.363756	-2.615608	0.250989
H	0.363756	2.615608	0.250989
H	0.000000	0.000000	1.623945

Atom	X	Y	Z
Pt	0.000000	0.000000	-0.046962
N	0.000000	2.066477	-0.365512
N	0.000000	-2.066477	-0.365512
C	0.000000	0.000000	-2.044076
C	0.000000	-1.215513	-2.727191
C	0.000000	1.215513	-2.727191
C	0.000000	1.219696	-4.122133
C	0.000000	-1.219696	-4.122133
C	0.000000	0.000000	-4.807861
C	0.000000	2.448529	-1.845813
C	0.000000	-2.448529	-1.845813
H	0.000000	0.000000	-5.891569
H	0.000000	2.146459	-4.688100
H	0.000000	-2.146459	-4.688100
H	-0.877938	3.072293	-2.029768
H	0.877938	3.072293	-2.029768
H	0.877938	-3.072293	-2.029768
H	-0.877938	-3.072293	-2.029768
H	0.811887	-2.467017	0.094995
H	-0.811887	-2.467017	0.094995
H	-0.811887	2.467017	0.094995
H	0.811887	2.467017	0.094995
H	0.000000	0.000000	1.624375

As can be seen in Table 3.3, *spin-orbit* state $|\psi_g\rangle$ has contributions from *spin-free* states 2^3B_2 and 1^3A_2, $|\psi_1\rangle$ from 1^1B_2, and $|\psi_3\rangle$ from 2^1A_1.

The oscillator strengths between the excited *spin-orbit* states and the ground state $|\psi_g\rangle$ are depicted in blue in Fig. 3.8. The oscillator strengths corresponding to the lowest triplet are encircled. The corresponding nonzero components of the transition dipole moments are $\langle\psi_1|\, y\, |\psi_g\rangle \approx 0.0003 - i0.0112$ and $\langle\psi_3|\, z\, |\psi_g\rangle \approx 0.0063$ in atomic units. In other words, a transition from $|\psi_g\rangle$ is allowed only with y and z polarized light to state $|\psi_1\rangle$ and $|\psi_3\rangle$ respectively, but forbidden to state $|\psi_2\rangle$ (Fig. 3.9).

Table 3.2: Lowest *spin-free* states (SFSs) for $PtN_2C_8H_{12}$. For the SFSs with important contributions to the states $|\psi_g\rangle$, $|\psi_1\rangle$, $|\psi_2\rangle$ and $|\psi_3\rangle$ (Table 3.3), the main MO configurations are given as well, corresponding to transitions between the MOs depicted in Fig. 3.7.

SFS	Energy (eV)	Conf., Weight	Conf., Weight
1^1A_1	0.00	Hartree-Fock, 0.92	
1^3B_1	3.78	$13b_1 \Rightarrow 35a_1$, 0.76	
1^3A_1	3.91	$13b_1 \Rightarrow 14b_1$, 0.42	$7a_2 \Rightarrow 8a_2$, 0.34
1^3A_2	3.99	$6a_2 \Rightarrow 35a_1$, 0.85	
2^3A_1	4.03	$33a_1 \Rightarrow 35a_1$, 0.77	
1^3B_2	4.06	$22b_2 \Rightarrow 35a_1$, 0.85	
1^1B_1	4.08	$13b_1 \Rightarrow 35a_1$, 0.65	
2^3B_2	4.18	$13b_1 \Rightarrow 8a_2$, 0.64	
2^1A_1	4.27	$33a_1 \Rightarrow 35a_1$, 0.80	
3^3A_1	4.42	$7a_2 \Rightarrow 8a_2$, 0.43	$13b_1 \Rightarrow 14b_1$, 0.33
3^1A_1	4.47	$34a_1 \Rightarrow 35a_1$, 0.53	$34a_1 \Rightarrow 36a_1$, 0.26
1^1B_2	4.48	$22b_2 \Rightarrow 35a_1$, 0.50	$13b_1 \Rightarrow 8a_2$, 0.21

Table 3.3: Main contributions for $PtN_2C_8H_{12}$ of the four lowest *spin-orbit* states (SOSs) in terms of the *spin-free* states (SFSs) for which the MO configurations are tabulated in Table 3.2.

SOS	Energy (eV)	SFS, Weight	SFS, Weight	SFS, Weight
$\lvert\psi_g\rangle$	0.00	1^1A_1, 0.97	2^3B_2, 0.015	1^3A_2, 0.0081
$\lvert\psi_1\rangle$	3.544	1^3B_1, 0.61	1^3A_1, 0.33	1^1B_2, 0.042
$\lvert\psi_2\rangle$	3.558	1^3B_1, 0.59	1^3A_1, 0.33	2^3B_2, 0.066
$\lvert\psi_3\rangle$	3.564	1^3B_1, 0.59 2^1A_1, 0.011	1^3A_2, 0.21	2^3B_2, 0.17

3.12 SI: Symmetry analysis

The aforementioned optical selection rules (Fig. 3.9) can also be obtained from group theoretical arguments. Here, we discuss two different approaches to come to the same conclusion.

Approach (1): The states $|\psi_1\rangle$, $|\psi_2\rangle$ and $|\psi_3\rangle$ mainly originate from *spin-free* state 1^3B_1 (Table 3.3). SOC has allowed this state to mix with singlets

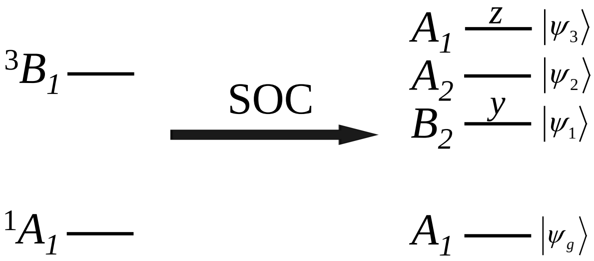

Figure 3.9: Energy diagram illustrating the effect of SOC on optical selection rules of originally forbidden singlet-triplet transitions. When SOC is not taken into account, the lowest triplet excited state of $PtN_2C_8H_{12}$ has B_1 symmetry. Due to SOC, three separate sublevels $|\psi_1\rangle$, $|\psi_2\rangle$ and $|\psi_3\rangle$ are obtained, having A_2, B_2 and A_1 symmetry, respectively. It is assumed here that the ground state has C_{2v} geometry. Excitations from the ground state can only take place to $|\psi_1\rangle$ and $|\psi_3\rangle$ with y and z polarized light respectively, whereas a transition to state $|\psi_2\rangle$ is forbidden.

having symmetry A_1, A_2 and B_2, as follows from the transformation of rotations, i.e. $B_2(R_x) + B_1(R_y) + A_2(R_z)$ within C_{2v}. Since the electric-dipole moment operator transforms as $B_1(x) + B_2(y) + A_1(z)$ within C_{2v}, it directly follows that excitations from the ground state are allowed to the lowest triplet only with y and z polarization (Fig. 3.9). Besides this contribution from singlets mixed into the lowest triplet (mainly 1^1B_2 for $|\psi_1\rangle$ and 2^1A_1 for $|\psi_3\rangle$), also triplets mixed into the ground state contribute to the mentioned transition dipole moments (mainly 2^3B_2 and 1^3A_2), as tabulated in Table 3.3.

Approach (2): The orbital part of the lowest triplet has B_1 symmetry. Let us now determine the symmetry of the triplet sublevels. In this regard it is convenient to consider the triplet spin functions T_x, T_y and T_z, defined as

$$T_x = \frac{T_{-1} - T_{+1}}{\sqrt{2}} = \frac{\beta_1\beta_2 - \alpha_1\alpha_2}{\sqrt{2}} \tag{3.77}$$

$$T_y = i\frac{T_{-1} + T_{+1}}{\sqrt{2}} = i\frac{\beta_1\beta_2 + \alpha_1\alpha_2}{\sqrt{2}} \tag{3.78}$$

$$T_z = T_0 = \frac{\alpha_1\beta_2 + \beta_1\alpha_2}{\sqrt{2}} \tag{3.79}$$

with α_i and β_i corresponding to the up and down spin of electron i respectively. T_x, T_y and T_z transform as rotations. For C_{2v} symmetry these are B_2, B_1 and A_2 for T_x, T_y and T_z, respectively. Taking the direct product between the orbital part (B_1) and the spin part (B_2, B_1 and A_2) implies that the sublevels have symmetry A_2, A_1 and B_2, respectively. To determine the possible excitations, one considers that x, y and z transform in C_{2v} as B_1, B_2 and A_1 respectively. From the A_1 ground state one can thus only excite to levels having symmetry B_1, B_2 and A_1, in order to let the integral $\langle\psi_e| D |\psi_g\rangle$ be nonzero. Hence, excitations from the ground state to the lowest triplet excited state can only take place for the B_2 and A_1 sublevels, when the system interacts with y and z polarized light respectively, whereas a transition to the B_1 sublevel is forbidden.

Table 3.4: FC-factors for 0-0 transition of different metal-organic molecules, as obtained from DFT calculations.

Molecule	FC-factor of 0-0 transition
$PtN_2C_8H_{12}$	$< 10^{-6}$
PtP (D_{4h} ground and excited state)	0.43
PtP (D_{4h} ground and C_{2h} excited state)	0.26
PtPπ (D_{4h} ground and excited state)	0.44

3.13 SI: Franck-Condon factors

The molecular TRFR experiment that we have introduced is based on measuring the triplet spin dynamics of a superposition of two electronic excited state sublevels (created by an on-resonance pump laser and probed via a probe laser that is slightly detuned with respect to the singlet-triplet transition). One should realize that electrons can couple to vibrations, implying that each electronic sublevel has a series of vibronic states. The Franck-Condon principle states that an electronic transition most likely occurs between vibronic states that have comparable geometry[35]. Creating and probing the excited state superposition is thus only possible if there is good vibrational overlap between the lowest vibronic sublevels of the electronic ground and excited state sublevels, for which the corresponding transition is commonly referred to as the 0-0 transition. In other words, the geometry should not distort too much upon excitation (within the timescale of the spin dynamics).

To study the geometry relaxation of the excited state, we have calculated the so-called Franck-Condon (FC) factors (a measure for the strength of a vibronic transition) for a series of vibronic states, of which we only report the 0-0 transition (for three molecules, Table 3.4). These FC-factors have been determined via DFT calculations with the ADF program[31, 32], using a B3LYP[69] functional and

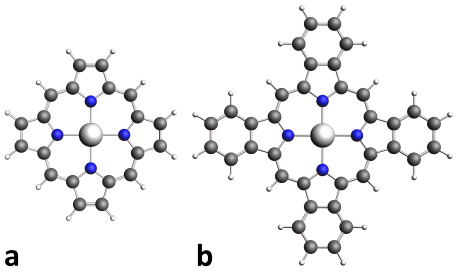

Figure 3.10: Platinum porphyrins, with **a**, an unsubstituted platinum porphyrin (PtP), and **b**, a π-extended platinum porphyrin (PtPπ). The platinum atom (white) is surrounded by nitrogen atoms (blue), which are surrounded by carbon (grey) and hydrogen (white) atoms.

TZP[70–72] basis set. Geometry optimizations and frequency calculations have been performed for both the singlet ground state (restricted DFT) and triplet excited state (unrestricted DFT).

Unfortunately, the geometry distortion turns out to be significant for the $PtN_2C_8H_{12}$ molecule that we consider in this work. This particularly follows from the fact that the FC-factor is extremely small for the 0-0 transition (Table 3.4). Although the detailed analysis for $PtN_2C_8H_{12}$ in our work is useful as a proof of principle for a molecular TRFR experiment, for a practical realization we should thus look for other candidate molecules.

The FC-factor of the 0-0 transition of a metal-organic molecule is typically large when the metal atom is well surrounded by the ligands. We found large FC-factors (Table 3.4) for the 0-0 transition of unsubstituted porphine platinum (to which we refer as PtP, Fig. 3.10a) and of a π-extended porphine platinum (to which we refer as PtPπ, Fig. 3.10b). Such a π-substitution is particularly interesting for manipulation of the transition energy of the molecule, since this wavelength was shown to increase (more than 200 nm) for an increasing number of fused-aromatic rings[80].

3.14 SI: Optical selection rules of platinum porphyrins

Platinum porphyrins are promising candidates for a molecular TRFR experiment. Diaconu et al. observed magnetic circular dichroism (different absorption for left and right circularly polarized light in a magnetic field) within the zero-phonon region of platinum porphyrins in organic hosts[45]. Their work summarizes polar-

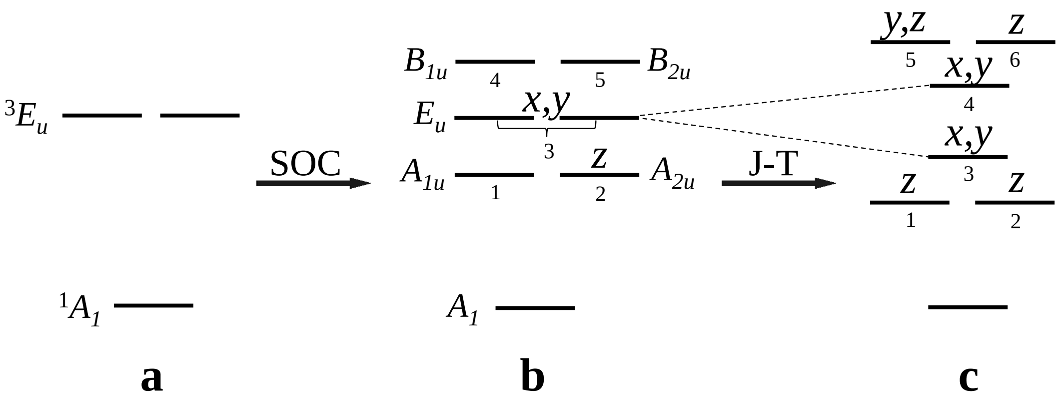

Figure 3.11: Energy diagram illustrating for PtP the effect of SOC and a Jahn-Teller (J-T) distortion on the optical selection rules of originally forbidden singlet-triplet transitions. **a**, When SOC is not taken into account, the lowest excited state of PtP is a doublet of two triplets with E_u symmetry, which according to our calculations originates from the molecular orbital excitation $a_{2u} \rightarrow e_g$. **b**, Due to SOC, a mixing of singlets and triplets occurs. Additionaly, the sublevels of the doublets split (labeled with a number (#) based on the energy (where 3 is a doublet) and their symmetry is depicted as well (within D_{4h})). Excitations from the ground state (D_{4h} geometry) can only take place to state 2 and 3 with z and (x, y) polarized light respectively, whereas the other transitions are forbidden (Table 3.5). **c**, After excitation, the system will undergo a Jahn-Teller distortion, which further splits the energy levels (Table 3.6) and the molecule gets C_{2h} symmetry.

ization selection rules that satisfy the criteria for a molecular TRFR experiment, and they present results with and without Jahn-Teller (J-T) and host interactions.

In order to study in more detail the optical transitions between the ground and excited state sublevels of PtP and PtPπ (Fig. 3.10), the CASSCF/CASPT2/-RASSI–SO method is not suitable, because of the relatively large number of atoms. Therefore, we perform TDDFT calculations (using ZORA) including SOC perturbatively[30]. These calculations are performed with ADF using a B3LYP functional and TZP basis set. In Table 3.5 we report for PtP (considering D_{4h} symmetry for both the ground and excited state geometry) the energies, oscillator strengths f and transition dipole moments μ, for the lowest 10 excitations from the ground state (from which the absorption spectrum can be derived).

When SOC is not taken into account, the lowest excited state of PtP is a doublet of two triplets with E_u symmetry, which according to our calculations originates from the molecular orbital excitation $a_{2u} \rightarrow e_g$. Instead, Diaconu *et*

Table 3.5: Transition dipole moments for the lowest 10 transitions from the ground state for PtP as obtained from TDDFT calculations, including SOC perturbatively (using ZORA). This calculation corresponds to the scheme in Fig. 3.11b (J-T distortion is still neglected). The oscillator strengths f and transition dipole moments μ determine the absorption spectrum of PtP, with their values given in atomic units (μ-values smaller than 10^{-5} are neglected). D_{4h} symmetry is considered. The excited states are labeled with a number (#) according to the energetic ordering. States 1-5 originate from a ${}^3E_u$ (which is a doublet of two triplets), and 6-10 from another ${}^3E_u$. States 3 and 8 are each a degenerate doublet, which further split due to a Jahn-Teller distortion (Fig. 3.11c and Table 3.6).

#	Symm.	E (eV)	f	μ_x	μ_y	μ_z
1	A_{1u}	2.0189	0	0	0	0
2	A_{2u}	2.0190	$6.11 \cdot 10^{-8}$	0	0	$-i1.11 \cdot 10^{-3}$
3	E_u	2.0335	$1.65 \cdot 10^{-6}$	$i5.76 \cdot 10^{-3}$	0	0
4	B_{1u}	2.0486	0	0	0	0
5	B_{2u}	2.0488	0	0	0	0
6	A_{1u}	2.2202	0	0	0	0
7	A_{2u}	2.2202	$3.82 \cdot 10^{-8}$	0	0	$-i8.38 \cdot 10^{-4}$
8	E_u	2.2328	$2.96 \cdot 10^{-5}$	$i2.32 \cdot 10^{-2}$	0	0
9	B_{1u}	2.2457	0	0	0	0
10	B_{2u}	2.2457	0	0	0	0

al.[45] find as the lowest excited state the other close lying ${}^3E_u$ originating from $a_{1u} \rightarrow e_g$, which ends up as our second ${}^3E_u$ (consisting of states 6-10 in Table 3.5 when SOC is included, which gives quite comparable results).

Due to SOC, a mixing of singlets and triplets occurs. Additionaly, the sublevels of the doublets split, as depicted in Fig. 3.11b (with the sublevels labeled with a number (#) based on the energy (where 3 is a doublet) and their symmetry is depicted as well (within D_{4h})). Excitations from the ground state (D_{4h} geometry) can only take place to state 2 and 3 with z and (x, y) polarized light respectively, whereas the other transitions are forbidden (Table 3.5). The polarization selection rules obtained as such seem to be promising for a molecular TRFR experiment. A pump pulse polarized in both the z and (x, y) direction will induce a superposition between states 2 and 3, which can be probed via the polarization rotation upon transmission of a detuned probe pulse with similar polarization.

Table 3.6: Transition dipole moments for the lowest 6 transitions of PtP as obtained from spin-unrestricted TDDFT calculations with the excited state geometry taken as the ground state (to simulate the Jahn-Teller distortion), including SOC perturbatively (using ZORA). This calculation corresponds to the scheme in Fig. 3.11c. The oscillator strengths f and transition dipole moments μ determine the emission spectrum of PtP, with their values given in atomic units (μ-values smaller than 10^{-5} are neglected). No symmetry analysis is performed during the TDDFT calculation. The states are labeled with a number (#) according to the energetic ordering.

#	E (eV)	f	μ_x	μ_y	μ_z
1	1.7616	$1.08 \cdot 10^{-10}$	0	0	$4.99 \cdot 10^{-5}$
2	1.7617	$1.99 \cdot 10^{-8}$	0	0	$i6.79 \cdot 10^{-4}$
3	1.7622	$3.22 \cdot 10^{-6}$	$-8.10 \cdot 10^{-3} +i7.56 \cdot 10^{-4}$	$-2.89 \cdot 10^{-3} +i2.70 \cdot 10^{-4}$	0
4	1.9997	$9.98 \cdot 10^{-6}$	$-3.85 \cdot 10^{-3} +i8.82 \cdot 10^{-4}$	$1.34 \cdot 10^{-2} -i3.06 \cdot 10^{-3}$	0
5	2.0003	$3.18 \cdot 10^{-9}$	0	$i1.37 \cdot 10^{-5}$	$-4.06 \cdot 10^{-5} +i2.51 \cdot 10^{-4}$
6	2.0004	$4.75 \cdot 10^{-9}$	0	0	$3.07 \cdot 10^{-4} +i5.11 \cdot 10^{-5}$

However, one should be aware that after excitation with a pump pulse, the system undergoes a geometry relaxation (towards C_{2h}), i.e. a J-T distortion (Fig. 3.11c), which further splits the energy levels. This is no problem if the relaxation takes place on a longer time scale than the spin dynamics. If it takes place on a comparable timescale, the changes of the geometry and energy eigenstates should be small to prevent quantum decoherence. From the calculation of the FCFs we concluded already that the geometry change is relatively small (Section 3.13). We therefore expect only a small effect on the energies of the electronic states. To calculate the effect, we perform a spin-unrestricted TDDFT calculation with the triplet excited state geometry taken as the ground state geometry (Table 3.6). Such an approach is common in the calculation of emission spectra. The doublet E_u (Fig. 3.11b and Table 3.6) splits due to the J-T distortion. The optical selection rules for states $\#1-5$ in Table 3.5 and $\#1-6$ in Table 3.6 seem quite comparable, with more transitions allowed for the latter case however. In case the timescales of the J-T distortion and spin dynamics are comparable, the polarization rotation of the probe pulse is determined by

Table 3.7: Transition dipole moments for the lowest 10 transitions from the ground state (D_{4h} geometry) for PtPπ as obtained from TDDFT calculations, including SOC perturbatively (using ZORA). The oscillator strengths f and transition dipole moments μ determine the absorption spectrum of PtPπ, with their values given in atomic units (μ-values smaller than 10^{-5} are neglected). No symmetry restrictions are imposed during the TDDFT calculation. The excited states are labeled with a number (#) according to the energetic ordering. State 7 consists mainly of a singlet (the other states are mainly of triplet origin).

#	E (eV)	f	μ_x	μ_y	μ_z
1	1.46716	0	0	0	0
2	1.46716	0	0	0	0
3	1.46786	$3.60 \cdot 10^{-5}$	$-5.69 \cdot 10^{-4}$	$3.09 \cdot 10^{-2}$	0
4	1.70006	$1.85 \cdot 10^{-4}$	$-6.53 \cdot 10^{-2}$	$-1.10 \cdot 10^{-3}$	0
5	1.70136	0	0	0	0
6	1.70136	0	0	0	0
7	2.13466	0.2793	2.274	$3.70 \cdot 10^{-2}$	$-1.62 \cdot 10^{-5}$
8	2.20166	0	0	0	0
9	2.20176	0	0	0	0
10	2.20246	$1.50 \cdot 10^{-3}$	$1.64 \cdot 10^{-1}$	$2.60 \cdot 10^{-3}$	0

the transition dipole moments given in Table 3.6. After having created a superposition between states $\#2, 3$ in Table 3.5, the probe pulse should thus address (though slightly detuned to prevent population transfer back to the ground state) states $\#2, 3$ in Table 3.6. To quantify the change of states $\#2, 3$ (in Table 3.6 with respect to $\#2, 3$ in Table 3.5) it would be even more insightful to calculate the overlap of the eigenstates before and after the J-T distortion, which we have not done.

For a molecular TRFR experiment, the laser frequencies of the pump and probe pulse should match the singlet-triplet frequency. In that regard, for a TRFR experiment with platinum porphyrins the substitution of aromatic rings to PtP can be useful. We have performed similar TDDFT calculations for PtPπ (Table 3.7), which quite closely resemble the results of PtP. However, the fact that the transition dipole moment in the z-direction remains negligible for all states makes a TRFR experiment unpractical for PtPπ.

3.15 SI: Ensemble of randomly oriented molecules

In our calculations we have considered a sample consisting of an ensemble of similarly oriented molecules, illuminated at $t = 0$ with a linearly polarized pump pulse having polarization $\hat{\mathbf{E}}_{pump} = \frac{\hat{\mathbf{z}}+\hat{\mathbf{y}}}{\sqrt{2}}$ (with respect to the molecular frame of reference, as in main text Fig. 3.1). Let us address the following important conclusion: the TRFR signal decreases when the sample is rotated along any axis. In the molecular frame, the signal ultimately goes to zero when the electric vector oscillates only along x, y or z, simply because each system ends up in a single sublevel instead of a superposition. Interestingly, when the sample is rotated an angle ϕ along x (the propagation axis of the pump), the signal does not depend on ϕ if a circular instead of a linear pump is used, which might be experimentally favourable.

Instead of using an ensemble of similarly oriented molecules, we can consider the case of random orientations. One should keep in mind that for our derivation to be valid, the number density N should be small enough to ensure that the molecules are well isolated from each other. A particular example to which this section applies is the case of an ensemble of the molecule of interest put with random orientation in a crystalline host material. Perhaps even more interesting would be the case of a liquid host (i.e. in solution), or the molecule of interest put in the gas phase, since the molecules are then also well isolated. However, in these latter cases the signal might suffer from broadening due to the larger temperatures compared to the case of a crystalline host.

Let us consider a random ensemble of $PtN_2C_8H_{12}$ molecules, illuminated at $t = 0$ with a circular pump pulse (satisfying assumptions (*i*) to (*iv*) of Sec. 3.7, where $|\psi_e\rangle$ follows from Eq. (3.26)). Within this random ensemble, molecules having their plane parallel to the propagation axis will be excited to a single sublevel and do therefore not contribute to the TRFR signal. Instead, any molecule having its molecular plane exactly perpendicular to the pump propagation axis will be excited to a superposition of sublevels and does therefore contribute to the TRFR signal. At delay times where the signal is maximally positive or negative, these are the molecules that contribute most. At these times, all remaining molecules (having an orientation that is neither parallel nor perpendicular to the propagation axis) contribute to the total TRFR signal with a value that lies between zero and the maximum. Clearly, for an ensemble of randomly oriented $PtN_2C_8H_{12}$ molecules, a net nonzero TRFR signal is obtained (presumed that all requirements for a TRFR experiment are satisfied). This implies that optically

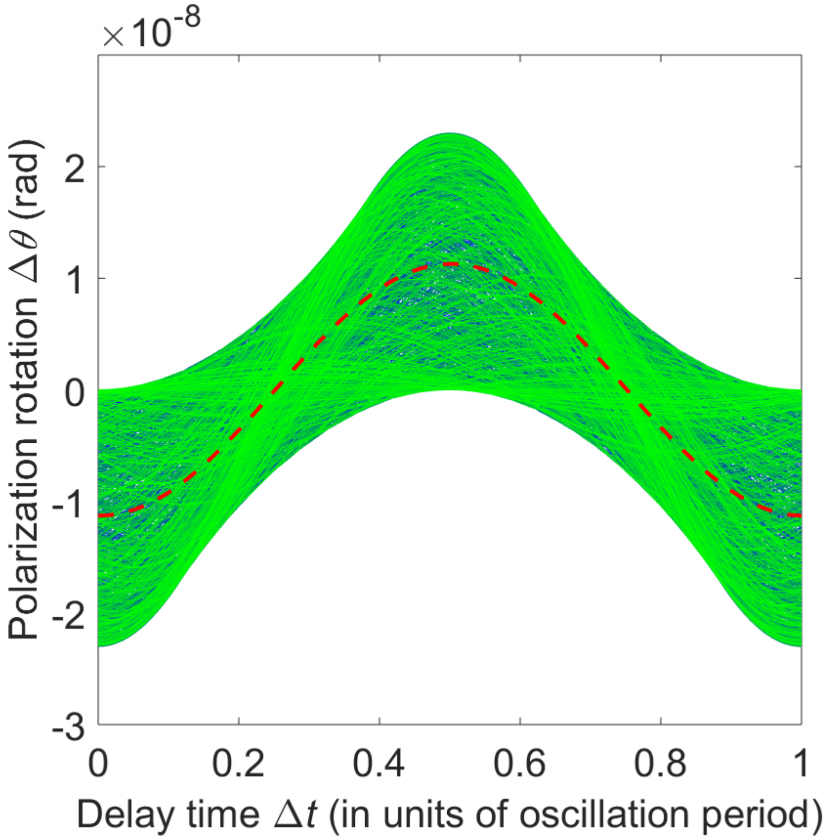

Figure 3.12: Calculation of $\Delta\theta(\Delta t)$ for the metal-organic molecule $\mathbf{PtN_2C_8H_{12}}$ (main text Fig. 3.1). Each line represents a different orientation of a sample with molecules all oriented similarly (where the color variation is merely intended for contrast). Besides, the only difference with respect to main text Fig. 3.4 is that a circular pump pulse is considered ($\hat{\mathbf{E}}_{pump} = \frac{-i\hat{\mathbf{z}}+\hat{\mathbf{y}}}{\sqrt{2}}$). Clearly, for an ensemble of randomly oriented $PtN_2C_8H_{12}$ molecules, a net TRFR signal is obtained. More specific, the total average TRFR signal (dashed line) for such an ensemble decreases with only a factor 2 with respect to an ensemble with all molecules oriented such that the maximum signal is obtained (i.e. perpendicular to the incoming light).

induced spin polarization can be applied to an ensemble of randomly oriented molecules.

To verify this conclusion with calculations, we study how $\Delta\theta(\Delta t)$ depends on the sample orientation with respect to the incoming pump and probe. We calculate $\Delta\theta(\Delta t)$ as in main text Fig. 3.4 for a sample consisting of similarly oriented $PtN_2C_8H_{12}$ molecules, with the only difference that a circular pump pulse is considered ($\hat{\mathbf{E}}_{pump} = \frac{-i\hat{\mathbf{z}}+\hat{\mathbf{y}}}{\sqrt{2}}$) and that the sample has a random orientation, obtained by using random values for the so-called proper Euler angles (which

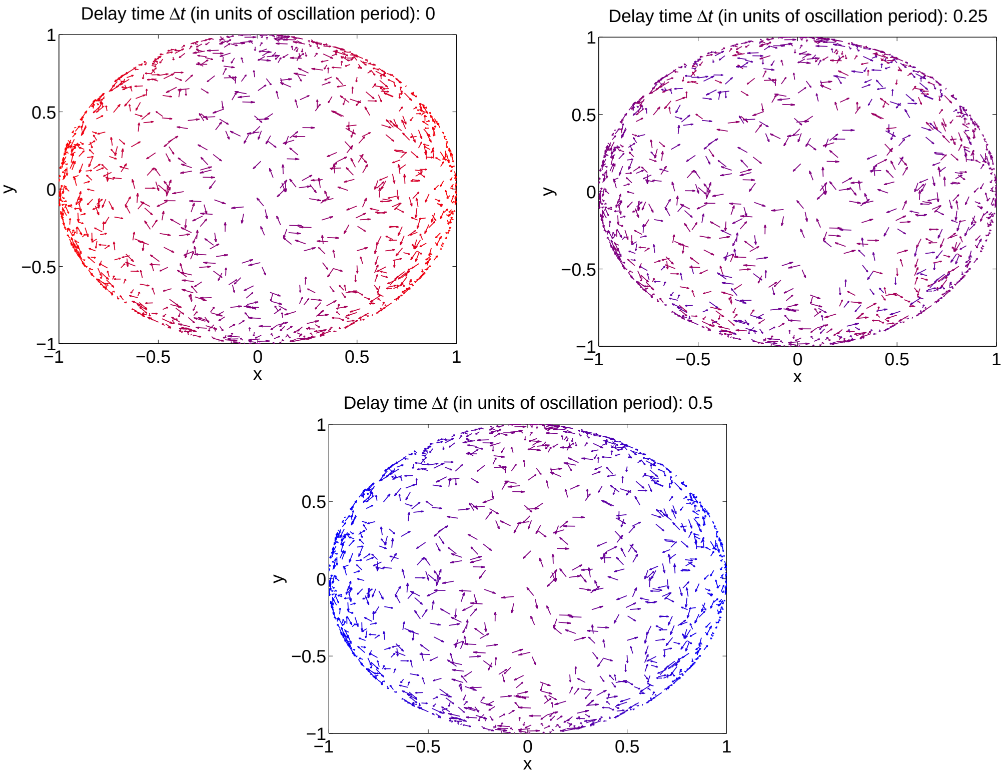
Delay time Δt (in units of oscillation period): 0

Delay time Δt (in units of oscillation period): 0.25

Delay time Δt (in units of oscillation period): 0.5

Figure 3.13: Visualization of the TRFR signal for different sample orientations (with the molecules in the sample oriented similarly) for the metal-organic molecule $PtN_2C_8H_{12}$ (main text Fig. 3.1). We consider a circular pump pulse ($\hat{\mathbf{E}}_{pump} = \frac{-i\hat{\mathbf{z}}+\hat{\mathbf{y}}}{\sqrt{2}}$) and three delay times, where for each plot the arrow corresponds to the value of a line in Fig. 3.12 at the corresponding delay time (i.e. each arrow represents a different orientation of a sample with molecules all oriented similarly). The color of the arrows correlates with the value of the TRFR signal at delay times Δt (in units of the oscillation period) equal to (a) 0, (b) 0.25, (c) 0.5. Each arrow is plotted tangent to the surface of a sphere which visualizes a sample orientation where the molecular $y''z''$ plane is parallel to the sphere and the arrow points in the z''-direction of the molecular frame (double primes denote the molecular frame transformed with respect to the lab frame, where randomly selected values are used for the so-called proper Euler angles). The incoming pump and probe pulse always propagate in the x-direction of the lab frame. We conclude that for an ensemble of randomly oriented molecules a nonzero TRFR signal is obtained.

can in general be used to describe the orientation of a rigid body). Each line in Fig. 3.12 represents a different orientation of a sample with molecules all oriented similarly (where the color variation is merely intended for contrast). The total average equals half the maximum signal (i.e. for a molecule oriented perpendicular to the incoming light), confirming our statement that for an ensemble of randomly oriented $PtN_2C_8H_{12}$ molecules, a net TRFR signal will be obtained. Note that a nonzero signal will also be obtained for a linear pump pulse, but this signal will be smaller.

Fig. 3.13 is a visualization of the orientation of the sample for each of the traces in Fig. 3.12. We consider three delay times, where for each plot the color (red: maximal negative, blue: maximal positive) of an arrow correlates to the value of a line in Fig. 3.12, at the corresponding delay time (each arrow represents a different orientation of a sample with molecules all oriented similarly). We consider delay times Δt (in units of the oscillation period) equal to (a) 0, (b) 0.25, (c) 0.5. For each case, an arrow pointing from the point (1,0,0) to the original z-direction (representing a molecule with its $y''z''$ plane perpendicular to the x-direction) is transformed using the same Euler angles used to transform the sample (we use double primes for the molecular frame to distinguish it from the lab frame). Accordingly, each arrow is plotted tangent to the surface of a sphere which visualizes a sample orientation where the molecular $y''z''$ plane is parallel to the sphere and the arrow points in the z''-direction. The incoming pump and probe pulse always propagate in the x-direction of the lab frame. Molecules having their $y''z''$ plane oriented parallel to the x-direction give zero TRFR signal at all delay times (visualized by the arrows at $x = 0$). Instead, molecules having their $y''z''$ plane oriented perpendicular to the x-direction give maximal TRFR signal when Δt equals a multiple of a half period of oscillation (visualized by the arrows at $x = \pm 1$). As it should, Fig. 3.13 confirms our statement that for an ensemble of randomly oriented $PtN_2C_8H_{12}$ molecules an oscillating TRFR signal is obtained with nonzero amplitude.

It is important to realize that the molecular tumbling motion might affect the TRFR experiment. In order to obtain a nonzero TRFR signal, it is required that the orientation of the molecules at the arrival of the pump is comparable to when the probe arrives. Following Berg[81], we take as a suitable measure for the tumbling motion the mean square angular deviation as a function of the elapsed time t

$$\left\langle \Theta^2 \right\rangle = 2D_r t \tag{3.80}$$

with the rotation diffusion coefficient given by

$$D_r = \frac{kT}{f_r} \tag{3.81}$$

with f_r the rotational frictional drag coefficient. For $PtN_2C_8H_{12}$, a rotation about an axis perpendicular to the face through the center does not affect the TRFR signal, such that we should consider a parallel axis. For a disk (radius a), rotating about an axis parallel to the face through the center, the drag constant amounts

$$f_{r,disk} = \frac{32}{3}\eta a^3 \tag{3.82}$$

with η the viscosity. It turns out that for a relatively small molecule like $PtN_2C_8H_{12}$ (we assume $a = 3.75$ Å), we need an extremely viscous host fluid to keep the tumbling motion small enough. Let us as an example consider glycerol, because of its exceptional range (10 orders of magnitude) of viscosities between its glass temperature ($T_g = 190$ K) and room temperature. Between 195 and 283 K, its viscosity η can be well estimated according to the Vogel-Fulcher-Tammann-Hesse law[82]

$$\eta = \eta_0 10^{\frac{B}{T-T_0}} \tag{3.83}$$

with $\eta_0 = 7.9 \times 10^{-8}$ Pa s, $B = 1260$ K and $T_0 = 118$ K. At 195 K, we have $\eta = 1.83 \times 10^9$ Pa s. Taking the square-root of Eq. 3.80 as a measure for the angular deviation at time t, we obtain the root-mean-square value $\sqrt{\langle\Theta^2\rangle} \approx 32$ nrad for $t = 0.2$ ps (oscillation period of $\Delta\theta$ for $PtN_2C_8H_{12}$, main text Fig. 3.4), which is of the same order as the polarization rotation (up to 23 nrad, see Fig. 3.12 and main text Fig. 3.4) and will therefore strongly affect the signal. Hence, in order to perform a molecular TRFR experiment with a liquid host it would be better to take a larger molecule (such that the tumbling motion will be decreased), or one with a shorter oscillation period (such that the tumbling motion is on a longer time scale than the quantum dynamics). Probably, it is more practical to take a crystalline host, where (we have shown in this section that) the molecules of interest can have a random orientation.

Chapter 4

Proposal for time-resolved optical probing of electronic spin coherence in divacancy defects in SiC

Abstract

The Time-Resolved Faraday Rotation (TRFR) technique is an all-optical non-invasive measurement technique which can provide a measure of electron spin dynamics and is usually applied to materials with strong spin-orbit coupling. We propose for the first time to use this technique to characterize spin active color centers in materials with negligible spin-orbit coupling, like silicon carbide and diamond. The fundamentals and scenario for a TRFR experiment are here worked out for a homogeneous ensemble of c-axis divacancies in silicon carbide. We demonstrate that one of the indices of refraction of this material oscillates as a function of time in the presence of coherences. Due to this time-dependent birefringence, a probe pulse will undergo a polarization rotation as a function of the pump-probe delay time. This polarization rotation is a measure for the spin coherence of the triplet excited state.

This chapter is based on Ref. 3 on p. 177.

4.1 Introduction

The implementation of solid-state based quantum networks relies fundamentally on the possibility of initializing, manipulating and reading the information contained in a qubit[83]. Optical implementation of these operations increases the processing rates and simplify the network architecture, enabling faster and simpler circuits[84]. In this scenario, probing of the electronic spin (dynamics) based on the polarization rotation (referred to as Faraday and Kerr rotation for the case of transmission and reflection, respectively) of laser light has been extensively applied to the investigation of localized electronic states embedded in III-V and II-VI semiconductors[13, 46]. As compared to other optical techniques such as optically detected magnetic resonance and resonant absorption, these techniques have the advantage that they can preserve the coherence of the measured state[85], allowing further operations to be performed. Furthermore, since the polarization rotation measurements rely on the dispersive scattering of a large number of photons, they are less susceptible to photon losses and can usually be implemented without optical microcavities[59]. Finally, these techniques can be performed in a time-resolved manner, enabling the investigation of the time-evolution of the electronic spin with outstanding resolution.

In III-V and II-VI semiconductors, strong spin-orbit coupling (SOC) generates spin-dependent optical selection rules[9], such that the spin-state of a system is directly mapped into a shift of the polarization of a laser beam interacting with the material. In contrast, silicon carbide (SiC) and diamond, some of the most promising materials for the implementation of solid-state qubits, show negligible SOC. Nonetheless, in this theoretical work we demonstrate for SiC c-axis divacancies (missing neighboring Si and C atom along the growth axis) that the polarization of a probe pulse can also provide information about the spin-coherence in these systems due to effective selection rules that emerge from the symmetry of these localized triplet electronic states. Due to the axial symmetry of the system, the degeneracy within the ground and excited states is broken, generating a characteristic zero-field splitting (ZFS) in the absence of a magnetic field[86, 87]. If the ZFS of the ground and excited states is different, a weak magnetic field enables spin-flipping transitions with probabilities determined by the Franck-Condon factors for spin. This generates a dependency between the specific configuration of the electronic spin and the total transition probability between the ground and excited states. Accordingly, the linear susceptibility tensor (which governs the optical refractive indices) is modulated by the coherent spin precession of the system. In this way, time-resolved measurement of the polarization rotation allows for characterization of the electronic spin (dynamics) for systems with negligible SOC like many types of color centers in SiC and diamond, to which this technique has never been applied.

4.2 Fundamentals for a TRFR experiment with a homogeneous ensemble of c-axis divacancies in SiC

For a proof of principle calculation of a Time-Resolved Faraday Rotation (TRFR) experiment (Fig. 4.1) applied to color centers in SiC, we consider an ultrashort polarized pump pulse that excites a homogeneous ensemble of c-axis divacancies in SiC from their triplet ground state (after preparation in the required state)

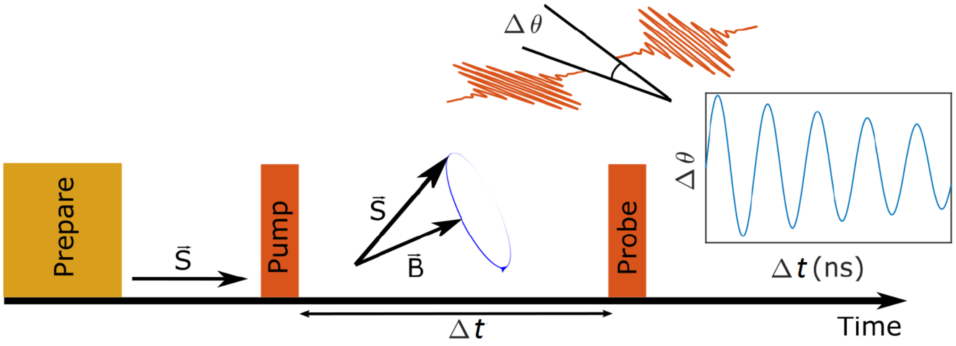

Figure 4.1: Outline of a TRFR experiment. After the sample is prepared in a certain quantum state, it gets excited by a pump pulse to a superposition of excited state sublevels. Before a probe pulse arrives, the system remains in the dark during the pump-probe delay time Δt. The change of the polarization of the probe depends on the degree of birefringence of the sample at the time it gets hit by the probe. Measuring this change (usually the polarization rotation $\Delta\theta$) as a function of Δt gives a time-resolved image of the spin dynamics of the system. For a superposition of two excited state sublevels, the TRFR signal has a single frequency. A beating of up to three frequencies (corresponding to the energy differences) can occur for a superposition of three sublevels. Decoherence is expressed by a decay of the TRFR signal as a function of time. Analogously, for a probing of ground state coherence, one should prepare the system first in the excited state in order to create and probe a superposition of ground state sublevels.

into a superposition of sublevels of their lowest triplet excited state (Fig. 4.2a). Such a superposition ($|\psi_e(t)\rangle$ in Fig. 4.2b) will show spin precession as a function of time. We will derive that in addition also one of the indices of refraction of the material oscillates with time. Hence, the polarization of an ultrashort probe pulse is affected (upon transmission), since its components experience a different real part of the refractive index[16], as is worked out in more detail in Chapter 3. Specifically, the polarization rotation $\Delta\theta$ as a function of the (pump-probe) delay time Δt (Fig. 4.1, 4.2b) is a measure for the spin dynamics in the system. For a superposition of two excited state sublevels, the TRFR signal has a single frequency. A beating of up to three frequencies (corresponding to the energy differences of the spin sublevels in the excited state) can occur for a superposition of three sublevels. Taking a detuned probe limits population transfer back to the ground state sublevels, which allows to consider dispersion only[54]. In this section (4.2) we derive for a homogeneous ensemble of SiC divacancies the fundamentals of a TRFR experiment. Although this derivation is quite general, we make in Fig. 4.2 and Section 4.3 several assumptions (like excited state coherence for two sublevels only) for the sake of simplicity.

If we assume that in SiC c-axis divacancy defects the SOC effects have negligible influence, the Hamiltonian describing the ground(excited) state is given by[86, 88, 89]

$$\begin{aligned} H_{g(e)} &= hD_{g(e)}S_z^2 + g_{g(e)}\mu_B \vec{B}\cdot\vec{S} \\ &= hD_{g(e)}S_z^2 + g_{g(e)}\mu_B(S_xB_x + S_yB_y + S_zB_z) \end{aligned} \tag{4.1}$$

where the zero-field splitting $D_{g(e)}$ is determined by the spatial distribution of the ground(excited) state. S_i is the spin S=1 operator in the i direction, $\vec{B}$ is the magnetic field, $g_{g(e)}$ is the g-factor for the ground(excited) state and μ_B is the Bohr magneton.

Due to the absence of SOC, the eigenstates of the Hamiltonian can be written as a product of a spatial part $|\chi\rangle$ and a spin state. In this way, the eigenstates of the ground (excited) state Hamiltonian are (in the basis of the total Hamiltonian in Eq. 4.1) given by $\left|\chi_{g(e)}\right\rangle|g(e)_i\rangle$, where $i = l, m, u$ correspond to the spin of lowest, median and upper energy, respectively (as illustrated in Fig. 4.2, where the orbital part is neglected). The Frank-Condon factor for spin, which determines the overlap between a sublevel i of the ground-state Hamiltonian and a sublevel j of the excited-state Hamiltonian, is given by $\langle e_j|g_i\rangle$. If the zero-field splittings for the ground and excited state are different, i.e. if $D_g \neq D_e$, all nine

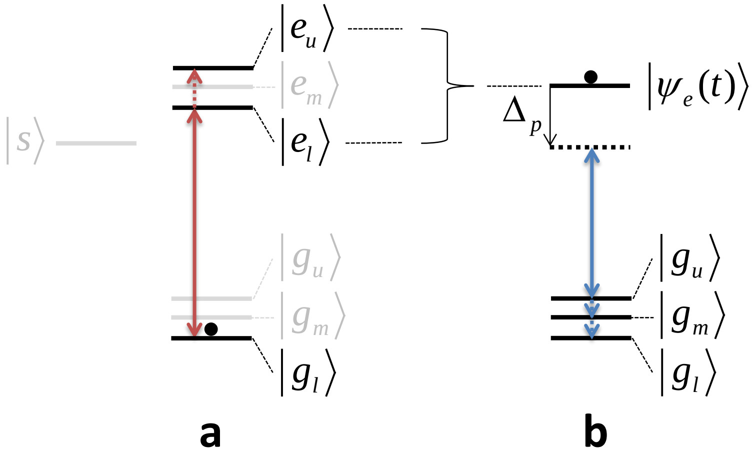

Figure 4.2: Schematic of the (de)tuning of the pump and probe pulse for a TRFR experiment with a homogeneous ensemble of c-axis divacancies in SiC. Although Section 4.2 describes the fundamentals for quite general conditions, several assumptions are made in this figure for the sake of simplicity. **a**, We assume that the system is prepared with its population only in the lowest ground state sublevel. With $\vec{B} \perp$ to the c-axis, several transitions remain forbidden, such that we can neglect $|e_m\rangle$ in this example. Just before the pump pulse (red arrow) arrives at $t = 0$, only $|g_l\rangle$ is populated, as indicated with the dot. Full absorption of a photon out of a short optical pump pulse induces the state $|\psi_e(t = 0)\rangle$, being a superposition of $|e_l\rangle$ and $|e_u\rangle$ (we neglect here the orbital part, Eq. 4.2). **b**, Directly after excitation with the pump, $|\psi_e(t)\rangle$ is populated as indicated with the dot. A linear probe pulse (blue arrow) with detuning Δ_p experiences a polarization rotation $\Delta\theta$, which oscillates as a function of the delay time Δt. This oscillation is a measure for the spin precession related to the coherence of $|\psi_e(t)\rangle$.

transitions (from the three sublevels of the ground state to the three sublevels of the excited state) are allowed, unless $\vec{B} \perp$ to the c-axis. In that special case, some transitions remain still forbidden, as derived in Supplementary Information Section 4.7 (p. 112).

Alternative non-radiative decay paths from levels $|e_j\rangle$ to $|g_i\rangle$ are possible via the intermediate singlet state $|s\rangle$[90]. This process, known as intersystem crossing (ISC) (which also occurs for nitrogen-vacancy (NV^-) centers in diamond[91]), allows for high-fidelity preparation of the initial quantum state (via a continuous wave laser which should be turned off just before the pump pulse arrives, Fig. 4.1) via preferred relaxation into $|g_l\rangle$.

For simplicity, we assume in Fig. 4.2 and Section 4.3 that (before the pump-pulse arrives) the divacancies are prepared with all the population in the lowest sublevel of the ground-state, i.e. $|\psi_{prep}\rangle = |\chi_g\rangle\, |g_l\rangle$. Also, we assume that $\vec{B} \perp$ to the c-axis, such that certain optical transitions remain forbidden. However, we will consider the general case for the following derivation of the polarization change of a probe pulse within a TRFR experiment applied to SiC with a homogeneous ensemble of c-axis divacancies.

At time $t = 0$, the system is excited by the pump-pulse which brings the divacancies into a state described by

$$|\psi_e(t=0)\rangle = |\chi_e\rangle\, (c_l\, |e_l\rangle + c_m\, |e_m\rangle + c_u\, |e_u\rangle) \tag{4.2}$$

where the normalization coefficients c_i are proportional to $\langle e_i|g_l\rangle$.

Thus, for a SiC divacancy in an excited state given by $|\psi_e(t)\rangle = \sum_i c_i(t)\, |\psi_{e,i}\rangle$, the driven coherent transition rate into the j-th eigenvector of the ground state Hamiltonian $|\psi_{g,j}\rangle$, via excitation with an optical field, is given by the Rabi frequency

$$\Omega_j = \frac{\vec{E}\cdot\vec{\mu}_{e\to j}}{\hbar} = \frac{\langle\psi_e(t)|\, \vec{E}\vec{r}\, |\psi_{g,j}\rangle}{\hbar} \tag{4.3}$$

The total transition rate into the ground state is given by

$$\begin{aligned} \Omega = \sum_j \Omega_j = \sum_j \frac{\langle\psi_e|\, \vec{E}\vec{r}\, |\psi_{g,j}\rangle}{\hbar} &= \sum_{i,j} -e \frac{\langle\chi_e|\, (E_x x + E_y y + E_z z)\, |\chi_g\rangle}{\hbar} c_i(t)\, \langle e_i|g_j\rangle \\ &= \sum_{\alpha=x,y,z} E_\alpha \frac{-e}{\hbar}\, \langle\chi_e|\, \alpha\, |\chi_g\rangle \sum_{i,j} c_i(t)\, \langle e_i|g_j\rangle = \sum_\alpha \frac{E_\alpha d^\alpha}{\hbar} \sum_{i,j} c_i(t)\, \langle e_i|g_j\rangle \end{aligned} \tag{4.4}$$

where we have defined $d^\alpha \equiv -e\, \langle\chi_e|\, \alpha\, |\chi_g\rangle$. By combining Eq. 4.3 and 4.4, we can thus write for $\mu^\alpha_{e(\to)g}$

$$\mu^\alpha_{eg} = d^\alpha \sum_{i,j} c_i(t)\, \langle e_i|g_j\rangle \tag{4.5}$$

The linear susceptibility tensor of the medium, which describes how the medium interacts with light polarized in the x, y, z directions, has components

$$\tilde{\chi}^{(1)}_{\alpha\beta} = \frac{N}{\epsilon_0 \hbar}\Big(\frac{\Delta_p - i\gamma}{\Delta_p^2 + \gamma^2}\Big)\mu^\alpha_{eg}\mu^\beta_{ge} \tag{4.6}$$

where the tilde denotes a complex number, N is the number density of defects, ϵ_0 is the vacuum permittivity, $\hbar$ is the reduced Planck's constant, Δ_p is the detuning between the driving field and the transition frequency of the system, and γ is the damping rate of the system. Substituting the transition dipole moments obtained from Eq. 4.5 into Eq. 4.6, we get

$$\tilde{\chi}^{(1)}_{\alpha\beta} = \frac{N}{\epsilon_0\hbar}\Big(\frac{\Delta_p - i\gamma}{\Delta_p^2+\gamma^2}\Big) d^{\alpha} d^{\beta *}\phi(t) \tag{4.7}$$

with the time-dependent term $\phi(t)$ defined as

$$\phi(t) = \sum_{w,v} c_w(t)\left\langle e_w|g_v\right\rangle \sum_{i,j} c_i^*(t)\left\langle g_j|e_i\right\rangle = \sum_{w} c_w(t)\left\langle e_w\right| \sum_{v,j}\left|g_v\right\rangle\left\langle g_j\right| \sum_{i} c_i^*(t)\left|e_i\right\rangle \tag{4.8}$$

We define the operator $\mathbf{O} = \sum_{v,j}\left|g_v\right\rangle\left\langle g_j\right|$, which is clearly Hermitian. In these terms, the expression for $\phi(t)$ obtained in Eq. 4.8 can be simplified as

$$\begin{aligned}\phi(t) &= \sum_{w,i} c_w(t)c_i^*(t)\left\langle e_w\right|\mathbf{O}\left|e_i\right\rangle \\ &= \sum_{i}|c_i(t)|^2\left\langle e_i\right|\mathbf{O}\left|e_i\right\rangle + \sum_{w<i}\left[c_w(t)c_i^*(t)\left\langle e_w\right|\mathbf{O}\left|e_i\right\rangle + c_w^*(t)c_i(t)\left\langle e_i\right|\mathbf{O}\left|e_w\right\rangle\right]\end{aligned} \tag{4.9}$$

Since the operator $\mathbf{O}$ is Hermitian, the term $\left\langle e_i\right|\mathbf{O}\left|e_i\right\rangle$ is real and $\left\langle e_w\right|\mathbf{O}\left|e_i\right\rangle = \left\langle e_i\right|\mathbf{O}\left|e_w\right\rangle^*$, which yields

$$\phi(t) = \sum_{i}|c_i(t)|^2 O_{ii} + \sum_{w<i}\left[O_{wi}c_w(t)c_i^*(t) + c.c.\right] \tag{4.10}$$

where we have defined $O_{ij} \equiv \left\langle e_i\right|\mathbf{O}\left|e_j\right\rangle$, and the abbreviation *c.c.* denotes the complex conjugate of $O_{wi}c_w(t)c_i^*(t)$. Thus, $\phi(t)$ is real valued, and (the second term) varies in time. Since the operator $\mathbf{O}$ is time-independent, the time-dependence of $\phi(t)$ comes directly from the time-evolution of the excited state given by $c_i(t)$.

Previous work revealed that the absorption of c-axis divacancies in SiC happens only for light polarized along the basal plane[87]. This means that if $\hat{z}$ coincides with the c-axis, $d^z = 0$, and the first-order susceptibility tensor is given by

$$\tilde{\chi}^{(1)} = \frac{N}{\epsilon_0 \hbar}\Big(\frac{\Delta_p - i\gamma}{\Delta_p^2 + \gamma^2}\Big)\phi(t)\begin{bmatrix} d^{x*}d^x & d^{x*}d^y & 0 \\ d^{y*}d^x & d^{y*}d^y & 0 \\ 0 & 0 & 0 \end{bmatrix} \tag{4.11}$$

This matrix can be diagonalized, so that in its eigenbasis $\{\hat{x}', \hat{y}', \hat{z}'\}$ it is given by

$$\tilde{\chi}^{(1)} = \frac{N}{\epsilon_0 \hbar}\Big(\frac{\Delta_p - i\gamma}{\Delta_p^2 + \gamma^2}\Big)\phi(t)\begin{bmatrix} d_0^2 & 0 & 0 \\ 0 & 0 & 0 \\ 0 & 0 & 0 \end{bmatrix} \tag{4.12}$$

where we have defined $d_0^2 = d^{x*}d^x + d^{y*}d^y$. Its eigenvectors are given by

$$\begin{aligned} \hat{x}' &= \frac{d^{x*}\hat{x} + d^{y*}\hat{y}}{d_0} \\ \hat{y}' &= \frac{-d^y\hat{x} + d^x\hat{y}}{d_0} \\ \hat{z}' &= \hat{z} \end{aligned} \tag{4.13}$$

Here we can note the difference between the case considered in this chapter compared to Chapter 3. There, the polarization selection rules for the transition to different eigenvectors of the excited state give a time-dependence specific to each component of the susceptibility tensor, implying that the eigenbasis of the susceptibility tensor is time-dependent. In contrast, in the current chapter the eigenbasis is time-independent, whereas the time-dependence for the components of $\tilde{\chi}^{(1)}$ originates from $\phi(t)$.

Once the susceptibility tensor is diagonalized, we can calculate the complex refractive indices $\tilde{n}_\alpha = \sqrt{1 + \tilde{\chi}^{(1)}_{\alpha\alpha}} \approx 1 + \tilde{\chi}^{(1)}_{\alpha\alpha}/2$ of the material in the direction of the eigenvectors of $\tilde{\chi}^{(1)}$, i.e.

$$\begin{aligned} \tilde{n}_{x'} &= 1 + \frac{N d_0^2}{2\epsilon_0 \hbar}\Big(\frac{\Delta_p - i\gamma}{\Delta_p^2 + \gamma^2}\Big)\phi(t) \\ \tilde{n}_{y'} &= 1 \\ \tilde{n}_{z'} &= 1 \end{aligned} \tag{4.14}$$

Thus, the sample functions as a birefringent plate, such that the electric field components of the probe pulse along the $\hat{z}'$ and $\hat{y}'$ directions propagate as they would in the bulk material (unaffected by divacancy transitions), while the component along the $\hat{x}'$ direction feels the presence of the divacancy defects in a time-dependent way.

The Jones matrix formalism allows us to calculate the polarization and ellipticity of an outcoming beam after it interacts with a sample whose principal axes have different refractive indices, $n_{x'}$ and $n_{y'}$. In the basis of the principal axes of the sample $\{\hat{x}', \hat{y}'\}$, the Jones matrix describing the effect of the interaction with the sample on the propagating electromagnetic field is given by

$$J_{\hat{x}',\hat{y}'} = \begin{bmatrix} e^{i\Lambda n_{x'}} & 0 \\ 0 & e^{i\Lambda n_{y'}} \end{bmatrix} \tag{4.15}$$

where $\Lambda = 2\pi d/\lambda$, with d denoting the thickness of the sample, and λ the wavelength of light. A multiplication by a common phase factor yields

$$J_{\hat{x}',\hat{y}'} = \begin{bmatrix} e^{i\Lambda\Delta n} & 0 \\ 0 & 1 \end{bmatrix} \tag{4.16}$$

where $\Delta n = n_{x'} - n_{y'}$. The matrix $T_{\hat{x},\hat{y}\to\hat{x}',\hat{y}'}$

$$T_{\hat{x},\hat{y}\to\hat{x}',\hat{y}'} = \frac{1}{d_0}\begin{bmatrix} d^{x*} & d^{y*} \\ -d^{y} & d^{x} \end{bmatrix} \tag{4.17}$$

allows us to write the Jones matrix in the $\{\hat{x}, \hat{y}\}$ basis, such that

$$\begin{aligned} J_{\hat{x},\hat{y}} =& T^{-1}_{\hat{x},\hat{y}\to\hat{x}',\hat{y}'} J_{\hat{x}',\hat{y}'} T_{\hat{x},\hat{y}\to\hat{x}',\hat{y}'} \\ J_{\hat{x},\hat{y}} =& \frac{1}{d_0^2}\begin{bmatrix} d^{x} & -d^{y*} \\ d^{y} & d^{x*} \end{bmatrix}\begin{bmatrix} e^{i\Lambda\Delta n} & 0 \\ 0 & 1 \end{bmatrix}\begin{bmatrix} d^{x*} & d^{y*} \\ -d^{y} & d^{x} \end{bmatrix} \\ J_{\hat{x},\hat{y}} =& \frac{1}{d_0^2}\begin{bmatrix} |d^{x}|^2 e^{i\Lambda\Delta n} + |d^{y}|^2 & d^{x}d^{y*}(e^{i\Lambda\Delta n} - 1) \\ d^{x*}d^{y}(e^{i\Lambda\Delta n} - 1) & |d^{y}|^2 e^{i\Lambda\Delta n} + |d^{x}|^2 \end{bmatrix} \end{aligned} \tag{4.18}$$

After interacting with the sample, the electromagnetic field is transformed such that

$$\vec{E}_{out} = J_{\hat{x},\hat{y}}\vec{E}_{in} \tag{4.19}$$

where $\vec{E}_{in}$ and $\vec{E}_{out}$ are the incoming and outcoming beam, respectively. Within the Jones formalism, the generalized electric field vector $\vec{E}_{in}$ of an incoming beam (normalized and global phase factor set to zero) in terms of the azimuth θ and the ellipticity ϵ is given by Eq. 1.2, i.e.

$$\vec{E}_{in} = E_0 \begin{bmatrix} \cos(\theta)\cos(\epsilon) - i\sin(\theta)\sin(\epsilon) \\ \sin(\theta)\cos(\epsilon) + i\cos(\theta)\sin(\epsilon) \end{bmatrix} \tag{4.20}$$

It is convenient (following the Cartesian complex-plane representation of polarized light as in [16] and analogous to Chapter 3) to define the ratio

$$\kappa = E_x/E_y \tag{4.21}$$

After substituting Eq. 4.20 and 4.18 into 4.19, one can calculate the change in the azimuth $\Delta\theta = \theta_{out} - \theta_{in}$ and the change in the ellipticity $\Delta\epsilon = \epsilon_{out} - \epsilon_{in}$ from

$$\tan 2\theta = \frac{\kappa^* + \kappa}{1 - |\kappa|^2} \tag{4.22}$$

and

$$\sin 2\epsilon = \frac{i(\kappa^* - \kappa)}{1 + |\kappa|^2} \tag{4.23}$$

respectively.

4.3 Estimating the polarization rotation of a linear probe for a TRFR experiment with c-axis divacancies in SiC

4.3.1 Assumptions and parameters

To determine whether a TRFR experiment can be applied to SiC divacancies, we will in this section calculate $\Delta\theta(\Delta t)$, i.e the polarization rotation as a function of the pump-probe delay time, based on the parameters (Table 4.1) and assumptions that we here elaborate on.

We will here consider a TRFR experiment applied to a homogeneous ensemble of c-axis divacancies (C_{3v} symmetry) in a SiC sample with thickness $d = 2$

mm and a divacancy number density of $N = 10^{16}$ cm^{-3}, based on [87]. For an inhomogeneously broadened ensemble, the TRFR signal will drop, typically proportional to $1/\sigma$, with σ the standard deviation of the inhomogeneous broadening[92]. For the initially prepared state (before the pump pulse arrives), we assume that only the lowest ground state sublevel is populated, i.e. $|\psi_{prep}\rangle = |g_l\rangle$. It is assumed that the transition dipole moments are equal for the x and y direction, i.e. $|d^x| = |d^y| = d_0/\sqrt{2}$, based on previous work showing a weak polarization dependence on the transition dipoles in the basal plane[86, 87]. We have estimated $d_0 = 6.4 \cdot 10^{-32}$ C·m, as worked out in Supplementary Information Section 4.6 (p. 111). For both the pump and probe we assume a transition wavelength of 1082 nm (corresponding to $E_e - E_g$, with $E_{g(e)}$ the ground(excited) state energy), although the probe will be slightly detuned. We take the incoming pump and probe pulse polarized along the x-direction (i.e. both having $\theta_{in} = 0$). We assume that the delay time Δt between pump and probe is taken such that $\Delta t << \omega_{ij}^{-1}$ and $\Delta t >> \omega_{eg}^{-1}$ (with $\hbar\omega_{ij} = E_{e,i} - E_{e,j}$ and $\hbar\omega_{eg} = E_e - E_g$). This ensures that the TRFR experiment will take only account of coherences between excited state sublevels (not between ground and excited state). The magnetic field is taken $B = 50$ mT, along the x-axis (perpendicular to the c-axis). This implies an excited state energy splitting $E_{e,u} - E_{e,l} \approx 1.9$ μeV (2.9 GHz angular frequency). To simultaneously address $|e_l\rangle$ and $|e_u\rangle$, we propose to use ultrashort laser pulses with an uncertainty in the photon energy given by $\sigma_{E_{ph}} > E_{e,u} - E_{e,l}$. This requires that the standard deviation of the time duration σ_t of the pulses should not exceed 0.17 ns, as follows from the time−energy uncertainty relation. It should be noted here that although any σ_t smaller than 0.17 ns satisfies the criterion of simultaneously addressing the excited state sublevels in order to cre-

Table 4.1: Parameters for a SiC divacancy TRFR experiment applied to a homogeneous ensemble of spin S=1 divacancies in SiC.

Parameter	Value
B_x ($\perp$ to c-axis)	50 mT
d	2 mm
N	10^{16} cm^{-3}
λ	1082 nm
Δ_p	-3($E_{e,u} - E_{e,l}$) = 8.7 GHz
γ	0.1 GHz
d_0	$6.4 \cdot 10^{-32}$ C·m

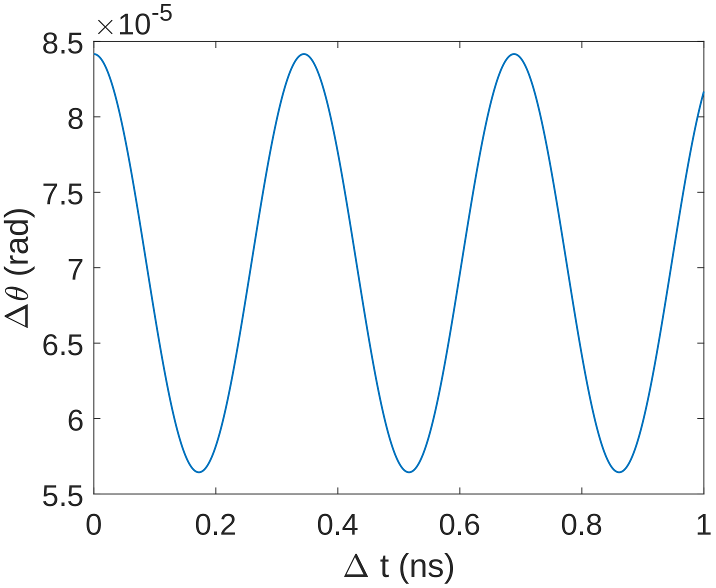

Figure 4.3: Polarization rotation $\Delta\theta$ of a probe pulse after transmission through a 2 mm SiC sample, containing a homogeneous ensemble (number density $N = 10^{16}$ cm^{-3}) of divacancies (with estimated transition dipole moment $d_0 = 6.4 \cdot 10^{-32}$ C·m. Furthermore, we consider a magnetic field along the x-axis with $B = 50$ mT, a detuning $\Delta_p = 8.7$ GHz for the probe laser, and a dephasing $\gamma = 0.1$ GHz. The incoming pump and probe pulse are linearly polarized with $\theta_{in} = 0$.

ate a superposition with the pump pulse, one should keep σ_t as close to 0.17 ns as possible in order to suppress population transfer to the ground state via the detuned probe pulse (which requires $|\Delta_p| >> |E_{e,u} - E_{e,l}|/\hbar$, which we assume to be satisfied by taking $\Delta_p = -3|E_{e,u} - E_{e,l}|/\hbar \approx -8.7$ GHz). Since most pulsed lasers have $\sigma_t << 0.17$ ns, it might (for the suppression of population transfer to the ground state) be required to use a larger magnetic field in order to increase (according to the Zeeman effect) the energy splitting $E_{e,u} - E_{e,l}$ or to take the detuning Δ_p (much) more than 3 times the sublevel splitting. We take $\gamma = 0.1$ GHz (in order to have $\Delta_p >> \gamma$). This value might be exceeded for high temperatures, but γ is in the order of MHz below 10 K[87].

4.3.2 Results and discussion

Fig. 4.3 shows the polarization rotation $\Delta\theta(\Delta t)$ (Eq. 4.22) of a linearly polarized probe pulse after transmission through a SiC sample with a homogeneous ensemble of c-axis divacancies, based on the assumptions given in Section 4.3.1.

In practice, the TRFR signal (and other oscillations) will decay as a function of (delay) time due to decoherence, which we have not taken into account in our model. Hence, the TRFR signal is to a good approximation given by the sine function $\Delta\theta = A_{\Delta\theta}\sin(\omega_{ul}\Delta t + \varphi) + b_{\Delta\theta}$, with amplitude $A_{\Delta\theta} \approx 1.4 \cdot 10^{-5}$ rad, angular frequency $\omega_{ul} = (E_{e,u} - E_{e,l})/\hbar \approx 2.9$ GHz, constant $b_{\Delta\theta} \approx 6.9 \cdot 10^{-5}$ rad, and phase $\varphi = \pi/2$ (which originate from the first and second term in Eq. 4.10, respectively).

Analogously, $\phi(t)$ (Eq. 4.10), $\Delta n(t)$ (Eq. 4.16) and the change of ellipticity $\Delta\epsilon(\Delta t)$ (Eq. 4.23) are to a good approximation sines with the same angular frequency ω_{ul} and phase φ, but different amplitudes ($A_\phi \approx 0.16$, $A_{\Delta\epsilon} \approx 1.2 \cdot 10^{-3}$ rad, $A_{\Delta n} \approx 0.2 \cdot 10^{-6}$) and constant b ($b_\phi \approx 0.84$, $b_{\Delta\epsilon} \approx 6.0 \cdot 10^{-3}$ rad, $b_{\Delta n} \approx 1.05 \cdot 10^{-6}$).

We have verified that the polarization rotation scales to a good approximation linearly with the thickness d (compare Chapter 3.9), as long as the product $\Lambda\Delta_n$ (Eq. 4.16) is small.

When the magnetic field is not taken perpendicular to the c-axis, all nine optical transitions between ground and excited state become allowed. As such, the pump pulse can induce a superposition of three excited state sublevels, which ends up as a beating of up to three frequencies in the polarization rotation $\Delta\theta(\Delta t)$ of the probe pulse (as well as in $\phi(t)$, $\Delta n(t)$ and $\Delta\epsilon(\Delta t)$).

4.4 Summary and Outlook

In SiC and diamond, SOC is weak. Nonetheless, the crystal symmetry is responsible for effective selection rules which yield a correlation between the spin-polarization of color centers and the refractive indices along the principal axes, allowing the TRFR experiment to be applied to these materials. We have worked out the fundamentals and scenario for a homogeneous ensemble of c-axis divacancies in SiC. A derivation is given for the polarization rotation of a probe pulse, induced by time-dependent birefringence. Realistic parameters and assumptions are considered, giving a polarization rotation (of the probe pulse upon transmission) of $1.4 \cdot 10^{-5}$ rad amplitude, which is well within the measurable range ($>$ nrad). If a SiC sample with an inhomogeneous ensemble of c-axis divacancies is used instead, this TRFR signal will drop, but even then it should be possible to realize a TRFR experiment[92].

4.5 Author contributions

This chapter is based on Ref. 3 on p. 177. The project was initiated by C.H.W. and C.G. Derivations, calculations and data analysis were performed by C.G., G.J.J.L and F.H. C.G and G.J.J.L. had the lead on writing the manuscript. All authors read and commented on the manuscript.

Supplementary Information (SI)

4.6 SI: Estimating the transition dipole moment of divacancies in SiC

For a monochromatic propagating wave, such as a plane wave or a Gaussian beam, the optical intensity I relates to the amplitude $|E|$ of the electric field as

$$I = \frac{c\epsilon_0 n}{2}|E|^2 \tag{4.24}$$

with c the speed of light in vacuum, ϵ_0 the vacuum permittivity, and n the refractive index.

Let us assume that our laser beam can be approximated as a Gaussian beam for which the peak intensity is given in terms of the optical power P and beam radius w as

$$I = \frac{2P}{\pi w^2} \tag{4.25}$$

Assuming that the electric field component of light is parallel to the transition dipole moment of the system of interest, the Rabi frequency (Eq. 4.3) is given by

$$\Omega = \frac{|\mu_{ij}||E|}{\hbar} \tag{4.26}$$

where μ_{ij} is the transition dipole moment related to states ψ_i and ψ_j.

From Eq. 4.24-4.26 we obtain

$$|\mu_{ij}| = \frac{\hbar}{2}\sqrt{\pi c\epsilon_0 n}\frac{\Omega w}{\sqrt{P}} \tag{4.27}$$

For a transition between the ground and (lowest) excited state of a spin S=1 SiC divacancy system, our estimate for the transition dipole moment (d_0 in the main text) is $6.4 \cdot 10^{-32}$ C·m, based on the following parameters: $n = 2.64$ corresponding to 6H-SiC at room temperature (becoming somewhat lower at cryogenic temperatures[93]), $\Omega = 7.4$ MHz, $w = 35$ μm and $P = 1$ mW, with the last three parameters based on [87].

4.7 SI: Dependency on the magnetic field angle for the optical selection rules of c-axis divacancies in SiC

The c-axis divacancy in SiC is characterized by a ground and excited state with spin 1, with addressable optical transitions and weak spin-orbit coupling. Due to this last feature, we can regard the ground(excited) state eigenvectors as a product of a spatial component (denoted by $\left|\chi_{g(e)}\right\rangle$) and a spin component ($|g(e)_i\rangle$, where $g(e)$ refers to the ground(excited) state and $i = l, m, u$ refers to the lowest, middle and upper spin eigenstates, respectively). Here, we are interested in obtaining the transition probability between ground state sublevel ($|\phi_{g,j}\rangle = |\chi_g\rangle |g_j\rangle$) and an excited state sublevel ($|\phi_{e,i}\rangle = |\chi_e\rangle |e_i\rangle$), given by $\langle\phi_{g,j}| \vec{\mu} |\phi_{e,i}\rangle$, where $\vec{\mu}$ is the electric dipole operator. Since the electric dipole operator operates on the spatial component of the electronic wavefunction, we can rewrite

$$\langle\phi_{g,j}| \vec{\mu} |\phi_{e,i}\rangle = \langle\chi_g| \vec{\mu} |\chi_e\rangle \langle g_j|e_i\rangle \tag{4.28}$$

which shows that the transition probability between a ground and excited state sublevel is proportional to the overlap of the spin wavefunctions, $\langle e_i|g_j\rangle$. In order to calculate this overlap as a function of magnetic field, we refer to the spin Hamiltonian describing the ground(excited) state of the c-axis divacancy defect in SiC under the action of a magnetic field, i.e.

$$H_{g(e)} = hD_{g(e)}S_z^2 + g_{g(e)}\mu_B(S_xB_x + S_yB_y + S_zB_z) \tag{4.29}$$

where h is Planck's constant, D is the zero field splitting (ZFS), S_i and B_i denote the Cartesian components of the spin-1 operator and the magnetic field, respectively. The $\hat{z}$ axis is defined by the symmetries of the crystal and coincides with the c-axis.

In the absence of a magnetic field, the Hamiltonian is given by the ZFS term alone, whose eigenvectors are given by the eigenvectors of the operator S_z^2. Thus, the spin eigenvectors in the ground and excited states coincide, despite the ZFS constant D taking on different values. In this case, the overlap of the spin eigenfunctions in ground and excited states is given by

$$\langle g_j | e_i \rangle = \delta_{ij} \tag{4.30}$$

where δ_{ij} denotes the Kronecker delta. This means that only direct transitions ($|\phi_{e,i}\rangle \leftrightarrow |\phi_{g,i}\rangle$) are allowed. The same occurs if a magnetic field is applied along the $\hat{z}$ direction. In this case, the eigenvectors of both ground and excited states coincide with the eigenvectors of the operator S_z.

In contrast, if a magnetic field is applied at an angle with the c-axis, the sublevels of the ground(excited) state spin Hamiltonian are given by the eigenvectors of Eq. 4.29. In the basis $\{|+\rangle, |0\rangle, |-\rangle\}$ given by the eigenvectors of S_z (where $\hat{z}$ coincides with the crystal c-axis), this operator can be written in matrix form as

$$H_{g(e)} = \begin{bmatrix} hD_{g(e)} + g_{g(e)}\mu_B B\cos(\theta) & g_{g(e)}\mu_B B\sin(\theta) & 0 \\ g_{g(e)}\mu_B B\sin(\theta) & 0 & g_{g(e)}\mu_B B\sin(\theta) \\ 0 & g_{g(e)}\mu_B B\sin(\theta) & hD_{g(e)} - g_{g(e)}\mu_B B\cos(\theta) \end{bmatrix} \tag{4.31}$$

Here we assume that the magnetic field makes an angle θ with the crystal c-axis, and its component along the $\hat{y}$ axis is zero. This last assumption is allowed due to the symmetry of the defect. For a general θ different from 0 (i.e. for a magnetic field non-collinear with the c-axis), the eigenvectors of this operator depend on the value of the ZFS constant $D_{g(e)}$, such that the eigenvectors of ground and excited state Hamiltonians differ. In this case, the overlap between sublevels of ground and excited state $\langle g_j | e_i \rangle \neq \delta_{ij}$, and diagonal transitions ($|\phi_{g,j}\rangle \leftrightarrow |\phi_{e,i}\rangle$, for $i \neq j$) are allowed for arbitrary i and j.

We note finally the case of a magnetic field perpendicular to the crystal c-axis (parallel to the basal plane). In this case the angle is $\theta = \pi/2$ and the Hamiltonian given in Eq. 4.31 becomes

$$H_{g(e)} = \begin{bmatrix} hD_{g(e)} & g_{g(e)}\mu_B B & 0 \\ g_{g(e)}\mu_B B & 0 & g_{g(e)}\mu_B B \\ 0 & g_{g(e)}\mu_B B & hD_{g(e)} \end{bmatrix} \tag{4.32}$$

The lowest and upper eigenvectors of this operator depend on the value of $D_{g(e)}$ and are thus given by different vectors in ground and excited states. However, the middle eigenvector of this operator is given by $|g(e)_m\rangle = (|+\rangle - |-\rangle)/\sqrt(2)$ (which is an eigenvector of S_x and S_z^2), regardless of the value of $D_{g(e)}$ or $g_{g(e)}$.

Thus, this eigenvector is the same in the ground and excited states, i.e. $|g_m\rangle = |e_m\rangle$. Within ground and excited states, the eigenvectors of the Hamiltonian are orthogonal to each other (since $\langle g_m|g_{l,u}\rangle = 0$ and $\langle e_m|e_{l,u}\rangle = 0$). This means that $\langle e_m|g_{l,u}\rangle = \langle g_m|e_{l,u}\rangle = 0$. Thus, although diagonal transitions between the lower and upper sublevels of ground and excited states are allowed ($|\phi_{e,l}\rangle \leftrightarrow |\phi_{g,u}\rangle$ and $|\phi_{g,l}\rangle \leftrightarrow |\phi_{e,u}\rangle$), diagonal transitions into or out of $|g_m\rangle$ and $|e_m\rangle$ are forbidden.

We consider then a pump pulse used to excite the c-axis divacancies. Just before the pulse arrives in the sample, the population is entirely in the lowest level of the ground state. Since the overlap between the lowest level of the ground state and the middle level of the excited state is zero, the pump pulse is only able to excite population into the lowest and upper levels of the excited state. Thus, in this case the only relevant coherence in the system after the pump pulse arrives is the coherence between the lowest and upper levels of the excited state, such that only one characteristic frequency is present.

In contrast, if the magnetic field is applied at an angle $\theta \neq 0, \pi/2$, all optical transitions are allowed. In this case, population from the lowest level of the ground state can be excited into all three levels of the excited state. Thus, after the pump pulse arrives in the sample, all three sublevels of the excited state are populated, and the coherences in the system are characterized by three oscillating frequencies corresponding to the three energy differences between the sublevels of the excited state.

Chapter 5

Identification and tunable optical coherent control of transition-metal spins in silicon carbide

Abstract

Color centers in wide-bandgap semiconductors are attractive systems for quantum technologies since they can combine long-coherent electronic spin and bright optical properties. Several suitable centers have been identified, most famously the nitrogen-vacancy defect in diamond. However, integration in communication technology is hindered by the fact that their optical transitions lie outside telecom wavelength bands. Several transition-metal impurities in silicon carbide do emit at and near telecom wavelengths, but knowledge about their spin and optical properties is incomplete. We present all-optical identification and coherent control of molybdenum-impurity spins in silicon carbide with transitions at near-infrared wavelengths. Our results identify spin $S = 1/2$ for both the electronic ground and excited state, with highly anisotropic spin properties that we apply for implementing optical control of ground-state spin coherence. Our results show optical lifetimes of $\sim$60 ns and inhomogeneous spin dephasing times of $\sim$0.3 μs, establishing relevance for quantum spin-photon interfacing.

This chapter is based on Ref. 4 on p. 177.

5.1 Introduction

Electronic spins of lattice defects in wide-bandgap semiconductors have come forward as an important platform for quantum technologies[94], in particular for applications that require both manipulation of long-coherent spin and spin-photon interfacing via bright optical transitions. In recent years this field showed strong development, with demonstrations of distribution and storage of non-local entanglement in networks for quantum communication[95–99], and quantum-enhanced field-sensing[100–104]. The nitrogen-vacancy defect in diamond is the material system that is most widely used[105, 106] and best characterized[107–109] for these applications. However, its zero-phonon-line (ZPL) transition wavelength (637 nm) is not optimal for integration in standard telecom technology, which uses near-infrared wavelength bands where losses in optical fibers are minimal. A workaround could be to convert photon energies between the emitter-resonance and telecom values[110–112], but optimizing these processes is very challenging.

This situation has been driving a search for similar lattice defects that do combine favorable spin properties with bright emission directly at telecom wavelength. It was shown that both diamond and silicon carbide (SiC) can host many other spin-active color centers that could have suitable properties[113–116] (where SiC is also an attractive material for its established position in the semiconductor device industry[117, 118]). However, for many of these color centers detailed knowledge about the spin and optical properties is lacking. In SiC the divacancy[86, 119, 120] and silicon vacancy[103, 121–123] were recently explored, and these indeed show millisecond homogeneous spin coherence times with bright ZPL transitions closer to the telecom band.

We present here a study of transition-metal impurity defects in SiC, which exist in great variety[89, 124–128]. There is at least one case (the vanadium impurity) that has ZPL transitions at telecom wavelengths[125], around 1300 nm, but we focus here (directed by availability of lasers in our lab) on the molybdenum impurity with ZPL transitions at 1076 nm (in 4H-SiC) and 1121 nm (in 6H-SiC), which turns out to be a highly analogous system. Theoretical investigations[129], early electron paramagnetic resonance[125, 130] (EPR), and photoluminescence (PL) studies[131–133] indicate that these transition-metal impurities have promising properties. These studies show that they are deep-level defects that can be in several stable charge states, each with a distinctive value for its electronic spin S and near-infrared optical transitions. Further tuning and engineering possibilities come from the fact that these impurities can be embedded in a variety of SiC polytypes (4H, 6H, etc., see Fig. 1a). Recent work by Koehl *et al.*[128] studied chromium impurities in 4H-SiC using optically detected magnetic resonance. They identified efficient ZPL (little phonon-sideband) emission at 1042 nm and 1070 nm, and their charge state as neutral with an electronic spin $S = 1$ for the ground state.

Our work is an all-optical study of ensembles of molybdenum impurities in p-type 4H-SiC and 6H-SiC material. The charge and spin configuration of these impurities, and the defect configuration in the SiC lattice that is energetically favored, was until our work not yet identified with certainty. Our results show that these Mo impurities are in the $\mathrm{Mo}^{5+}(4\mathrm{d}^1)$ charge state (we follow here conventional notation[125]: the label 5+ indicates that of an original Mo atom 4 electrons participate in bonds with SiC and that 1 electron is transferred to the p-type lattice environment). The single remaining electron in the 4d shell gives spin $S = 1/2$ for the ground state and optically excited state that we address. While we will show later that this can be concluded from our measurements, we assume it as a fact from the beginning since this simplifies the explanation of our experimental approach.

In addition to this identification of the impurity properties, we explore whether ground-state spin coherence is compatible with optical control. Using a two-laser magneto-spectroscopy method[86, 134, 135], we identify the spin Hamiltonian of the $S = 1/2$ ground state and optically excited state, which behave as doublets with highly anisotropic Landé g-factors. This gives insight in how a situation with only spin-conserving transitions can be broken, and we find that we can use a weak magnetic field to enable optical transitions from both ground-state spin levels to a common excited-state level (Λ level scheme). Upon two-laser driving of such Λ schemes, we observe coherent population trapping (CPT, all-optical control of ground-state spin coherence and fundamental to operating quantum memories[15, 136]). The observed CPT reflects inhomogeneous spin dephasing times comparable to that of the SiC divacancy[86, 87] (near 1 μs).

In what follows, we first present our methods and results of single-laser spectroscopy performed on ensembles of Mo impurities in both SiC polytypes. Next, we discuss a two-laser method where optical spin pumping is detected. This allows for characterizing the spin sublevels in the ground and excited state, and we demonstrate how this can be extended to controlling spin coherence.

Both the 6H-SiC and 4H-SiC (Fig. 1a) samples were intentionally doped with Mo. There was no further intentional doping, but near-band-gap photoluminescence revealed that both materials had p-type characteristics. The Mo concentrations in the 4H and 6H samples were estimated[132, 133] to be in the range 10^{15}-10^{17} cm^{-3} and 10^{14}-10^{16} cm^{-3}, respectively. The samples were cooled in a liquid-helium flow cryostat with optical access, which was equipped with a superconducting magnet system. The setup geometry is depicted in Fig. 1b. The angle ϕ between the direction of the magnetic field and the c-axis of the crystal could be varied, while both of these directions were kept orthogonal to the propagation direction of excitation laser beams. In all experiments where we resonantly addressed ZPL transitions the laser fields had linear polarization, and we always kept the direction of the linear polarization parallel to the c-axis. Earlier studies[129, 132, 133] of these materials showed that the ZPL transition dipoles are parallel to the c-axis. For our experiments we confirmed that the photoluminescence response was clearly the strongest for excitation with linear polarization parallel to the c-axis, for all directions and magnitudes of the magnetic fields that we applied. All results presented in this work come from photoluminescence (PL) or photoluminescence-excitation (PLE) measurements. The excitation lasers were focused to a ∼100 μm spot in the sample. PL emission was measured from the side. A more complete description of experimental aspects is presented in the Methods section.

5.2 Materials and experimental methods

Both the 6H-SiC and 4H-SiC (Fig. 5.1a) samples were intentionally doped with Mo. There was no further intentional doping, but near-band-gap photoluminescence revealed that both materials had p-type characteristics. The Mo concentrations in the 4H and 6H samples were estimated[132, 133] to be in the range 10^{15}-10^{17} cm^{-3} and 10^{14}-10^{16} cm^{-3}, respectively. The samples were cooled in a liquid-helium flow cryostat with optical access, which was equipped with a superconducting magnet system. The setup geometry is depicted in Fig. 5.1b. The angle ϕ between the direction of the magnetic field and the c-axis of the crystal could be varied, while both of these directions were kept orthogonal to the propagation direction of excitation laser beams. In all experiments where we resonantly addressed ZPL transitions the laser fields had linear polarization, and we always kept the direction of the linear polarization parallel to the c-axis (our work and earlier studies[132, 133] of these materials showed that the ZPL transition dipoles are parallel to the c-axis). All results presented in this work come from photoluminescence (PL) or photoluminescence-excitation (PLE) measurements. The excitation lasers were focused to a ∼100 μm spot in the sample. PL emission was

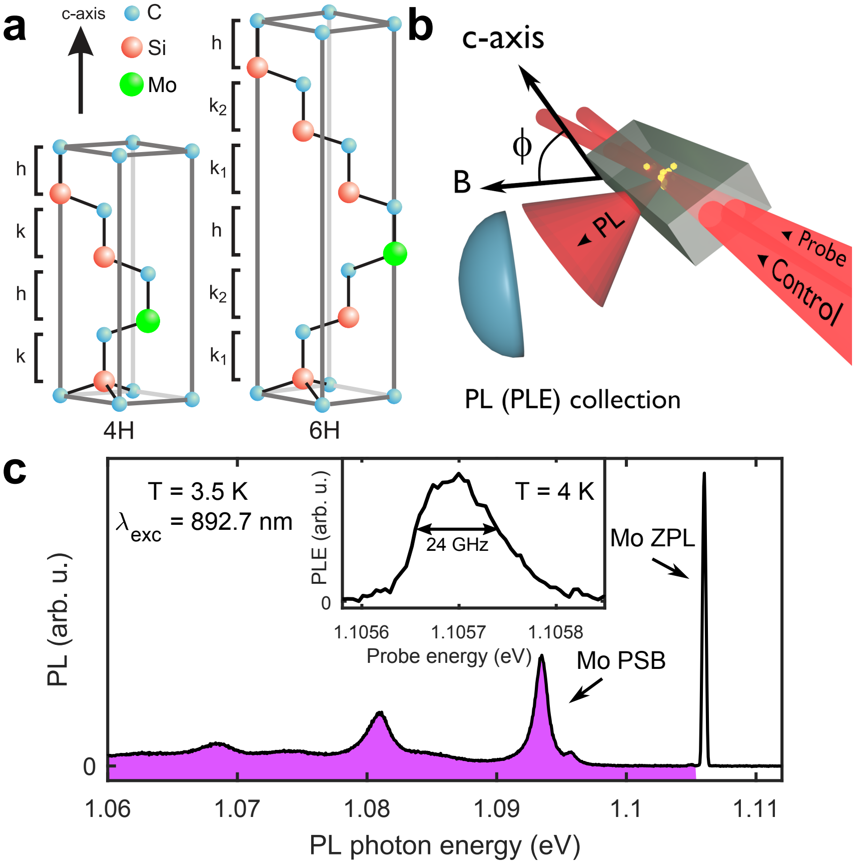

Figure 5.1: Crystal structures of SiC, setup schematic and optical signatures of Mo in 6H-SiC. a, Schematic illustration of the stacking of Si-C bilayers in the crystal structure of the 4H-SiC and 6H-SiC polytypes, which gives lattice sites with cubic and hexagonal local environment labeled by $k_{(1,2)}$ and h, respectively. Our work revisits the question whether Mo impurities are present as substitutional atoms or residing inside Si-C divacancies. The c-axis coincides with the growth direction. **b**, Schematic of SiC crystal in the setup. The crystal is placed in a cryostat with optical access. Laser excitation beams are incident on a side facet of the SiC crystal and propagate along the optical axis (see label), normal to the c-axis. Magnetic fields **B** are applied in a direction orthogonal to the optical axis and at angle ϕ with the c-axis. Photoluminescence (PL) is detected out of another side facet of the SiC crystal. **c**, PL from Mo in 6H-SiC at 3.5 K and zero field, resulting from excitation with an 892.7 nm laser, with labels identifying the zero-phonon-line (ZPL, at 1.1057 eV) emission and phonon replicas (shaded and labeled as phonon sideband, PSB). The inset shows the ZPL as measured by photoluminescence excitation (PLE). Here, the excitation laser is scanned across the ZPL peak and emission from the PSB is used for detection.

measured from the side. A more complete description of experimental aspects is presented in the Methods section.

5.3 Single-laser characterization

For initial characterization of Mo transitions in 6H-SiC and 4H-SiC we used PL and PLE spectroscopy (see Methods). Figure 5.1c shows the PL emission spectrum of the 6H-SiC sample at 3.5 K, measured using an 892.7 nm laser for excitation. The ZPL transition of the Mo defect visible in this spectrum will be studied in detail throughout this work. The shaded region indicates the emission of phonon replicas related to this ZPL[132, 133]. While we could not perform a detailed analysis, the peak area of the ZPL in comparison with that of the phonon replicas indicates that the ZPL carries clearly more than a few percent of the full PL emission. Similar PL data from Mo in the 4H-SiC sample, together with a study of the temperature dependence of the PL, can be found in the Supplementary Information (Fig. 5.6) (p. 132).

For a more detailed study of the ZPL of the Mo defects, PLE was used. In PLE measurements, the photon energy of a narrow-linewidth excitation laser is scanned across the ZPL part of the spectrum, while resulting PL of phonon-sideband (phonon-replica) emission is detected (Fig. 5.1b, we used filters to keep light from the excitation laser from reaching the detector, see Methods). The inset of Fig. 5.1c shows the resulting ZPL for Mo in 6H-SiC at 1.1057 eV (1121.3 nm). For 4H-SiC we measured the ZPL at 1.1521 eV (1076.2 nm, see Supplementary Information). Both are in close agreement with literature[132, 133]. Temperature dependence of the PLE from the Mo defects in both 4H-SiC and 6H-SiC can be found in the Supplementary Information (Fig. 5.7) (p. 133).

The width of the ZPL is governed by the inhomogeneous broadening of the electronic transition throughout the ensemble of Mo impurities, which is typically caused by nonuniform strain in the crystal. For Mo in 6H-SiC we observe a broadening of 24±1 GHz FWHM, and 23±1 GHz for 4H-SiC. This inhomogeneous broadening is larger than the anticipated electronic spin splittings[125], and it thus masks signatures of spin levels in optical transitions between the ground and excited state.

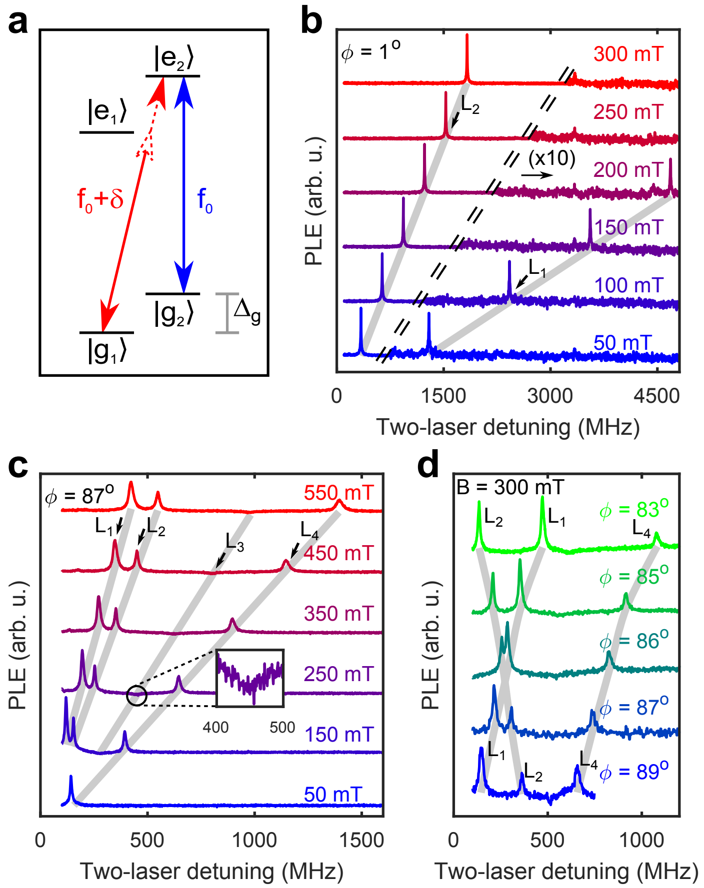

Figure 5.2: Two-laser spectroscopy results for Mo in 6H-SiC. **a**, Working principle of two-laser spectroscopy: one laser at frequency f_0 is resonant with the $|g_2\rangle$-$|e_2\rangle$ transition, the second laser is detuned from the first laser by δ. If δ is such that the second laser becomes resonant with another transition (here sketched for $|g_1\rangle$-$|e_2\rangle$) the photoluminescence will increase since optical spin-pumping by the first laser is counteracted by the second and vice versa. **b-d**, Photoluminescence excitation (PLE) signals as function of two-laser detuning at 4 K. **b**, Magnetic field dependence with field parallel to the c-axis ($\phi = 1°$). For clarity, data in the plot have been magnified by a factor 10 right from the dashed line. Two peaks are visible, labeled L_1 and L_2 (the small peak at 3300 MHz is an artefact from the Fabry-Pérot interferometer in the setup). **c**, Magnetic field dependence with the field nearly perpendicular to the c-axis ($\phi = 87°$). Three peaks and a dip (enlarged in the inset) are visible. These four features are labeled L_1 through L_4. The peak positions as a function of field in **b-c** coincide with straight lines through the origin (within 0.2% error). **d**, Angle dependence of the PLE signal at 300 mT. Peaks L_1 and L_4 move to the left with increasing angle, whereas L_2 moves to the right. The data in **b-d** are offset vertically for clarity.

5.4 Two-laser characterization

In order to characterize the spin-related fine structure of the Mo defects, a two-laser spectroscopy technique was employed[86, 134, 135]. We introduce this for the four-level system sketched in Fig. 5.2a. A laser fixed at frequency f_0 is resonant with one possible transition from ground to excited state (for the example in Fig. 5.2a $|g_2\rangle$ to $|e_2\rangle$), and causes PL from a sequence of excitation and emission events. However, if the system decays from the state $|e_2\rangle$ to $|g_1\rangle$, the laser field at frequency f_0 is no longer resonantly driving optical excitations (the system goes dark due to optical pumping). In this situation, the PL is limited by the (typically long) lifetime of the $|g_1\rangle$ state. Addressing the system with a second laser field, in frequency detuned from the first by an amount δ, counteracts optical pumping into off-resonant energy levels if the detuning δ equals the splitting Δ_g between the ground-state sublevels. Thus, for specific two-laser detuning values corresponding to the energy spacings between ground-state and excited-state sublevels the PL response of the ensemble is greatly increased. Notably, this technique gives a clear signal for sublevel splittings that are smaller than the inhomogeneous broadening of the optical transition, and the spectral features now reflect the homogeneous linewidth of optical transitions[86, 87].

In our measurements a 200 μW continuous-wave control and probe laser were made to overlap in the sample. For investigating Mo in 6H-SiC the control beam was tuned to the ZPL at 1121.32 nm ($f_{\text{control}} = f_0 = 267.3567$ THz), the probe beam was detuned from f_0 by a variable detuning δ (*i.e.* $f_{\text{probe}} = f_0 + \delta$). In addition, a 100 μW pulsed 770 nm re-pump laser was focused onto the defects to counteract bleaching of the Mo impurities due to charge-state switching[86, 137, 138] (which we observed to only occur partially without re-pump laser). All three lasers were parallel to within 3° inside the sample. A magnetic field was applied to ensure that the spin sublevels were at non-degenerate energies. Finally, we observed that the spectral signatures due to spin show strong broadening above a temperature of ~10 K, and we thus performed measurements at 4 K (unless stated otherwise).

Figure 5.2b shows the dependence of the PLE on the two-laser detuning for the 6H-SiC sample (4H-SiC data in Supplementary Information Fig. 5.10 (p. 137)), for a range of magnitudes of the magnetic field (here aligned close to parallel with the c-axis, $\phi = 1°$). Two emission peaks can be distinguished, labeled line L_1 and L_2. The emission (peak height) of L_2 is much stronger than that of L_1. Figure 5.2c shows the results of a similar measurement with the magnetic field nearly orthogonal to the crystal c-axis ($\phi = 87°$), where four spin-related emission signatures are visible, labeled as lines L_1 through L_4 (a very small peak feature left from L_1, at half its detuning, is an artifact that occurs due to a leakage effect in the spectral filtering that is used for beam preparation, see Methods). The two-laser detuning frequencies corresponding to all four lines emerge from the origin ($\mathbf{B} = 0$, $\delta = 0$) and evolve linearly with magnetic field (we checked this up to 1.2 T). The slopes of all four lines (in Hertz per Tesla) are smaller in Fig. 5.2c than in Fig 5.2b. In contrast to lines L_1, L_2 and L_4, which are peaks in the PLE spectrum, L_3 shows a dip.

In order to identify the lines at various angles ϕ between the magnetic field and the c-axis, we follow how each line evolves with increasing angle. Figure 5.2d shows that as ϕ increases, L_1, L_3, and L_4 move to the left, whereas L_2 moves to the right. Near 86°, L_2 and L_1 cross. At this angle, the left-to-right order of the emission lines is swapped, justifying the assignment of L_1, L_2, L_3 and L_4 as in Fig. 5.2b,c. The Supplementary Information presents further results from two-laser magneto-spectroscopy at intermediate angles ϕ (section 5.12a (p. 133)).

5.5 Analysis

We show below that the results in Fig. 5.2 indicate that the Mo impurities have electronic spin $S = 1/2$ for the ground and excited state. This contradicts predictions and interpretations of initial results[125, 129, 132, 133]. Theoretically, it was predicted that the defect associated with the ZPL under study here is a Mo impurity in the asymmetric split-vacancy configuration (Mo impurity asymmetrically located inside a Si-C divacancy), where it would have a spin $S = 1$ ground state with zero-field splittings of about 3 to 6 GHz[125, 129, 132, 133]. However, this would lead to the observation of additional emission lines in our measurements. Particularly, in the presence of a zero-field splitting, we would expect to observe two-laser spectroscopy lines emerging from a nonzero detuning[86]. We have measured near zero fields and up to 1.2 T, as well as up to 21 GHz detuning (Supplementary Information section 5.12b (p. 133)), but found no more peaks than the four present in Fig. 5.2c. A larger splitting would have been visible as a splitting of the ZPL in measurements as presented in the inset of Fig. 5.1c, which was not observed in scans up to 1000 GHz. Additionally, a zero-field splitting and corresponding avoided crossings at certain magnetic fields would result in curved behavior for the positions of lines in magneto-spectroscopy. Thus, our observations rule out that there is a zero-field splitting for the ground-state and excited-state spin sublevels. In this case the effective spin-Hamiltonian[139] can only take the form of a Zeeman term

$$H_{g(e)} = \mu_B g_{g(e)} \mathbf{B} \cdot \tilde{\mathbf{S}} \tag{5.1}$$

where $g_{g(e)}$ is the g-factor for the electronic ground (excited) state (both assumed positive), μ_B the Bohr magneton, $\mathbf{B}$ the magnetic field vector of an externally applied field, and $\tilde{\mathbf{S}}$ the effective spin vector. The observation of four emission lines can be explained, in the simplest manner, by a system with spin $S = 1/2$ (doublet) in both the ground and excited state.

For such a system, Fig. 5.3 presents the two-laser optical pumping schemes that correspond to the observed emission lines L_1 through L_4. Addressing the system with the V-scheme excitation pathways from Fig. 5.3c leads to increased pumping into a dark ground-state sublevel, since two excited states contribute to decay into the off-resonant ground-state energy level while optical excitation out of the other ground-state level is enhanced. This results in reduced emission observed as the PLE dip feature of L_3 in Fig. 5.2c (for details see Supplementary Information section 5.15 (p.140)).

We find that for data as in Fig. 5.2c the slopes of the emission lines are correlated by a set of sum rules

$$\Theta_{L3} = \Theta_{L1} + \Theta_{L2} \tag{5.2}$$

$$\Theta_{L4} = 2\Theta_{L1} + \Theta_{L2} \tag{5.3}$$

Here Θ_{Ln} denotes the slope of emission line L_n in Hertz per Tesla. The two-laser detuning frequencies for the pumping schemes in Fig. 5.3a-d are related in the same way, which justifies the assignment of these four schemes to the emission lines L_1 through L_4, respectively. These schemes and equations directly yield the g-factor values g_g and g_e for the ground and excited state (Supplementary Information section 5.12 (p. 133)).

We find that the g-factor values g_g and g_e strongly depend on ϕ, that is, they are highly anisotropic. While this is in accordance with earlier observations for transition metal defects in SiC[125], we did not find a comprehensive report on the underlying physical picture. In Supplementary Information section 5.17 (p. 144) we present a group-theoretical analysis that explains the anisotropy $g_g \approx 1.7$ for $\phi = 0°$ and $g_g = 0$ for $\phi = 90°$, and similar behavior for g_e (which we also use to identify the orbital character of the ground and excited state). In this scenario the effective Landé g-factor[139] is given by

$$g(\phi) = \sqrt{\left(g_{\parallel} \cos\phi\right)^2 + \left(g_{\perp} \sin\phi\right)^2} \tag{5.4}$$

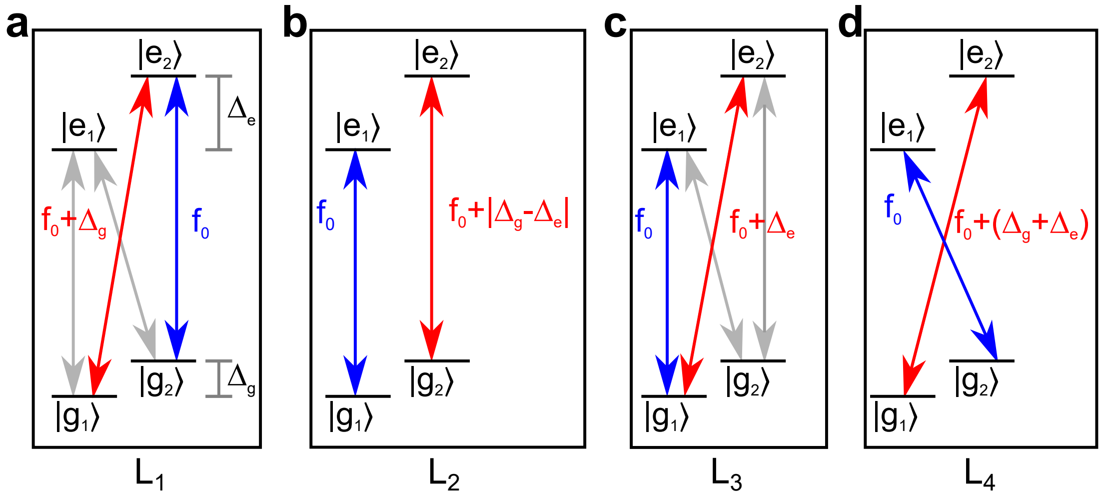

Figure 5.3: Two-laser pumping schemes with optical transitions between $S = 1/2$ ground and excited states. **a**, Λ scheme, responsible for L_1 emission feature: Two lasers are resonant with transitions from both ground states $|g_1\rangle$ (red arrow) and $|g_2\rangle$ (blue arrow) to a common excited state $|e_2\rangle$. This is achieved when the detuning equals the ground-state splitting Δ_g. The gray arrows indicate a secondary Λ scheme via $|e_1\rangle$ that is simultaneously driven in an ensemble when it has inhomogeneous values for its optical transition energies. **b**, Π scheme, responsible for L_2 emission feature: Two lasers are resonant with both vertical transitions. This is achieved when the detuning equals the difference between the ground-state and excited-state splittings, $|\Delta_g - \Delta_e|$. **c**, V scheme, responsible for L_3 emission feature: Two lasers are resonant with transitions from a common ground state $|g_1\rangle$ to both excited states $|e_1\rangle$ (blue arrow) and $|e_2\rangle$ (red arrow). This is achieved when the laser detuning equals the excited state splitting Δ_e. The gray arrows indicate a secondary V scheme that is simultaneously driven when the optical transition energies are inhomogeneously broadened. **d**, X scheme, responsible for the L_4 emission feature: Two lasers are resonant with the diagonal transitions in the scheme. This is achieved when the detuning is equal to the sum of the ground-state and the excited-state splittings, $(\Delta_g + \Delta_e)$.

where $g_{\parallel}$ represents the component of g along the c-axis of the silicon carbide structure and $g_{\perp}$ the component in the basal plane. Figure 5.4 shows the ground and excited state effective g-factors extracted from our two-laser magnetospectroscopy experiments for 6H-SiC and 4H-SiC (additional experimental data can be found in the Supplementary Information). The solid lines represent fits to the equation (5.4) for the effective g-factor. The resulting $g_{\parallel}$ and $g_{\perp}$ parameters are given in table 5.1.

The reason why diagonal transitions (in Fig. 5.3 panels a,c), and thus the

Table 5.1: Components of the g-factors for the spin of Mo impurities in SiC

	$g_{\|}$	$g_{\perp}$
4H-SiC		
ground state	1.87 ± 0.2	0.04 ± 0.04
excited state	1.39 ± 0.2	0.10 ± 0.02
6H-SiC		
ground state	1.61 ± 0.02	0.000 ± 0.004
excited state	1.20 ± 0.02	0.11 ± 0.02

Λ and V scheme are allowed, lies in the different behavior of g_e and g_g. When the magnetic field direction coincides with the internal quantization axis of the defect, the spin states in both the ground and excited state are given by the basis of the S_z operator, where the z-axis is defined along the c-axis. This means that the spin-state overlap for vertical transitions, *e.g.* from $|g_1\rangle$ to $|e_1\rangle$, is unity. In such cases, diagonal transitions are forbidden as the overlap between *e.g.* $|g_1\rangle$ and $|e_2\rangle$ is zero. Tilting the magnetic field away from the internal quantization axis introduces mixing of the spin states. The amount of mixing depends on the g-factor, such that it differs for the ground and excited state. This results in a tunable non-zero overlap for all transitions, allowing all four schemes to be observed (as in Fig. 5.2b where $\phi = 87°$). This reasoning also explains the suppression of all emission lines except L_2 in Fig. 5.2b, where the magnetic field is nearly along the c-axis. A detailed analysis of the relative peak heights in Fig. 5.2b-c compared to wave function overlap can be found in the Supplementary Information (section 5.14 (p. 138)).

5.6 Coherent Population Trapping

The Λ driving scheme depicted in Fig. 5.3a, where both ground states are coupled to a common excited state, is of particular interest. In such cases it is possible to achieve all-optical coherent population trapping (CPT)[15], which is of great significance in quantum-optical operations that use ground-state spin coherence. This phenomenon occurs when two lasers address a Λ system at exact two-photon resonance, *i.e.* when the two-laser detuning matches the ground-state splitting. The ground-state spin system is then driven towards a superposition state that

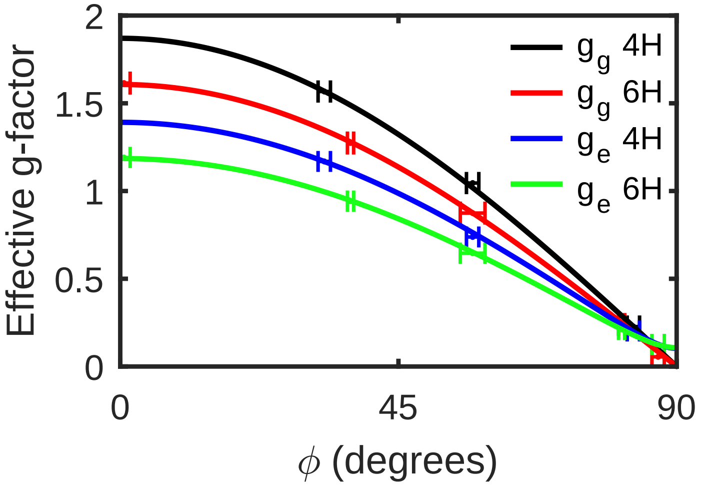

Figure 5.4: Effective g-factors for the spin of Mo impurities in SiC. Angular dependence of the g-factor for the $S = 1/2$ ground (g_g) and excited states (g_e) of the Mo impurity in 4H-SiC and 6H-SiC. The solid lines indicate fits of equation (5.4) to the data points extracted from two-laser magneto-spectroscopy measurements as in Fig. 5.2b,c.

approaches $|\Psi_{CPT}\rangle \propto \Omega_2 |g_1\rangle - \Omega_1 |g_2\rangle$ for ideal spin coherence. Here Ω_n is the Rabi frequency for the driven transition from the $|g_n\rangle$ state to the common excited state. Since the system is now coherently trapped in the ground state, the photoluminescence decreases.

In order to study the occurrence of CPT, we focus on the two-laser PLE features that result from a Λ scheme. A probe field with variable two-laser detuning relative to a fixed control laser was scanned across this line in frequency steps of 50 kHz, at 200 μW. The control laser power was varied between 200 μW and 5 mW. This indeed yields signatures of CPT, as presented in Fig. 5.5. A clear power dependence is visible: when the control beam power is increased, the depth of the CPT dip increases (and can fully develop at higher laser powers or by concentrating laser fields in SiC waveguides[87]). This observation of CPT also confirms our earlier interpretation of lines L_1-L_4, in that it confirms that L_1 results from a Λ scheme.

Using a standard model for CPT[15], adapted to account for strong inhomogeneous broadening of the optical transitions[87] (see also Supplementary Information section 5.16 (p. 143)) we extract an inhomogeneous spin dephasing time T_2^* of 0.32 ± 0.08 μs and an optical lifetime of the excited state of 56 ± 8 ns. The optical life time is about a factor two longer than that of the nitrogen-

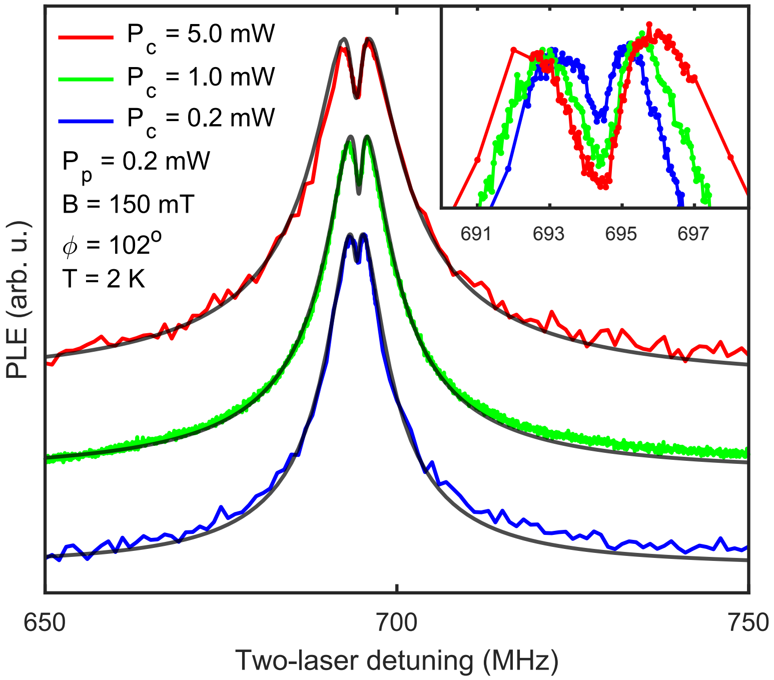

Figure 5.5: Signatures of coherent population trapping of Mo spin states in 6H-SiC. Two-laser spectroscopy of the L_1 peak in the PLE signals reveals a dipped structure in the peak at several combinations of probe-beam and control-beam power. This results from coherent population trapping (CPT) upon Λ-scheme driving. Temperature, magnetic field orientation and magnitude, and laser powers, were as labeled. The data are offset vertically for clarity. Solid lines are fits of a theoretical model of CPT (see main text). The inset shows the normalized CPT feature depths.

vacancy defect in diamond[105], indicating that the Mo defects can be applied as bright emitters. The value of T_2^* is relatively short but sufficient for applications based on CPT[15]. Moreover, the EPR studies by Baur *et al.*[125] on various transition-metal impurities show that the inhomogeneity probably has a strong static contribution from an effect linked to the spread in mass for Mo isotopes in natural abundance (nearly absent for the mentioned vanadium case), compatible with elongating spin coherence via spin-echo techniques. In addition, this work showed that the hyperfine coupling to the impurity nuclear spin can be resolved. There is thus clearly a prospect for storage times in quantum memory applications that are considerably longer than T_2^*.

5.7 Further discussion

The anisotropic behavior of the g-factor similar to what we observe for Mo was also observed in the EPR studies by Baur *et al.*[125] (for vanadium and titanium $g_{\parallel} \approx 1.7$ and $g_{\perp} = 0$ for the ground state was observed). In these cases the transition metal has a single electron in its 3d orbital and occupies the hexagonal (h) Si substitutional site. The correspondence with what we observe for the Mo impurity strongly suggests that our materials have Mo impurities present as $\mathrm{Mo}^{5+}(4\mathrm{d}^1)$ systems residing on a hexagonal h silicon substitutional site. In this case, the molybdenum would be bonded in a tetrahedral geometry, sharing four electrons with its nearest neighbors, and the defect is in a singly ionized $+|e|$ charge state (e denotes the elementary charge). This is plausible for the p-type SiC host material in our experiments.

However, recently Ivády *et al.* proposed the existence of the asymmetric split-vacancy (ASV) defect in SiC based on theoretical work[126]. An ASV defect in SiC occurs when an impurity occupies the divacancy formed by adjacent silicon and carbon vacancies. The local symmetry of this defect is a distorted octahedron with a threefold symmetry axis in which the strong g-factor anisotropy ($g_{\perp} = 0$) may also be present for the $S = 1/2$ state[139]. Considering six shared electrons for this divacancy environment, the $4\mathrm{d}^1$ Mo configuration would now occur for the singly charged $-|e|$ state (which is not a likely scenario for our case given that we have p-type material).

In addition, Baur *et al.*[125] studied the $\mathrm{Mo}^{5+}(4\mathrm{d}^1)$ charge state in slightly n-type 6H-SiC and reported a fully isotropic g-factor. This corresponds to Mo on a site with cubic symmetry (k) in the crystal field[139] (see also Supplementary Information section 5.17 (p. 144)). Furthermore, it was mentioned that $\mathrm{Mo}^{5+}(4\mathrm{d}^1)$ in n-type SiC could not be addressed optically. We thus propose that $\mathrm{Mo}^{5+}(4\mathrm{d}^1)$ on a lattice site with cubic symmetry may only be stable in n-type SiC, and that its transitions are possibly optically forbidden. On the other hand, $\mathrm{Mo}^{5+}(4\mathrm{d}^1)$ in hexagonal symmetry is stable in p-type SiC and optically accessible.

5.8 Summary and Outlook

We have studied ensembles of molybdenum defect centers in 6H and 4H silicon carbide with 1.1521 eV and 1.1057 eV transition energies, respectively. The ground-state and excited-state spin of both defects was determined to be $S = 1/2$ with large g-factor anisotropy. Since this is allowed in hexagonal symmetry, but forbidden in cubic, we find this to be consistent with theoretical descriptions that predict that Mo resides at a hexagonal lattice site in 4H-SiC and 6H-SiC[126, 129], and our p-type host environment strongly suggests that this occurs for Mo at a silicon substitutional site. We used the measured insight in the $S = 1/2$ spin Hamiltonians for tuning control schemes where two-laser driving addresses transitions of a Λ system, and observed CPT for such cases. This demonstrates that the Mo defect and similar transition-metal impurities are promising for quantum information technology. In particular for the highly analogous vanadium color center, engineered to be in SiC material where it stays in its neutral $V^{4+}(3d^1)$ charge state, this holds promise for combining $S = 1/2$ spin coherence with operation directly at telecom wavelengths.

5.9 Methods

Cryostat During all measurements, the sample was mounted in a helium flow cryostat with optical access through four windows and equipped with a superconducting magnet system.

Photoluminescence (PL) The PL spectrum of the 6H-SiC sample was measured by exciting the material with an 892.7 nm laser, and using a double monochromator equipped with infrared-sensitive photomultiplier. For the 4H-SiC sample, we used a 514.5 nm excitation laser and an FTIR spectrometer.

Photoluminescence Excitation (PLE) The PLE spectrum was measured by exciting the defects using a CW diode laser tunable from 1178 nm to 1158 nm with linewidth below 50 kHz, stabilized within 1 MHz using feedback from a HighFinesse WS-7 wavelength meter. The polarization was linear along the sample c-axis. The laser spot diameter was ∼100 μm at the sample. The PL exiting the sample sideways was collected with a high-NA lens, and detected by a single-photon counter. The excitation laser was filtered from this signal using a set of three 1082 nm (for the 4H-SiC case) or 1130 nm (for the 6H-SiC case) longpass interference filters. PLE was measured using an ID230 single-photon counter. Additionally, to counter charge state switching of the defects, a 770 nm re-pump beam from a tunable pulsed Ti:sapphire laser was focused at the same region in the sample. Laser powers as mentioned in the main text.

Two-laser characterization The PLE setup described above was modified by focusing a detuned laser beam to the sample, in addition to the present beams. The detuned laser field was generated by splitting off part of the stabilized diode laser beam. This secondary beam was coupled into a single-mode fiber and passed through an electro-optic phase modulator in which an RF signal (up to ∼5 GHz) modulated the phase. Several sidebands were created next to the fundamental laser frequency, the spacing of these sidebands was determined by the RF frequency. Next, a Fabry-Pérot interferometer was used to select one of the first-order sidebands (and it was locked to the selected mode). The resulting beam was focused on the same region in the sample as the original PLE beams (diode laser and re-pump) with similar spot size and polarization along the sample c-axis. Laser powers were as mentioned in the main text. Small rotations of the c-axis with respect to the magnetic field were performed using a piezo-actuated goniometer with 7.2 degrees travel.

5.10 Author contributions

This chapter is based on Ref. 4 on p. 177. The project was initiated by C.H.W., O.V.Z, I.G.I and N.T.S. SiC materials were grown and prepared by A.E. and B.M. Experiments were performed by T.B., G.J.J.L. and O.V.Z, except for the PL measurements which were done by A.G. and I.G.I. Data analysis was performed by T.B., G.J.J.L., C.G., O.V.Z., F.H., R.W.A.H. and C.H.W. T.B., G.J.J.L. and C.H.W. had the lead on writing the manuscript, and T.B. and G.J.J.L. are co-first author. All authors read and commented on the manuscript.

Supplementary Information (SI)

5.11 SI: Single-laser spectroscopy

Figure 5.6 shows the photoluminescence (PL) emission spectrum of the 4H-SiC sample at 5 and 20 K, characterized using a 514.5 nm excitation laser. The Mo zero-phonon line (ZPL) at 1.1521 eV is marked by a dashed box and shown enlarged in the inset. The broader peaks at lower energies are phonon replicas of the ZPL. There is almost no dependence on temperature for both the ZPL and the phonon replicas.

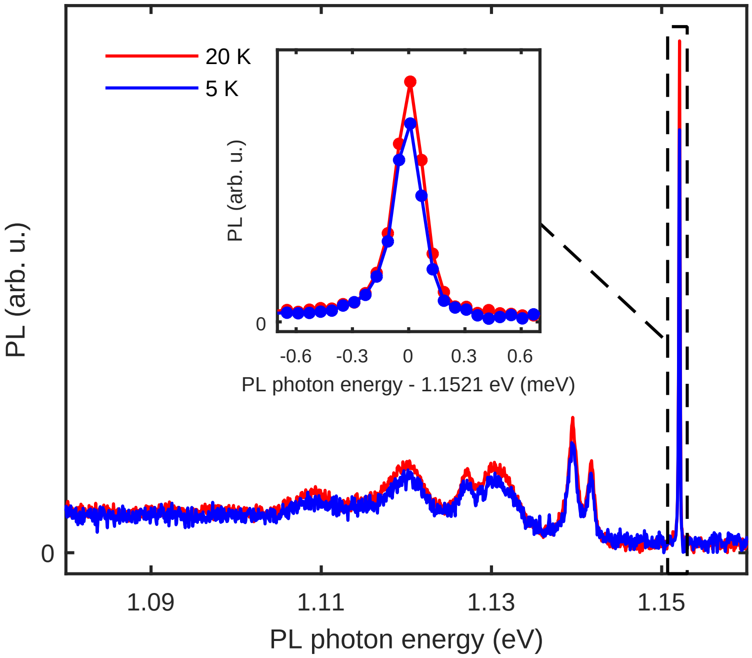

Figure 5.6: Temperature dependence of Mo PL spectrum in 4H-SiC. PL from excitation with a 514.5 nm laser, for 5 and 20 K sample temperatures. The dashed box marks the ZPL at 1.1521 eV. The inset gives a magnified view of the ZPL. The broader peaks at lower photon energies are phonon replicas of the ZPL.

Figures 5.7a,b show results of PLE measurements of the ZPL for Mo in 4H-SiC at 1.1521 eV and 6H-SiC at 1.1057 eV, and the temperature dependence of these PLE signals. When the temperature is decreased, the width of the ZPL stays roughly the same, but its height drops significantly. Combined with the near-independence on temperature of the emission spectrum in Fig. 5.6, this is an indication for optical spin pumping for Mo-impurity states at lower temperatures, where a single resonant laser pumps then the system into long-lived off-resonant spin states.

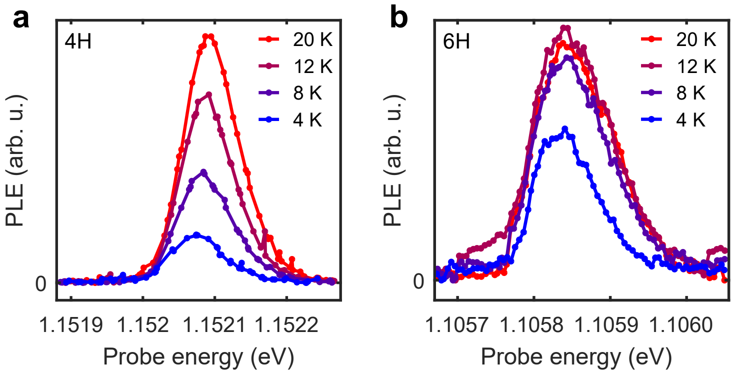

Figure 5.7: Temperature dependence of the PLE signals from the Mo ZPL in 4H-SiC and 6H-SiC. PLE signals from scanning a single CW narrow-linewidth laser across the ZPL photon-energy range. The temperature was varied between 4 and 20 K. The ZPL for Mo in (**a**) 4H-SiC is at 1.1521 eV, and for Mo in (**b**) 6H-SiC at 1.1057 eV.

5.12 SI: Additional two-laser spectroscopy for Mo in 6H-SiC

Angle dependence. In addition to Fig. 5.2b,c in the main text, we also measured the magnetic field dependence of the spin related emission signatures at intermediate angles ϕ. Figure 5.8 shows this dependence for $\phi = 37°$, 57° and 81°. The spectroscopic position of emission lines L_n show a linear dependence on magnetic field, with slopes Θ_{Ln} (in Hertz per Tesla) that decrease as ϕ increases. The effective g-factors in Fig. 5.4 are acquired from the emission lines by relating their slopes to the Zeeman splittings in the ground and excited state. Using the four pumping schemes depicted in Fig. 5.3 in the main text, we derive

$$\Theta_{L1} = \frac{\mu_B}{h} g_g \tag{5.5}$$

$$\Theta_{L2} = \frac{\mu_B}{h} |g_e - g_g| \tag{5.6}$$

$$\Theta_{L3} = \frac{\mu_B}{h} g_e \tag{5.7}$$

$$\Theta_{L4} = \frac{\mu_B}{h} (g_e + g_g) \tag{5.8}$$

where h is Planck's constant, μ_B the Bohr magneton and $g_{g(e)}$ the ground (excited) state g-factor.

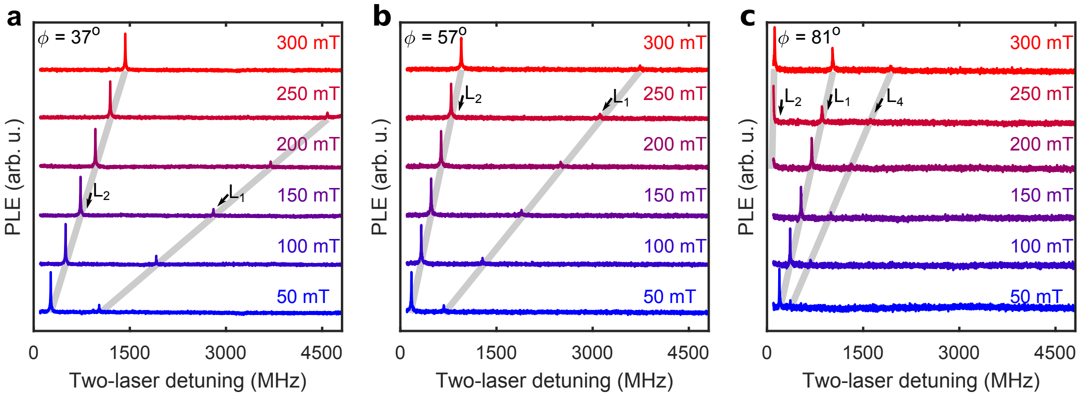

Figure 5.8: Magneto-spectroscopy of two-laser spin signatures in PLE from Mo in 6H-SiC. Magnetic field dependence of the PLE signal versus two-laser detuning, for angles ϕ between the magnetic field and c-axis set to $\phi = 37°$ (**a**), $\phi = 57°$ (**b**) and $\phi = 81°$ (**c**). Results for the temperature at 4 K. The labeling of the emission lines (L_1 - L_4) is consistent with Fig. 5.2. The data are offset vertically for clarity.

Two-laser spectroscopy for the 5-21 GHz detuning range. In order to check for a possible presence of spin-related emission features at detunings larger than 5 GHz (checking for a possible zero-field splitting), we modified the setup such that we could control two-laser detunings up to 21 GHz. The electro-optical phase modulator (EOM) we used for generating the detuned laser field could generate first-order sidebands up to 7 GHz. In order to check for two-laser spectroscopy emission features at larger detunings, we removed the Fabry-Pérot (FP) resonator that had the role of filtering out a single sideband. Now, all sidebands (on the same optical axis) were focused onto the sample with 2 mW total laser power. Apart from the re-pump beam, no additional laser was focused onto the sample in this experiment. In this way, the Mo defects could interact with several combinations of sidebands. Figure 5.9a shows the spectral content of this beam (here characterized by still using the FP resonator). The first and second order sidebands at negative and positive detuning take a significant portion of the total optical power. Hence, pairs of sidebands spaced by single, double or triple frequency intervals (EOM frequency f_{EOM}) now perform two-laser spectroscopy on the Mo defects. The relevant sideband spacings are indicated in Fig. 5.9a.

Figure 5.9b presents results of these measurements, showing various peaks that we identified and label as $L_{n,m}$. Here n is identifying the peak as a line L_n as in the main text, while the label m identifies it as a spectroscopic response for two-laser detuning at $m \cdot f_{\mathrm{EOM}}$ (that is, $m = 1$ is for first-order EOM sideband spacing, *etc.*). Note that second-order manifestations of the known peaks L_1-L_4 (from double sideband spacings, labeled as $L_{n,2}$) are now visible at $\frac{1}{2}f_{\mathrm{EOM}}$, and third-order response of the known L_1-L_4 occurs at $\frac{1}{3}f_{\mathrm{EOM}}$ (but for preserving clarity these have not been labeled in Fig. 5.9b).

Figure 5.9c depicts a continuation of this experiment with f_{EOM} up to 7 GHz with the same resolution as Fig. 5.9b. No new peaks are observed. Considering that third-order peaks were clearly visible before, we conclude that no additional two-laser emission features exist up to 21 GHz.

5.13 SI: Two-laser spectroscopy for Mo in 4H-SiC

We also studied the spin-related fine structure of Mo defects in 4H-SiC. Our 4H-SiC sample suffered from large background absorption, which drastically lowered the signal-to-noise ratio. We relate this absorption to a larger impurity content (of unknown character, but giving broad-band absorption) in our 4H-SiC material as compared to our 6H-SiC material. Therefore, the lasers were incident on a corner of the sample, so as to minimize the decay of the emitted PL. We present the results in gray-scale plots in Fig. 5.10 for optimized contrast. The figure shows the magnetic field and two-laser detuning dependence of the PLE.

Analogous to Fig. 5.2 for 6H-SiC in the main text, the spectroscopic position features appear as straight lines that emerge from zero detuning, indicating the absence of a zero-field splitting. When the magnetic field is nearly perpendicular to the c-axis (Fig. 5.10c), four lines are visible. This is consistent with an $S = 1/2$ ground and excited state.

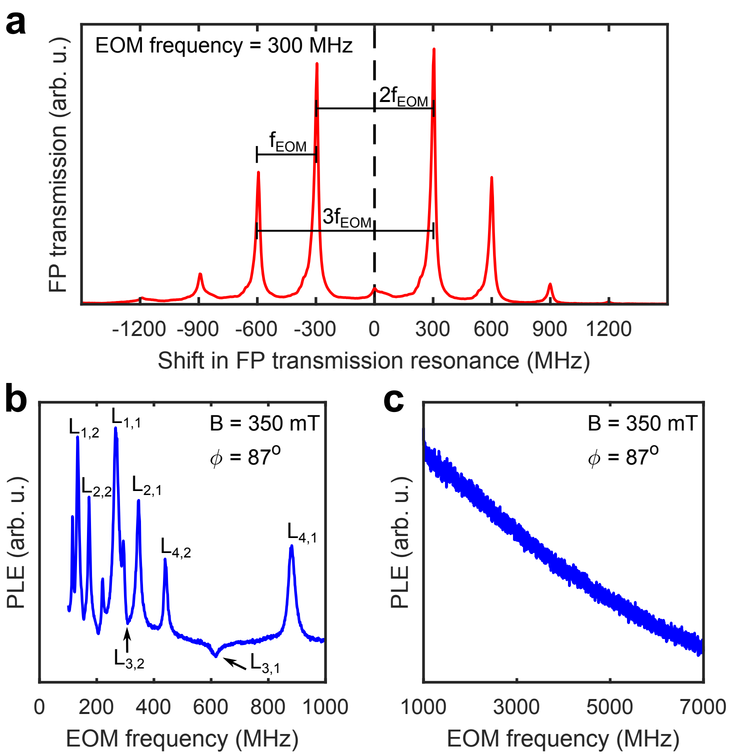

Figure 5.9: Two-laser spin signatures of Mo in 6H-SiC at large detuning. **a**, Transmission scan of the Fabry-Pérot resonator, characterizing which optical frequencies are present in the beam after passing through the electro-optical modulator (EOM). The first-order sidebands at ±300 MHz have the highest intensity, whereas the fundamental laser frequency is suppressed (but not fully removed) by the EOM. Relevant sideband spacings are indicated. **b**, Spin signatures at low two-laser detuning. PLE is increased when two sidebands are appropriately detuned from each other. Emission features similar to those in Fig. 5.2c of the main text are visible, and labeled $L_{n,m}$ (see main text of this section). **c**, The PLE signal from two-laser spectroscopy at larger detuning. No peaked features from single, double or triple sideband spacings are visible.

The data from Fig. 5.10c was measured at 10 K, whereas Fig. 5.10a,b was at 4.2 K. At 10 K, all emission lines become dips, while for 6H-SiC only the V system shows a dip. The temperature dependence of L_3 and L_1 is shown in Fig. 5.11 for the same configuration as in Fig. 5.10c ($\phi = 83°$). At low temperatures L_1 shows a peak and L_3 shows a dip. Upon increasing the temperature, both features become dips. This phenomenon was only observed for Mo in 4H-SiC, it could not be seen in 6H-SiC. We therefore conclude that this probably arises from effects where Mo absorption and emission is influenced by the large background

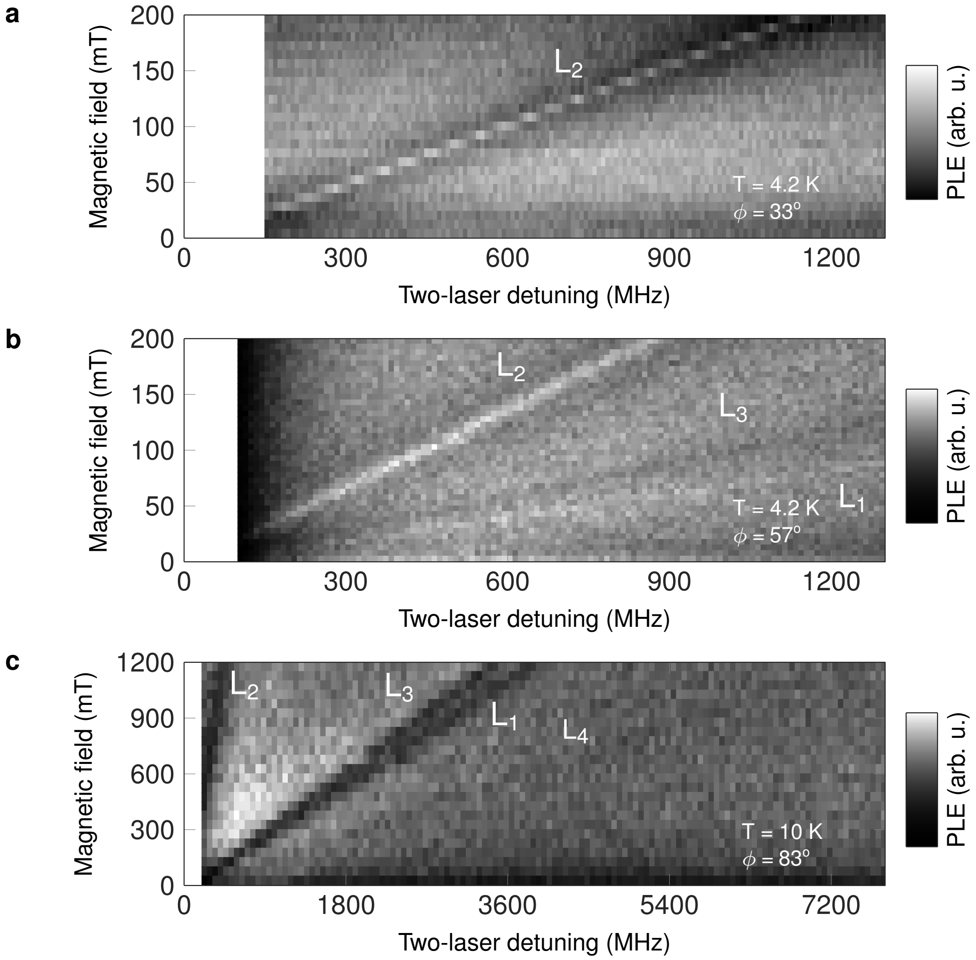

Figure 5.10: Two-laser spin signatures of Mo in 4H-SiC. PLE signal as function of two-laser detuning and magnetic field strength, for various angles ϕ between the magnetic field and c-axis. **a**, Measurement at 4.2 K, with $\phi = 33°$. A single emission line (peak) is visible, labeled L_2. **b**, Measurement at 4.2 K, with $\phi = 57°$. Three emission lines are visible, labeled L_1, L_2 (peaks), and L_3 (dip). **c**, Measurement at 10 K, with $\phi = 83°$. Four emission lines are visible, labeled L_1 through L_4 (all dips). Note that the measurement range of **c** is six time as large as **a** and **b**, but the plot aspect ratio is the same. The labeling is consistent with the main text. A gray-scale plot has been used for optimal contrast.

absorption in the 4H-SiC material.

The labels in Fig. 5.10 are assigned based on the sum rules from equation (5.2) and (5.3) (main text), which indeed also hold for the observed emission lines observed here. Like in the main text, L_1 through L_4 indicate Λ, Π, V and X two-laser pumping schemes, respectively. The L_1 and L_3 labels are interchange-

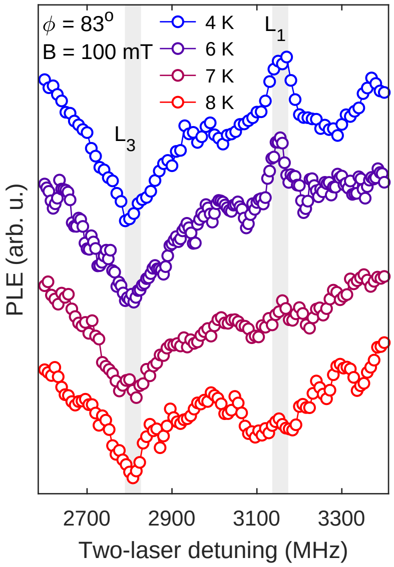

Figure 5.11: Temperature dependence of PLE spin signatures from Mo in 4H-SiC. PLE signal as function of two-laser detuning and temperature with magnetic field at $\phi = 83°$ from the sample c-axis at 100 mT. As the temperature increases, the signal from L_1 changes from a peak to a broad dip, while L_3 remains a dip. The labeling is consistent with the main text.

able in Fig. 5.10c when only considering the sum rules. However, the fact that the left feature in Fig. 5.11 shows a dip for all temperatures means that it should be related to a V scheme. Thus, the current assignment of the labels with corresponding pumping schemes is justified. Using equations 5.5 through 5.8 (Suppl. Inf.), the effective g-factors can be determined. Fitting these to equation (5.4) gives the values for $g_\parallel$ and $g_\perp$ reported in the main text.

5.14 SI: Franck-Condon principle with respect to spin

The amplitude of the two-laser emission signatures is determined by the strength of the underlying optical transitions. For a transition $|g_i\rangle$-$|e_j\rangle$, this strength is determined by the spin overlap $\langle g_i|e_j\rangle$, according to the Franck-Condon principle with respect to spin[10]. The quantum states of the spin in the electronic ground and excited state can be described using effective spin Hamiltonian

$$H_{g(e)} = \mu_B \mathbf{B} \cdot \mathbf{g}_{g(e)} \cdot \tilde{\mathbf{S}} \tag{5.9}$$

with μ_B the Bohr magneton, $\mathbf{B}$ the applied magnetic field vector, $\tilde{\mathbf{S}}$ the effective spin vector, and where the ground (excited) state g-parameter is a tensor $\mathbf{g}_{g(e)}$. Using Cartesian coordinates this can be written as

$$\mathbf{g}_{g(e)} = \begin{pmatrix} g_{\perp}^{g(e)} & 0 & 0 \\ 0 & g_{\perp}^{g(e)} & 0 \\ 0 & 0 & g_{\parallel}^{g(e)} \end{pmatrix} \tag{5.10}$$

Here the z-axis is parallel to the SiC c-axis, and the x and y-axes lay in the plane perpendicular to the c-axis. Due to the symmetry of the defect, the magnetic field $\mathbf{B}$ can be written as

$$\mathbf{B} = \begin{pmatrix} 0 \\ B\sin\phi \\ B\cos\phi \end{pmatrix} \tag{5.11}$$

where B indicates the magnitude of the magnetic field. The resulting Hamiltonian $H_{g(e)}$ may be found by substituting $\mathbf{B}$ and $\mathbf{g}_{g(e)}$ into equation (5.9), and considering that $S = 1/2$. The basis of $H_{g(e)}$ can be found from the eigenvectors.

For the ground state $g_{\perp}^{g}$ is zero, thus the bases of H_g and S_z coincide, independent of ϕ. Therefore, there is no mixing of spins in the ground state. However, in the excited state $g_{\perp}^{e}$ is nonzero, causing its eigenbasis to rotate if a magnetic field is applied non-parallel to the c-axis. The new eigenbasis is a linear combination of eigenstates of S_x, S_y and S_z, such that there will be mixing for spins in the excited state for any nonzero angle ϕ.

We calculate the spin overlap for the $|g_i\rangle$-$|e_j\rangle$ transition from the inner product of two basis states $|g_i\rangle$ and $|e_j\rangle$. The strength of a two-laser pumping scheme is then the product of the strength of both transitions. For example, the strength of the Λ scheme from Fig. 5.3a equals the inner product $\langle g_1|e_2\rangle$ multiplied by $\langle g_2|e_2\rangle$. The resulting strengths for all four pumping schemes are depicted in Fig. 5.12.

We now compare these transition strengths to the data in Fig. 5.2b,c and Fig. 5.8 and 5.10. It is clear that the Π scheme is the strongest pumping scheme for all angles $\phi \neq 90°$. This explains the large relative amplitude of L_2 in our measurements. The Λ and V scheme transition strengths are equal, starting from zero for $\phi = 0°$ and increasing as ϕ approaches $90°$. For the Λ scheme, this is consistent with the increasing relative amplitude of L_1. For ϕ close to $90°$ the amplitude of L_1 is even larger than for L_2. The reason for this is that a Λ scheme is emitting more effectively than a Π scheme. The V scheme is harder to observe

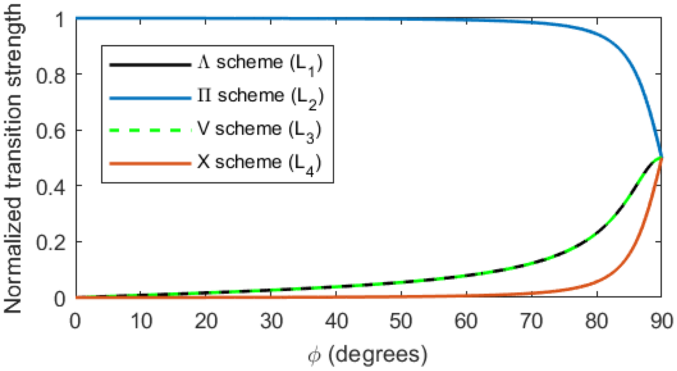

Figure 5.12: Two-laser pumping scheme transition strengths. For each scheme the product of the spin overlaps from both underlying transitions is shown. The strength of the Π scheme is near unity for large angles and never vanishes. The strengths of the Λ and V schemes are equal, they vanish at $\phi = 0°$. The X scheme strength vanishes more rapidly than any other scheme for angles ϕ close to 0°.

in the background emission, such that L_3 is only visible for ϕ close to 90°. Finally, the transition strength of the X scheme is only significant for ϕ close to 90°, which is why we have not been able to observe L_4 below 81° in 6H-SiC.

5.15 SI: V-scheme dip

Understanding the observation of a dip for the V pumping scheme in a four-level system (Fig. 5.2c in the main text) is less trivial than for the observation of peaks from the other three pumping schemes. The latter can be readily understood from the fact that for proper two-laser detuning values both ground states are addressed simultaneously, such that there is no optical pumping into dark states. In this section we will investigate how a dip feature can occur in the PLE signals. Our modeling will be based on solving a master equation in Lindblad form with a density matrix in rotating wave approximation for a four-level system with two near-resonant lasers[15].

Consider the four-level system depicted in Fig. 5.13a. A control laser is near-resonant with the $|g_1\rangle$-$|e_1\rangle$ (vertical) transition and a probe laser near-resonant with $|g_1\rangle$-$|e_2\rangle$ (diagonal) transition. Here the two-laser detuning is defined as $\delta = \Delta_p - \Delta_c$, *i.e.* the difference between the detunings Δ of both lasers from their respective near-resonant transitions, such that the emission feature appears at zero two-laser detuning. The decay rates from the excited states are Γ_v and Γ_d for vertical and diagonal transitions, respectively. They are quadratically

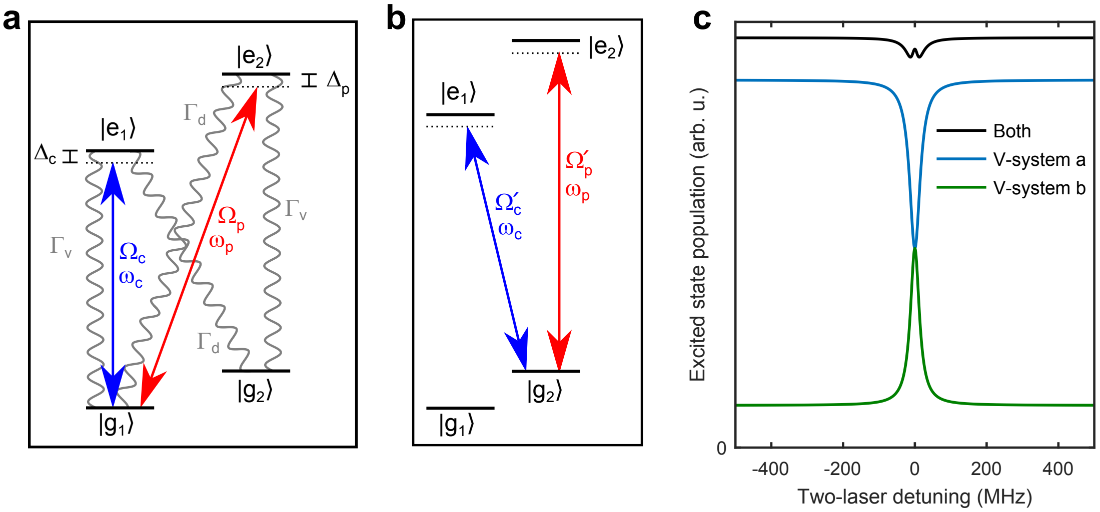

Figure 5.13: Four-level V-scheme model. a, V pumping scheme in a four level system. Here Ω is the Rabi frequency for the control and probe lasers, and ω their (angular) frequency. Γ_v and Γ_d are the decay rates for vertical and diagonal decay, respectively. Δ represents the detuning from resonance of the control and probe beam. **b,** V-scheme simultaneously resonant (with the scheme in panel **a**) for another part of the inhomogeneously broadened ensemble. Probe and control Rabi frequencies Ω' differ from **a**, since both lasers drive other transitions with different dipole strengths. **c,** Total population in the excited-state levels ($|e_1\rangle$ and $|e_2\rangle$) for both schemes separately (blue and green) as well as their sum (black).

proportional to the spin-state overlap $\langle g_i|e_j\rangle$

$$\Gamma_v \propto |\langle g_1|e_1\rangle|^2\,, \tag{5.12}$$

$$\Gamma_d \propto |\langle g_1|e_2\rangle|^2\,. \tag{5.13}$$

These rates are unequal, since the spin-state overlap for diagonal transitions is generally smaller than for vertical transitions (see previous section). The decay rates Γ_e between excited-state levels and Γ_g ground-state levels are assumed very small compared to the decay rates from the excited-state levels. The decay rates from ground-state levels towards the excited-state levels are set to zero. Dephasing rates are taken relative to the $|g_1\rangle$ state ($\gamma_{g1} = 0$). The choices for parameters are listed in table 5.2. The Rabi frequencies Ω_c and Ω_p of the driven transitions are linearly proportional to the spin-state overlap

$$\Omega_c \propto |\langle g_1|e_1\rangle|\,, \tag{5.14}$$

$$\Omega_p \propto |\langle g_1|e_2\rangle|\,. \tag{5.15}$$

Table 5.2: Parameter choices for V-scheme model

parameter	value (Hz)	parameter	value (Hz)
Γ_v	$0.9 \cdot 10^7$	γ_{g1}	0
Γ_d	$0.1 \cdot 10^7$	γ_{g2}	$5 \cdot 10^6$
Γ_g	$1 \cdot 10^4$	γ_{g3}	$5 \cdot 10^6$
Γ_e	$1 \cdot 10^4$	γ_{g4}	$5 \cdot 10^6$
Δ_c	0	Ω_c	$\sqrt{.9} \cdot 10^7$
Δ_p	$\in [-500, 500] \cdot 10^6$	Ω_p	$\sqrt{.1} \cdot 10^7$

Additionally, we have to consider a secondary V-scheme (Fig. 5.13b) resonant with another part of the inhomogeneously broadened ensemble. The control and probe laser are swapped, as the former now addresses a diagonal transition, while the latter addresses a vertical one. The new Rabi frequency is taken to be $\Omega_c' = \sqrt{\frac{\Gamma_d}{\Gamma_v}}\Omega_c$ for the control beam, which is now driving a diagonal transition (with reduced strength). The probe beam is driving a vertical transition (with increased strength), and its Rabi frequency is $\Omega_p' = \sqrt{\frac{\Gamma_v}{\Gamma_d}}\Omega_p$.

Considering both V-schemes, we calculate the total population in both excited-state levels as it reflects the amount of photoluminescence resulting from decay back to the ground states. The two-laser detuning dependence of the excited-state population is shown in Fig. 5.13c. The black curve considers both schemes simultaneously, which represents the situation in our measurements. Here the dip indeed appears, although both separate schemes (a and b) display a dip and peak (respectively). The competition between both schemes limits the depth of the observed dip, which explains our observation of shallow dips in contrast to sharp peaks in Fig. 5.2c in the main text.

Interestingly, the black curve displays a peak within the dip, which might seem like a CPT feature. However, this feature is not visible in either curve from the two separate pumping schemes. This peak appears because the peak from the second V-scheme (green) is slightly sharper than the dip from the first one (blue). The peak might still be caused by CPT, as the blunting of the dip relative to the peak can be caused by a long dephasing time of the ground state.

Key to understanding the appearance of a dip in the total photoluminescence emission is the difference in decay rates, vertical decay being favored over diagonal decay. Consider the pumping scheme from Fig. 5.13a. When the probe laser is off-resonant the control laser drives the $|g_1\rangle$-$|e_1\rangle$ transition. Decay will occur mostly towards the $|g_1\rangle$ state and occasionally to the dark $|g_2\rangle$ state. If the probe laser becomes resonant with the $|g_1\rangle$-$|e_2\rangle$ transition, the increased population in the $|e_2\rangle$ state will prefer to decay towards the dark $|g_2\rangle$ state. The overall decay towards the dark state is now increased. The secondary pumping scheme (Fig. 5.13b) works the other way around, where the diagonal transition is always driven by the control beam and a resonant probe beam will counteract some of the pumping into the dark state (now $|g_1\rangle$). However, the slightly increased emission from scheme b cannot fully counteract the decreased emission from scheme a (even when $\Omega_p = \Omega_c = \Omega'_p = \Omega'_c$).

5.16 SI: Modeling of coherent population trapping

For fitting the CPT traces in Fig. 5.5 in the main text, we use a standard CPT description[15], extended for strong inhomogeneous broadening of the optical transitions, and an approach similar to the one from the previous section. However (as compared to the previous section), the behavior of CPT has a more pronounced dependence on parameters, such that almost no assumptions have to be made. When taking the spin Hamiltonians as established input (section 4), the only assumption made is that the spin relaxation time in the ground state and excited state is much slower than all other decay process. This allows for setting up fitting of the CPT traces with only two free fit parameters, which correspond to the optical lifetime and the inhomogeneous dephasing time T_2^*.

Since two lasers couple both ground-state levels to a single common excited-state level, the other excited-state level will be empty. Therefore, we may describe this situation with a three-level system, where the PL is directly proportional to the excited-state population. The decay rates and Rabi frequencies are proportional to the Franck-Condon factors for spin-state overlaps $\langle g_i|e\rangle$ in the same way as before (equations (5.12)-(5.15)). At this angle ($\phi = 102°$) we calculate these factors to be

$$\langle g_1|e\rangle = 0.9793 \tag{5.16}$$

$$\langle g_2|e\rangle = 0.2022 \tag{5.17}$$

according to the reasoning in section 5.14. We take that the $|g_1\rangle$-$|e\rangle$ is a vertical transition and $|g_2\rangle$-$|e\rangle$ a diagonal one.

In order to account for inhomogeneous broadening throughout the ensemble, the solution of the master equation is computed for a set of control-laser detunings Δ_c (see Fig. 5.13a) around zero, its range extending far beyond the two-laser detuning values δ (since we experimentally observed an inhomogeneous broadening much in excess of the spin splittings). In this case the probe-laser detuning becomes $\Delta_p = \Delta_c + \delta$. The resulting excited-state populations are integrated along the inhomogeneous broadening Δ_c (up to the point where the signal contribution vanishes) to give the PL emission versus two-laser detuning δ. Analogous to the previous section, we have to consider a secondary Λ-scheme in order to fully account for the inhomogeneous broadening. The total PL emission is found by adding together the excited-state populations from both schemes.

We fit this model to the data presented in Fig. 5.5 after subtracting a static background. We extract the inhomogeneous dephasing time $T_2^* = 0.32 \pm 0.08$ μs and an optical lifetime of 56 ± 8 ns. The errors are estimated from the spread in extracted dephasing times and lifetimes throughout the data sets.

5.17 SI: Anisotropic g-factor in the effective spin-Hamiltonian

5.17.1 Relationship between effective spin Hamiltonian and local configuration of the defect

An effective spin-Hamiltonian as the one used in the main text is a convenient tool which allows us to describe the behavior of the system in a wide range of configurations, as long as the effective parameters are experimentally determined and all relevant states are considered. It is often the meeting point between experimentalists, who measure the relevant parameters, and theoreticians, who attempt to correlate them to the Hamiltonian that describes the configuration of the system. A careful description of the latter, and how it modifies the parameters at hand, allows us to rationalize our choices when investigating defects with varying characteristics (such as a different charge state or element). This task is more approachable when we consider the group-theoretical properties of the system at hand. Here we combine group-theoretical considerations with ligand field theory in order to qualitatively describe the features observed in our experiment. In particular, we aim at explaining the large Zeeman splitting anisotropy observed in both ground and excited states, and correlating it to the charge and spatial configuration of the defect.

In our experiments, we observe a single zero-phonon line (ZPL) associated with optical transitions between two Kramers doublets (KD, doublets whose degeneracy is protected by time-reversal symmetry and is thus broken in the presence of a magnetic field) in defects which contain Mo. The presence of a single zero-phonon line in both 4H and 6H-SiC samples indicates that the defect occupies a lattice site with hexagonal symmetry. The lattice of 6H-SiC has two inequivalent sites with cubic symmetry. Thus, if the defect were to occupy sites of cubic symmetry, we would expect to observe two ZPLs closely spaced in this sample. The absence of the ZPL associated with this defect in samples of 3C-SiC[140] further corroborates this assumption. Additionally, we observe strong anisotropy in the Zeeman splitting of the ground and excited states. Specifically, when the magnetic field is perpendicular to the symmetry axis of the crystal, the Zeeman splitting of the ground state goes to zero, whereas that of the excited state is very small. This feature is observed in other transition-metal defects in SiC situated at Si substitutional sites of hexagonal symmetry and with one electron in its 3d orbital[141], but we are not aware of a clear explanation of the phenomenon.

In our experiments, we observed transitions between sublevels of doubly degenerate ground and excited states, whose degeneracy is broken in the presence of a magnetic field. Thus, we note that ground and excited states are isolated KDs, indicating that the defect contains an odd number of electrons. A Mo atom has 6 electrons in its valence shell. The atom can occupy a Si substitutional site ($\mathrm{Mo_{Si}}$), where it needs to bond to 4 neighboring atoms, or an asymmetric split vacancy (ASV) site ($\mathrm{Mo}_{\mathrm{V_{Si}}-\mathrm{V_C}}$), where it bonds to 6 neighboring atoms. These defects can, respectively, be described by a Mo ion in the configurations $4\mathrm{d}^2$ and $4\mathrm{d}^0$, indicating that the defect must be ionized in order to contain an odd number of electrons. Its charge state, which could be ±1, ±3, *etc.*, is determined by the Fermi level in the crystal of interest. We note that the ZPL could only be observed in p-doped samples, which indicates that the features investigated here are unlikely to arise from negatively charged defect. The defect $\mathrm{Mo}_{\mathrm{Si}}^{+1}$ (where $+1$ represents the charge state of the defect, not the Mo atom) can be approximately described by a Mo in a configuration $4\mathrm{d}^1$, which facilitates the treatment of its configuration in terms of d orbitals. In contrast, the defect $\mathrm{Mo}_{\mathrm{V_{Si}}-\mathrm{V_C}}^{+1}$ is described by an electronic configuration containing a hole in the bonding orbitals. These orbitals show strong hybridization between the d orbitals of the Mo and the orbitals of the ligands, and cannot be straight-forwardly analyzed using the formalism described below. Nonetheless, inspired by the similarities between our system and other transition-metal defects reported in SiC[141], we investigate the effect of the crystal field of $\mathrm{C_{3v}}$ symmetry –which is expected to be significant in hexagonal lattice sites in 4H-SiC and 6H-SiC– on the one-electron levels of the 5 sublevels (10, if spin multiplicity is included) of the 4d shell of a Mo atom. We qualitatively predict the spin-hamiltonian parameters expected for a Mo ion in a $4\mathrm{d}^1$ configuration, and compare our analysis to the experimental results.

5.17.2 Ion in $4\mathrm{d}^1$ configuration in the presence of crystal field of $\mathrm{C_{3v}}$ symmetry and spin-orbit coupling

The 5 degenerate sublevels of a 4d-orbital are split by a crystal field of $\mathrm{C_{3v}}$ symmetry[142]. The energy splittings induced by this field are much smaller than the energy difference between the 4d shell and the next orbital excited state (5s). This allows us to, initially, consider the 5 orbitals of the 4d shell as a complete set. Since Mo is a heavy atom, we cannot disregard the effect of spin-orbit interaction. However, we assume that the crystal field is larger than the effect of SOC, that is, $\Delta E_{free} \gg \Delta E_{crystal} \gg \Delta E_{spin-orbit} \gg \Delta E_{Zeeman}$, where ΔE denotes the energy splitting induced by each term (see Fig. 5.14).

The 5 orbital states of the d-orbital form a 5-dimensional irreducible representation (irrep) of the full rotation group SO(3). When the symmetry is lowered by the crystal field to $\mathrm{C_{3v}}$, the 5-dimensional representation is split into 2 doublets (E_1, E_2) and 1 singlet (A) that are irreps of $\mathrm{C_{3v}}$. Writing the 5 components of the 4d orbital in terms of the quadratic functions z^2, x^2-y^2, xy, xz, yz allows us to identify which orbitals are degenerate in the presence of a crystal field of trigonal symmetry. We find that the singlet A is composed of the orbital $4\mathrm{d_{z^2}}$. Furthermore, the orbitals $4\mathrm{d_{xz}}$ and $4\mathrm{d_{yz}}$ are degenerate upon action of the crystal field and make up doublet E_1. Finally the orbitals $4\mathrm{d_{x^2-y^2}}$ and $4\mathrm{d_{xy}}$ correspond to doublet E_2. Group-theoretical considerations alone are not capable of elucidating which irrep corresponds to the ground state, that is, they do not provide information about the order of the energy levels.

Comparison between the Cartesian form of these 5 orbitals and the spherical harmonics which span a 5-dimensional space (that is, the spherical harmonics Y_l^m with $l = 2$) allows us to rewrite the relevant orbitals as linear combinations of the eigenstates of the operators L^2, L_z. This yields a new basis for each irrep

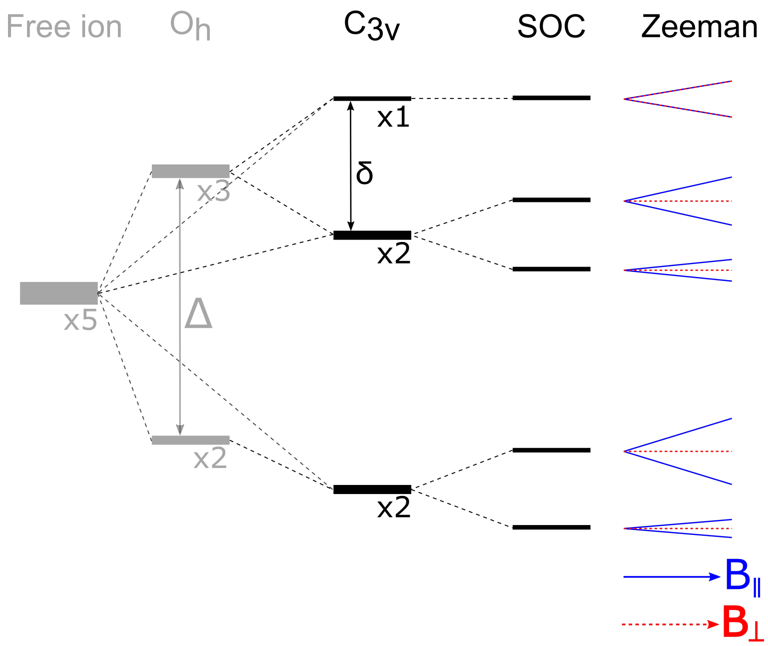

Figure 5.14: Splitting of one-electron energy levels of a 4d orbital, under the action of a crystal field and spin-orbit coupling. In the free atom, the 5 orbitals corresponding to the 4d shell (disregarding the spin) are degenerate. A crystal field of cubic symmetry breaks this degeneracy, generating an orbital triplet and a doublet, whereas a crystal field of C_{3v} symmetry, splits the 5 orbitals into one singlet and two doublets. In the text, we focus on a crystal field of C_{3v} symmetry, and disregard the cubic term. Although we recognize that this is an approximation, we argue that this approach clarifies the physics governing the strong magnetic anisotropy observed, and is thus justified. Spin-orbit coupling is responsible for splitting the doublets, generating in total 5 sets of Kramers doublets (here, the spin of the electron is taken into account). The energy splittings caused by a magnetic field within these KD give rise to the effective spin Hamiltonian parameters considered. We note that a group-theoretical approach alone is not capable of providing the order of the energy levels shown in the figure. We take this order to be the one observed in transition-metal defects in a tetrahedral crystal field with strong trigonal distortion[142].

considered above:

$$E_1 : Y_2^{-2} = |d_{-2}\rangle\,; Y_2^{2} = |d_2\rangle \qquad \text{1st orbital doublet} \tag{5.18}$$

$$E_2 : Y_2^{-1} = |d_{-1}\rangle\,; Y_2^{1} = |d_1\rangle \qquad \text{2nd orbital doublet} \tag{5.19}$$

$$A : Y_2^{0} = |d_0\rangle \qquad \text{orbital singlet} \tag{5.20}$$

When the spin multiplicity is considered, each orbital doublet yields 4 possible states, whereas the orbital singlet yields 2 possible states. Spin-orbit coupling (represented by the operator $H_{SO} = -\lambda \mathbf{L} \cdot \mathbf{S}$) is responsible for splitting these states into 5 different Kramers doublets:

$$\text{KD1} : \left|d_{+2}, +\tfrac{1}{2}\right\rangle ; \left|d_{-2}, -\tfrac{1}{2}\right\rangle \tag{5.21}$$

$$\text{KD2} : \left|d_{+2}, -\tfrac{1}{2}\right\rangle ; \left|d_{-2}, +\tfrac{1}{2}\right\rangle \tag{5.22}$$

$$\text{KD3} : \left|d_{+1}, +\tfrac{1}{2}\right\rangle ; \left|d_{-1}, -\tfrac{1}{2}\right\rangle \tag{5.23}$$

$$\text{KD4} : \left|d_{+1}, -\tfrac{1}{2}\right\rangle ; \left|d_{-1}, +\tfrac{1}{2}\right\rangle \tag{5.24}$$

$$\text{KD5} : \left|d_{0}, +\tfrac{1}{2}\right\rangle ; \left|d_{0}, -\tfrac{1}{2}\right\rangle \tag{5.25}$$

where the basis vectors are given in terms of the quantum numbers m_l and m_s which denote the projection of the orbital and spin angular momentum along the quantization axis, respectively (Fig. 5.14). Here, the spin-orbit coupling is considered up to first order in the energy correction, whereas the wave function is corrected up to zeroth order.

A magnetic field lifts the degeneracy between the two components of each KD. This splitting is usually described phenomenologically by an effective Zeeman Hamiltonian in a system with pseudospin $\tilde{\mathbf{S}} = \frac{1}{2}$.

$$H_{eff} = -\mu_B \mathbf{B} \cdot \mathbf{g} \cdot \tilde{\mathbf{S}}_{1/2} \tag{5.26}$$

where μ_B is the Bohr magneton, $\mathbf{B}$ the magnetic field vector, $\tilde{\mathbf{S}}_{1/2}$ the pseudo spin $\frac{1}{2}$ operator and $\mathbf{g}$ the g-tensor. In the presence of axial symmetry, $\mathbf{g}$ can be diagonalized such that equation (5.26) can be rewritten in terms of the symmetry axis of the crystal

$$H_{eff} = -\mu_B \Big(g_{\parallel} B_z \tilde{S}_{1/2,z} + (g_{\perp} B_x \tilde{S}_{1/2,x} + g_{\perp} B_y \tilde{S}_{1/2,y}) \Big) \tag{5.27}$$

In terms of the eigenstates belonging to each KD, the splitting is described by the Zeeman Hamiltonian given by

$$H_{Zee} = -\mathbf{B} \cdot \boldsymbol{\mu} = -\mu_B \mathbf{B} \cdot (g_0 \mathbf{S} + k\mathbf{L}) \tag{5.28}$$

where $\boldsymbol{\mu}$ is the magnetic moment operator, g_0 the g-factor for a free electron, $\mathbf{S}$ the total spin operator, k the orbital reduction factor, and $\mathbf{L}$ the orbital angular momentum operator[142, 143]. The orbital reduction factor k, is a factor between 0 and 1 which corrects for partial covalent bonding between the electron and the ligands[142] (note that the value of k differs for each of the 5 KDs in equations (5.21-5.25)). Comparison of equations (5.27) and (5.28) shows that

$$g_{\parallel} = 2 \langle g_e S_z + k L_z \rangle = \frac{2 \langle \mu_z \rangle}{\mu_B} \tag{5.29}$$

$$g_{\perp} = 2 \langle g_e (S_x + S_y) + k(L_x + L_y) \rangle = \frac{2 \langle \mu_x + \mu_y \rangle}{\mu_B} \tag{5.30}$$

As long as the magnitude of this Zeeman splitting is small compared to the spin-orbit interaction we can consider, to first order, the effect of the magnetic field in the sets formed by each KD independently. That is, we consider that the magnetic field does not mix states pertaining to two different KDs.

In order to calculate the values of $g_{\|}$ and $g_{\perp}$ for each KD defined by trigonal symmetry and spin-orbit coupling, we rewrite equation (5.28) as

$$H_{Zee} = -(B_z\mu_z + B_x\mu_x + B_y\mu_y) = -\big(B_z\mu_z + \tfrac{1}{2}(B_+\mu_- + B_-\mu_+)\big) \tag{5.31}$$

where the + and − subindices denote the raising and lowering magnetic moment operators and the linear combinations $B_x \pm iB_y$, respectively. When we consider the basis given in equations (5.21-5.24), the matrix elements of both μ_+ and μ_- are zero between two eigenvectors pertaining to one KD. This arises from the fact that the operator μ_+ couples states with (m_l, m_s) to states with (m_l+1, m_s) or (m_l, m_s+1). Since, within a KD, there is a change in both m_l and m_s when going from one eigenvector to the other, the operators μ_+ and μ_- cannot couple these states to each other. Explicitly, for KD1 for example, we obtain

$$\big\langle d_{+2}, -\tfrac{1}{2}\big|\mu_\pm\big|d_{+2}, -\tfrac{1}{2}\big\rangle = 0 \tag{5.32}$$

$$\big\langle d_{+2}, -\tfrac{1}{2}\big|\mu_\pm\big|d_{-2}, +\tfrac{1}{2}\big\rangle = 0 \tag{5.33}$$

$$\big\langle d_{-2}, +\tfrac{1}{2}\big|\mu_\pm\big|d_{-2}, +\tfrac{1}{2}\big\rangle = 0 \tag{5.34}$$

and in a similar way for KDs 2 through 4. Thus, up to first order, a magnetic field applied perpendicular to the crystal c-axis is not capable of lifting the degeneracies of the 4 KDs given in equations (5.21)-(5.24). Comparing these results to equation (5.30) we conclude that, for the 8 sublevels of the KDs 1 through 4, $g_{\perp} = 0$. This arises from the effect of both the crystal field of $\mathrm{C_{3v}}$ symmetry and SOC in decoupling and isolating KDs with the properties mentioned above. This is not the case for KD5, given in equation (5.25). In this case,

$$\big\langle d_0, -\tfrac{1}{2}\big|\mu_\pm\big|d_0, +\tfrac{1}{2}\big\rangle \neq 0 \tag{5.35}$$

and the degeneracy of this KD is broken in the presence of a magnetic field perpendicular to the c-axis of the crystal.

We can consider in addition the effect of spin-orbit coupling in mixing the eigenstates presented in equations (5.21-5.25). Spin-orbit coupling is responsible for mixing between the eigenstates of KD2 and KD3 (equations (5.22) and (5.23)). Since both of these KDs show $g_{\perp} = 0$, this mixing does not modify the expected value of $g_{\perp}$ in neither KD. In contrast, the SOC induced mixing between KD4 and KD5 causes some deviation of $g_\perp$ from 0 in KD4, since $g_\perp \neq 0$ in KD5. The values of $g_\parallel$ and $g_\perp$ for one electron in each of the KDs described in this section are presented in table 5.3.

From the 5 KDs in equations (5.21-5.25), one KD is the ground state and one KD is the excited state that we address in our experiments. As said before, our group-theoretical approach cannot identify the ordering in energy of these 5 KDs. However, by looking at the g-factor properties of the KDs in table 5.3 we can check which ones show consistent behavior with that of the observed ground and excited state. For the observed ground state, we found $|g_\parallel| < 2$ and $g_\perp = 0$. Concerning possible values for the orbital reduction factor k, by definition $k < 1$, and we must have $k > 0.1$ since $|g_\parallel|$ deviates substantially from 2. This suggests that KD2 is the ground state. For the excited state, we also have $|g_\parallel| < 2$, but with $g_\perp \gtrapprox 0$. This suggests KD4 is the excited state we observed in our experiments. In addition, the optical transition observed is mainly polarized along the crystal c-axis of the defect. Careful analysis of the selection rules associated with the double trigonal group (which includes, besides the spatial symmetry, the spin of the electron) has been reported by Kunzer *et al.*[144]. Comparing their results to the considerations presented in the previous paragraphs confirms that the transition between KD2 and KD4 is predominantly polarized along the crystal c-axis, as observed. Finally, we note that we could not experimentally identify secondary ZPLs corresponding to transitions between other sets of KDs, even though they are allowed by symmetry. This could be explained by a series of factors. On the one hand, some of the KDs treated could have energies above the conduction band edge in the crystal, which would impede the observation of optical transitions from and into these levels. On the other hand, the presence of these lines could be masked by the intense phonon sideband at the red side of the ZPL, or the associated photon energies fall outside our detection window.

5.17.3 Validity of our assumptions

The model considered here is capable of qualitatively informing us about the behavior of orbitals with d character in the presence of trigonal crystal field and spin orbit coupling. It is clear that the full description of the configuration of the defect is far more subtle than the simple model applied here. We intend to comment on this in the next paragraphs.

Table 5.3: The g-factors of the Kramers Doublets originated due to spin-orbit coupling within each subspace of the electronic eigenstates in a field of C_{3v} symmetry. Spin-orbit coupling is added as a perturbation, and included up to first order. The parameters λ and δ are as defined in the text and in Fig. 5.14. Note that the g-factor values in this table can take on negative values, while in our experimental analysis we can only extract $|g_{||}|$ and $|g_{\perp}|$.

C_{3v}	Spin-Orbit	$g_{\parallel}$	$g_{\perp}$
Doublet, $m_l = \pm 2$	KD1, eq. 5.21	$2(2k+1)$	0
	KD2, eq. 5.22	$2(2k-1)$	0
Doublet, $m_l = \pm 1$	KD3, eq. 5.23	$2(k+1)$	0
	KD4, eq. 5.24	$2(k-1)$	$0 + \propto \frac{\lambda}{\delta}$
Singlet, $m_l = 0$	KD5, eq. 5.25	2	$2 - \propto \frac{\lambda}{\delta}$

Symmetry of the crystal field. In our derivation, we assume that the trigonal crystal field is the prevailing term in the Hamiltonian describing the defect. This assumption is not rigorously correct, since the symmetry of defects in SiC is more accurately described by a ligand field of cubic symmetry – which determine most of its ground and excited state properties. This field is modified in the presence of axial symmetry, as is the case for defects in hexagonal lattice sites, which is generally included as a first-order perturbation term in the Hamiltonian. Nonetheless, it can be shown[142, 145] that the large anisotropy in the Zeeman response described above, with the cancelation of $g_{\perp}$, is also observed in the case of a cubic field with trigonal distortion and spin-orbit coupling of similar magnitudes. The analysis, in this case, is more laborious due to the fact that mixing of the orbitals is involved, and calculating the matrix elements of the operators $L_{\pm}$, $S_{\pm}$, L_z and S_z is less trivial. Furthermore, this analysis would not increase our level of understanding of the system at this point, since we were only capable of observing transitions between the sublevels of two KDs in this experiment. This approach would be more profitable if transitions between other sets of KDs were observed, allowing us to unravel several parameters associated with the system, such as the strength of the spin-orbit coupling and trigonal crystal field.

Charge state of the defect. Similarly, it can be shown that the considerations presented here can be expanded to configurations where the 4d orbitals are filled by multiple electrons (for instance, a defect in a configuration $4d^3$). In this case, a doubly degenerate orbital configuration (in symmetry terms, a configuration of the kind ^{m}E, where m is the spin multiplicity) in the presence of a crystal field of C_{3v} symmetry gives rise to at least one KD with $g_\perp = 0$ when SOC is taken into account. Nonetheless, only a negatively charged Mo in a Si substitutional site would give rise to a defect in the configuration $4d^3$. The absence of the ZPL in n-doped samples indicates that this is unlikely.

In addition, a similar group theoretical analysis can show that one hole in a bonding orbital of symmetry E would also give rise to $g_\perp = 0$. Thus, the features observed here could also correspond to a positively charged $\mathrm{Mo}_{\mathrm{V_{Si}-V_C}}$ defect (where one of the six Mo electrons participating in bonding is lost to the crystal lattice). Due to the strong hybridization between the Mo and the divacancy orbitals in this case, the description of this case is more subtle and will not be performed here.

5.17.4 Summary

We showed that an analysis of the effect of the defect symmetry on the Zeeman energy splittings of its ground and excited states, combined with the experimental observations, helps us unravel the configuration of the defect studied in this work. We show that, in C_{3v} symmetry, a combination of the crystal field and spin-orbit interaction is responsible for the strong magnetic anisotropy observed experimentally. Furthermore, the fact that the defect studied in this work is only observed optically in samples which are p-doped indicates that the charge of the defect is more likely positive than negative. In this way, we conclude that the most probable configuration of our defect is a Mo ion on a Si substitutional site of h symmetry, with a charge +1, which can be approximately described by a Mo atom in a $4d^1$ configuration. The absence of other lines associated with the defect prevents us from providing a more accurate description of the system. Nonetheless, we have developed a qualitative description based on symmetry, which explains the Zeeman splittings observed. The considerations presented here allow us to predict and rationalize the presence of strong anisotropy in other transition-metal defects in SiC. We expect neutrally charged vanadium defects in hexagonal lattice sites to show a magnetic behavior similar to the one observed in the Mo defects investigated in this work.

References

1. Bartholin, E. *Experimenta cristalli islandici* (Copenhagen, 1669).
2. Uhlenbeck, G. E. & Goudsmit, S. Spinning electrons and the structure of spectra. *Nature* **117,** 264 (1926).
3. Thomson, W. XIX. On the electro-dynamic qualities of metals:—Effects of magnetization on the electric conductivity of nickel and of iron. *Proceedings of the Royal Society of London* **8,** 546–550 (1857).
4. Gerlach, W. & Stern, O. Der experimentelle nachweis der richtungsquantelung im magnetfeld. *Zeitschrift für Physik* **9,** 349–352 (1922).
5. Cohen-Tannoudji, C., Diu, B. & Laloe, F. *Quantum Mechanics* (Wiley, 1991).
6. R. Hughes, e. a. A Quantum Information Science and Technology Roadmap (2004).
7. Loss, D. & DiVincenzo, D. P. Quantum computation with quantum dots. *Physical Review A* **57,** 120 (1998).
8. Hensen, B. *et al.* Loophole-free Bell inequality violation using electron spins separated by 1.3 kilometres. *Nature* **526,** 682 (2015).
9. Dyakonov, M. & Perel, V. *Optical orientation* (North-Holland, Amsterdam, 1984).
10. Fox, M. *Optical Properties of Solids (2nd ed.)* (OUP Oxford, 2010).
11. Denega, S. Z. *Coherent control of electron spin dynamics in nano-engineered semiconductor structures* (PhD Thesis, University Library Groningen, 2011).
12. Kikkawa, J., Smorchkova, I., Samarth, N & Awschalom, D. Room-temperature spin memory in two-dimensional electron gases. *Science* **277,** 1284–1287 (1997).
13. Kikkawa, J. & Awschalom, D. Resonant spin amplification in n-type GaAs. *Physical Review Letters* **80,** 4313 (1998).

14. Denega, S. *et al.* Suppressed spin dephasing for two-dimensional and bulk electrons in GaAs wires due to engineered cancellation of spin-orbit interaction terms. *Physical Review B* **81,** 153302 (2010).
15. Fleischhauer, M., Imamoglu, A. & Marangos, J. P. Electromagnetically induced transparency: Optics in coherent media. *Rev. Mod. Phys.* **77,** 633 (2005).
16. Azzam, R. M. A. & Bashara, N. *Ellipsometry and polarized light* (North-Holland, 1987).
17. Roos, B. O. & Malmqvist, P.-Å. On the Effects of Spin–Orbit Coupling on Molecular Properties: Dipole Moment and Polarizability of PbO and Spectroscopic Constants for the Ground and Excited States. *Advances in Quantum Chemistry* **47,** 37–49 (2004).
18. Roos, B. O. & Malmqvist, P.-Å. Relativistic quantum chemistry: the multiconfigurational approach. *Physical Chemistry Chemical Physics* **6,** 2919–2927 (2004).
19. Desclaux, J. & Pyykko, P. Relativistic and non-relativistic Hartree-Fock one-centre expansion calculations for the series CH4 to PbH4 within the spherical approximation. *Chemical Physics Letters* **29,** 534–539 (1974).
20. Pyykkö, P. in *Advances in quantum chemistry* 353–409 (Elsevier, 1978).
21. Pitzer, K. S. Relativistic effects on chemical properties. *Accounts of Chemical Research* **12,** 271–276 (1979).
22. Pyykko, P. & Desclaux, J. P. Relativity and the periodic system of elements. *Accounts of Chemical Research* **12,** 276–281 (1979).
23. Andersson, K *et al. MOLCAS, version 6.4; Department of Theoretical Chemistry, Chemical Centre, University of Lund: Lund, Sweden* (2006).
24. Jensen, F. *Introduction to Computational Chemistry* (Wiley, 2013).
25. Malmqvist, P. Å., Rendell, A. & Roos, B. O. The restricted active space self-consistent-field method, implemented with a split graph unitary group approach. *Journal of Physical Chemistry* **94,** 5477–5482 (1990).
26. Andersson, K., Malmqvist, P.-Å. & Roos, B. O. Second-order perturbation theory with a complete active space self-consistent field reference function. *The Journal of chemical physics* **96,** 1218–1226 (1992).

27. Malmqvist, P. Å., Roos, B. O. & Schimmelpfennig, B. The restricted active space (RAS) state interaction approach with spin–orbit coupling. *Chemical physics letters* **357,** 230–240 (2002).
28. Hohenberg, P. & Kohn, W. Inhomogeneous electron gas. *Physical review* **136,** B864 (1964).
29. Runge, E. & Gross, E. K. Density-functional theory for time-dependent systems. *Physical Review Letters* **52,** 997 (1984).
30. Wang, F. & Ziegler, T. A simplified relativistic time-dependent density-functional theory formalism for the calculations of excitation energies including spin-orbit coupling effect. *The Journal of chemical physics* **123,** 154102 (2005).
31. Velde te, G. t. *et al.* Chemistry with ADF. *Journal of Computational Chemistry* **22,** 931–967 (2001).
32. Guerra, C. F., Snijders, J., Te Velde, G & Baerends, E. Towards an order-N DFT method. *Theoretical Chemistry Accounts* **99,** 391–403 (1998).
33. Grynberg, G., Aspect, A., Fabre, C. & Cohen-Tannoudji, C. *Introduction to Quantum Optics: From the Semi-classical Approach to Quantized Light* (Cambridge University Press, 2010).
34. Foot, C. & Foot, D. *Atomic Physics* (OUP Oxford, 2005).
35. Atkins, P. & Friedman, R. *Molecular Quantum Mechanics* (OUP Oxford, 2011).
36. Dediu, V. A., Hueso, L. E., Bergenti, I. & Taliani, C. Spin routes in organic semiconductors. *Nature materials* **8,** 707 (2009).
37. Chu, Y. & Lukin, M. D. *Quantum optics with nitrogen-vacancy centers in diamond* 2015.
38. Widmark, P.-O., Malmqvist, P.-Å. & Roos, B. O. Density matrix averaged atomic natural orbital (ANO) basis sets for correlated molecular wave functions. *Theoretica chimica acta* **77,** 291–306 (1990).
39. Sun, Y. *et al.* Management of singlet and triplet excitons for efficient white organic light-emitting devices. *Nature* **440,** 908 (2006).
40. Vardeny, V. Spintronics: Organics strike back. *Nature materials* **8,** 91 (2009).
41. Dediu, V. A., Hueso, L. E., Bergenti, I. & Taliani, C. Spin routes in organic semiconductors. *Nature materials* **8,** 707 (2009).

42. Lupton, J. M., McCamey, D. R. & Boehme, C. Coherent spin manipulation in molecular semiconductors: getting a handle on organic spintronics. *ChemPhysChem* **11,** 3040–3058 (2010).
43. Bobbert, P., Wagemans, W, Van Oost, F., Koopmans, B & Wohlgenannt, M. Theory for spin diffusion in disordered organic semiconductors. *Physical review letters* **102,** 156604 (2009).
44. Sanvito, S. Molecular spintronics: The rise of spinterface science. *Nature Physics* **6,** 562 (2010).
45. Diaconu, C. *et al.* Circularly polarized photoluminescence from platinum porphyrins in organic hosts: Magnetic field and temperature dependence. *Journal of Applied Physics* **109,** 073513 (2011).
46. Awschalom, D. D. & Kikkawa, J. M. Electron spin and optical coherence in semiconductors. *Physics Today* **52,** 33–39 (1999).
47. Yersin, H. & Strasser, J. Triplets in metal–organic compounds. Chemical tunability of relaxation dynamics. *Coordination Chemistry Reviews* **208,** 331–364 (2000).
48. Yersin, H. *Organometallic triplet emitters for OLED applications: controlling emission properties by chemical variation* in *Organic Light-Emitting Materials and Devices VII* **5214** (2004), 124–133.
49. Marian, C. M. Spin-orbit coupling in molecules. *Reviews in computational chemistry* **17,** 99–204 (2001).
50. Atherton, N. *Principles of electron spin resonance* (Ellis Horwood, 1993).
51. Gerardot, B. D. *et al.* Optical pumping of a single hole spin in a quantum dot. *Nature* **451,** 441 (2008).
52. Smith, A. R., Burn, P. L. & Powell, B. J. Spin–Orbit Coupling in Phosphorescent Iridium (III) Complexes. *ChemPhysChem* **12,** 2429–2438 (2011).
53. Albrecht, M. & van Koten, G. Platinum group organometallics based on “pincer” complexes: sensors, switches, and catalysts. *Angewandte Chemie International Edition* **40,** 3750–3781 (2001).
54. Boyd, R. W. *Nonlinear optics* (Academic press, 2008).
55. Lovett, D. *Tensor properties of crystals* (CRC Press, 1999).
56. Denega, S. *et al.* Ultrafast mapping of optical polarization states onto spin coherence of localized electrons in a semiconductor. *arXiv preprint arXiv:1103.4307* (2011).

57. Sharnoff, M. ESR-Produced Modulation of Triplet Phosphorescence. *The Journal of Chemical Physics* **46,** 3263–3264 (1967).
58. Köhler, J. Magnetic resonance of a single molecular spin. *Physics reports* **310,** 261–339 (1999).
59. Atatüre, M., Dreiser, J., Badolato, A. & Imamoglu, A. Observation of Faraday rotation from a single confined spin. *Nature Physics* **3,** 101–106 (2007).
60. Vrijen, R. & Yablonovitch, E. A spin-coherent semiconductor photo-detector for quantum communication. *Physica E: Low-dimensional Systems and Nanostructures* **10,** 569–575 (2001).
61. Kosaka, H. *et al.* Coherent transfer of light polarization to electron spins in a semiconductor. *Physical review letters* **100,** 096602 (2008).
62. Kosaka, H. *et al.* Spin state tomography of optically injected electrons in a semiconductor. *Nature* **457,** 702–705 (2009).
63. Jones, R. C. A New Calculus for the Treatment of Optical SystemsI. Description and Discussion of the Calculus. *JOSA* **31,** 488–493 (1941).
64. Moerner, W., Orrit, M., Wild, U. & Basché, T. *Single-Molecule Optical Detection, Imaging and Spectroscopy* ISBN: 9783527614707 (Wiley, 2008).
65. Van Lenthe, E., Baerends, E.-J. & Snijders, J. G. Relativistic regular two-component Hamiltonians. *The Journal of chemical physics* **99,** 4597–4610 (1993).
66. Van Lenthe, E., Baerends, E.-J. & Snijders, J. G. Relativistic total energy using regular approximations. *The Journal of chemical physics* **101,** 9783–9792 (1994).
67. Van Lenthe, E, Snijders, J. & Baerends, E. The zero-order regular approximation for relativistic effects: The effect of spin–orbit coupling in closed shell molecules. *The Journal of chemical physics* **105,** 6505–6516 (1996).
68. Van Lenthe, E., Ehlers, A. & Baerends, E.-J. Geometry optimizations in the zero order regular approximation for relativistic effects. *The Journal of chemical physics* **110,** 8943–8953 (1999).
69. Stephens, P., Devlin, F., Chabalowski, C. & Frisch, M. J. Ab initio calculation of vibrational absorption and circular dichroism spectra using density functional force fields. *The Journal of Physical Chemistry* **98,** 11623–11627 (1994).

70. Van Lenthe, E. & Baerends, E. J. Optimized Slater-type basis sets for the elements 1–118. *Journal of computational chemistry* **24,** 1142–1156 (2003).
71. Chong, D. P., Van Lenthe, E., Van Gisbergen, S. & Baerends, E. J. Even-tempered slater-type orbitals revisited: From hydrogen to krypton. *Journal of computational chemistry* **25,** 1030–1036 (2004).
72. Chong, D. Augmenting basis set for time-dependent density functional theory calculation of excitation energies: Slater-type orbitals for hydrogen to krypton. *Molecular Physics* **103,** 749–761 (2005).
73. Van Gisbergen, S., Snijders, J. & Baerends, E. Implementation of time-dependent density functional response equations. *Computer Physics Communications* **118,** 119–138 (1999).
74. Van Gisbergen, S. *et al.* Density-functional-theory response-property calculations with accurate exchange-correlation potentials. *Physical Review A* **57,** 2556 (1998).
75. Jamorski, C., Casida, M. E. & Salahub, D. R. Dynamic polarizabilities and excitation spectra from a molecular implementation of time-dependent density-functional response theory: N2 as a case study. *The Journal of chemical physics* **104,** 5134–5147 (1996).
76. Bauernschmitt, R. & Ahlrichs, R. Treatment of electronic excitations within the adiabatic approximation of time dependent density functional theory. *Chemical Physics Letters* **256,** 454–464 (1996).
77. Roos, B. O., Lindh, R., Malmqvist, P.-Å., Veryazov, V. & Widmark, P.-O. New relativistic ANO basis sets for transition metal atoms. *The Journal of Physical Chemistry A* **109,** 6575–6579 (2005).
78. Roos, B. O., Lindh, R., Malmqvist, P.-Å., Veryazov, V. & Widmark, P.-O. Main group atoms and dimers studied with a new relativistic ANO basis set. *The Journal of Physical Chemistry A* **108,** 2851–2858 (2004).
79. Douglas, M. & Kroll, N. *Acta Physica* **82** (1974).
80. Sommer, J. R. *et al.* Photophysical properties of near-infrared phosphorescent π-extended platinum porphyrins. *Chemistry of Materials* **23,** 5296–5304 (2011).
81. Berg, H. *Random Walks in Biology* (Princeton University Press, 1993).

82. Tammann, G. & Hesse, W. Die Abhängigkeit der Viscosität von der Temperatur bie unterkühlten Flüssigkeiten. *Zeitschrift für anorganische und allgemeine Chemie* **156,** 245–257 (1926).
83. DiVincenzo, D. P. *et al.* The physical implementation of quantum computation. *arXiv preprint quant-ph/0002077* (2000).
84. Clark, S. M. *et al.* Ultrafast optical spin echo for electron spins in semiconductors. *Physical review letters* **102,** 247601 (2009).
85. Berezovsky, J *et al.* Nondestructive optical measurements of a single electron spin in a quantum dot. *Science* **314,** 1916–1920 (2006).
86. Zwier, O. V., O'Shea, D., Onur, A. R. & van der Wal, C. H. All–optical coherent population trapping with defect spin ensembles in silicon carbide. *Sci. Rep.* **5,** 10931 (2015).
87. Zwier, O. V. *Two-laser spectroscopy and coherent manipulation of color-center spin ensembles in silicon carbide* (University of Groningen, 2016).
88. Falk, A. L. *et al.* Polytype control of spin qubits in silicon carbide. *Nature Communications* **4,** 1819 (2013).
89. Magnusson, B. & Janzén, E. Optical characterization of deep level defects in SiC. *Mater. Sci. Forum* **483,** 341–346 (2005).
90. Baranov, P. G. *et al.* EPR identification of the triplet ground state and photoinduced population inversion for a Si-C divacancy in silicon carbide. *Journal of Experimental and Theoretical Physics Letters* **82,** 441–443 (2005).
91. Goldman, M. L. *et al.* Phonon-induced population dynamics and intersystem crossing in nitrogen-vacancy centers. *Physical review letters* **114,** 145502 (2015).
92. Hendriks, F. *Spin-active colour centres in Silicon Carbide, fundamental description and novel experimental techniques* (Master Thesis, University of Groningen, 2018).
93. Xu, C. *et al.* Temperature dependence of refractive indices for 4H-and 6H-SiC. *Journal of Applied Physics* **115,** 113501 (2014).
94. Gao, W., Imamoglu, A, Bernien, H & Hanson, R. Coherent manipulation, measurement and entanglement of individual solid-state spins using optical fields. *Nat. Phot.* **9,** 363 (2015).

95. Togan, E. *et al.* Quantum entanglement between an optical photon and a solid-state spin qubit. *Nature* **466,** 730 (2010).

96. Dolde, F. *et al.* High-fidelity spin entanglement using optimal control. *Nat. Commun.* **5,** 3371 (2014).

97. Klimov, P. V., Falk, A. L., Christle, D. J., Dobrovitski, V. V. & Awschalom, D. D. Quantum entanglement at ambient conditions in a macroscopic solid-state spin ensemble. *Sci. Adv.* **1,** e1501015 (2015).

98. Hensen, B. *et al.* Loophole-free Bell inequality violation using electron spins separated by 1.3 kilometres. *Nature* **526,** 682–686 (2015).

99. Kalb, N. *et al.* Entanglement distillation between solid-state quantum network nodes. *Science* **356,** 928–932 (2017).

100. Budker, D. & Romalis, M. Optical magnetometry. *Nat. Phys.* **3,** 227–234 (2007).

101. Balasubramanian, G. *et al.* Nanoscale imaging magnetometry with diamond spins under ambient conditions. *Nature* **455,** 648–651 (2008).

102. Dolde, F. *et al.* Electric-field sensing using single diamond spins. *Nat. Phys.* **7,** 459–463 (2011).

103. Kraus, H *et al.* Magnetic field and temperature sensing with atomic-scale spin defects in silicon carbide. *Sci. Rep.* **4,** 5303 (2014).

104. Bonato, C. *et al.* Optimized quantum sensing with a single electron spin using real-time adaptive measurements. *Nat. Nanotechnol.* **11,** 247–252 (2016).

105. Dobrovitski, V., Fuchs, G., Falk, A., Santori, C & Awschalom, D. Quantum control over single spins in diamond. *Annu. Rev. Condens. Matter Phys.* **4,** 23–50 (2013).

106. Childress, L. & Hanson, R. Diamond NV centers for quantum computing and quantum networks. *MRS Bull* **38,** 134–138 (2013).

107. Doherty, M. W., Manson, N. B., Delaney, P. & Hollenberg, L. C. The negatively charged nitrogen-vacancy centre in diamond: the electronic solution. *New Journal of Physics* **13,** 025019 (2011).

108. Maze, J. *et al.* Properties of nitrogen-vacancy centers in diamond: the group theoretic approach. *New Journal of Physics* **13,** 025025 (2011).

109. Thiering, G. & Gali, A. Ab initio calculation of spin-orbit coupling for an NV center in diamond exhibiting dynamic Jahn-Teller effect. *Physical Review B* **96,** 081115 (2017).

110. Radnaev, A. *et al.* A quantum memory with telecom-wavelength conversion. *Nat. Phys.* **6,** 894–899 (2010).

111. Zaske, S. *et al.* Visible-to-telecom quantum frequency conversion of light from a single quantum emitter. *Phys. Rev. Lett.* **109,** 147404 (2012).

112. Dréau, A., Tcheborateva, A., Mahdaoui, A. E., Bonato, C. & Hanson, R. Quantum frequency conversion to telecom of single photons from a nitrogen-vacancy center in diamond. *preprint arXiv:1801.03304* (2018).

113. Weber, J. *et al.* Quantum computing with defects. *Proc. Natl. Acad. Sci. U.S.A.* **107,** 8513 (2010).

114. Weber, J. *et al.* Defects in SiC for quantum computing. *J. Appl. Phys.* **109,** 102417 (2011).

115. Von Bardeleben, H. *et al.* NV centers in 3C, 4H, and 6H silicon carbide: A variable platform for solid-state qubits and nanosensors. *Phys. Rev. B* **94,** 121202 (2016).

116. Zargaleh, S. *et al.* Evidence for near-infrared photoluminescence of nitrogen vacancy centers in 4H-SiC. *Phys. Rev. B* **94,** 060102 (2016).

117. Friedrichs, P., Kimoto, T., Ley, L. & Pensl, G. *Silicon Carbide* (Wiley, Weinheim, 2010).

118. Song, B.-S., Yamada, S., Asano, T. & Noda, S. Demonstration of two-dimensional photonic crystals based on silicon carbide. *Opt. Express* **19,** 11084–11089 (2011).

119. Koehl, W. F., Buckley, B. B., Heremans, F. J., Calusine, G. & Awschalom, D. D. Room temperature coherent control of defect spin qubits in silicon carbide. *Nature* **479,** 84–87 (2011).

120. Christle, D. J. *et al.* Isolated electron spins in silicon carbide with millisecond coherence times. *Nat. Mater.* **14,** 160 (2015).

121. Riedel, D *et al.* Resonant addressing and manipulation of silicon vacancy qubits in silicon carbide. *Phys. Rev. Lett.* **109,** 226402 (2012).

122. Kraus, H *et al.* Room-temperature quantum microwave emitters based on spin defects in silicon carbide. *Nat. Phys.* **10,** 157 (2014).

123. Widmann, M. *et al.* Coherent control of single spins in silicon carbide at room temperature. *Nat. Mater.* **14,** 164 (2015).

124. Hobgood, H. M. *et al.* Semi–insulating 6H—SiC grown by physical vapor transport. *Appl. Phys. Lett.* **66,** 1364 (1995).

125. Baur, J, Kunzer, M & Schneider, J. Transition metals in SiC polytypes, as studied by magnetic resonance techniques. *Phys. Status Solidi A* **162,** 153–172 (1997).

126. Ivády, V., Gällström, A., Son, N. T., Janzén, E. & Gali, A. Asymmetric Split-Vacancy Defects in SiC Polytypes: A Combined Theoretical and Electron Spin Resonance Study. *Phys. Rev. Lett.* **107,** 195501 (2011).

127. Son, N. T. *et al.* Electron paramagnetic resonance and theoretical studies of Nb in 4H-and 6H-SiC. *J. Appl. Phys.* **112,** 083711 (2012).

128. Koehl, W. F. *et al.* Resonant optical spectroscopy and coherent control of Cr4+ spin ensembles in SiC and GaN. *Phys. Rev. B* **95,** 035207 (2017).

129. Csóré, A., Gällström, A., Janzén, E. & Gali, Á. Investigation of Mo Defects in 4H-SiC by Means of Density Functional Theory. *Mater. Sci. Forum* **858,** 261–264 (2016).

130. Dombrowski, K. *et al.* Identification of molybdenum in 6H-SiC by magnetic resonance techniques. *Phys. Rev. B* **54,** 7323 (1996).

131. Kimoto, T., Nakajima, T., Matsunami, H., Nakata, T. & Inoue, M. Formation of semi-insulating 6H-SiC layers by vanadium ion implantations. *Appl. Phys. Lett.* **69,** 1113 (1996).

132. Gällström, A., Magnusson, B. & Janzén, E. Optical identification of Mo related deep level defect in 4H and 6H SiC. *Mater. Sci. Forum* **615,** 405–408 (2009).

133. Gällström, A. *Optical characterization of deep level defects in SiC* (Linköping University, 2015).

134. Manson, N. & Wei, C. Transient hole burning in NV centre in diamond. *J. Lumin.* **58,** 158–160 (1994).

135. Santori, C. *et al.* Coherent population trapping in diamond NV centers at zero magnetic field. *Opt. Express* **14,** 7986–7994 (2006).

136. Kimble, H. J. The quantum internet. *Nature* **453,** 1023 (2008).

137. Beha, K., Batalov, A., Manson, N. B., Bratschitsch, R. & Leitenstorfer, A. Optimum photoluminescence excitation and recharging cycle of single nitrogen-vacancy centers in ultrapure diamond. *Phys. Rev. Lett.* **109,** 097404 (2012).

138. Wolfowicz, G. *et al.* Optical charge state control of spin defects in 4H-SiC. *Nat. Commun.* **8,** 1876 (2017).

139. Abragam, A. & Bleaney, B. *Electron Paramagnetic Resonance Of Transition Ions* (Clarendon Press, Oxford, 1970).

140. Ivády, V. *et al. Transition Metal Defects in Cubic and Hexagonal Polytypes of SiC: Site Selection, Magnetic and Optical Properties from ab initio Calculations* in *Materials Science Forum* **717** (2012), 205–210.

141. Baur, J, Kunzer, M & Schneider, J. Transition metals in SiC polytypes, as studied by magnetic resonance techniques. *physica status solidi (a)* **162,** 153–172 (1997).

142. Abragam, A. & Bleaney, B. *Electron paramagnetic resonance of transition ions* (OUP Oxford, 2012).

143. Chibotaru, L. F., Hendrickx, M. F., Clima, S., Larionova, J. & Ceulemans, A. Magnetic anisotropy of $[\mathrm{Mo(CN)_7}]^{4-}$anions and fragments of cyano-bridged magnetic networks. *The Journal of Physical Chemistry A* **109,** 7251–7257 (2005).

144. Kunzer, M, Müller, H. & Kaufmann, U. Magnetic circular dichroism and site-selective optically detected magnetic resonance of the deep amphoteric vanadium impurity in 6H-SiC. *Physical Review B* **48,** 10846 (1993).

145. Dietz, R., Kamimura, H, Sturge, M. & Yariv, A. Electronic structure of copper impurities in ZnO. *Physical Review* **132,** 1559 (1963).

Scientific summary

Optical preparation and detection of spin coherence in molecules and crystal defects

This thesis presents the results of research aimed at exploring several possibilities of optically-induced electron spin coherence in molecules and crystal defects. In our approach we have performed a theoretical investigation of underlying fundamentals and forthcoming requirements (Chapter 2-4), as well as an experimental investigation of a system demonstrating optically induced electron spin coherence (Chapter 5). We believe that the scientific progress of our work contributes to a better characterization of various materials with opto-electronic functionality and provides better probing tools. Also, we believe our work is relevant for new quantum-information functionalities based on the selective coupling of photons to electronic spin states.

For atoms and crystals with a high symmetry, the optical selection rules for electronic transitions are well covered in physics textbooks. However, how optical selection rules change when the high symmetry is gradually distorted is less understood. In Chapter 2, we present a detailed analysis of how a gradual symmetry distortion leads to a complete alteration of optical selection rules. As a model system, we consider the transitions between $1s$ and $2p$ sublevels of the hydrogen atom, which get distorted by placing charged particles in its environment. Upon increasing the distortion, part of the optical selection rules evolve from circular via elliptical to linear character, with an associated evolution between allowed and forbidden transitions. Our presentation combines an analytical approach with quantitative results from numerical simulations, thus providing insight in how the evolution occurs as a function of the strength of the distortion. This study provides a useful theoretical framework for more complex systems. Moreover, it paves the road for manipulation of optical selection rules. The ability to manipulate selection rules allows to better control the interaction of photons and electrons, potentially allowing for new ways to control the flow of information within the field of quantum information.

Organic molecules are increasingly used for opto-electronic devices, because of their chemical tunability, low-cost and ease of processing. In such devices, the ratio of singlet to triplet excitons can be an important performance parameter. Moreover, because of the many interesting spin-related phenomena discovered in organic semiconductors and molecules, their application into organic spintronics is very promising. Both for organic opto-electronics and spintronics, being able to control and probe triplet spin states will be of great value. Optical polarization proves to be a promising candidate for this. One way to study correlations between spin and optical polarization is the Time-Resolved Faraday Rotation (TRFR) technique. Within this all-optical non-invasive pump-probe technique, a pump pulse induces spin polarization, after which the spin dynamics are probed by the polarization rotation of a probe pulse. In Chapter 3, we investigate how this technique allows for optical control and probing of triplet-exciton spin dynamics in metal-organic molecules. In our theoretical analysis, an ultrashort polarized pump pulse brings the molecular system in a superposition of triplet excited state sublevels. We derive how the polarization of a comparable but detuned probe pulse is affected upon transmission, from which the requirements for polarization rotation follow. Using the results of ab initio calculations, we calculate the time dependence of the polarization rotation angle and of the expectation value of the total electronic angular momentum. Both show an oscillation with a frequency corresponding to the sublevel splitting, implying that the oscillation of polarization rotation is a suitable measure for the coherent spin dynamics.

Color centers in wide-bandgap semiconductors are attractive systems for quantum technologies since they can combine long-coherent electronic spin and bright optical properties. Several suitable centers have been identified, most famously the nitrogen-vacancy defect in diamond. In Chapter 4, we propose to use the TRFR technique (usually being applied to materials with strong spin-orbit coupling) to characterize spin-active color centers in materials with negligible spin-orbit coupling, like silicon carbide and diamond. The fundamentals and scenario for a TRFR experiment are worked out in detail for a homogeneous ensemble of c-axis divacancies (pairs of missing neighboring silicon and carbon atoms along the growth axis) in silicon carbide. Under certain circumstances, the material is birefringent (two different refractive indices). Moreover, one of the indices of refraction oscillates as a function of time in the presence of coherences. Due to this time-dependent birefringence, a probe pulse will undergo a polarization rotation as a function of the pump-probe delay time. This polarization rotation is a measure for the spin coherence of the triplet excited state.

Integration of semiconductor color centers in communication technology is hindered by the fact that their optical transitions lie outside telecom wavelength bands. Several transition-metal impurities in silicon carbide do emit at and near telecom wavelengths, but knowledge about their spin and optical properties is incomplete. In Chapter 5, we present all-optical identification and coherent control of molybdenum-impurity spins in silicon carbide with transitions at near-infrared wavelengths. Our results identify spin $S = 1/2$ for both the electronic ground and excited state, with highly anisotropic spin properties that we apply for implementing optical control of ground-state spin coherence. Our results show optical lifetimes of $\sim$60 ns and inhomogeneous spin dephasing times of $\sim$0.3 μs, establishing relevance for quantum spin-photon interfacing.

Wetenschappelijke samenvatting

Optische voorbereiding en detectie van spincoherentie in moleculen en kristaldefecten

Dit proefschrift presenteert de resultaten van onderzoek bedoeld om verschillende mogelijkheden te onderzoeken van optisch geïnduceerde elektron spincoherentie in moleculen en kristaldefecten. In onze aanpak hebben we een theoretisch onderzoek uitgevoerd van de onderliggende fundamenten en daaruit voortvloeiende vereisten (Hoofdstuk 2-4), alsook een experimenteel onderzoek van een systeem dat optisch geïnduceerde spincoherentie vertoont (Hoofdstuk 5). Wij zijn ervan overtuigd dat de wetenschappelijke vooruitgang van ons werk bijdraagt aan een betere karakterisatie van verschillende materialen met opto-elektronische functionaliteit en betere middelen aanreikt voor detectie. Tevens zijn we ervan overtuigd dat ons werk relevant is voor nieuwe kwantum-informatica functionaliteiten die gebaseerd zijn op de selectieve koppeling van fotonen en elektronische spintoestanden.

De optische selectieregels zijn voor atomen en kristallen met een hoge symmetrie goed beschreven in natuurkundeboeken. Daarentegen is er minder kennis over hoe optische selectieregels veranderen wanneer de hoge symmetrie geleidelijk wordt verstoord. In Hoofdstuk 2 presenteren we een gedetailleerde analyse van hoe een geleidelijke symmetrieverstoring leidt tot een volledige wijziging van de optische selectieregels. We nemen de transities tussen $1s$ en $2p$ sublevels van het waterstofatoom als een modelsysteem dat verstoord wordt door de plaatsing van geladen deeltjes in diens omgeving. Met het vergroten van de verstoring veranderen sommige optische selectieregels van circulair via elliptisch naar een lineair karakter, terwijl andere veranderen tussen toegestaan en verboden. Ons werk combineert een analytische benadering met kwantitatieve resultaten van numerieke simulaties, daarbij inzicht verschaffend in hoe de verandering plaats vindt als functie van de sterkte van de verstoring. Deze studie verschaft een nuttig theoretisch kader voor complexere systemen. Bovendien bereidt het de weg voor manipulatie van optische selectieregels. De mogelijkheid om selectieregels te manipuleren staat een betere controle toe van de interactie tussen fotonen en elektronen, wat mogelijkerwijs nieuwe manieren toestaat ter controle van informatiestromen binnen het veld van de kwantuminformatica.

Organische moleculen worden steeds meer gebruikt voor opto-elektronische apparaten, vanwege diens chemische afstembaarheid, lage kosten en gemak van verwerking. In dergelijke apparaten kan de ratio van singlet- en tripletexcitonen een belangrijke parameter zijn in de prestatie. Vanwege de vele interessante spin-gerelateerde fenomenen die ontdekt zijn in organische halfgeleiders en moleculen is het bovendien zo dat hun toepassing in organische spintronica erg veelbelovend is. Zowel voor de organische opto-elektronica als de spintronica zal de mogelijkheid triplet spintoestanden te controleren en detecteren van grote waarde zijn. Optische polarisatie lijkt een veelbelovende kandidaat te zijn hiervoor. Een manier om correlaties tussen spin en optische polarizatie te bestuderen is de Time-Resolved Faraday Rotation (TRFR) techniek. Via deze volledig optische niet-invasieve pump-probe techniek induceert de pump puls spinpolarisatie, waarna de spindynamica wordt gedetecteerd via de polarisatierotatie van een probe puls. In Hoofdstuk 3 onderzoeken we hoe deze techniek optische controle toestaat en de detectie van triplet-exciton spindynamica in metaal-organische moleculen. In ons voorstel brengt een ultrakorte gepolariseerde pump puls het moleculaire systeem in een superpositie van triplet aangeslagen sublevels. We leiden af hoe de polarisatie van een vergelijkbare maar niet-resonante probe puls wordt beïnvloed bij transmissie, waaruit de vereisten voor polarisatierotatie volgen. Gebruik makend van de resultaten van ab initio berekeningen, berekenen we de tijdsafhankelijkheid van de polarisatierotatiehoek en van de verwachtingswaarde van het totale elektronische impulsmoment. Beide vertonen een oscillatie met een frequentie corresponderend met de sublevel splitsing, implicerend dat de oscillatie van de polarisatierotatie een geschikte maat is voor spinprecessie.

Kleurcentra in halfgeleiders met een grote energiekloof zijn aantrekkelijke systemen voor kwantumtechnologieën omdat ze lang-coherente elektronspin combineren met helder optische eigenschappen. Verschillende geschikte centra zijn geïdentificeerd, met name het stikstof-gat defect in diamant. In Hoofdstuk 4 stellen we voor de TRFR techniek te gebruiken (gewoonlijk toegepast op materialen met sterke spin-baan koppeling) om spin-actieve kleurcentra te karakteriseren in materialen met verwaarloosbare spin-baan koppeling, zoals siliciumcarbide en diamant. De fundamenten en het scenario voor een TRFR experiment zijn in detail uitgewerkt voor een homogeen ensemble van paren van missende aangrenzende silicium- en koolstofatomen liggend langs de groeirichting van siliciumcarbide. Onder sommige omstandigheden is het materiaal dubbelbrekend (twee verschillende brekingsindices). Bovendien oscilleert een van de brekingsindices als functie van tijd onder de aanwezigheid van coherenties. Vanwege deze tijdsafhankelijke dubbelbreking zal een probe puls een polarisatierotatie ondergaan als functie van de pump-probe vertragingstijd. Deze polarisatierotatie is een maat voor de spincoherentie van de triplet aangeslagen toestand.

Integratie van halfgeleider kleurcentra binnen de communicatietechnologie wordt gehinderd door het feit dat diens optische transities buiten de telecomgolflengtebanden liggen. Verschillende transitiemetaalonzuiverheden in siliciumcarbide zenden licht uit nabij telecomgolflengtes, maar de kennis over diens spin- en optische eigenschappen is incompleet. In Hoofdstuk 5 bespreken we volledig optische identificatie en coherente controle van de spins van molybdeenonzuiverheden in siliciumcarbide met transities in het nabij-infrarode golflengteregime. Onze resultaten identificeren een spin $S = 1/2$ voor zowel de elektronische grond- als aangeslagen toestand, met zeer anisotropische spineigenschappen die toegepast worden voor de implementatie van optische controle van spincoherentie in de grondtoestand. Onze resultaten tonen optische levensduren van $\sim$60 ns en inhomogene spinontfasingstijden van $\sim$0.3 μs. Deze resultaten vertonen relevantie voor kwantumtoepassingen met spin-foton koppelingen.

Acknowledgements

The work presented in this thesis was carried out in the groups Quantum Devices (part of Physics of Nanodevices, FND) and Theoretical Chemistry, at the University of Groningen, the Netherlands, between July 2014 and July 2018. I would like to thank several persons who directly or indirectly contributed to the realization of this work.

First of all I would like to thank Caspar van der Wal, Remco Havenith, Ria Broer-Braam and Maria Loi for giving me the opportunity to work on this versatile project you have set up. I really enjoyed the fruitful collaboration. Thank you for your trust in me, for the guidelines you provided, and for the freedom to carry out the work on my own way. Caspar, thank you for the experience and fun I could have within the group! I admire your personality as much as your professional way of working and your physics intuition. The amount of empathy you display is truly exceptional for a professor. Thank you also for your always flexible attitude. Remco, thank you for always arranging time to provide help or feedback. Your commitment, experience and enthusiasm were indispensable for working out the theoretical part of my PhD. I would also like to heartily thank prof. Koehler, prof. Orrit and prof. Broer-Braam for being my reading committee, thereby making the defence possible.

Also, big thanks to my paranymphs Tom Bosma and Carmem Gilardoni for your involvement in my work. Tom, I really enjoyed the collaboration, social interaction and fun we had in the lab! Your perseverance to solve a problem is truly inspiring. Carmem, it was amazing to see you creating a whole new research track out of my work. Moreover, your enthusiasm and willingness to help were of great value! Olger Zwier, thanks for familiarizing me with all lab tools. Your software legacy was of great use to carry out our experiments. Freddie Hendriks, I enjoyed to profit from your impressive ability to easily become a theoretical and experimental expert in seemingly any topic of physics. I would like to thank the technicians Martijn de Roosz, Johan Holstein, Tom Schouten for their assistance in the lab. Xin Gui, thank you for your interest in my theoretical work and for your critical review which had a positive effect on the conclusions of Chapter 3. Merlinde Wobben, thank you for your contribution to the calculation of Franck-Condon factors in several metal-organic molecules. I would like to thank all other members of TheoChem and FND for contributing to an enjoyable time and inspiring working place! Over the years I had fruitful discussions with several scientists of which I would like to particularly thank the following persons for their inspiring visions: Hélène Bolvin, Edwin Otten, Alex de Vries, Ria Broer-Braam, Nguyen Tien Son, Ivan Ivanov, Mete Atatüre and Pepijn Pinkse.

Tenslotte wil ik mijn vrienden en (schoon)familie bedanken voor een gezonde dosis afleiding en diepgang in mijn leven die het geheel in balans houden en waardevol maken. In het bijzonder wil ik mijn ouders bedanken voor de basis die zij hebben gelegd middels hun liefde en toewijding. De vrijheid die ik dankzij jullie heb mogen genieten bood ruimte voor de ontplooiing van mijn nieuwsgierigheid die de drijfveer was voor dit werk. Tevens ben ik onmeunig veel dank verschuldigd aan de vrouw van mijn leven. Emmely, jouw liefde was en is van onschatbare waarde. Wat een voorrecht was het telkens op te kunnen laden bij jou tijdens de toch wel pittige jaren van mijn PhD!

Curriculum vitae

Gerrit Jan Jacob Lof

30 March 1988	Born in Capelle aan den IJssel, the Netherlands.
2000-2006	Bonhoeffer College Enschede, the Netherlands.
2007-2010	Bachelor Applied Physics, University of Groningen, the Netherlands.
2010-2012	Master Energy and Environmental Sciences, University of Groningen, the Netherlands.
2012-2014	Top Master Nanoscience, University of Groningen, the Netherlands.
2014-2018	Ph.D. research, Zernike Institute for Advanced Materials, University of Groningen, the Netherlands. Supervisors: prof. dr. ir. C. H. van der Wal and dr. R. W. A. Havenith. Subject: Optical preparation and detection of spin coherence in molecules and crystal defects.

List of publications

1. *Evolution of atomic optical selection rules upon gradual symmetry lowering*
   G. J. J. Lof, C. H. van der Wal, R. W. A. Havenith; submitted for publication, available at *arXiv:1810.06355* (2018).

2. *Proposal for time-resolved optical preparation and detection of triplet-exciton spin coherence in organic molecules*
   G. J. J. Lof, X. Gui, R. W. A. Havenith, C. H. van der Wal, *in preparation* (2019).

3. *Proposal for time-resolved optical probing of electronic spin coherence in divacancy defects in SiC*
   C. M. Gilardoni*, G. J. J. Lof*, F. Hendriks, R. W. A. Havenith, C. H. van der Wal, *in preparation* (2019).

4. *Identification and tunable optical coherent control of transition-metal spins in silicon carbide*
   T. Bosma*, G. J. J. Lof*, C. M. Gilardoni, F. Hendriks, O. V. Zwier, B. Magnusson, A. Ellison, A. Gällström, I. G. Ivanov, N. T. Son, R. W. A. Havenith, C. H. van der Wal; published in *npj Quantum Information* **4**, 48 (2018); also available at *arXiv:1802.06714* (2018).

   * These authors contributed equally to this work.